EFFECT OF TIG SURFACING ON FATIGUE PROPERTIES OF AISI 4340 STRUCTURAL STEEL

Ph.D. THESIS

by

SUDHIR KUMAR

**DEPARTMENT OF METALLURGICAL AND MATERIALS ENGINEERING
INDIAN INSTITUTE OF TECHNOLOGY ROORKEE
ROORKEE-247 667 (INDIA)
JUNE, 2018**

EFFECT OF TIG SURFACING ON FATIGUE PROPERTIES OF AISI 4340 STRUCTURAL STEEL

A THESIS

*Submitted in partial fulfilment of the
requirements for the award of the degree*

of

DOCTOR OF PHILOSOPHY

in

METALLURGICAL AND MATERIALS ENGINEERING

by

SUDHIR KUMAR

**DEPARTMENT OF METALLURGICAL AND MATERIALS ENGINEERING
INDIAN INSTITUTE OF TECHNOLOGY ROORKEE
ROORKEE-247 667 (INDIA)
JUNE, 2018**

INDIAN INSTITUTE OF TECHNOLOGY ROORKEE
ROORKEE

CANDIDATE'S DECLARATION

I hereby certify that the work which is being presented in the thesis entitled "**EFFECT OF TIG SURFACING ON FATIGUE PROPERTIES OF AISI 4340 STRUCTURAL STEEL**" in the partial fulfilment of the requirements for the award of the Degree of Doctor of Philosophy and submitted in the Department of Metallurgical and Materials Engineering of the Indian Institute of Technology Roorkee, Roorkee in an authentic record of my own work carried out during a period from January, 2014 to June, 2018 under the supervision of Dr. P.K. Ghosh, Vice-President, Siddharth Group of Engineering Institutions, Puttur-517581, India.

The matter presented in the thesis has not been submitted by me for the award of any other degree of this or any other Institute.

(SUDHIR KUMAR)

This is to certify that the above statement made by the candidate is correct to the best of my knowledge.

(P.K. Ghosh)
Supervisor

Date:

ABSTRACT

Surface modification can be achieved by using advanced high energy heat sources such as plasma, laser, and electron beam. These techniques use high energy concentrated beam on the work piece which generates steep thermal gradients leading to rapid solidification and quick phase transformation in the matrix of limited depth at the substrate surface. The electron beam process is widely used for surface modification of steel. But a shallow case depth (≤ 1.5 mm) of modification, requirement of high vacuum and a limited use for relatively small components make this process non-versatile for application at site. The laser beam process also has certain disadvantages like high cost of investment in the equipment, poor laser light absorption in the metal, radiation problem and requirement of highly skilled operator.

In view of the above the use of readily available autogenous tungsten inert gas (TIG) arcing process, which requires relatively lower cost of investment but provides concentric high energy arc heat source, is considered as a new alternative for surface modification of metal. The TIG arcing process is having some more advantages such as its easy applicability at site, requirement of less skilled worker, support to high heat absorption in metal and operation with relatively less environmental pollution. It makes TIG arcing process quite favourable for surface modification of steel. In this process, the heat energy is provided by an electric arc maintained between a tungsten electrode and workpiece. The TIG arcing process operates in two modes. The first mode is known as continuous current tungsten inert gas (C-TIG) arcing and second mode is known as pulse current tungsten inert gas (P-TIG) arcing. In C-TIG arcing process continuous arc conventionally acts over the surface of base plate to modify its surface, whereas in P-TIG arcing process a pulsing of arc at regular frequency operates on substrate surface for its modification under interrupted arc energy which works more precisely by controlled melting and solidification. The variable parameters in C-TIG arcing are the arc current (I), arc voltage (V) and travel speed (S) whereas in P-TIG arcing the operating parameters are frequency (f), pulse time (t_p), base time (t_b), base current (I_b), and pulse current (I_p). Thus, the control of pulse arc is comparatively more complicated than control of continuous arc due to involvement of a large number of simultaneously interactive pulse parameters. The difficulty in control of pulse parameters is effectively resolved by using a summarized influence of pulse parameters proposed earlier and defined by a dimensionless

hypothetical factor $\phi = \dfrac{I_b}{I_p} \times f \times t_b$ where, $t_b = \left[\dfrac{1}{f}\right] - t_p$ derived on the basis of the energy balance concept of the system.

The primary objective of this work is to understand the effect of single and multi-pass C-TIG arcing under different heat input on surface modification of AISI 4340 structural steel characterized by its microstructure, hardness, tensile properties and fatigue behaviour. At optimum condition of C-TIG arcing parameters the characteristics of the single and multi-pass modified surface are also compared to the same produced by using P-TIG arcing at the same heat input of C-TIG arcing. The pulse parameters of the P-TIG arcing process are taken as an optimum one found in an earlier work for providing optimum surface modified properties of steel. The AISI 4340 steel is chromium, molybdenum, nickel based high strength low alloy steel that gives superior case properties on a good back-up core properties after surface modification.

The complete work has been carried out in eight parts. **1.** Optimization of process parameters for single-pass C-TIG arcing process. It is done on the basis of the studies on thermal characteristics, geometry of fusion modified zone (depth of penetration and zone width) and heat affected zone (HAZ). **2.** An analytical modelling to estimate the thermal characteristics known as isothermal curve, thermal cycle and cooling rate of single-pass C-TIG arcing process. The estimated results of analytical model are compared to the experimental results for validation of the model. **3.** Microstructural analysis and studies on hardness profile of the surface modified substrate prepared at different process parameters and correlated with cooling rate for the single-pass C-TIG arcing process. **4.** Microstructural characterization of different zones of modification and analyse the hardness profile in surface modified substrate prepared by multi-pass C-TIG arcing process with 50 % overlaps. **5.** Analysis of mechanical properties using uniaxial tensile test of surface modified substrate and three-point bend test applied (tensile) on modified surface of the substrate prepared by C-TIG arcing process. **6.** Residual stress analysis of the modified surface by using hole drill method. The magnitude, type and distribution of stresses in the surface modified substrate are correlated with the procedural aspects (single and multi-pass) of modification and heat input of the arcing process. **7.** Characterization of single and multi-pass C-TIG processed substrate for fatigue life (S-N curve) under dynamic uniaxial tensile and bending load conditions. **8.** Comparative studies on various characteristics of the single-pass and multi-pass surface modified substrate prepared by C-TIG and P-TIG arcing processes applied at given heat input.

After finding the potentials of TIG arcing process to produce improved surface modification, effort has been made to develop knowledge of critical application of autogenous TIG arcing process to obtain optimum surface modification of AISI 4340 structural steel substrate. The knowledge includes appropriate control of process parameters primarily in order to manage the thermal cycle and isotherm of the heating zone, giving desired surface modification of the substrate primarily defined by its geometry and microstructure. In this regard the relatively low heating characteristics of the pulse current arcing process is also kept under consideration for comparatively lower distortion and residual stresses of the substrate than that observed in case of the conventional (non-pulse) arcing process.

The use of single-pass C-TIG arcing process gives 175 % and 50 % increment in hardness of fusion zone (FZ) and HAZ respectively of the modified zone with respect to that of base metal with adequate depth of modified zone of 2 ± 1 mm. The use of single-pass P-TIG arcing process further increases 5 to 10 % hardness in the modified zone as compared to that observed in case of C-TIG arcing process at the similar heat input, arc current and travel speed. It is observed that the P-TIG arcing is relatively more advantageous over the C-TIG arcing process, as it leads to relatively higher depth of penetration, higher hardness, and a better control over surface characteristics. The increment in hardness with sufficient case depth makes P-TIG arcing process more suitable for bearing industry. The mechanical properties have been significantly affected by single-pass C-TIG and P-TIG arcing process. In case of tensile properties, C-TIG arcing process improves yield strength and ultimate strength to 600 and 900 MPa respectively, but the ductility and toughness are decreased to 6 % and 38 J/mm^3 respectively as compared to those of the base found as 395 and 705 MPA and 19.24 % and 119 J/mm^3 respectively. Similar behaviour was also observed in flexural properties of bend test of modified surface of the substrate produced by C-TIG arcing process. In case of single-pass P-TIG arcing, further reduction in ductility (% strain) is observed. The effect of C-TIG and P-TIG arcing process was discussed with different parameters and variables along with the residual stresses.

Multi-pass C-TIG and P-TIG arcing process was performed at the optimized parameter of C-TIG and P-TIG arcing processes used for optimum properties of single-pass surface modification. A back tempering effect was observed by the subsequent pass during multi-pass C-TIG and P-TIG arcing. Due to back tempering significant changes are occurred in hardness, tensile, bending and fatigue properties. These properties are studied in detail. The use of surface modification processes develops residual stress over the surface. It is found that the use of multi-pass C-TIG and P-TIG arcing process produces compressive stresses in longitudinal

and transverse direction. The development of compressive stresses over the surface is found beneficial primarily to improve the fatigue properties of modified matrix of the substrate.

This dissertation is dedicated to my parents,

Shri Dina Ram and Smt. Urmila Devi,

wife Poonam and my beloved daughter Vidisha

ACKNOWLEDGEMENTS

Place: Roorkee

Dated: **SUDHIR KUMAR**

TABLES OF CONTENTS

LIST OF TABLES

LIST OF FIGURES

xix

xx

xxiii

NOMENCLATURE

Symbol	Description
ξ	Distance of the point along the x-axis with respect to the origin of moving heat source, m
Ω, Q	Heat input per unit length of weld, kJ mm^{-1}
v	Kinematic viscosity of ionized shielding gas (Kg m^{-1}s^{-1}) (0.0044)
ρ	Mass density of the base metal, kg m^{-3}
σ	Stefan-boltzman constant, w m^{-2} k^{-4}
σ_{tr}	Transverse shrinkage stress, MPa
ϕ	Summarized influence of pulse parameters factor
λ_a	Thermal conductivity of argon, J m^{-1} s^{-1} K^{-1}
η_a	Arc efficiency (%)
$1/2\lambda$	Thermal diffusivity of the base plate
a	Thermal diffusivity of the base plate (m^2/sec) (Al-Mg = 8.418×10^{-5} and Mild Steel = 1.172×10^{-5})
a_1	Width of weld metal deposited in current pass, mm
a_h, b_h, c_h	Ellipsoidal heat source parameters (m)
c_{hf}, c_{hb}	Double ellipsoidal heat source parameters (m)
A_F	Area of fusion, mm^2
W	Plate width, mm
c	Specific heat of the base plate (J g^{-1}K^{-1}), (Al-Mg = 1.03 and AISI 4340 = 0.475)
CR	Cooling rate, °K/sec
d	Thickness of the base plate, m
$D.C$	Direct current
E	Young's modulus of base material, 210×10^3MPa

E_W	Electrode extension, m
f	Pulse frequency, Hz
I	Arc current, A
I_b	Base current, A
I_{eff}	Effective current, A
I_m	Mean current, A
I_p	Peak current, A
k	Thermal conductivity of the base metal (J m^{-1} s^{-1} K^{-1}) (Al-Mg = 222 and AISI 4340 steel= 47)
k_p	Pulse duty cycle
L	Plate length, mm and Latent heat of fusion, J kg^{-1}
l_p	Length of fusion pool, mm
Q_{arc}	Arc heat generated by the energy input, J s^{-1}
Q_{AW}	Arc heat transferred to the fusion pool, J s^{-1}
Q_T	Total heat transferred per unit time, J s^{-1}
r_f, r_b	Proportion coefficients in front and behind the heat source
R	Distance (mm) of the point with respect to the central axis
S	Travel speed, cm/min
T_a	Ambient temperature, K
t_b	Base current duration, s
T_d	Temperature at any point in the weld due to arc heating, K
T_m	Melting temperature, K
T_{wp}	Estimated temperature of weld pool, K
T_{ST}	Surface temperature of torch nozzle due to combined heating by convection heat transfer from argon gas plasma and radiation from the arc, K
T_{WP}	Average weld pool temperature, K
T_o	Initial temperature of the base plate, K

t_p	Peak current duration, s
t_{pul}	Pulse cycle time, s
V	Arc voltage, V
HV	Vickers hardness number
W_b	Bead width
x, y, z	Rectangular coordinates w.r.t. to a fixed origin
x_{hw}	Distance between the heat source and the rear of the weld pool, mm

The other symbols used in the text are explained as and when they are introduced

xxx

The surface properties of engineering components play a vital role in their service performance when interactive mechanical exposure causes severe damage to them. This necessitates desired modification of surface properties of a part in terms of its physical, chemical, and mechanical properties, especially when a more economically viable material that has other favourable bulk properties is selected in critical industrial applications [Bakshi and Harimkar., 2015; Saeidi and Ekrami, 2009]. The types of applications are ranging from heavy-duty axles, shafts, gears, connecting rods and so on to relatively small components such as spindles, pins, studs, collets, bolts, couplings, sprockets, pinions and so on [Sun et al., 2014; Nascimento et al., 2001]. Depending upon service conditions in many occasions, they require improved surface characteristics to provide a longer reliable service life. The surface properties, such as hardness and wear resistance of a metallic material can be primarily modified either by introducing some new phase or element into the surface or by surface treatment of base material to develop desired hard and tough phases in the matrix [Bakshi and Harimkar., 2015; Llaneza and Belzunce, 2015; Harimkar et. al., 2013].

Modification of metallic surface by in-si-tu treatment is largely used in industries by employing various techniques. In recent years, a number of research groups have shown their further interest in surface modification of high strength low alloy steel by different techniques such as carburizing, ion nitriding, chemical vapour deposition, flame hardening, thermal spray coating, laser cladding and electron beam surfacing [Yang et al., 2018; Panfil et al., 2017; Fu et al., 2017; Yilbas, 2017; Cao et al., 2017; Sirin and Kaluc, 2012; Nascimento et al., 2001; Rajeev, et. al., 2014]. However, the hard modified surface must have sufficient toughness and resistance to cracking to give desired reliability in service performance.

Generally the surface was modified by using thermal process such as carburizing, nitriding thermal spray coating and so on, but these processes are having number of disadvantages. Such as they produce relatively narrow modified zone thickness and are also difficult to apply on large components (large gear, spindles, connecting road, large rollers, etc.) with development of a uniform modified zone thickness [Przybylowicz, K., 1999]. Further these processes are uneconomical to apply for modification of small section or area in limited quantity. For example in case of flame hardening of cams, leavers, push roads and so on, it is difficult to control overheating of the component due to heat spread of flame hardening and in

case of induction hardening it is difficult to do surface modification of complex shape work piece [Nemkov, 2004]. To overcome these problems, researchers are trying to do surface modification by using concentrated point heat source such as Laser surface modification and electron beam surface modification [Mohseni et al., 2014; Akamatsu, 2003]. But it is realized that these processes are also having some limitation such as primarily they are not always economical for general purpose use due to large overhead expenditure and producing relatively shallow depth and width of surface modification per pass [Brockhoff and Brinksmeier, 1999].

In this context, it is found that the thermal effect of Tungsten Inert Gas (TIG) arcing of the well-known tungsten inert gas welding process can be successfully used for surface modification of metals and alloys. The conventional TIG (C-TIG) arcing has several advantages over the above mentioned methods, primarily in reference to precision control, health hazards and versatility in application at relatively low cost [Ghosh and Kumar, 2015; Patel et al., 2014]. Technically, it is capable of producing superior products with greater depth of uniform surface modification (in the range of mm) in comparison to carburizing and nitriding [Ghosh and Kumar, 2015]. In the TIG arcing process, the surface is modified by melting the substrate with quick application of intense arc heat. This results in a large thermal gradient with high heating and cooling rates similar to the principle of laser and electron beam surfacing [R. Kumar et al., 2017]. It facilitates more precise control of phase transformation in the matrix up to a desired extent. In this process, the shape and size of the fused zone (FZ) on the surface of the substrate are governed by arcing parameters such as the current, voltage and speed of arc movement, while the molten metal pool is protected from atmospheric contamination under the inert argon gas shielding of the process. However, due to the limited spread of arc heat for fusion, multi-pass TIG arcing is required for modification of a large surface area of a component. Multi-pass arcing heat treats the former modified zone primarily depending upon the heat content and the rate of heat removal from the FZ governed by its geometry, which determines the final metallurgical and mechanical characteristics of the modified surface [Lakhkar et al., 2008; Ghosh and Kumar, 2015]. Thus, it is important to know primarily the effects of heat input and the geometry of the FZ on the thermal cycle of the matrix undergoing microstructural modification that dictates its mechanical properties.

However, it is reported [Ghosh et al., 2000; Ghosh and Kumar,2014] that in place of the conventional (C-TIG) using continuous current, the application of pulse current in TIG arcing has capacity to control more precisely the thermal characteristics of the system. The control of pulse arc is comparatively more complicated than control of continuous arc due to involvement of large number of simultaneously interactive pulse parameters in it [Ghosh et al., 2006;

Hussian et al., 1996; Randhawa et al., 1998; Randhawa et al., 2000]. Thus, the effect of pulse current TIG (P-TIG) arcing on characteristics of thermal behavior can be estimated as a function of a summarized influence of pulse parameters such as the frequency (f), pulse time (t_p), base time (t_b), base current (I_b), and pulse current (I_p). The summarized influence of pulse parameters in P-TIG arcing process is defined by a hypothetical dimensionless factor ϕ and it is amply justified in case of the pulse current metal inert gas welding process [Ghosh et al 1994, Ghosh 1999, Ghosh et al 2000, Ghosh et al 2001 and Ghosh et al 2007 (a, b)]. The hypothetical factor $\left[\phi = \left(\dfrac{I_b}{I_p} \times f \times t_b \right) \right]$ where, $t_b = \dfrac{1}{f} - t_p$, is derived on the basis of the energy balance concept of the system [Give reference of my book].

The utility of using this concept of Φ in control of pulse current process is amply justified in large amount of work carried out in pulse current gas metal arc welding (P-GMAW) process [Ghosh et al., 2008, Goyal et al., 2008 (b)]. The control of this basic nature of the pulsed process with the help of the factor Φ may also remain valid in case of P-TIG arcing process as it is also primarily based on the basic energy balance concept of pulse control phenomenon [Ghosh, P.K., 2017]. It is successfully tried in case of P-TIG arcing process by several researchers [Reddy et al., 2013; Suresh et al., 2004; Ghosh and Kumar,2014]. The use of this concept of Φ to control the P-TIG arcing process may prove to be significantly effective to add a new dimension to this process in order to introduce high critical control of weld thermal cycle with considerable flexibility. Thus, this innovative controlled process may also be desirably used to improve various properties of modified surface of components for critical applications.

In this work, surface modification has been performed over the AISI 4340 structural steel to enhance its harness and mechanical properties primarily by applying conventional tungsten inert gas arcing process. The AISI 4340 steel is also known as nickel, chromium, molybdenum based high strength low alloy structural steel. This steel is widely used in numerous applications in the automobile, aerospace and naval industries. The types of application are ranging from heavy-duty axles, shafts, gears, connecting rods and so on to relatively small components such as spindles, pins, studs, collets, bolts, couplings, sprockets, pinions and so on, especially because of its high strength and fatigue life. In many of its applications often the components require superior surface properties like resistance to wear and corrosion with acceptable fatigue life for a given service condition. In such cases surface modification of this steel to satisfy the service condition with improved properties is of considerable interest in advanced technology.

In view of the above, the primary objective for this work has been kept as to study in detail the effect of applying conventional TIG (C-TIG) arcing process to produce a modified surface layer with enhanced mechanical and fatigue properties of AISI 4340 structural steel substrate. However, considering the reported advantage of using P-TIG arcing for more precise control of thermal characteristics of the system it is also tried and compared to the effect of application of C-TIG arcing process on surface modification of the same substrate. The complete work has been carried out in eight parts. **1.** Optimization of process parameters for single-pass C-TIG arcing process. It is done on the basis of the studies on thermal characteristics, geometry of fusion modified zone (depth of penetration and zone width) and heat affected zone (HAZ). **2.** An analytical modelling to estimate the thermal characteristics known as isothermal curve, thermal cycle and cooling characteristics of single-pass C-TIG arcing process. The estimated results of analytical model were compared with the experimental results for validation of the model. **3.** Microstructural analysis and studies on hardness profile of the surface modified substrate prepared at different process parameters and correlated with cooling rate of the single-pass C-TIG arcing process. **4.** Microstructural characterization of different zones of modification and analyse the hardness distribution at different locations in surface modified substrate prepared by multi-pass C-TIG arcing process with 50 % overlaps. **5.** Analysis of mechanical properties using uniaxial tensile test and three-point bend test after C-TIG surface modification. **6.** Residual stress analysis of the modified surface by using hole drill method. **7.** Characterization of single and multi-pass C-TIG processed substrate for fatigue life (S-N curve) under dynamic tensile and bending loading conditions. **8.** Comparative studies on various characteristics of the surface modified substrate prepared by C-TIG and P-TIG arcing processes.

After finding the potentials of C-TIG arcing process to produce improved surface modification, effort has been made to develop the knowledge of critical application of autogenous C-TIG arcing process parameter for optimum surface modification of AISI 4340 structural steel substrates. The knowledge includes appropriate control of C-TIG arcing process parameters primarily in order to manage the thermal cycle and isotherm of the heating zone giving rise to desired surface modification of the substrate primarily defined by its geometry and microstructure. A comparison also conducted with the surface modified by P-TIG arcing process. In this regard the relatively low heating characteristics of the pulse current arcing process is also kept under consideration for comparatively lower distortion and residual stresses of the substrate than that observed in case of the conventional non pulse arcing process.

LITERATURE REVIEW

2.1 Surface Modification Processes

The aim of Surface modification of metals and alloys is to meet application oriented requirement by improving surface properties like hardness, wear resistance, corrosion resistance, residual stresses to various components without affecting their bulk properties like strength, toughness etc. [Wei et al., 2018]. In order to achieve required surface properties in the matrix of modified surface is generally made by four different techniques as shown in fig. 2.1.

1 Depositing material of desired chemistry on the surface

2 Changing surface chemistry of the matrix by manipulating its composition

3 Microstructural modification

4 Mechanical treatment
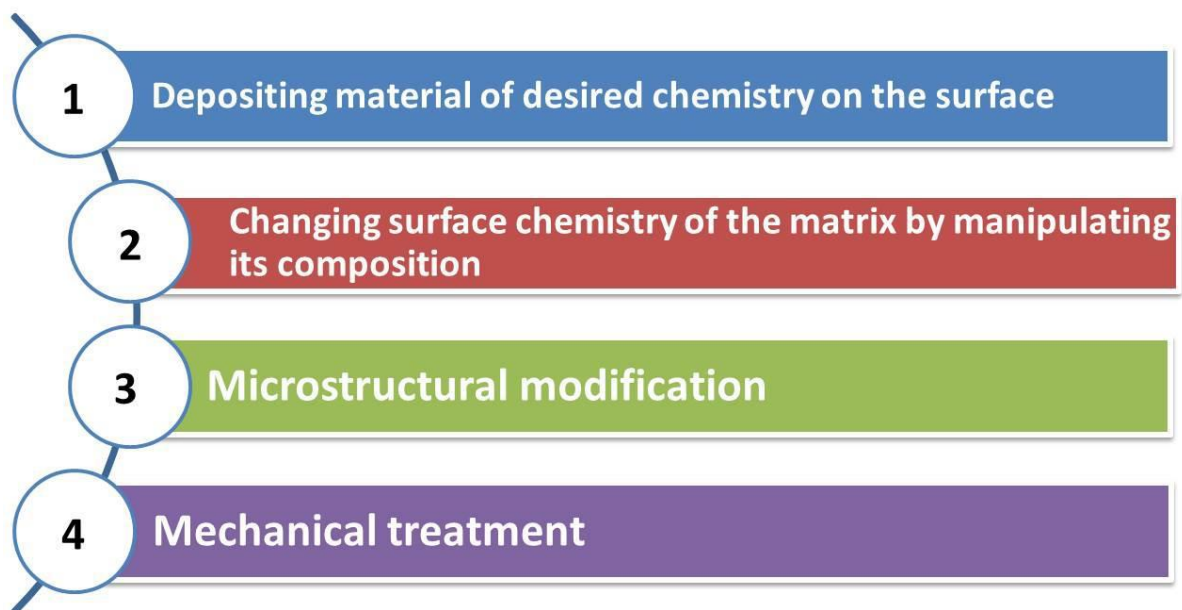
Fig. 2.1   Type of surface modifications technique.

Based on the surface modifications technique, there are many surface modification processes are adopted by industries such as:-

1) Depositing material of desired chemistry on the surface
    i)   Laser cladding
    ii) CVD (chemical vapour deposition)
    iii) PVD (physical vapour deposition)
2) Changing surface chemistry of the matrix by manipulating its composition
    i)   Cardurizing
    ii) Nitriding
    iii) Boronishing

3) Microstructural modification
   i)   Induction and induction hardening
   ii) Laser beam process
   iii) Electron beam process
   iv) TIG Process
4) Mechanical treatment
   i)   Shot blasting
   ii) Deep rolling
   iii) Shot pinning

2.1.1 Depositing material of desired chemistry on the surface

In this technique, a desired material has been deposit on the substrate surface with a required thickness. This technique was basically adopted when the surface is very reactive with the environment or any other surrounding chemical. This technique may create a barrier to the reaction by depositing a desired metal on surface. There are number of process for such a surface modification technique, some of these are discuss below.

2.1.1.1 Laser cladding

In this process, the substrate and desired material has been melted by the intense heat of laser radiation. The laser cladding process has been successfully employed in the industry for surface modification. Ray et al., [2014] investigated the effect of laser cladding by three Ni base powders with varying chromium, molybdenum, boron and niobium content in lateral rolls of a continuous slab caster. Reich et al.,[2014] describes the effect of laser treatment on clinching of hardened steel. Speidel et al., [2016] developed a new approach to modify the surface of mild steel by using a combination of laser and electrochemical processes. Tewary et al., [2014] successfully applied the laser surface hardening on C-Mn steel with a case depth of 300 μm. Yip et al., [2014] developed a clad layer of Silicon Carbide (SiC) particle reinforced Metal Matrix Composite (MMC) using the iron based alloys (P25) by laser process. Yip and Barnes [2013] applied the laser cladding process to modify the mild steel surface by introducing Silicon Carbide (SiC) particles.

2.1.1.2 chemical vapour deposition

The chemical vapour deposition (CVD) is a process in which a controlled reaction has been made on the surface of the substrate in a closed chamber with a particular gas uses [Ali et. al., 2002]. The reaction in the chamber was take place at an elevated temperature in the range

of 1000 to 1200°C [Schmich, 2007]. This process is quite usefully for the thin film deposition such as semiconductor industry.

2.1.1.3 physical vapour deposition

The physical vapour deposition (PVD) requires a vacuum in which the material goes from a condensed phase to a vapor phase and then back to a thin film condensed phase. The most common PVD processes are sputtering and evaporation. PVD is used in the manufacture of items which require thin films for mechanical, optical, chemical or electronic functions. Panjan et. al., [2018] deposit a hard phase coating on tool steel H11, and they found that the PVD gives an significant effect on tribological properties and provide the relation between process parameter and surface characteristics such as friction and wear. Baragetti et. al., [2005] discussed the effect of process parameter of PVD coating on the fatigue properties of stainless steel, tool steel and aluminium. Poursaiedi and Salarvand [2016] investigated the effect of PVD coating in fatigue properties of C450 steel, they found that fatigue properties are improved by 15 %. Selvakumar and Barshilia., [2012], they stated that the PVD coatings such as: SS–AlN, CrN–Cr2O3, eta Plus, TiNOX, Al–AlN, Ni–NiO, a-C:H/Cr, etc. have been developed and are being commercially used for solar hot water applications.

2.1.2 Changing surface chemistry of the matrix by manipulating its composition

Thermochemical processes modify the chemical composition of the substrate surface of a part without affecting its core properties [Mencík, 2013]. The thermochemical processes are basically a diffusion method which involves diffusion of hardening elements such as carbon, nitrogen and boron. The thermochemical diffusion processes having advantage of localized heating of workpiece, where the surface modification are desired [Totten and Liang, 2005].

2.1.2.1 Carburizing

Carburizing is a one of the important process used for surface modification of steel by the accumulation of carbon into the steel surface [Cajner et al., 2010]. The carburizing is a time and temperature dependent diffusion process which involves heating a component at a temperature in the range of 850-950°C for a certain period [Aramide et al., 2009]. Hosseini et al., 2012 described that in carburization process, the carbon atom layer diffuses into the low carbon steel to form a martensitic case to increase the wear and fatigue resistance with a tough, low-carbon steel core. Carburization process includes gas, vacuum, plasma, salt bath and pack carburizing [Asi et al., 2007]. The gas carburization process in which the component is placed in an environment of some carbonaceous gas like Methane, Ethane or any natural gas [Collins et al., 2014]. In the vacuum carburization process the workpiece is placed in a rough vacuum

with a hydrocarbon gas under some pressure and then followed by quenching in either gas or oil [Harry W. Antes, 2005]. The plasma ion process uses glow discharge technology under vacuum to introduce carbon bearing ions to the steel substrate [Conrad and Radtke, 1987]. Liquid or salt bath carburization process is implemented in molten salt pots in an environment of carburizing salt such as sodium cyanide. The pack carburizing process is the oldest process in which components are surrounded by a blend of charcoal and activators and then heated in a closed chamber [Foreman, 1990].

2.1.2.2 Nitriding and Carbonitriding

Nitriding is the thermochemical process like carburizing except that instead of carbon here nitrogen is diffused into the metallic surface to produce a hard case [Bernal, 2006]. In this process nitrogen is introduced in a temperature range of 500 to 550^0 C which is below the austenizing temperature range for steel and quenching is not required in this case [Michalski et al., 2009]. Similar to carburizing process, nitriding process includes gas, liquid and plasma nitriding [Moller et al., 2001]. The gas nitriding process takes place in the presence of ammonia gas which produces nitrogen rich white nitride layer over the surface [Yang, 2012]. The liquid nitriding process is performed in a molten salt bath containing either cyanides or cyanates at a temperature similar to the gas nitriding process. Plasma Nitriding is another approach in which glow discharge technology is used to introduce elemental nitrogen to the surface of a component in a vacuum using high voltage electrical energy.

Carbonitriding process involves dispersing of both C_2 and N_2 into the surface of steel substrate in a furnace. The process is performed in an environment of carburizing gas (propane or methane) mixed with ammonia followed by gas quenching [Shen et al., 2007]. The advantage of carbonitriding is improvement in fatigue and impact strength. The ferritic nitro carburizing is another approach to modify the steel surface by diffusion of nitrogen and carbon into substrate surface. The process forms a white layer of nitrogen and carbon in steel surface. The process forms the surface having high resistance to wear and significant improvement in fatigue endurance limit [Benedettiet al., 2002].

2.1.2.3 Boronizing

Boronizing is another method to modify the surface properties by introducing boron into the substrate surface. The component is surrounded with the boron containing compound (Boron powder or ferro boron) with some activators like chlorine and fluorine compounds in a temperature range of 850 to 950^0C for some time [Jain and Sundararajan, 2002]. Mostly the tool steel and heat treated steels are modified by this method [Ozdemir et al., 2008]. Béjar and Henríquez [2009] modify the surface of different steel by a new approach using plasma-

electrolysis boronizing. They found that the presence of Cr in the steel promotes the boronizing while C and Ni retard the hardening process. However, several disadvantages of boronizing process like inflexibility, high labor intensive and high brittleness of boronizing layers make the process less cost effective [Przybylowicz, 1999].

2.1.3 Microstructural modification

The surface modification (hardening) processes are not basically different from conventional surface treatment processes of materials. The hardness and strength both are achieved by heating the material over the austenite region and then quenched the material in oil or water to form hard phase like martensite. The main difference between the conventional heat treatment processes and surface modification processes is that in case of surface modification process only surface is heated to austenizing temperature before quenching. The core properties like toughness inside the surface remain unaffected by surface modification processes due to the high heat conductivity of ferrous materials. The use of very concentrated heat fluxes to heat the substrate surface over austenizing temperature is necessary without improperly affecting the bulk temperature of the component. The hot intense flames or high frequency induction heating is used to obtain desired temperature. After using selective surface heating the substrate surface to austenitization temperatures, desired surface hardening is achieved by use of a quench medium to the hot surface, or by self-quenching. The area beneath the surface is act a heat sink to transfer the heat quickly from heated zone to adjacent material (heat sink) by conduction. The process of transfer of heat is known as self-quenching. The rate of transfer of heat should be high enough to allow the formation of hard phases at the surface [Singh J, 1995].

Thermal surface hardening processes involve localized heating and quenching of the component without any chemical modification of the surface [Davis, 2002]. The surface modification of steel is mostly carried out by conventional surface hardening processes like flame and induction hardening [Davis, 2004]. Laser beam and electron beam are the new advanced applied energy techniques to modify the surface properties [Picraux and Pope, 1984].

2.1.3.1 Flame and Induction hardening

Flame hardening process is a method of austenizing the surface of the substrate by heating with oxyacetylene gas before quenching the steel in a spray of water [Schneider et al., 2013]. After quenching, the surface of the steel is converted into hard martensitic phase with soft and ductile core. The flame hardening is a simple and cheap process as compare to other hardening process. However, use of explosive gases, difficult to control the heating temperature, coarse martensitic structure due to overheating, high cost per piece in mass

9

production, difficult to control the case depth are some disadvantages of this process [Brockhoff and Brinksmeier, 1999].

Induction hardening is a versatile process where heating is performed by locating a workpiece in the magnetic field produced by high frequency AC current passing through a water cooled Cu coil followed by quenching. The advantages of induction hardening are faster process, less distortion, and small footprints. However, care must be taken when special geometries like hole, corners and complex shapes are treated with this process. Otherwise eddy currents become concentrated at the corners and result in overheating and cracking over the substrate surface [Nemkov, 2004]. It is very difficult to harden the complex shapes by this process and high capital investment is required to harden the workpiece. The conductor coil is designed according to the shape of the substrate and some shapes are very difficult to be induction hardened.

2.1.3.2 Electron beam hardening

The electron beam hardening process uses high velocity focused beam of electron as an energy source to modify the surface properties [Ormanova, 2017]. Modification of surface is performed under conditions which reduce substrate heating so that upon removal of the heat source, the cooling and solidification become rapid into the substrate [Akamatsu, 2003]. The electron beam hardening uses two approaches to modify the surface. The first one is to melt the surface and second one is a transformation hardening in which material is heated upto austenizing temperature range [Bugaev et al., 2002] followed by self-quenching. The process is performed in a high vacuum of 10^{-3} Pa in the region where the electrons are discharged and augmented to avoid oxidizing and scattering of electrons [Boiko et al., 1999]. The Pulse electron beam process is also another approach to modify the substrate surface by allowing energy deposition in a short time [Ivanov et al., 2000]. The advantage of the pulse electron beam process is high surface finishing without any change in the chemical composition and short irradiation time [Ivanov et al., 2002]. The electron beam energy deposition technique makes rapid solidification, fast evaporation, thermally induced compressive stresses, shocking wave, and enhanced diffusion in the substrate surface [Rotshtein et al., 2004]. However, necessity of vacuum, limitation for the bulk component, high capital investment are some limiting factors to use this process for surface modification [Renk et al., 2004]. Ming et al., [2004] developed the wear resistant surfaces by an electron beam process. Walker et al., [2013] investigated the effect of pulsing in the electron beam process to increase the surface properties of Co-Cr-Mo alloy for biomedical application.

2.1.3.3 Laser surface hardening

Laser surface modification is primarily used to increase the mechanical properties of extremely stressed machine components like bearings and gears [Damborenea, 1998]. Surface treatment by the laser process rises the wear resistance by improving surface hardness, and induces the residual compressive stresses in the workpiece surface to increase the fatigue properties [Mohseni et al., 2014]. In recent years, industrial lasers are successfully used for surface hardening of steel by melting and transformation hardening approach [Ramadan and Moussa, 2013]. The main advantage of laser that it can produce very concentrated energy fluxes at the substrate surface and the resulting steeper thermal cycle in the workpiece avoid the need of quenching. Other advantages of laser beam are easy to control, no need of a vacuum, and generate no combustion products. However, laser process also has some difficulties to use this process in-situ application. These drawbacks may include the need for complex optics and the use of coatings because of the low infrared absorption characteristics of steel. Barnes et al., [2003] used laser surface hardening for powder metallurgy component and found a case depth of 0.90 mm with hardness of 952 HV as compared to as received component of 210 HV hardness. Clare et al., [2012] used the laser cladding process to the maintenance, improvement and repair of the surface of a rail material. Grum [2007] compared the different laser surface technique and found that under different conditions quite different surface layer properties are obtained. Liu et al., [2007] investigated the effect of laser shocked peened process on fatigue life of Al alloy. They pointed out that proper selection of parameters is necessary to increase the fatigue life of materials otherwise internal cracks are developed in the samples. McDaniels et al., [2008] investigated the effect of laser processing on mechanical and fatigue properties of AISI 4340 steel and found improvement. Montross et al., [2002] reviewed the laser shock processing and pointed out that laser shock processing of materials is capable to increase the surface properties and compressive residual stresses into the surface up to 1 mm depth. Pashby et al., [2003] investigated the effect of high power diode laser surface hardening on low alloy steel and found increases in the mechanical properties.

2.1.3.4 TIG arcing process

Tungsten inert gas arcing process is an advancement of the welding process to modify the substrate surface in which an electric arc is struck between a non-consumable tungsten electrode and the substrate surface in a controlled atmosphere of inert gases [Guile, 1984]. The three procedures are used to modify the substrate surface by this process. First one is the tungsten inert gas melting process in which surface is heated up to melting temperature followed by self-quenching [Khan et al., 2000]. Second one is the changing the chemistry of

the surface by alloying of various alloying elements such as; Cr, Ti and W using TIG arcing process [Korkut et al., 2002]. Third one is the deposition of different metals and alloys on the base material by TIG arcing process. The advantage of TIG cladding is an improvement in performance and long life of the components [Atamert and Bhadeshia, 1989]. The low operating cost, low maintenance, cheaper labour cost, minimum distortion of the workpiece and higher flexibility at site makes this process more advantageous for surface modification of materials. However, less work has been done on the area of surface engineering by this method. Orlowicz and Trytek [2005] studied the effect of TIG arcing process on cast iron and found the rapid crystallization of melted region with very hard surface. They pointed out that the proper selection of TIG arcing parameters effectively produce a very high surface hardness and therefore, high wear and abrasion resistance of the surface. Dziedzic and Bylica [2008] used multi-pass TIG arcing treatment to modify the surface of high speed steel. Mohamadzadeh et al., [2009] have increased the mechanical and wear properties of cast iron by the use of the TIG melting process. Bochnowski [2010] successfully modified the surface of carbon tool steel by TIG arcing process. He studied the effect of arcing parameters on the tool steel surface and found the appreciable microstructural modification of the substrate surface up to 3 mm of depth with the precipitation of martensite phase.

2.1.4 Mechanical treatment

The elastic-plastic cold working of the substrate surface is the basic methodology of the mechanical surface treatment [Wagner, 1999]. The basic purpose of mechanical surface treatment is to introduce the compressive stresses over the substrate surface to increase resistance against corrosion fatigue, fatigue crack initiation and propagation and improves the structural performance under cyclic loading. Mechanical surface treatment is characterized into Shot peening, Deep rolling and Shot blasting processes [Nalla et al., 2003].

2.1.4.1 Shot blasting

Shot blasting method is another approach to modify the surface properties of materials by introducing compressive stresses in the materials. Shot blasting consists on bombarding a surface with small, hard particles like alumina, silicon carbide, titanium oxide etc.[Liu et al., 2004, Ummenhofer and Weidner, 2013]. Xingeng and Jiawen [2003] studied the effect of Shot blasting in Cr-Ni-Mo steel and found protective layer of chromium oxide with high Cr concentration and reduction in the activation diffusion energy. The shot blasting is effectively used to enhance the surface properties like corrosion resistance, hardness and wear resistance of the steel surface [Xingeng and Jiawen, 2006].

2.1.4.2 Deep rolling

Deep rolling is an axial-symmetric modification process in which a hardened roller produces plastic deformation in the workpiece. In this process roller is pressed into a fillet to make plastic deformation while the workpiece is revolved with respect to roller [Matlock et al., 2010]. Deep rolling produces a hardened surface with residual compressive stresses which retards the fatigue crack initiation and crack growth [Nikitin, 2007]. Juijerm and Altenberger [2007] studied the combined effect of deep rolling followed by an ageing treatment of Al alloy and found significant increment in hardness and in both low and high cycle fatigue. The effective decrement in the surface roughness with higher rate of work hardening by deep rolling process makes the Ti alloy component more effective in application [R.K. Nalla et al., 2002; Tsuji et al.,, 1992]. The main drawback of deep rolling is the complex calculation of suitable process parameters for surface treatment [Jeswiet et al., 2008]. Mandal et al., [2016] developed a low carbon micro alloyed steel and modify with thermo mechanical processing (Hot rolling followed by air cooling and water quenching). They found considerably improvement in yield stress and UTS due to the formation of coarse bainite and lath martensite in air cooled sample and a mixture of lath martensite and lower bainite in water quenched sample.

2.1.4.3 Shot peening

The shot peening process is a surface modification process in which bombardment of shots (Glass, round metallic or ceramic particles) with sufficient force on a substrate surface to induce the compressive stresses. The process uses the shooting of hardened balls under controlled parameters on the substrates surface of the workpiece. The use of this process increases the fatigue properties of AISI 4340 steel up to 70 % more than untreated SAE 4140 steel [Matlock, 2005]. The strain hardening of the surface increases the yield stresses of the material [Rice and Rosengren, 1968]. The plastic deformation prompted by shot peening is advantageous for both the soft as well as hard materials [Pandey and Deshmukh]. For hard materials, shot peening produces a hard zone at the surface and somewhat softened layer beneath the surface, whereas for soft materials it produces a homogeneous type of plastic deformation promoting hardening without crack nucleation affinity. Pandey and Deshmukh described that the fatigue life of the component can be improved by shot peening through the increase in hardness of surface (by strain hardening), by microstructural modification, by change in surface conditions and by an optimum spreading of compressive stresses in the surface/subsurface layers. The fatigue properties of AISI 9310 spur gear has been found 1.6 times the life of the standard gears without shot peening [Townsend and Zaretsky, 1982].

However the major disadvantages of this process are bed surface quality and difficulty in thin workpiece deformation [Qandil, 2016].

2.2 Tungsten Inert Gas Process

The TIG process has been developed in the middle of the twentieth century for joining of reactive metals and alloys such as stainless steel, magnesium and aluminum alloys with more accuracy and precise [Stava, 1990, and Reddy, 2014]. In the TIG process the electric arc is established between a tungsten electrode (non-consumable) and base material. The arc gap is kept constant and current is controlled by the power source. The heat of the electric arc produced is employed to achieve coalescence of metals with and without filler metal [Parmar, 1997]. Filler metal, generally available in 1 meter length of wire, is added to the leading edge of the weld pool as required. The arcing electrode and molten zones are generally protected by inert gas or gas mixture of argon and/or helium. The current and energy input range of the process is followed of the order of 10-300 A and 0.2 to 30 kJ/s respectively [ASM handbook 1994]. However TIG process is a welding process, but successfully used for surface modification of different materials [Carry, 199]. TIG melting or TIG arcing process involves heating the substrate material over melting temperature followed by self-quenching.

2.2.1 Power source characteristics

The tungsten inert gas arcing process uses constant current power source static characteristic for their application [Venkatramani, 2002]. The volt-ampere output curves are also named as 'drooper' because of significant downward or negative slope of the curves. In the constant current power source characteristics the little variation in arc voltage causes smaller change in arc current (Fig. 2.1). The constant current power source is used for non-consumable tungsten electrode which may sometimes damage during touching of electrode with workpiece for initiation of electric arc Under this power source characteristics, the short circuiting current shall be limited which would provide safety to power source and the electrode. The constant current power source characteristics are useful to maintain the constant arc length and stable arcing condition.
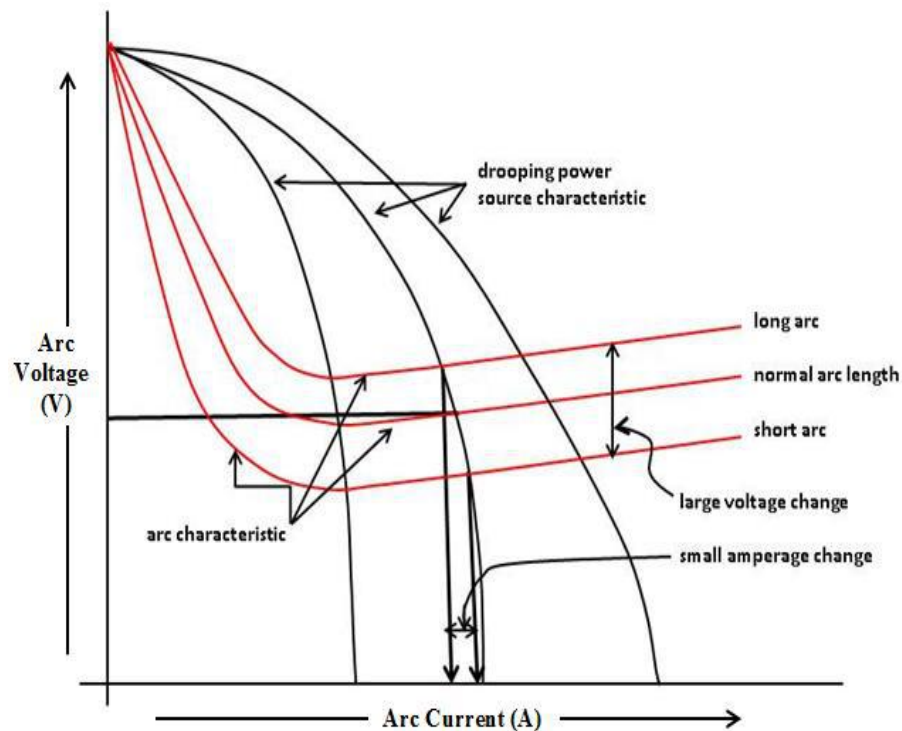
Fig. 2.2   Constant current power source characteristic.

2.2.2   Process variables and their control

The arc current, arc voltage and travelling speed are the primary variable to control the C-TIG arcing process. The arc current and arc voltage is used to control the energy input into the system while travelling speed is used to control the energy distribution into the system. The control of energy input and energy distribution into the system primarily determine the stability of the process [Liu and Siewert 1989] which is dependent upon the process variables [Choi et al., 1998, Kim and Eagar 1993 (a)]. These have considerable influence on the behaviour of the FZ and HAZ [Johnson et al., 1989], which in turn affects the properties of modified zones through influence on penetration, solidification mechanism and heat flow.

Arc current

Arc current plays primary role in deciding the thermal and metallurgical behavior of the modified zone. At a comparatively lower value of it, the size of fusion zone is reduces and at a higher value of arc current, the size of FZ increases. A still higher value of current, the serious distortion and damage of workpiece is possible [Lancaster 1984].

Arc voltage

The arc voltage primarily depends upon the TIG welding apparatus, whether it may fix or adjustable. The arc initiation and arc length are basically controlled by high initial arc voltage. The welding quality or surface modification become poor if the arc voltage is too high

15

[Li and Zhang, 2001]. It is the well-known fact that the arc voltage is primarily controlled by the arc length, hence affects the modified zone's shape and size. The too short arc length causes short circuiting the electrode with workpiece resulting the chances of forming the weld defects and narrow weld bead due to variation in heat input. The disadvantage of long arc length is narrow weld bead, The arc length in excess causes a flat and shallow deposit, chances of an electric arc to wander, growth in spattering and may also responsible for porosity in the fusion zone due to air aspiration in the shielding gas jacket [Johnson et al., 1995]. The extended arc length rises the perimeter of electric arc plasma, due to which there is a broader fusion zone. The long arc length also reduces the concentration of heat directly under the tungsten electrode and makes the fusion zone response to weave very sluggish [Matthews et al., 1992]. Smaller arc length advances wetting appearances and control of fusion zone. Hence, it is significant to select the proper arc voltage / arc length to obtain control of the fusion zone resulting in prevailing of the properties of the modified region.

Travel speed

The travel or welding speed plays an important role in TIG arcing process to improve the properties of modified region. The depth of penetration and arc reinforcement decreases with increasing the travel speed due to a reduction in heat input per unit length or power [Shirali and Mills, 1993]. The depth of modified zone and fusion bead size is primarily controlled by travel speed and arc current. So travel speed and arc current are interdependent to each other. The use of high travel speed reduces the wetting action, increases the irregular bead shape, and increases several defects like porosity and undercut while slower travel speed decreases the porosity in the modified zone [Norman et al., 1999].

Shielding Gas

The selection of shielding gas is very important because it directly affects the welding expenditure, arc stability and electrode life etc. The shielding gas also controls the depth of penetration, fusion zone temperature, surface profile, porosity, physical and mechanical properties of the modified zone [Murphy et al., 2009]. Generally Ar and He gases are used in TIG process [Murphy et al., 2009]. The pure Ar gas is used for welding of thin materials. Ar gas normally delivers more smooth and quiet arc. However, arc penetration is found less when Ar is used. The Ar gas is chosen for most of the applications due to easy availability and lower cost of Ar gas [Durgutlu, 2004]. Helium gas is used where higher depth of penetration and heat is required. So He gas is preferred for welding metals of high thermal conductivity and large thickness [Kah and Martikainen, 2013]. Generally use of He gas is useful for welding of thick

16

sections of Al and Cu. The Ar gas is used for welding of structural steels, stainless steels, micro alloyed steel, Ti and Mg alloy, Cu and Al alloys. Sometimes Ar+H_2 mixture is applied for joining of some grades of stainless steel and Ni alloys [Kumar et al., 2011]. Helium argon mixtures may be used for low alloy steels, aluminium and copper.

2.2.3 Arcing current polarities

The three types of arcing current or polarities (Fig. 2.3) can be used for TIG arcing process. Each polarity has a distinct characteristic which makes it more anticipated for specific conditions or with certain kinds of materials. The main change among the polarities is in their energy distribution and the degree of arc cleaning.

DCEN (Direct current electrode negative)

In direct current straight polarity mode, tungsten electrode is connected to the negative terminal of the power supply. The total energy transfer from electrode to workpiece is 70 % and 30 % electric energy (Heat energy) remains to the negative terminal. The advantage of DCEN mode is higher depth of penetration with a narrow weld bead profile. Due to high percentage of heat energy transfer to workpiece, this is the most common and widely used polarity mode.

DCEP (Direct current electrode positive)

In DCEP mode the tungsten electrode is coupled to the positive terminal of the power supply. The total heat supply to the workpiece is 30 % and 70 % of heat remains to the positive terminal. The DCEP mode is used very hardly because almost 70 % heat is on the electrode which can easily overheat and burns the tungsten electrode. DCEP mode creates a shallow depth of penetration, wide bead width. The DCEP mode is mainly used for thin and very light material with a low arc current.

AC (Alternating Current):

In AC mode 50 % of energy is transferred to the workpiece and remaining 50 % moved to Tungsten electrode. On the first half of AC cycle where the tungsten electrode is positive, the heat energy is transferred from workpiece to electrode. Similarly in the second half of AC cycle the energy is transferred from the tungsten electrode to workpiece. So the energy input towards the tungsten electrode is averaged out as the AC wave passes from one side of the wave to the other. The AC mode is largely used for white metals like Al and Mg. The first half of the cycle is known as cleaning half because during the first half of the cycle the electrons will flow from workpiece to Tungsten electrode. This will cause the removing of any oxide layer from the base material. The second half of the cycle is known as the penetration half of the AC

waveform because in this half mode the electron (energy) is transferred from electrode to workpiece.
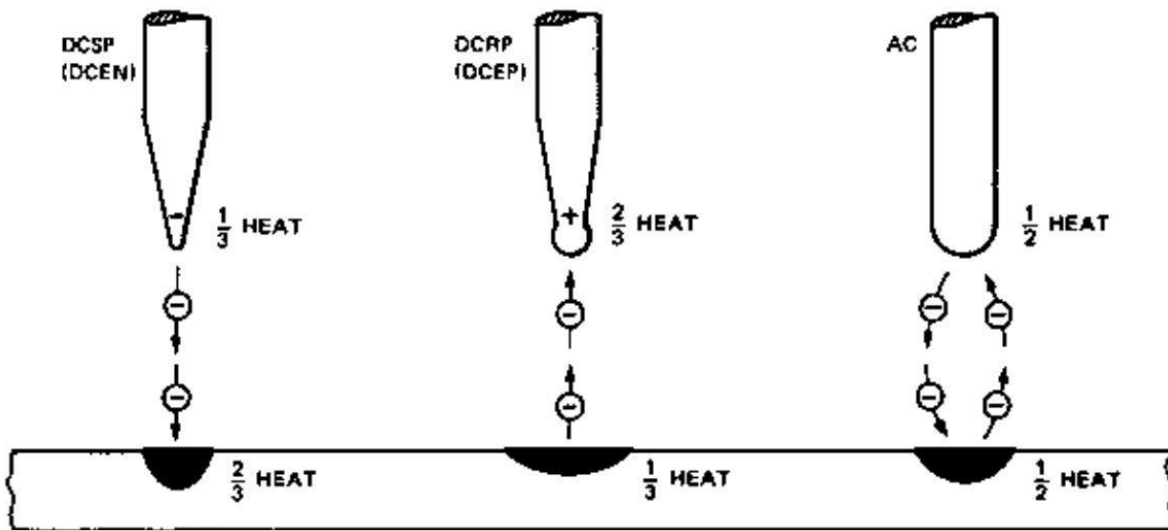
Fig. 2.3   Effect of polarity in the heat distribution between the tungsten electrode and workpiece [Messeler Jr, 1999].

2.3 Pulsed current tungsten inert gas arcing process (P-TIG)

The pulse tungsten inert gas arcing process is one where the current is pulsed between current is varied between the low level to the high level as shown in fig. 2.4 [Phillips et al., 1994]. So, this kind of the process where current is varied continuously as a function of the time during the arcing is called the pulse arcing. The advanced version of C-TIG arcing process uses pulsed current instead of continuous current. Both low frequency pulsation typically (0.1-20Hz) and high frequency pulsation (>100Hz) is often used in this process [Richard, 2001].

The heat input depends on the mean current which is a correlation of the pulse height, pulse duration and frequency [Sakai et al., 2009]. The pulsed current mode of this process offers a better control over the size of fusion zone and its fluidity to manage the pool in position as well as over the penetration behavior of the modified zone. The use of autogenous pulse current tungsten inert gas arcing (P-TIG) has become extremely popular in weld fabrication of relatively thin section and root pass of thick section in various industries due to its ability to precise control of energy input and to introduce control of energy distribution in the process [Tsai and Hou, 2013]. Unique possibility of control of energy distribution in the process may significantly influence the solidification behavior, nature of phase transformation as well as morphology of various phases in the matrix. This process can be accredited for the possibility of introducing more controlled weld thermal cycle, primarily due to its merit of developing relatively lower heat build-up in weld pool than the conventional TIG (C-TIG) arcing process

18

[Balasubramanian et al., 2008]. Moreover as the P-TIG arcing is also a relatively low heat process, it may reduce residual stresses and favourably affect the control of dilution and phase transformation in the substrate. In addition, it allows greater control of fusion with enhanced penetration [Kim et al., 1998].

It is generally understood that the total heat input in pulse current arcing process becomes relatively lower than that of conventional arcing because the heat energy required to melt the base metal is primarily supplied at peak current during the pulse on time when a low base current just keeps the arc alive [Chen et al., 2000]. The melting at the stiff arc of peak current gives rise to more penetration which permits more efficient use of arc energy limiting the wastage of heat by conduction into the base metal as it occurs in conventional constant (non-pulsed) current welding. [Nadkarni, 2010]. The heat transfer and fluid flow in the fusion pool can significantly influence its geometry, temperature gradient, local cooling rates, microstructure and mechanical properties. It is well known that P-TIG arcing process works at a mean current which is significantly lower than the current used for C-TIG arcing, but it produces deeper penetration due to high arc pressure at relatively large current of long peak duration [Saedi and Unkel, 1988]. Thus, the effective heat input in P-TIG arcing becomes considerably lower than the heat input of C-TIG arcing result in lower average fusion pool temperature. Accordingly the P-TIG arcing exhibits lower thermal distortion than the C-TIG arcing at a given penetration [Tseng and Chou, 2001]. In other words the P-TIG arcing process gives an opportunity of using fine-tuned arc wave form and significant energy saving. The P-TIG arcing has numbers of advantages that primarily include intended operation at relatively low heating, less distortion of substrate and precise control of thermal cycle and isotherm leading to necessary phase transformation and microstructure [Atabaki et al., 2014; Ghosh and Kumar, 2015].
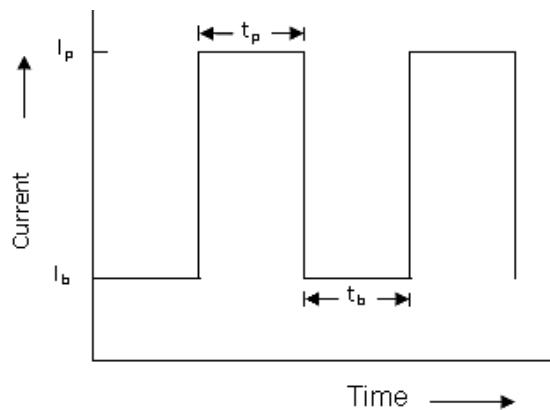
Fig. 2.4   Arc current characteristics in pulsed current TIG arcing process.

The effective use of pulsing in GMAW process is described by Ghosh and Dorn (1993) and found that use of pulse current effectively controls the metal deposition. The pulsing effect is capable of joining at a relatively low energy input and hence more valuable as compared to GMAW [Ghosh and Dorn 1993]. The similar principle of pulsing is also applied in TIG arcing process for welding and surfacing [Ghosh and Kumar, 2015] and found comparatively lower heat input and better control of the process. However, it is very difficult to take a combination of accurate pulse parameters, but clear understanding of correlations among pulse parameters and characteristics makes this process easy to use. [Amin, 1983]. In P-GMAW process, mean current, I_m, for a square wave pulse is expressed [Amin1981, Lancaster 1984] as,

$$I_m = \frac{\left(I_p \ t_p + I_b \ t_b\right)}{(t_p + t_b)}$$ …………………………………………..………… (2.1)

Where, t_b is base current duration and t_p is peak current duration, I_p and I_b are pulse current and base current respectively.

Pulse frequency, *f*, may also be expressed as

$$f = \frac{1}{t_{pul}}$$ …………………………………………………………………… (2.2)

Where, $t_{pul} = t_b + t_p$

The above mention equations are successfully used to determine mean current and frequency for P-TIG arcing process by several researchers [Traidia et al., 2010; Stephan et al., 2015].

2.3.1 Process variables and their control

The merits of P-TIG arcing process is primarily dependent upon the right selection of operating parameters, like mean current (I_m), peak current (I_p), base current (I_b), pulse duration (t_p) and pulse frequency (f) as they affect the microstructure of fusion zone (FZ) and heat affected zone (HAZ) as well as chemistry due to their influence on weld thermal cycle and weld isotherm [Ghosh and Dorn 1993, Ghosh and Rai 1998, Ghosh and Sharma1991, Lambentt 1989].

Peak current (I_p)

The peak current is used to proper melting of the material. The level of the high current is decided on the bases of the heat that is to be generated for melting the faying surfaces [Farahani et al., 2012]. Higher peak currents will result in greater axial force due to magnetic field generated by the current carried through the electrode due to which distortion of the workpiece is possible Hence, to ensure appropriate amplitude and duration of peak current, power law relations ($I_p^n \ t_p$ = constant, n=2) have been used for determining the amplitude of

20

peak current and duration [Quintino and Allum 1984, Rajasekaran et.al. 1998, Wang et. al 2004].

Peak current duration (t$_p$)

The pulse duration is an important operating parameter to control the modified zone. Increase in peak current duration in general, increases the modified zone size and the kind of penetration. So, the higher peak current duration, greater will be the penetration. So, the weld pool size and the penetration requirement govern the pulse current duration [Pal and Pal, 2011].

Base current (I$_b$)

The base current is required to continue the minimum welding arc between the pulses [Needham, 1965; Nemchinsky, 1997; Praveen et al., 2005]. The fusion zone and geometry of weld bead can be smoothly controlled by the suitable base current level. Sometimes the base current is frequently fixed to a minimum level to control the heat input. Due to which there is a poor fusion geometry and high crowned weld bead. Background current or low level of current must be high enough to maintain the stable arc with lowest possible heat input so that the solidification of the molten weld can take place without any heat build-up [Kumar and Sundarrajan, 2009]. So the low level current that is called base current performs the two functions. One, it helps maintain the arc during the welding with the very low heat. During this period, the solidification of the weld metal takes place.

Base current duration (t$_b$)

The base current duration is required to avoid the additional heat built up into the base material to avoid the excessive distortion of the workpiece [Yousefieh et al., 2011]. During this period the low arc current is maintained to transfer the heat from the fusion zone to adjacent material which causes better control in the cooling rate of the process. However, sometimes due to excessive base current period the cooling rate becomes so much high. Because of the high cooling rate the gas in trap take place, which in turn leads to the development of the polar city [Manti and Dwivedi, 2007]. So, in which way the solidification of the fusion zone that decides the base current value depends upon the base current duration.

Pulse frequency (*f*)

The duration of the peak current and the base current determines the pulse frequency [Cook and Hussam, 1985]. The frequency of the pulse is set as per the requirement of the heat input. High frequency pulse should be selected to increase heat input. If we require less heat then, the few pulses of the peak current will be there. That will help in having the lower heat input. Very low pulse frequency (conversely longer background current duration and short

21

peak current period) during P-TIG arcing, reduces heat available for modification which in turn increases the solidification rate. Too high solidification rate increases martensitic transformation in the fusion zone. A fine grained structure can be achieved using both low and high pulse frequencies [Arivarasu et al., 2014]. Fine microstructure is known to improve the mechanical properties of the weld joint in general except creep resistance. Low pulse frequency (up to 20 Hz) has more effect on the microstructure and mechanical properties [Qi et al., 2013].

Several researchers pointed out that in P-TIG arcing process, the weld bead is composed of a series of overlapping fusion spots. Fig. 2.5 shows the effect of frequency on the arc bead. When arcing is done with low frequency, these effects can be clearly observed in the fig. 2.5 (a and b). When working with very low pulse frequency the overlapping of fusion nuggets is less. So the heat transfer in between the generated fusion nuggets is high from fusion zone to adjacent workpiece material. When pulse frequency increases the gap between the fusion nuggets are reduces. Due to which fusion zone size increases and heat transfer from fusion zone to adjacent material reduces [Suresh et al., 2004]. So, when the pulse frequency is increased, the peak current is generated at very short intervals. It developed the fusion zone and making possible to solidify quickly at very short interval of the times. So, in the increasing in pulse frequency, the time after which heat is generated; lot of heat is generated and reduced. The continuous, almost very fine with the great overlapping of the molten fusion zone areas with each other. So, increasing the pulse frequency obviously increases the heat input to the base material with more overlapping [Yang et al., 2013]. It has been observed that when we work with the low pulse frequencies, the effect of the P-TIG arcing is found more on the structure and on the mechanical properties as compared to the situation, where high pulse frequency is used. When working with high pulse frequency the pulsing takes place very frequently for long period due to which the fusion zone bead being developed like a C-TIG arcing processed fusion bead [Reddy et al., 2013].
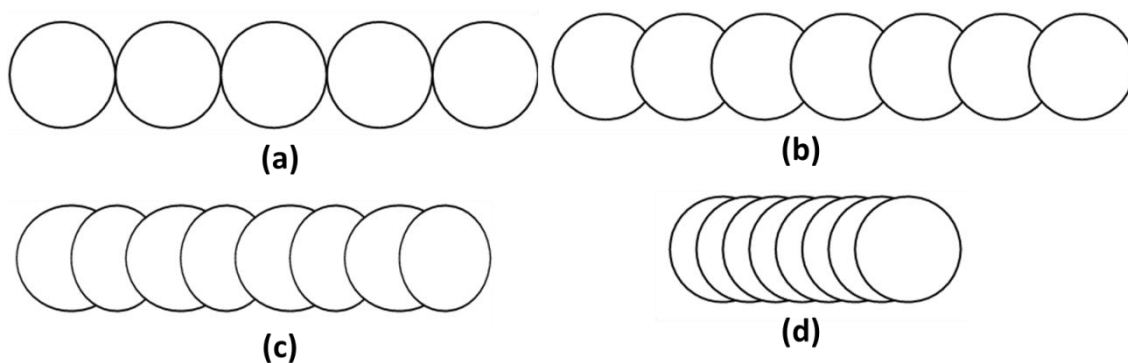
Fig. 2.5 Schematic diagram showing the effect of frequency on fusion track using P-TIG arcing process.

2.3.2 Ratio of peak current to base current (I_p / I_b)

The peak-to-background current ratios basically provide a means for the welding current to pulse form one level to another. Several researchers describe that for good fusion the peak to base current ratio should be varies from 2:1 to 5:1 ratios. Ghosh and Sharma [1991] investigated the effect of Ip/Ib on the arc pressure. Earlier investigation [Ghosh and Sharma 1991, Ghosh and Gupta 1996] carried out on single-pass pulsed current MIG of Al-Zn-Mg alloy have shown the influence of the ratio of I_p/I_b on the porosity content of weld deposit and suggested that the I_p/I_b ratio should be maintained in the range of 7.5 at a mean current of 150 A and around 4 at a mean current of 220 A to achieve a significant reduction in porosity content of the weld deposit.

2.3.3 Heat transferred to fusion zone

The heat transferred (Q_T) to the fusion zone of P-TIG arc was estimated in consideration of the arc heat transmitted to the weld pool (Q_{AW}, Js^{-1}) and travel speed (S) as follows [Ghosh et al., 2006, Goyal et al., 2008 (b)].

$$Q_T = Q / S \dotfill 2.3$$

Where, $Q = Q_{AW}$

Q_{AW} may be estimated as (Js^{-1})

$$Q_{AW} = \eta_a \left(V\, I_{eff} \right) \dotfill 2.4$$

Where, V and I_{eff} are the arc voltage and effective current (root mean square value of the pulsed current wave form) respectively. The I_{eff} is calculated by the following equation [Praveen et al., 2005].

$$I_{eff} = \sqrt{\left[k_p.I_p^2 + \left(1 - k_p \right).I_b^2 \right]} \dotfill 2.5$$

Where, the pulse duty cycle k_p [Ghosh, 2017]

$$k_p = {t_p}/{t_{pul}} \dotfill 2.6$$

2.3.4 Estimation of weld pool temperature

It is assumed that during pulsed current TIG (P-TIG) arcing method, the energy transfer primarily takes place at peak current (I_p) so the net heat content is mostly directed by it. During arcing the heat transfer to the fusion zone is primarily attributed to the primary arc heating (Q_{AW}). Accordingly the continuous heat source (arc heat source) of double ellipsoidal [Robert W. Messler, Jr., 1999, ASM Handbook 1994] nature acting at the base plate surface, which melts the

area of workpiece and produces an initial fusion zone in the workpiece. Thus the distribution of temperature at any place in the fusion zone area may be estimated by the analytical solution of the distributed heat source. The expressions for the temperature, T_d, at any point $(x(\xi), y, z)$ in the modified zone due to arc heating using the distributed heat source expressed as follows:

$$T_d = \frac{3\sqrt{3}.Q_{AW}}{\rho.c.\pi\sqrt{\pi}} \int_0^t \left[\frac{\frac{dt^{'}}{\sqrt{\left(12a(t-t^{'})+a_h^2\right)}.\sqrt{\left(12a(t-t^{'})+b_h^2\right)}}}{\left(\frac{A^{'}}{\sqrt{\left(12a(t-t^{'})+c_{hf}^2\right)}} + \frac{B^{'}}{\sqrt{\left(12a(t-t^{'})+c_{hb}^2\right)}} \right)} \right] + T_0 ....2.7$$

Where, Q_{AW} is the arc heat transferred to the weld pool.

2.3.5 Concept of summarized influence of pulse parameters

It is very complicated to govern the pulse arc as compared to continuous arc due to envelopment of a huge number of instantaneously collaborating pulse parameters in it. Thus, the consequence of P-TIG arcing on appearances of thermal characteristics can be expected as a function of a summarized influence of pulse parameters such as frequency (f), peak time (t_p), background time (t_b),background current (I_b), and peak current (I_p). The concise influence of pulse parameters in P-TIG arcing process can be defined by the following hypothetical dimensionless factor ϕ as it is thoroughly acceptable in case of the pulse current metal inert gas welding process by the hypothetical equation $\left[\phi = \left(\frac{I_b}{I_p} \times (f \times t_b) \right) \right]$ where, $t_b = \frac{1}{f} - t_p$, is derived

on the basis of energy balance concept of the system suggested [Ghosh, 2017, Ghosh et al., 1994, Ghosh 1999, Ghosh et al., 2000, Ghosh et al., 2001 and Ghosh et al., 2007 (a, b)]. Control of basic nature of pulsed process with the help of the factor Φ has also been repeated effective in case of P-TIG arcing process as it is also primarily based on the basic energy balance concept of pulse control phenomenon. The use of this concept of Φ to control the P-TIG arcing process may prove to be highly effective to add a new dimension to this process for highly critical control of weld thermal cycle with considerable flexibility. Thus, this more precisely controlled process may be used to improve various properties of modified surface of components for critical applications of advanced materials.

2.4 AISI 4340 Steel

AISI 4340 is a low alloy steel having 3-5 weight % of alloying element, including some selective element in order to meet high wear resistance, high strength along with other properties [AWS handbook 1978]. AISI 4340 is a high strength low alloy structural steel which

provides better mechanical and fatigue properties than other conventional carbon steels. [AWS handbook 1978, Metals handbook 1979 (a), (b), Rothwell and Malcolm Gray 1976]. AISI 4340 steel keeps medium carbon content (0.37 - 0.43 Wt. %) with varying manganese content up to 0.8 wt%, in order to exhibit sufficient hardenability, ductility and wear resistance. Manganese marginally raises the strength of ferrite, and also raises the hardness of steel during the quenching process by reducing the critical quenching speed. The presence of Cr in the steel significantly increases the toughness and resistance to wear. The Cr also increases the critical quenching temperature in the surface hardening treatment. The presence of Ni in low alloy steel increases the strength of ferrite, toughness and hardenability. During quenching of surface hardening process, Ni effectively reduces the cracking and distortion by converting needle phase martensitic to lath type martensitic structure. The Mo also intensifications the hardness penetration of steel, reduces the critical quenching speed, and rises high temperature tensile strength [Rowan and Sisson, 2009].

2.4.1 Mechanical properties of AISI 4340 Steel

AISI 4340 steel must have certain characteristics and properties to use in construction of various advanced components such as wear resistance, strength, toughness, ductility, and weldability so that it can be fabricated successfully by customary methods depending upon applications. In addition to this, improved wear and fatigue resistance is generally required [Sirin et al., 2013]. Generally AISI 4340 steel has higher core strength and toughness than the majority of as rolled or normalized structural carbon steels and has fairly good strength and fatigue life. The wear and fatigue resistance of steel depends upon the method and processing used to modify the surface properties without affecting the core properties.

The AISI 4340 is a low alloy steel specially developed for high strength and toughness in heat treated condition. The mechanical, physical and thermal properties of AISI 4340 steel are primarily dictated by their microstructure and phase transformation. Generally AISI 4340 steel consists of ferrite-pearlite microstructure, and the properties are affected by changes in the microstructure. The case hardening techniques is used to modify the surface properties, the fineness of the microstructure, and the amount of dispersed phases. The minimum mechanical properties of AISI 4340 steel have been given in Table-2.1.

Table 2.1   Minimum mechanical properties of AISI 4340 steel.

Property	Minimum value
Tensile strength	690 MPa
Yield strength	380 MPa

Elongation % in 2"	21.0
Reduction in area, %	49.0
Vickers Hardness	260
Poissons Ratio	0.29

2.4.2 Heat Treatment and Surface modification of AISI 4340 steel

AISI 4340 steel is specially designed for high strength and fatigue life for various application and it is also heat treatable. The thermochemical heat treatment processes are successfully applied to increase the wear resistance, fracture toughness, fatigue resistance, hardness of the surface without affecting the core properties [Garcés et al., 1999]. The through hardening is not performed for this steel because the tough core requirement. In furnace heat treating process, the surface hardness depends upon the carbon content and hardenability of the material. This steel is hardened by heating to $815\,^0C$ followed by a water quenching. AISI 4340 may be given a full anneal at $850\,^0C$ and slow cooling at not more than $10\,^0C$ per hour down to $450\,^0C$ to remove stresses and micro cracks. The tempering of AISI 4340 is done at $120\,^0C$ to $150\,^0C$ to increase the toughness, minimize the effect of residual stresses and remove the micro cracks after the formation of martensite over the surface after surface hardening process. Sirin et al., [2008] studied the effect of ion nitriding on 4340 steel and found that heat treatment considerably improve the ductile to brittle transition as compared to as received materials.

2.4.3 Hardenability

The ability of steel to form a martensitic structure after surface hardening is referred to as hardenability. The grain size and composition are the two most significant variables which affect hardenability. The various researchers describe that due to increase in austenite grain size, there is a reduction in the grain size area. The reduction in grain size area causes the reduction in the number of sites for the nucleation of ferrite and pearlite. Due to which transformations are slowed down, and the hardenability is therefore increased.

Heat treated low-alloy AISI 4340 steel have better hardenability than untreated and carbon steel and therefore can deliver high strength and good toughness in hardened zone. Their alloy content provides improved heat, wear and corrosion resistance [Meyers and Wittman, 1990]. The fig. 2.6 shows the isothermal transformation curves of the as received AISI 4340 steel which shows the significant improvement in hardness after hardening process as compare to as received unhardened 4340 alloy steel [American society for metal, 1977].
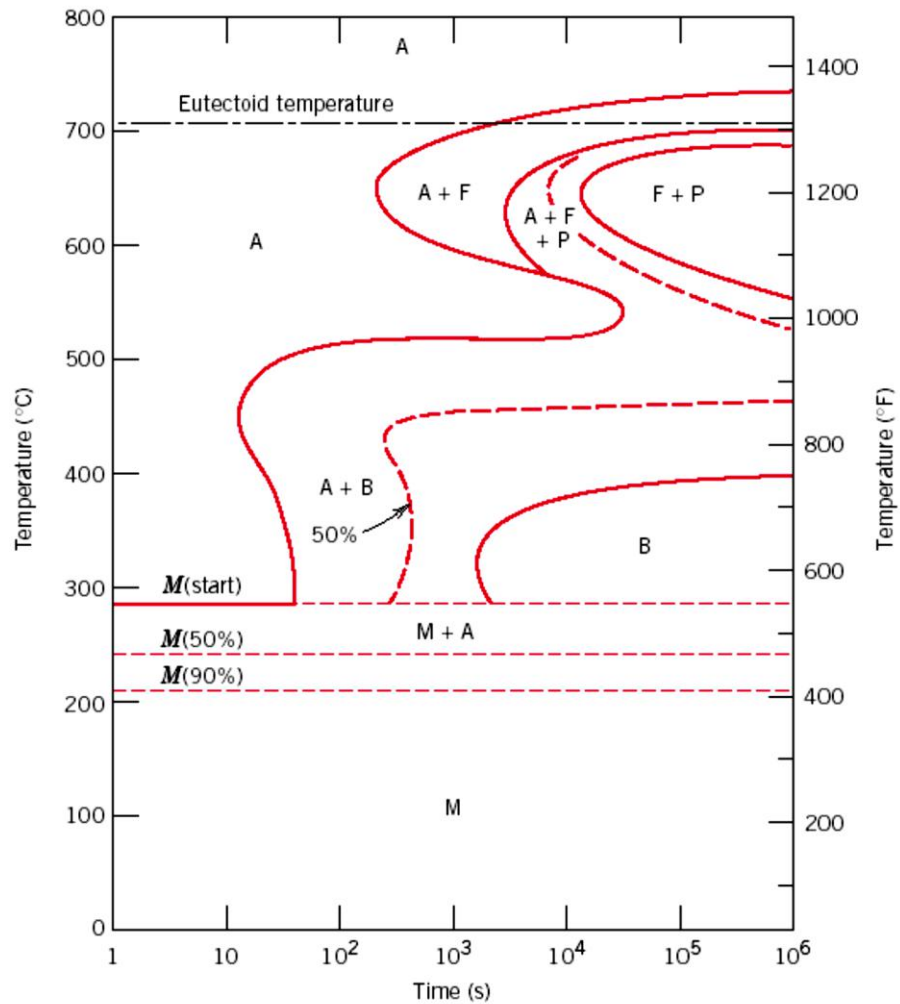
Fig. 2.6   Isothermal transformation diagram for AISI 4340 steel, A-austenite, B-bainite, P-pearlite, M-martensite, F-proeutectoid ferrite (American society for metal, 1977)

2.4.4 Applications of 4340 Steel

The AISI 4340 steel known as high strength low alloy steel is widely used in various critical structures and components of modern aircraft [Sun et al., 2014], automobile and naval industries [Nascimento et al., 2001]. The types of applications are ranging from heavy-duty axles, shafts, gears, connecting rods, undercarriages to relatively small components such as spindles, pins, studs, collets, bolts, couplings, sprockets, pinions and so on. In many of its critical applications the AISI 4340 steel requires enhanced specific surface properties that calls for surface modification without affecting the bulk properties [Saeidi and Ekrami, 2009]. It is observed that in large wind turbines the flanks and toes bear maximum loads particularly when there is an unexpected change in wind speed. So there is a need of a hard case with a tough core in a wear resistant gear to handle high impact loads. Gear noise increases during life due to abrasion of gear tooth surfaces. Increasing the surface hardness and abrasion resistance of gears

27

will thus decrease gearbox noise. The AISI 4340 steel is used for manufacturing of gears used in large wind turbine having the advantage of increased core tensile strength and toughness, higher fatigue strength in both core and case, improved hardenability and low distortion. The typical applications of AISI 4340 steel include

- **General mechanical engineering:** Applications in this area include forging presses, metal rolling equipment, machine tools; drivelines of mining equipment and heavy-duty transmissions; earth exploring equipments and heavy-duty construction cranes.
- **Transportation:** The case hardened AISI 4340 steel is required in every field of transportation like railways, automobiles, waterways and airways (landing gear).
- **Energy production:** The AISI 4340 steel material should be capable to withstand cyclic stress, thermal and mechanical loads. So AISI 4340 steel is largely used in hydroelectric power stations, wind-turbine generators, and propeller drives of drilling rigs and steam-turbine gears of power stations.

2.5 Factors Affecting the Properties of AISI 4340 steel

2.5.1 Effect of alloying elements

The chemical composition of the steel, time and temperature are the typical surface modification variables to control the austenite grain size [Sufirez et al., 1994, Tamura et al., 1988]. The Cr, Ni, Mo and Mn are the main alloying element in the AISI 4340 steel.The decomposition behavior of steel is governed by the austenite grain size in it. Thus this behavior of steel affects the subsequent microstructure and mechanical properties after surface modification [Rothwell and Malcolm Gray 1976, Shome et al., 2003, Shome et al., 2004, Shome 2007, Stasko et al., 2006, Varughese et al., 1993].

The Ni in AISI 4340 steel works as a austenite stabilizer and as such lowers the temperature at which austenite decomposition will occur on cooling [Isakov, 2009]. The Ni influences the yield behavior by facilitating cross slip resulting a more homogeneous distribution of the slip throughout the metal crystal, and this is reflected as increased toughness after hardening. The presence of Ni in AISI 4340 steel also decreases the dependence of yield strength on temperature and strain rate with raising the cleavage strength. The Cr and Mo are carbide forming elements in AISI 4340 steel lowered the carbon diffusivity in austenite [Rowan, 2009]. Nickel increases the strength of ferrite, therefore increasing the strength of the steel. It is used in AISI 4340 steel to increase toughness and hardenability [Clark and Varney 1962; Aver 1974]. Nickel also tends to help reduce distortion and cracking during the quenching phase of heat treatment.

28

Manganese is tends to reduce eutectoid C content and transformation temperature. Several researchers describe that Mn is a most cost effective intensifier [David et al., 2009]. The Mn is used in all types of case hardenable steel to retard the transformation. Generally around 1% Mn is quantified in case hardenable steels. The lower transformation temperature produced by Mn addition encourages reduction in grain size, whether the steel may be either as-rolled or normalized. The reduction in grain size (pearlite, ferrite and bainite) promotes the higher yield strength and impact toughness. The researchers found that the addition of Mn for a given C content increases the pearlite phase in the matrix [Mangonon, 1976]. The increase in the pearlite phase causes the increment in the tensile strength without affecting weldability. The researchers studied the effect of Mn on martensite start (Ms) temperature and found that the Mn reduces the Ms temperature. There is a high probability to contain higher residual austenite in high Mn steel. Although in high Mn steels, Mn promotes to form a carbide phase, which is similar to cementite.

Chromium has affinity to form a solid solution with both the α and γ phases of iron and it is a strong carbide forming element in steel similar to Mo and W. The Cr in the presence of Fe and C forms a typical series of carbide compounds. The presence of Cr increases the Ac" critical point and lower down the eutectoid point of carbon [Briant, 1981]. Cr combine with carbon forms the chromium carbide, augmented the tensile strength by precipitation hardening. The grain growth is inhibited by the secondary chromium carbides (second phase particles) by surrounding the grain boundary. Due to grain refinement and second phase particles the dislocation movement becomes very difficult. The presence of chromium carbide in the matrix raises the energy required for elastic /plastic deformation hence causes the improvement in the mechanical and physical properties [Razzak, 2012]. Cr also acts as a hardening element in case hardenable steel and frequently used with Ni to produce higher mechanical properties. The presence of chromium carbide in the steel increases the wear resistance and cutting ability due to the high hardness.

Molybdenum forms a complex carbide phase in the presence of carbon. The addition of Mo in small amount (0.12 to 0.62) increases the Ac3 critical point in low alloy steel. If there is a presence of Mo in a solid solution of austenite before quenching, the reaction rate for alteration of austenite becomes slowdown as compared to mild steels [Yasumoto et al., 1987]. Due to this there is in depth hardening of low alloy steel. The sufficient amount of Mo in steel causes a higher tempering temperature during quenching and the same degree of softness as compare to carbon steel. So the steel with Mo having ability to retain their mechanical properties specially their strength at high temperature due to high tempering temperature. The

steel with Mo has the sufficient resistance to creep under constant loads below their elastic limit at a temperature up to 1150 F. The low alloy steels with a Mo up to 0.40 % shows a minimum affinity to temper embrittlement [Stott et al., 1995]. Some researchers reported that after quenching and tempering some low alloyed steel shows brittleness when gradually cooled from the tempering temperature. The impact resistance is clearly reduced due to this brittleness. The tempered brittleness become more dangerous when large components are being manufactured by these highly susceptible steels because it is very difficult to fast cooling of large components to prevent damage. Mo additions in the amounts noted prevent temper brittleness and allow usual cooling rates to be used after tempering.

2.5.2 Effect of cooling rate

The hardness and other mechanical properties (static and dynamic) of AISI 4340 steel are improved by surface modification methods through phase transformation, grain refinement, dislocation hardening, and inducing compressive stresses over the surface. The variation in the cumulative amount of deformation, temperatures of working and cooling rates can produce a variety of microstructures as per the requirement. The rapid heating up to and over from austenitic temperature and then cooling with different cooling rates results in various types of microstructures, along with different combinations of properties. The dendrite formation in the steel is the distinctive technique of solidification, which is reliant on the heating and cooling cycle. The researchers reported that the precipitation starts simultaneously during the solidification from liquid to solid and dependent on the cooling rate.

The CCT diagram describes the substantial suppression of polygonal ferrite creation and a noticeable transformation area, usually recognized to bainite formation, at the temperatures in between to ferrite and martensite formation. In the area between the ferrite and martensite transformation, the ferrite having the groups of equally oriented particles around 1 µm of size and high dislocation density conquered the significant conversion of austenite during continuous cooling. The ferrite grains anticipated two types of phase in the matrix during continuous cooling leading to the "acicular ferrite" and "granular ferrite". The phase transformation from austenite region depends upon the cooling cycle. At high cooling rate the austenite is transformed into the complete martensite structure. At medium cooling rate the austenite is transformed into martensite and bainite and at slow cooling rates, polygonal ferrite and Widmanstätten ferrite formed. Uzlov and Danchenko [1971] studied the effect of cooling rate in the mechanical, physical properties and phase transformation of different carbon steels

up to cooling rate of 6°c/sec. They found that the properties of carbon steel with different C percentage differ to each other.

The material strengthening effect is carbide related, and limited by steel chemistry and subgrain structure (i.e. matensite laths). Material case strengthening in the case due to quench rate is likely minimal. Consequently, the fatigue Stage I crack initiation for carburized Pyrowear53 may be more controlled by surface residual compressive stresses arising from the differences in quench rate than by material strength. Calik A. [2009] studied the effect of cooling rate in AISI 1020, AISI 1040 and AISI 1060 Steels. The effective phase transformation and solid solution hardening due to increase in percent carbon and cooling rate is the main key factor of increasing mechanical properties. Davis and King [1993] reported the appreciable refinement of microstructure and improvement in the toughness due to change in cooling rate in low alloy steel. Karmakar et al., [2017] studied the effect of different range of cooling rate (0.07 to 3.33 K/s) for micro-alloyed and plain C-Mn steel. They described that high cooling rate increases the formation of hard phase like martensite and bainite by reducing the austenite to ferrite transformation temperature and ferrite grain size.

2.5.3 Effect of microstructure

The different cooling rates give rise to variation in microstructure resulting in different mechanical properties of AISI 4340. Lee and Su, [1999] investigated quenched and tempered AISI 4340. They pointed out that the quenching converts the ferrite-pearlite microstructure into martensitic phase transformation at the surface and dual phase microstructure having ferrite and martensite at the subsurface. The initial microstructure of specimen produced coarse, nodular martensite particles restricted to the former pearlite colonies and a quasi-continuous network of martensite along the ferrite grain boundaries. Guguloth et al., [2014] describes the effect of low cycle fatigue on the Cr-Mo steel and found that modified Cr–Mo steel, having tempered martensitic structure containing coarse-precipitates (such as $Cr_{23}C_6$) and fine-precipitates (such as Mo_2C, NbC and VC), showed the continuous softening to failure under cyclic loading both at ambient and at elevated temperatures. Samanta et al., [2013] studied the effect of quenching and partitioning (Q&P) treatment of low alloy steel to produce a higher fraction of retained austenite by carbon partitioning from supersaturated martensite.

Sun et. al., [2014] did an investigation of laser beam classing of AISI 4340 steel on AISI 4340 steel substrate. They observed that the martensitic transformation in the cladded as well as heat affected zone of laser beam as shown in fig. 2.7, They state that such a martensitic structure was developed by high cooling due to due to self-quenching phenomena. Wang and

Hwand [1994] did the surface microstructural modification by electron beam hardening process to improve the wear characteristics.
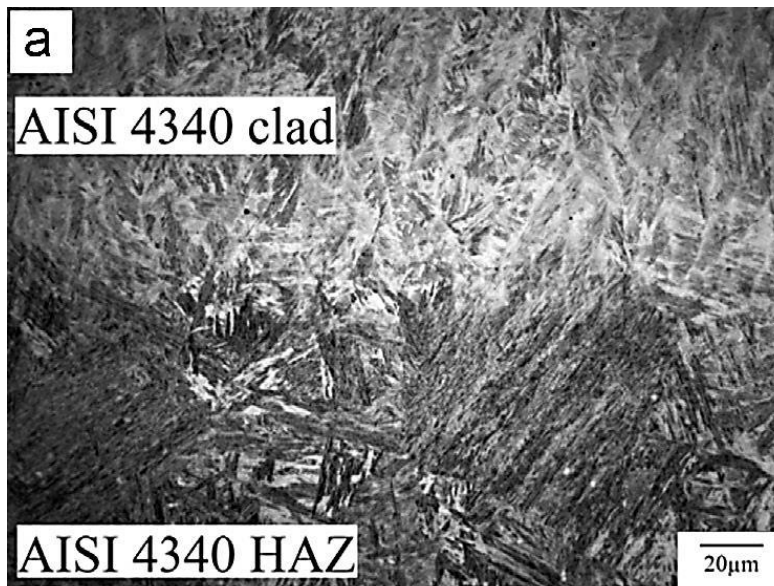
Fig. 2.7   Optical micrograph of the laser cladding of the AISI 4340 steel [Sun et. al., 2014].

2.5.4 Factor affecting the hardenability of AISI 4340 steel

Bain [1979] described that the transformation rate at which the austenite in the steel converted into fine pearlite at the defined temperature controls the hardenability of steel. The composition of the steel is the main key factor to control the rate of transformation at a precise temperature. The maximum transformation rate is observed at temperature of 510 ^{0}C which is used to predict the critical quenching speed and the temperature must be exceeded to become steel hardened.

The AISI 4340 steel consists of Mn, Cr, Ni, Mo and Al as an alloying constituent. The manganese, chromium and nickel contribute directly to deep hardening by increasing the hardening rate and molybdenum appears to induce shallow hardening though restricting grain growth. The hardenability is reduced if the austenite is rapidly transformed into fine pearlite. The hardenability is effectively influence by the grain size and controlled largely, for any specified temperature, by the obstruction to grain growth offered by large numbers of very finely dispersed particles, of exceedingly small aggregate mass, comprised presumably of stable oxides such as alumina, vanadium, and probably silica or silicates.

2.6 Modelling of modified zone

Rosenthal et al., 1946 has used the Fourier partial differential equation of heat conduction and introduced the moving coordinate system to develop solutions for the point and

line heat sources and applied it successfully to address a wide range of welding problems. In his solutions, quasi steady state condition (an observer stationed at the point heat source fails to notice any change in the temperature around him as the source moves on) was assumed which can also be justified experimentally for a long weld. Starting from the partial differential equation of heat conduction, expressed in rectangular coordinates (x, y, and z) w.r.t. a fixed origin in the solid, he applied it successfully for welding by considering a moving coordinate system. It is well known that Rosenthal's solutions are valid at locations away from the heat source but are subjected to considerable error at or near the heat source due to assumption of a point or line heat source.

Wells et al.,, 1952, considered a two-dimensional moving rectangular heat source with a uniform distribution of heat intensity. He proposed the estimation of heat input and welding speed by examining the finished weld. Paley et al.,, 1975, investigated the heat flow in welding thick steel plates by considering the effects of boundary surfaces (bottom or edge of the plate) assuming them adiabatic based on the Rosenthal's solution for point heat source. Christensen et al.,, [1965], developed generalized plots of temperature distribution in dimensionless form at surface as well as at different depths of any substrate, which was found useful for estimation of HAZ, cooling rate and residence time between two temperatures. Pavelic et al., [1969] developed a finite difference method to determine the temperature distribution in a 2-D plate using line heat source. By using melting temperature isotherms as a boundary condition, the shape of the weld pool was correlated with the welding variables. In this method experimental work is required to determine the boundary conditions. The details of the weld pool shape could not be correlated using line source theory therefore distributed heat source with Gaussian distribution of heat flux (W/m^2) was suggested. Friedman [1975] developed a thermo mechanical analysis of welding process using FEM. The model enables calculation of temperatures, stresses, and distortions resulting from the welding process. Friedman and Glickstein [1976] developed FEM analysis for transient heat conduction to investigate the effect of various welding parameters such as heat input and its duration from the arc and its distribution at the surface of the weldments on the thermal response characteristics, in particular the weld bead shape and the depth of penetration. Tsai et al., [1992] developed a semi empirical 2-D finite element heat transfer model that treats the melting interface as an inner boundary to calculate the quasi steady state temperature field and cooling rate in HAZ. Eager and Tsai [1983] modified the Rosenthal's model considering a 2-D Gaussian distributed heat source after assuming (i) no convective or radioactive heat flow, (ii) constant average thermal properties, and (iii) a quasi-steady state semi-infinite medium. They also developed its

solution for the temperature of a semi-infinite body using a constant distribution parameter and obtained results were compared with their experimental values on various metals. Goldak et al., [1984] developed a mathematical model based on a Gaussian distribution of the power density and proposed a three-dimensional double ellipsoidal moving heat source. Finite element modelling was used to calculate the temperature field for bead on plate study and found that the use of 3-D heat source can predict the temperature of the weld joints with much deeper penetration compared to the 2-D model. The computed results of temperature distributions for submerged arc welds in thick work pieces were compared with the experimental values of Christensen et al., [1965].

Tekriwal and Mazumder [1988, 1986] developed a 3-D transient heat conduction model for arc welding using FEM analysis and compared the predicted size of the weld pool and HAZ with the experimental results and found good agreement. Na and Lee [1987] conducted 3-D finite element analysis of the transient temperature distribution in GTA welding by introduced a solution domain which moves along with the welding heat source and it was verified with the experiments on medium carbon steel under various welding conditions. Boo and Cho [1990] developed an analytical solution of 3-D heat conduction equation with convective boundary conditions at welding surface to predict the transient temperature distribution in a finite thick plate. The results were compared with the experimental values of GTA bead on plate weld on medium carbon steel. Vishnu Ravi et al., [1991] developed an analytical model of heat flow during pulsed current GTAW considering Gaussian distributed heat source and the results were compared with mild steel weld. The investigation shows that pulsed current welding refines the grain structure of the weld metal. Kumar Subodh et al., [1992] developed three dimensional finite element modelling of gas metal arc welding. He has considered volumetric distribution of heat content of transferring droplets. The model is validated by predicting weld bead dimensions and comparing them with experimental data. Ghosh et al., [1993, 2006 and 1999] developed a model to predict the thermal and metal transfer behaviour during P-GMAW process and validated the model considering a summarized influence of pulse parameter factor ϕ. Prasad S. and Sankara N. [1996] developed a technique involving finite element analysis of temperature distribution during arc welding by using a transient adaptive grid technique. It gives a finer mesh around the arc source, where the temperature gradients are high, and a coarser mesh in other places to increase computational efficiency of the analysis. Fan et al., (1997) proposed a two-dimensional model using the boundary fitted coordinate system to simulate the P-TIG process. Kim and Na (1998) used the FDM to analysis the fluid flow and heat transfer in partially penetrated fusion zone under P-TIG process.

Nguyen et al., [1999], Nguyen et al., [2004] developed the analytical solutions for transient temperature field of a semi-infinite body subjected to a double ellipsoidal power density moving heat source with conduction only. The results were compared with the bead on plate deposition on HT-780 plates using GMA welding. The model failed to predict the shape of the weld pool in the transversal cross section. Pathak and Datta [2000] presented a three-dimensional transient finite element analysis of heat flow in arc welding using Gaussian distributed heat source and the results were compared with the published values. It was found that arc length significantly affects the temperature of weld pool and adjacent base metal. Komanduri and Hou [2000] developed an analytical solution for the temperature rise distribution in short work pieces in arc welding considering the arc beam as a moving plane (disc) heat source with a pseudo-Gaussian distribution of heat intensity. Christensen et al., [2003]has proposed a neural network approach for GMA butt joint welding. Mahaptra et al., [2006] developed 3D finite element analysis to predict the effect of shielded metal arc welding process parameters on temperature distribution, angular distortion and weldment zones in but and one sided fillet welds. The predicted temperature distributions in butt bead on plate and one sided fillet weld under various conditions of welding are compared with experimental results and found to be in good agreement.

Bag and De [2008] have developed a finite element based 3 dimensional quasi steady heat transfer model to compute temperature field in gas tungsten arc welding process. The welding heat has been considered as volumetirc heat source. The model is validated with experimentally measured weld dimensions. Goyal et al., [2008] has developed analytical solution to find the temperature distribution in weld pool for pulse current gas metal arc welding considering two types of heat source acting simultaneously. Arc heat source has been considered as double ellipsoidal while transfer of heat by super-heated metal droplets as point heat source. The results are validated by comparing the results of bead on plate study. The equation is unable to determine the temperature within a radius of 2mm from arc centre. Bag S. and De [2009] have developed efficient numerical heat transfer model coupled with genetic algorithm based optimization for prediction of process variables in GTA spot welding. Genetic algorithm identifies suitable value of process variable for a target weld dimensions. A B Murphy et al., [2009] reviewed the thermal modelling in plasma generated in TIG welding process and found that the thermo physical properties affects the characteristics of welding arc, including the weld pool depth and geometry.

Schnick et al., (2010) proposed a mathematical model for arc welding process to to predict the local central minimum in the radial distributions of temperature and electric current

density which is caused by a high concentration of metal vapour in the arc core and its high radioactive emission. They also described the effect of the metal vapour in increasing electrical conductivity at low temperatures, which leads to lower heat flux density and current density at the weld pool, implying a shallower weld pool. M. Chiumenti et al., [2010] developed a FEM model to describe the material behavior when the material transforms from liquid (purely viscous)to solid (elasto-plastic) in the multi-pass welding process.

Anca et al., (2011) developed a FEM model to predict the thermal and mechanical phenomena in the arc welding process. Traidia and Roger (2011) proposed the unified time-dependent model to define the fluid flow, heat transfer and electromagnetic fields in the modified zone by P-TIG process. Tseng and Huang [2013] performed a FEM analysis by Gaussian distribution of the heat flux with an effective arc radius to describe the distributive nature of the heat source provided by the welding arc. They pointed out that arc efficiency has an effect on temperature history during welding. Tong et al., 2013 developed a time dependent heat source model (dynamic model) according to the characteristics of P-TIG process. However many investigations have been accompanied, but far less work has been done on the development of the welding heat source model under P-TIG process. Adak et al., 2015 developed the multiple linear regression equations to predict different results (weld bead geometry, as a function of multiple input variables for 'bead-on-plate' type GMAW process. Bag and De [2008] developed a three dimensional quasi steady heat transfer model to estimate the temperature distribution in gas tungsten arc welding (GTAW) process. De et al., [2003] developed an analytical model to predict the cooling rate and microstructure in laser spot welds. Häßler et al., [2015] developed a FEM model to characterization of the arc for narrow gap welding. The model allows the specific improvement of the shielding gas flow and the prediction of the temperature profile of the workpiece for real component applications. Hertel et al., [2014] simulated the plasma-MIG process to investigate the influence of process parameters and thus helps to improve the properties of the weld. Manvatkar et al., [2011] developed a three-dimensional (3-D) heat transfer analysis based on the finite element method to predict the weld pool geometry, thermal cycle and mechanical properties in laser assisted shaping process for ASS. Schnick et al., [2012] developed a numerical model to study the arc behaviour and interaction phenomena between a plasma arc and a superimposed laser beam. M. Shome [2007] used Ashby–Easterling analytical model based on Gaussian heat source distribution to determine the peak temperature at different locations of the HAZ in a butt welded situation by considering a disc diameter proportional to the electrode diameter and limiting conditions defined by the current density. Shome et al., [2004] developed an analytical

model to accurately predict the grain size of the HAZ that experience thermal cycles with large kinetic strengths, taking into consideration the transition in grain growth kinetics following precipitate dissolution. Shome et al., [2006, 2004] simulated the HAZ using the Rykalin-3D (thick plate) heat-transfer model and generated a continuous cooling transformation (CCT) diagrams for HSLA steel. Tadamalle et al., [2014] estimated the weld pool geometry and cooling rate in laser welding. Yang et al., [2008] simulated the laser shock peening of Al alloy by FEM modelling to provide the overall numerical assessment of the characteristic physical processes and transformations. Zähr et al., [2012] simulated the effect of process gases in the TIG welding process.

2.7 Effect of Residual Stresses on steel

The residual thermal stresses are introduced by the surface hardening processes into the substrate surface. The thermal gradient during heating and cooling also make the substantial change in the volume of the component [Elmesalamy et. al., [2014]. There is the expansion of the surface during heating due to thermal gradient. The heat is rapidly transferred to core by conduction due to which the cooling of surface becomes very fast compared to interior [Dieter, 1988]. The temperature difference between the interior and surface increase upto maximum limit and then reduces. As a result when the heat is transferred from the surface to core the surface shrinks more than the interior which creates the pressure against the interior. Since the core is heated at the same time due to transfer of heat so interior is not much shrink by the same volume. This condition builds the tension in the substrate surface and compression in the interior region. Due to this irreversible plastic flow occurs into the system. The further reducing of temperature with time, there is a change in situation. The compressive stresses are generated at the surface with decrease of temperature and tensile stresses in the interior side [Dieter, 1992].

The researches explained that the residual stresses generated into the system may be destructive or constructive. If the nature of stresses is tensile, it adversely affects the fatigue and wear properties. The compressive nature of stresses is beneficial same for wear and fatigue properties. It is very essential for a design engineer to know the beneficial and adverse effects of residual stresses so that he could maintain the prescribe safety limit of applied force for an engineering component. Sometimes residual stresses are induced into the components to increase the wear, corrosion and fatigue properties [Totten, 2002]. Residual stress is defined as the non-uniform plastic flow due to application of manufacturing operations like welding, surface hardening, cold and hot working, forging and so on [Mohanty, 1994, Francis, 2013].

The various factors are involved to introduce residual stresses into the system. The surface hardening processes also increase the volume due to phase transformation. However, every product of austenite decomposition, i.e., martensite, bainite or pearlite would be associated with a volume increase [Inoue et al., 1981]. The martensite forms promptly on the substrate surface of steel after quenching. The martensitic formation is primarily associated with the volume expansion, whereas for a certain time the interior remains as austenite because of it is still hot. After some time when the austenite phase beneath the surface transform into martensite, the expansion of volume due to conversion is constrained by the hardened surface layer causing in compression in the core and tension at the surface [Leggatt, 2008]. The thermal shrinkage in the interior is delayed by the hard surface layer. Researchers described that this type of volume expansion and contraction may cause severe plastic deformation leading to distortion of the workpiece or even localized braking which is known as quench cracking. The component of large size have a high cooling rate due to rapid heat transfer contribute to high thermal contraction and suppresses the volumetric expansion. The researchers studied that for a fix cooling rate there is a decrease in the residual stress if the thermal gradient decreases with the decreasing cross section. So the residual stresses are primarily depend upon the size of workpiece, cooling rate, phase transformation and hardenability of steel [Shipley and Moore, 2002]

2.8 Fundamental of fatigue

In 18th century, It was reported that the component or structure was failing under cyclic load having much below applied stress with comparison of it maximum strength. More no of fatigue failure was reported as the requirements of the machine and structure are increased year by year. These machine and structure were failed due to cyclic loading, so that the the fatigue is an important criteria for design. In recent year, research are more focused on the advanced aluminium, steel and other alloys, that may provide more fatigue life as compare to incumbent alloy by delaying the crack initiation and proportion also improve strength and toughness.

2.8.1 Type of fatigue

`   **1. Low cycle fatigue (LCF)-** component fail before 10000 cycles of loading. In LCF gross plastic deformation will occur. Due to this interpretation is difficult.

2. High cycle fatigue (HCF)- component fail between 10^4 to 10^7 cycles of loading. In this material fail due to localized yielding occur below the elastic point of material. If the life is more than 10^6 or 10^7, then it is called endurance limit.

Fatigue failure is primarily caused by any or in combination of the following factors.

> - Type of loading (uniaxial, bending, torsional)
> - Shape of loading curve
> - frequency of load cycling
> - loading pattern (periodic loading at constant or variable amplitude, programmed loading or random loading)

Fatigue Failure in a component is basically influence by different parameter. Some parameters are listed below-

- Magnitude of stresses
- Part size and shape
- Fabrication method
  - During fabrication like grinding, cutting forging, drawing etc having microstructure, morphology, stresses, notch in the component.
- Operating temperature and environment
- Residual stresses

    The methods of inducing residual stresses in parts can be divided into four main groups:
    - Mechanical Methods
    - Thermal (microstructural) Methods
    - Plating
    - Machining
- Microstructure and Fretting damage

Methods to change microstructure and fretting properties are following

- Surface treatment with deposition
- Surface treatment without deposition

2.8.2 Stress Cycle

Basically three type of stress cycle are are appled during fatigue test as shown in fig. 2.8 (a-c) The fig. 2.8 (a) shows the complete reversal cycle, in which the maximum and minimum stress are same but apposite in nature (tensile and compression). The fig. 2.8 (b) shows the repeated cycle, in which maximum and minimum stress are not same, means that the cycle may be tensile- tensile or tensile – compressive nature depending upon the stress ratio. Third type of stress cycle is irregular or spectrum loading as shown in fig. 2.8 (c)
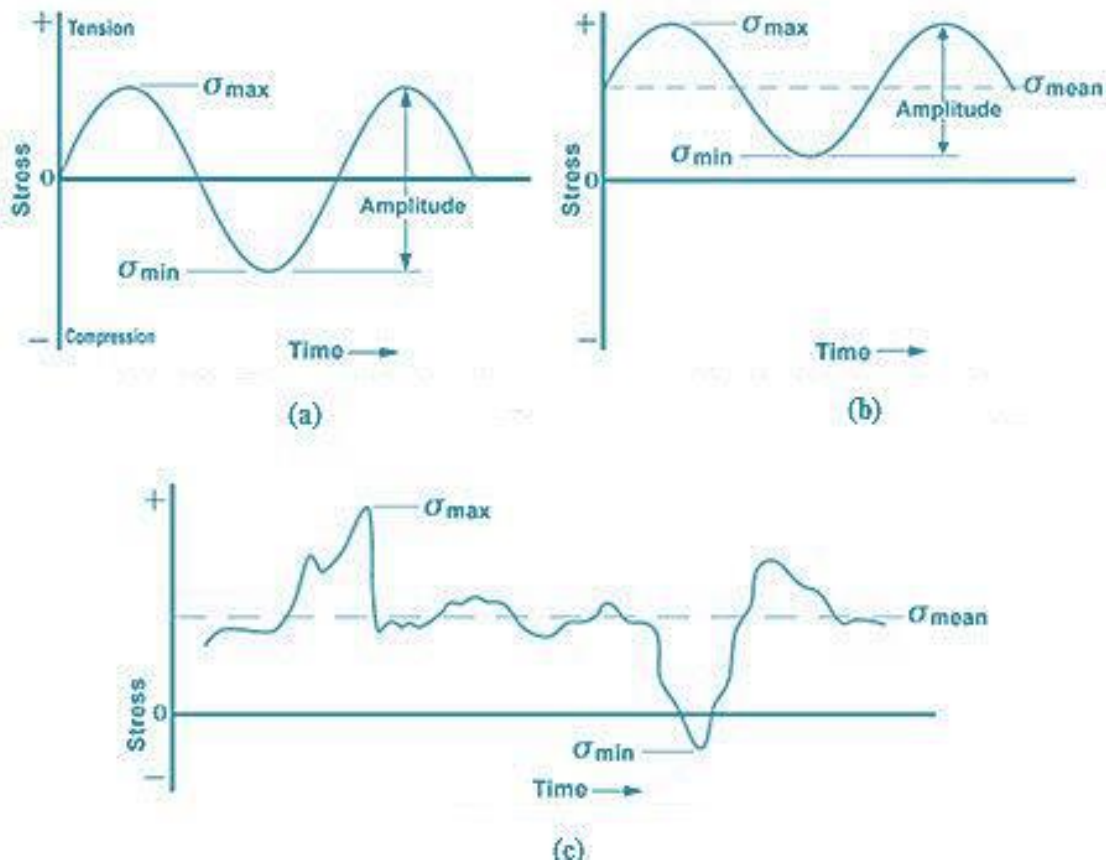
Fig. 2.8   Type of tress cycle (a) complete reversal, (b) repeated cycle and (c) irregular or spectrum cycle

Component of fluctuation stress in fatigue cycle has been shown in fig. 2.9, These are calculated by following equations.

Stress range $(\sigma_r) = \sigma_{max} - \sigma_{min}$ …………………………………………………….(2.8)

Alternating stress $(\sigma_a) = \dfrac{\sigma_r}{2} = \dfrac{\sigma_{max} - \sigma_{min}}{2}$ …………………………………………..(2.9)

Mean stress $(\sigma_m) = \dfrac{\sigma_{max} + \sigma_{min}}{2}$ ……………………………………………….....(2.10)

Stress ratio $(R) = \dfrac{\sigma_{min}}{\sigma_{max}}$ ………………………………………………………………….(2.11)

Amplitude ratio $= \dfrac{\sigma_a}{\sigma_m} = \dfrac{1-R}{1+R}$ …………………………………………………….(2.12)

In the consideration of stress ratio, R is always lives between -1 to 1

If   R= -1   then a fully reversal cycle

       R= Between -1 to 0 ,   a partial reversal cycle

       R= 0 , $\sigma_{min}= 0$

       R= 0 to 1,   a tensile-tensile cycle

40
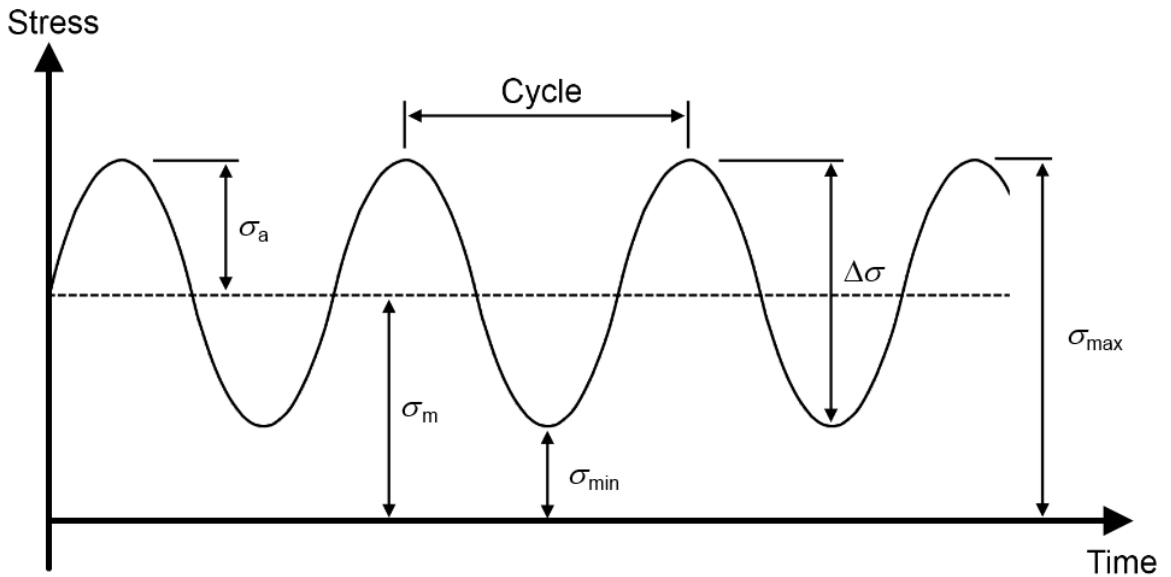
Fig. 2.9   **Detailed view of fatigue cycle with its component.**

2.8.3 S-N curve

The fatigue test gives number of data set for information of the maximum stress at failure verses number of cycle. These data set are basically presented in S-N (stress-cycle)curve, in which X-axis is represent the no. of cycles (N) in a logarithmic scale and y-axis shows the Maximum stress, stress range, stress amplitude in an arithmetic or logarithmic scale. A standard procedure for the preparation was provided by the different standard such as ASTM E468.
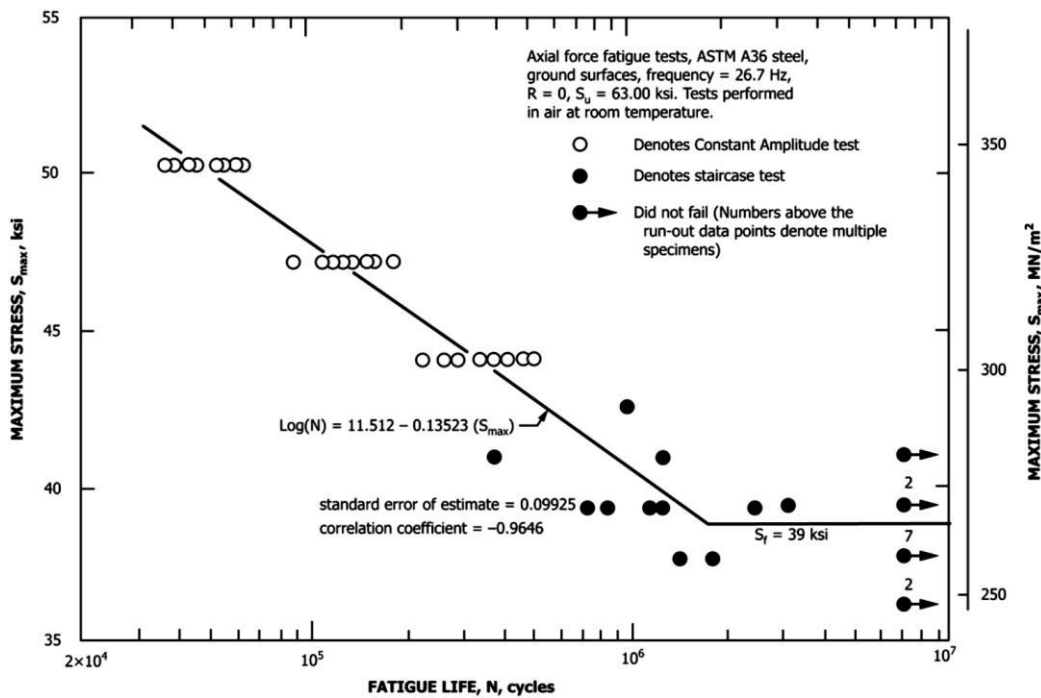
Fig. 2.10   S-N curve representation [ASTM E468].

41

For the preparation of S-N curve, the first sample was tested at the maximum stress at 65 – 75 % of UTS so that the sample was failed in fairly less no of cycle further σmax was reduced until the sample did not fail in 106 or 107 cycle, such sample consider as it have infinite no of cycle known as endurance limit. The endurance limit was clearly observed in case of steel as shown in fig. 2.10, but it was not observed for some material like alu, cu [Zhao and Jiang, 2008].

2.8.4 Fatigue Mechanisms

W.A.Wood [1955] gives the information of fundamental aspects of the fatigue mechanism, the metals are crystalline in nature and atoms are in atomic structure and staked one upon another. When load applied on the material, deformation was observed in slip. When deformation is less (its lives in elastic region), then it came back to previous position otherwise a deformation as take place in the slip and form a systematic fine slip movement as shown in fig. 2.11. As the number of fatigue cycle increase, intensity of slip was increase and it forms slip bands that was damage the microstructure and initiate the crack on the surface by forming notches or ridges. The cracks have been found to initiate at slip-band intrusions and extrusions
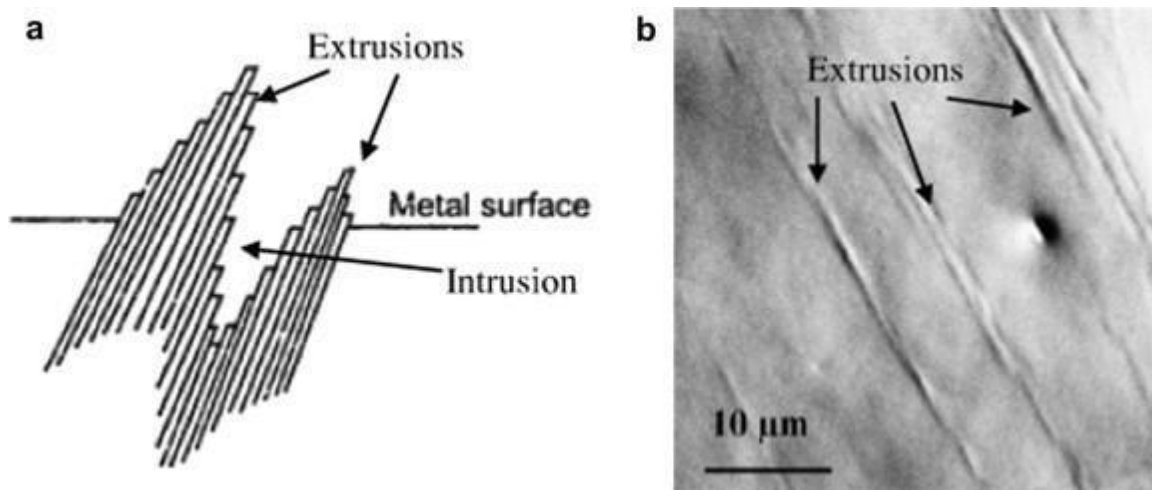
Fig. 2.11   Slip Mechanism [W.A. Wood, 1955]

2.8.5 Fatigue failure

The failure mode of the fatigue is primarily divided in three stages.

- Crack initiation (Stage I)
- Crack Propagation (Stage II)
- Final sudden fracture (Stage III)

1) **Crack Initiation:-**

The first stage of the failure is crack initiation, this stage is generating from the slip plane movement and it extends in the 45° of applied load. This zone extends up to $2 -$ grain and each grain crack propagates along well defined crystallographic plane and it grow approximate 1 angstrom per cycle. Usually these zones have no fatigue striations

2) **Crack Propagation:-**

Zone II, changes its orientation of main fracture plane in each grain. The fracture may grow with approximate rate of 1 micron per cycle. The flow of fracture is to the normal of maximum of tensile stress.

3) **Final sudden fracture:-**

This zone was occurred in the last fatigue cycle, when the crack propagation was increase the area of the component decrease and it was reach a critical limit such that the cross section of a component was unstable during loading and a sudden fracture was observed. The fracture of this zone was primarily associated brittle or ductile or mixed mode of fracture.
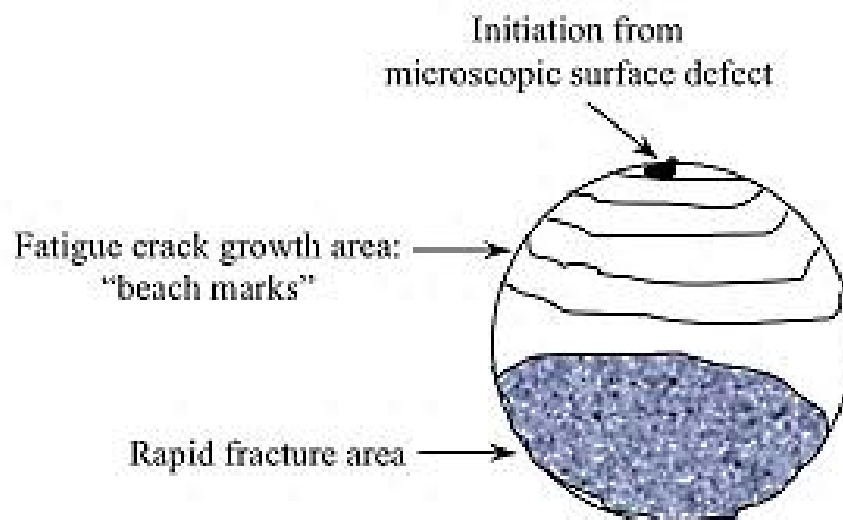
Fig. 2.12   The failure mode of the fatigue

2.9 Effect of surface modification processes on fatigue properties of steel

Surface modification is a one of the important parameter for fatigue properties of a component because crack initiation is primarily observed from the surface and followed by the crack propagation. Ji-Liang et al., [1989], gives the information about the effect of hard phase transformation in 4140 steel by laser hardening, he observed that the hardened material reduces the crack propagation up to the some value of ΔK after that it increases crack propagation. Lai

et al., [2016] did an investigation on the effect of surface microstructure modification on the fatigue properties of medium and high carbon steel and shows that the crack initiation was more easy to generate in martensitic as compare to bainite during three point bending load.

The use of surface modification process introduces the residual stresses on the material by phase transformation and non-uniform deformation during heating and cooling cycles [Shipley and Moore, 2002]. If the transfer of phase is ferrite to pearlite or martensite, the volume increases hindered by the bulk material produces compressive residual stresses. Collins [1993] described that the compressive residual stress is induced by surface hardening process to retard the nucleation and propagation of surface cracks. Researchers [Kobasko et al.,2007; Kobasko, 2010 Kobasko, 2012] investigated that thermochemical treatment like caruburizing introduces the compressive stresses by delay in surface martensite formation due to the high surface carbon content. Kobasko et al., [1985] described that carburizing followed by intensive quenching produces the compressive stresses on the surface with subsequent increase in fatigue and fracture properties of steel. Farfan et al., [2004] found that the fatigue strength is effectively increases by the hardening case depth and brittle fracture is observed in a hard case layer and ductile fracture in the core of the specimen.

Terent et al., [2007] investigated the effect of nitriding on residual stress and fatigue strength of structural steel. He pointed out that the ion nitriding essentially increases fatigue resistance of all structural steels due to the saturation of metal surface by nitrogen and causing in surface layer compressive stresses. Kanchanomai et al., [2008] studied the effect of residual stress on fatigue behavior and mechanism of carbonitrided AISI 1015 steel under uniaxial cyclic loading and found higher fatigue resistance due to the presence of compressive stresses in case layer. Leskovsek, V. et al., [2008] have studied the effect of plasma nitriding and nitrocarburizing for surface treatment of AISI H11 steel and found residual compressive stresses in the diffusion zone.

Lee et al., [2006] have investigated the effect of flame hardening of 12 Cr steel and found that tensile stresses are produced due to a phase transformation and compressive stresses due to thermal contraction. Researchers [Sadowski, 2015,Schöpfel et al., 1997; Grum et al., 2001; Lin and Ericsson, 1992; Kristoffersen and Vomacka, 2001] have studied the effect of induction hardening on the residual stresses and found the compressive stresses at the surface followed by tensile residual stresses at the core. Sochalski-Kolbus et al., [2015] have investigated the residual stresses in Inconel 718 by neutron diffraction technique and found compressive stresses over the surface due to precipitation of different phases and thermal shrinkage developed by high heating and cooling rate. De and Debroy [2011] described in a

perspective way the effect of residual stresses in welding and concluded that residual stresses occur in the welding process due to difference in cooling rates in the distinct regions of the welding, non-uniform instantaneous thermal cycle, and volume change due to phase transformations. Wavare and Ramgir [2015] studied the effect of magnetic arc blow on the stresses during arc welding processes.

FORMULATION OF PROBLEMS

3.1 Formulation of Problem

The surface properties of engineering components play a vital role in their service performance when interactive mechanical exposure causes severe fatigue and wear to them. This necessitates desired modification of the surface properties of a part, especially when a more economically viable material that has other favourable bulk properties is selected in critical industrial applications. Therefore lots of researches are carried out for developing and optimization of processes to fulfill service requirement and it is also considered that the process should be economical. The surface modification by TIG arcing process is a comparatively new approach to modify the surface properties by introducing an arc between the non-consumable tungsten electrode and work-piece under an inert shield environment. In this process a rapid heating and cooling of the substrate introduces desirable phase transformation to the surface that increases its wear resistance, corrosion resistance and residual stress up to a certain depth. It is generally understood that high hardness materials are good wear resistant as compared to the relatively soft materials.

Surface modification of steel through TIG arcing process creates two different zones named as FZ and HAZ in the substrate. The phase transformation of these zones depends upon their thermal cycle defined by heating rate, peak temperature and cooling rate. Several researchers have found that cooling rate effectively controls the phase transformation in steel surface. Higher cooling rates make the hard phase transformation from austenite into the steel surface. The temperature distribution of modified zone, affected by the heat content and geometry of the fusion zone, largely dictates its thermal cycle and influences the solidification behaviour of the melt. Hence a suitable control of these aspects of fusion zone often becomes a matter of great interest.

The primary controlling parameters for autogenous TIG arcing processes are arcing current, arc voltage and arc travel speed, these are the governing parameter for isotherm, thermal cycle and solidification mechanism of FZ and also influence the HAZ of base material. However, the TIG arcing process may be proved as a better process of surface modification, especially when it is used with pulse current. This is because the use of pulse current instead of continuous current facilitates more precise control of energy input and its distribution in the system. The P-TIG arcing process has number of advantages that primarily include intended

operation at relatively low heating, less distortion of the substrate and precise control of isotherm and thermal cycle leading to control necessary phase transformation and microstructure. The knowledge can be used in various industries including electrical power generation, bearing manufacturing, turbine manufacturing and gear manufacturing, where surface modification of steel provides superior mechanical properties (static and dynamic) and wear resistance that gives rise to more reliability and longer life of the system. A concentrated arc has been applied over the surface in TIG arcing process, However, due to the limited spread of arc heat for fusion, multi-pass TIG arcing is required for modification of a large surface area of a component. Multi-pass arcing heat treats the former modified zone primarily depending upon the heat content and the rate of heat removal from the FZ governed by its geometry, which determines the final metallurgical and mechanical characteristics of the modified surface.

3.2 Objectives

After finding the potentials of C-TIG arcing process to produce improved surface modification, effort has been made to develop knowledge of critical application of autogenous C-TIG arcing process for optimum surface hardening of AISI 4340 steel substrates. The knowledge includes appropriate control of parameters primarily in order to manage the thermal cycle and isotherm of the heating zone giving rise to desired surface modification of the substrate primarily defined by its geometry and microstructure. In this regard the relatively low heating characteristics of the pulse current arcing process is also kept under consideration for comparatively lower distortion and residual stresses of the substrate than that observed in case of the conventional (non-pulse) current arcing process. The innovation in surfacing is planned to establish after carrying out detail studies using the C-TIG arcing process and comparing it to the surfacing by employing the P-TIG arcing for the same purpose. It is primarily approached from the following angles as stated below.

1. Mathematical modeling of thermal behavior of autogenous C-TIG arcing as a function of process parameters and its effect on profile of heating and phase transformation in AISI 4340 steel.

2. Experimental verification of the model outcome in control of isotherm and thermal cycle especially in reference to cooling rate and behavior of phase transformation in autogenous C-TIG arcing up to a desired depth in AISI 4340 steel substrates.

3. To develop a thorough understanding of the scientific and technological aspects of the C-TIG arcing process to explore the possibilities of its application in more challenging areas of hard surfacing of steels especially with respect to control of microstructure.

4. To study the characteristics of surface modified AISI 4340 steel substrate under the uniaxial tensile test of surface modified substrate and the behavior of modified matrix of the substrate exposed to tensile stress under three point bend test, while the modification is made by single and multi-pass C-TIG arcing with various parameters.

5. To study the fatigue properties of all the surface modified substrate under dynamic loading of uniaxial tensile and bending mode as stated above in order to generate S-N curve and compare.

6. To study the effect of arcing process parameters on the residual stresses generated during C-TIG arc surfacing.

7. To make a comparative study of the effect of using P-TIG and C-TIG arcing processes on various properties of the surface modified AISI 4340 steel substrate, such as bead geometry, microstructure, three point bend and tensile properties, fatigue life and generation of residual stresses.

The chapter consists of the analytical and experimental procedures employed in the present work and describes details of the processing route employed for surface modification of AISI 4340 steel substrate. The surface modification of AISI 4340 steel is carried out by C-TIG and P-TIG arcing process using single and multi-pass procedures. Further, various equipment's/ instruments and procedures used to investigate composition, hardness, mechanical properties, fatigue properties and residual stress analysis of the modified surface are discussed.

4.1 Base Material

The surface modification has been carried out on a 10 mm thick plate of AISI 4340 steel as base material using direct current electrode negative (DCEN) continuous tungsten inert gas (C-TIG) arcing and pulsed tungsten inert gas (P-TIG) arcing processes using 3.2 mm diameter tungsten electrode of specification AWS EWTh-2 grade. Chemical composition as per ASTM of the base plates and tested certificates provided by the supplier as well as obtained through spark emission optical spectroscopy have been shown in Table 4.1. The results of chemical analysis obtained by using spark emission spectroscopy are found to be in good agreement with the results of the test certificates given by the supplier. The surface modification of AISI 4340 steel was performed with DCEN polarity under commercial Ar (99.98%) gas shielding at a flow rate of 16 Lit/min.

During surface modification the plate was tightly placed in a fixture to avoid distortion. The surface modification of plate was executed in horizontal position by a perpendicularly positioned centrally located welding gun, which was travelling on an automated trolley. Surface modification was performed by maintaining the arc gap of 2 mm between the electrode tip and the substrate surface. The flow rate of gas was controlled with the help of a flow meter and a pressure regulator fitted to the gas cylinder.

Table 4.1   Chemical compositions of AISI 4340 steel.

	Chemical composition (wt. %)								
	C	Cr	Ni	Mo	Mn	S	P	Si	Fe
ASTM A29	0.38-0.43	0.7-0.9	1.65-2.0	0.2-0.3	0.6-0.8	0.04	0.035	0.15-0.35	remaining
Test Certificate	0.39	0.8	1.69	0.23	0.69	0.04	0.04	0.22	remaining
*	0.39	0.79	1.65	0.22	0.71	0.04	0.04	0.21	remaining

*-Spark emission optical spectroscopy

4.2 TIG arcing Power Source

A, DC (direct current) arcing/welding power source made by ESAB (Model no. MIG-U5000i) was used in the current study and a complete setup with power source has been shown in fig. 4.1. The power source was having an advantage of operating different arcing and welding operations such as MIG, GMAW, SMAW,GTAW, C-TIGA and P-TIGA. The machine can be oprated in synergic and non-synergic modes by using several command in respect to different materials, electrode diameter and filler wire in the presence of protective environment. During operation with the C-TIG and P-TIG arcing the non-synergic mode is used to operate the power source where all the parameters are manually settled with maintainance of appropriate correlations among them. The power source was fitted with a control panel along with screen for displaying different set of parameters as well as soft push buttons to input different parameters of arcing process. The power source was connected with 3-phase electrical supply for its operation as per requirement.
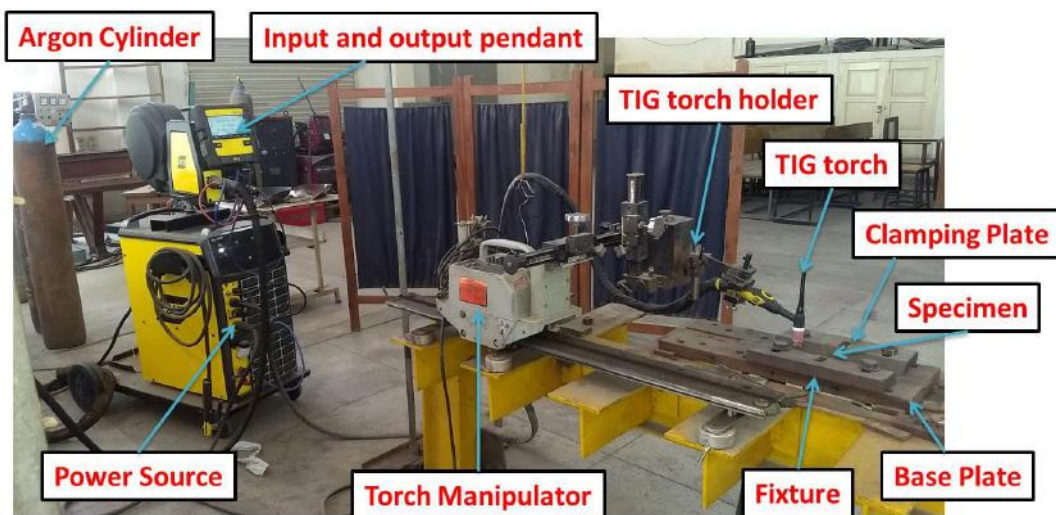
Fig. 4.1   Photograph of the experimental setup used for TIG arcing process.

4.3 Fixture and Torch Manipulator

The fixture and torch manipulator are required to hold the base material properly and guide the welding torch during operations of surface modification by TIG arcing process.

4.3.1 Welding fixture

To fix the base plate rigidly in order to avoid distortion during TIG arcing process, a fixture was used as shown in Fig. 4.2. The fixture consists of a thick mild steel supporting plate of size $450 \times 350 \times 40$ mm and two clamping plates of dimension 300 x 150 x 40 mm. During TIG arcing process the base plate was tightly stable and clamped in the fixture. The clamping force was released after the plates naturally cool down to ambient temperature.
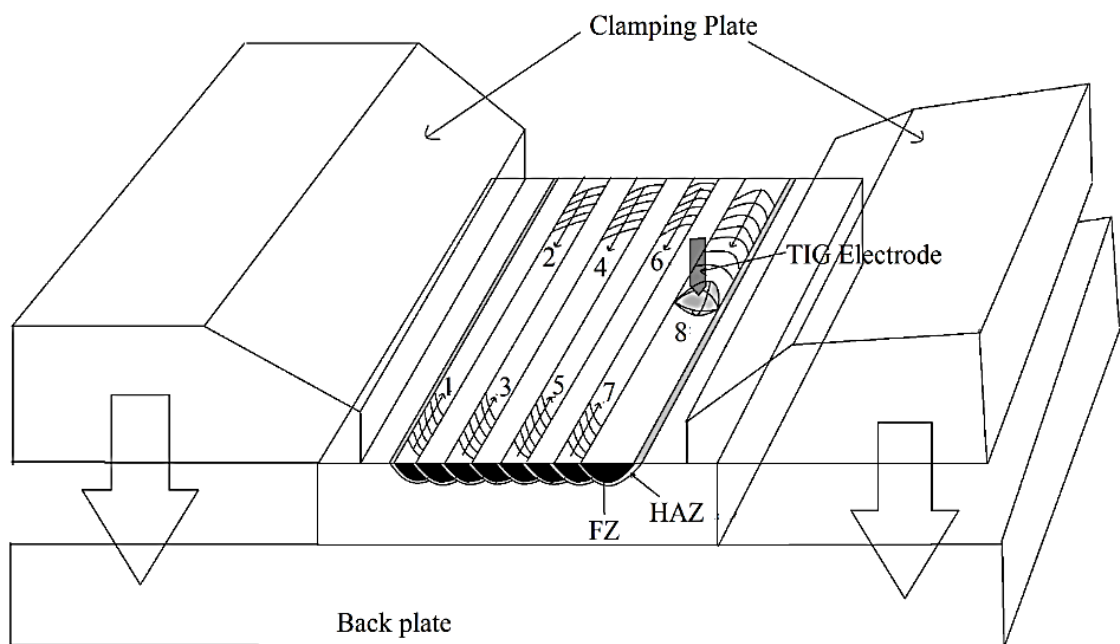
Fig. 4.2   Schematic diagram of fixture and work piece for surface modification by TIG arcing process.

4.3.2 Torch manipulator

A automated TIG arcing torch manipulator, "Gullco make KAT" travel carriage has been used in this work as shown in fig. 4.3. It was capable to grip the torch strictly in the arms and clamping pivots to regulate it at any anticipated position with the help of rack and pinion arrangement. The torch manipulater was also capable to increase the travel speed in the range of 2.5 to 85 cm/min with an electronic display during surface treatment. The reliability of the digital reading of travel speed of the carriage was verified before use by measuring the length and time of travel with the help of a scale and a stopwatch of least count of 0.01 second respectively at different speeds.
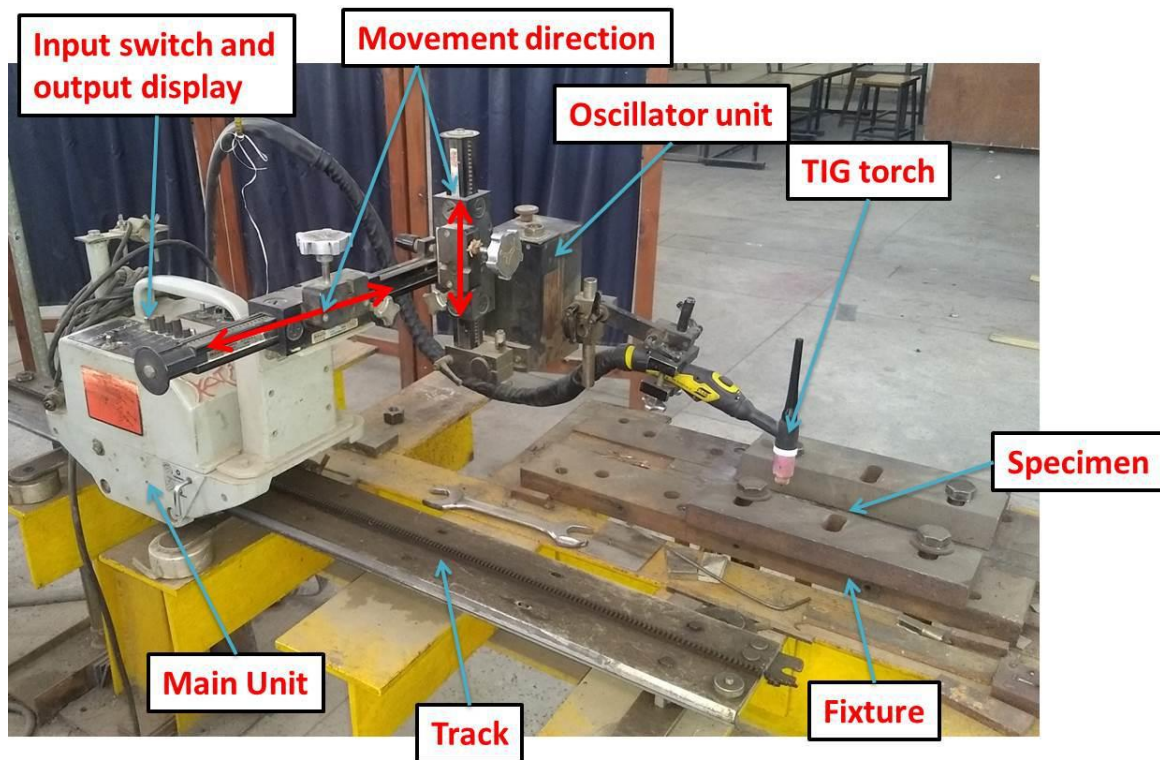
Fig. 4.3   Photograph of Torch Manipulator and fixture.

4.4 Instrumentation and Recording

Instrumentation and recording include recording of thermal characteristics of the fused pool at different operating parameters.

4.4.1 Measurement of temperature of fusion pool

The temperature of the fusion pool was recorded with the help of an R-Type thermocouple (Pt-13 % Pt-Rh) of 0.25 mm diameter. The thermocouple was connected with a computer through a "Strain Buster" (decentralized strain/temperature measuring module) for recording the output. The Strain buster was capable of recording the output of the thermocouple at a time interval of 10 ms in both of its two channels. Before using the thermocouples and "strain buster" for recording of temperatures, they were calibrated within the required temperature range by a known heating source. The output of thermocouple in terms of volt was converted to temperature. The output of the thermocouple as a function of temperature considered through its calibration has been shown in Fig. 4.4.
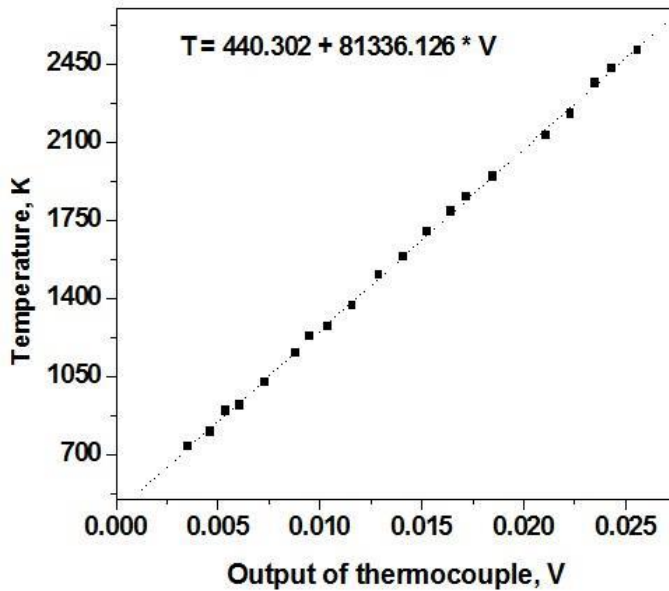
Fig. 4.4   **Diagram showing the calibration of strain buster and thermocouple.**

4.4.2 Estimation of heat input (Ω)

The heat input (Ω) during C-TIG and P-TIG arcing processes can be predicted as a function of arc voltage (V), travel speed (S) and arc current or mean current (I or I_m), and arc efficiency (η_a) as follows [Maruo et. al, 1984].

$$\Omega = \frac{\eta_a \times V \times [I(or)I_m]}{S} \quad\text{...(4.1)}$$

The mean current (I_m) of the P-TIG arcing process as a function of background current (I_b), peak current (I_p), duration of background current (t_b) and peak current duration (t_p) may be obtained as [Lancaster, 1984] as

$$I_m = \frac{(I_b t_b + I_p t_p)}{(t_b + t_p)} \quad\text{..(4.2)}$$

In case of AWS EWTh-2 grade electrode under protection of argon gas the η_a of TIG arcing process was taken as 70% to 85% [Dupont and Marder, 1995].

4.4.3 Estimation of average fusion pool temperature

The average fusion pool temperature ($T_{WP}=T_d$) generated during TIG arcing process was estimated [Goyal et al., 2008] by considering the temperature (T_d) of the point (x(ξ), y, z) due to concentrated arc heating using double ellipsoidal heat source as follows (Fig.4.5).

$$T_d = \frac{3\sqrt{3}.Q_{AW}}{\rho.c.\pi\sqrt{\pi}} \int_0^t \left[\frac{\dfrac{dt'}{\sqrt{\left(12a(t-t')+a_h^2\right)}.\sqrt{\left(12a(t-t')+b_h^2\right)}}}{\left(\dfrac{A'}{\sqrt{\left(12a(t-t')+c_{hf}^2\right)}} + \dfrac{55 \quad B'}{\sqrt{\left(12a(t-t')+c_{hb}^2\right)}} \right)} \right] + T_0 \text{...................(4.3)}$$

Where,

ρ, c and a are mass density, specific heat and thermal diffusivity of the workpiece. The a_h, b_h, c_{hf} and c_{hb} are the ellipsoidal heat source parameters defined by a location having at least a power density of 5% to that of the center on surface of the ellipsoid. Q_{AW} is the arc heat transferred to the weld pool and estimated by the following equation.

$$Q_{AW} = \eta.V.I \quad \text{...(4.4)}$$

The η is arc efficiency, V is arc voltage and I is arc curren respectively,

$$A' = r_f.\exp\left(-\frac{3(x - v.t')^2}{12a(t - t') + c_{hf}^2} - \frac{3y^2}{12a(t - t') + a_h^2} - \frac{3z^2}{12a(t - t') + b_h^2}\right) \text{...................(4.5)}$$

$$B' = r_b.\exp\left(-\frac{3(x - v.t')^2}{12a(t - t') + c_{hb}^2} - \frac{3y^2}{12a(t - t') + a_h^2} - \frac{3z^2}{12a(t - t') + b_h^2}\right) \text{.......................(4.6)}$$

Where, r_f and r_b are the proportion coefficients in front and behind the heat source, estimated as:

$$r_f = \frac{2.c_{hf}}{(c_{hf} + c_{hb})} \quad \text{...(4.7)}$$

$$r_b = \frac{2.c_{hb}}{(c_{hf} + c_{hb})} \quad \text{...(4.8)}$$

The arc efficiency for the TIG arcing process is considered as 75% and the suitable values of the ellipsoidal axis parameters are selected by measurement of fusion pool geometry. The c_{hf} (in front of the heat source) and c_{hb} (behind the heat source) are considered as $c_{hf}= a_h$ and $c_{hb}= 2\ c_{hf}$ described by Goyal et al., 2008.
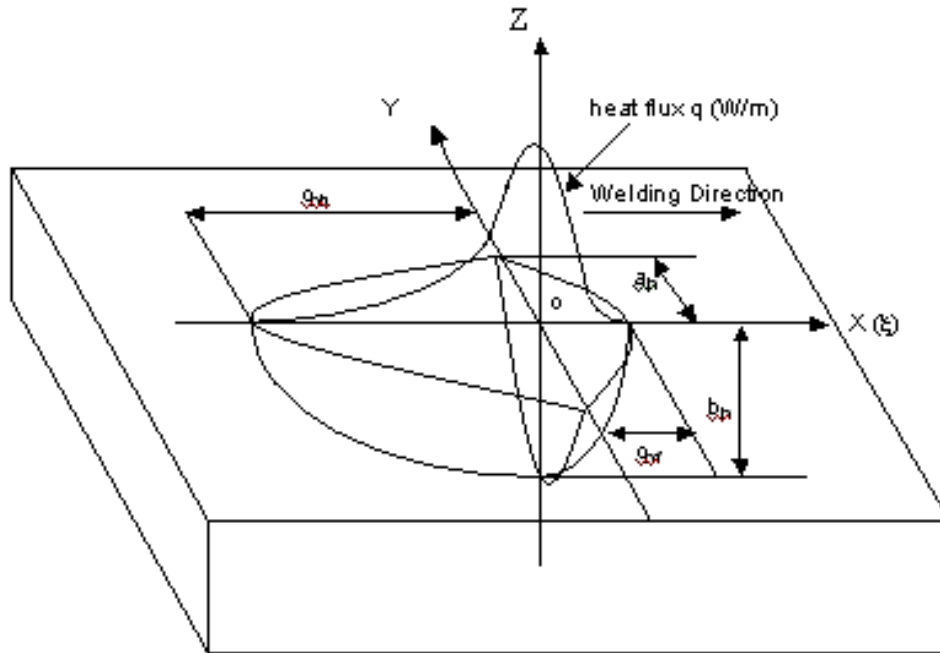
Fig. 4.5 **Schematic illustration of double ellipsoidal heat source (volumetric heat source)**

4.4.4 Estimation of fusion isotherm

The fusion isotherm as a function of arc current (I) and travel speed (S) of different temperature for C-TIG arcing process has been estimated and plotted in longitudinal (XY) and transverse (YZ) direction using the software origin 8 using equation 4.3. The fusion isotherm dictates the geometrical and thermal aspects of fusion pool ultimately governing the properties of the modified zone.

4.5 Single-pass TIG arcing Experimentation

The single-pass TIG arcing experimentation gives a thorough understanding of thermal and geometrical aspects of modified zone through which it is possible to identify an optimized arcing condition to apply in substrate surface for desired phase transformation and properties. The single-pass treatment is applied over the surface to optimized the arcing parameters in terms of higher hardness, high depth of modified zone and minimum distortion of the workpiece.

4.5.1 Single-pass C-TIG arcing process

The surface modification of AISI 4340 steel was carried out by single-pass C-TIG arcing process. The base plate was thoroughly mechanical and chemically cleaned before carrying out surface modification to remove any corrosion product or foreign particles adhering to the surface. The single-pass TIG arcing process was carried out at a constant arc voltage of 10.5 ± 1.0V considering increment of arc current from 80 A to 160 A with variation of travel speed from 6 to 15 cm/min. The heat input was varied through a variation of arc current and

travel speed. The arcing parameters used during single-pass C-TIG arcing process has been shown in Table 4.2.

Table 4.2   Parameters used in single-pass C-TIG arcing process.

Arc Voltage (V)	Travel Speed (S) (cm/min)	Arc Current (I) A	Heat Input (kJ/mm)
10.5 ± 1.0	6	80	0.60
		100	0.79
		120	0.99
		140	1.20
		160	1.42
	9	80	0.40
		100	0.53
		120	0.66
		140	0.80
		160	0.93
	12	80	0.30
		100	0.39
		120	0.50
		140	0.60
		160	0.70
	15	80	0.24
		100	0.32
		120	0.40
		140	0.48
		160	0.56

4.5.2 Single-pass P-TIG arcing process

Achieving all the aspects of TIG arcing can be more precisely addressed by using P-TIG arcing process controlled by I_m and travel speed (S), the pulse parameters I_p, I_b, t_p and f, the summarized influence of pulse parameters proposed earlier [Ghosh et al., 2000, Ghosh and Kumar,2014] and defined by a hypothetical factor ϕ derived on the basis of the energy balance concept of the system. In the present study, pulse parameter was selected from already

58

established by P.K. Ghosh and R. Kumar, 2017, P-TIG arcing process was presented and discussed in reference to change of its microstructure and hardness characteristics as a function of thermal behaviour governed by the arc control of the process. The pulse parameter for present study is shown in table 4.3.

Table 4.3   Parameters used in single-pass P-TIG arcing process.

Arc Voltage (V)	Travel speed (cm/min)	Heat Input (kJ/cm)	I_m (A)	I_{eff} (A)	ϕ	Pulse Parameters				
						I_P	I_b	t_P (sec)	t_b (sec)	f (Hz)
10.5 ± 1.0	12	0.39	100	108	0.21	141	59	0.034	0.034	15
		0.60	140	151	0.21	197	84	0.034	0.034	15

4.5.3 Measurement of thermal behaviour of modified zones (FZ and HAZ)

At a selected set of C-TIG and P-TIG arcing parameters, the temperature of fusion pool was measured during single-pass TIG arcing process in order to verify validity of the analytical expression of eq. 4.3. To get fusion pool temperature after achieving its stability two thermocouples were inserted from the bottom of the workpiece in two dissimilar locations at distances of about 50 and 100 mm from the run on position of arcing as schematically shown in Fig. 4.6(a). The two wires of the thermocouple are kept separate with the help of sleeve and beads. The beads were push fitted in the hole prepared by drilling process. Thermocouples were placed at different depths corresponding to FZ and HAZ from the substrate bottom surface as shown in Fig. 4.6(a). The depth of placement, D_T, of thermocouple as schematically shown in Fig. 4.6 (b and c) respectively was calculated according to the estimation of fusion isotherm matching with melting temperature of the AISI 4340 steel as substrate plate using the analytical equation 4.3 given earlier [Goyal et al 2008], so that the tip of the thermocouple wire fits under FZ and HAZ without having a direct contact with the arc. The isotherm was estimated by considering the temperature dependent thermo-physical properties of materials [Tamura et al, 1988] as shown in Fig. 4.7 for commercial mild steel which are assumed to be in close approximation to those of the AISI 4340 steel used in this work. The thermal cycle was measured by using computerized data recorded as output of the thermocouples through "Strain Buster" as explained in section 4.3.
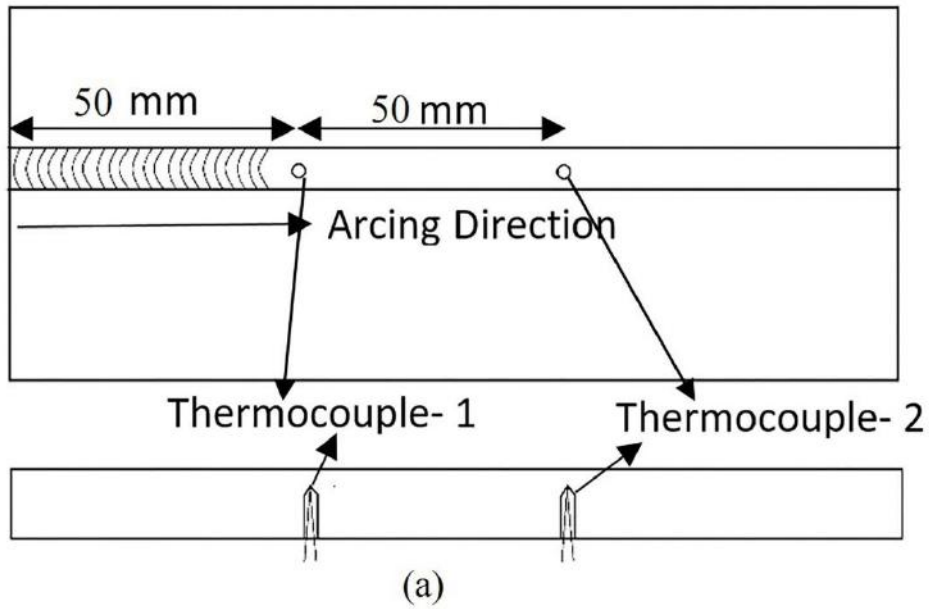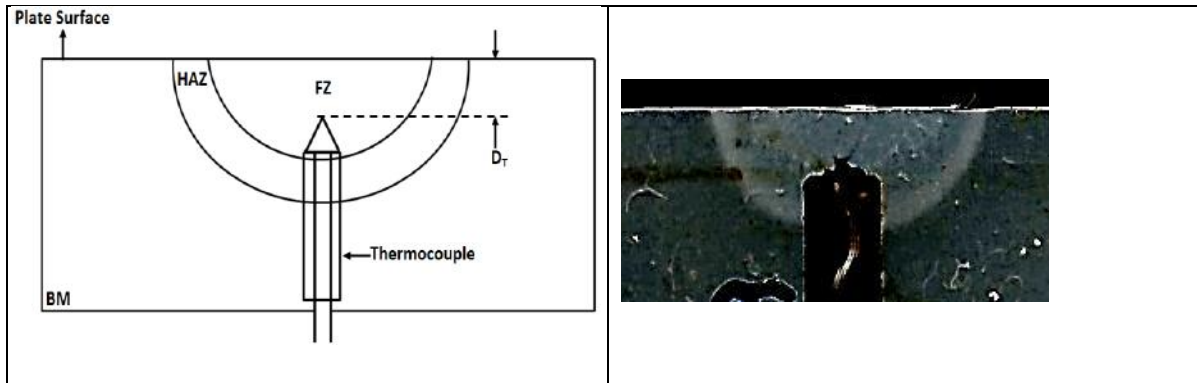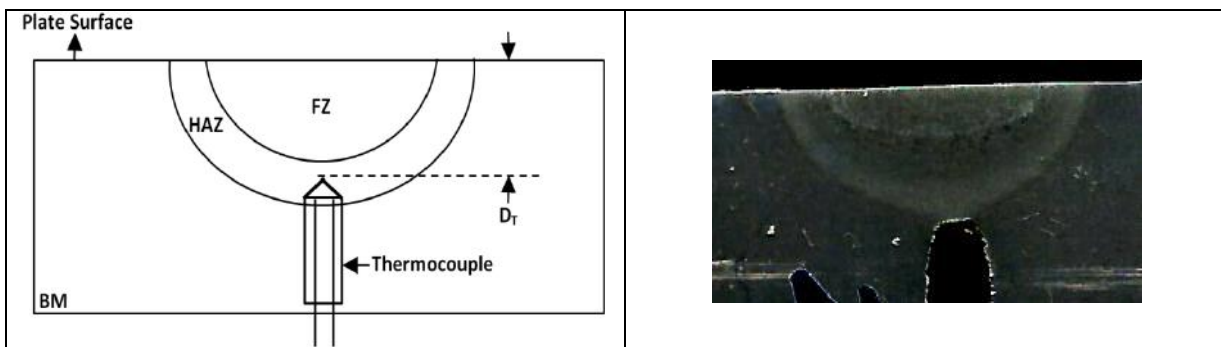
Fig. 4.6 (a) Schematic diagram showing location of thermocouples in modified zone. (b) Schematic diagram showing placement of thermocouple in FZ. (c) Schematic diagram showing placement of thermocouple in HAZ
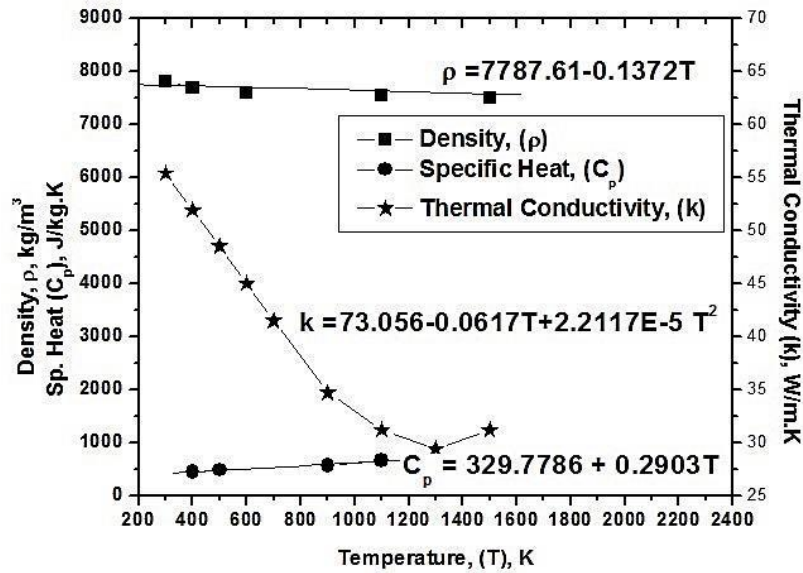
Fig. 4.7 Temperature dependent thermo-physical properties of commercial mild steel.

4.5.4 Estimation of single-pass modified zone (FZ and HAZ) characteristics

The characteristics of modified zones observed at various arcing parameters of TIG arcing processes were analyzed with respect to geometrical aspects of modified zones (FZ and HAZ) as well as the microstructure of modified zones. The different aspects of the studies on modified zone characteristics have been detailed out as below.

4.5.4.1 Geometrical aspects of modified zone

The transverse section of the modified zone collected from its central part of fusion track assuring a stable arcing was polished by standard metallographic procedure and etched in 4% nital solution to reveal the FZ and HAZ geometry and its microstructure. The schematic diagram of geometrical aspects of FZ and HAZ and its typical macrograph was shown in Fig.s. 4.8 (a) and (b) respectively. The characteristics of different aspects of modified zone were studied by measuring the bead width (W_b), depth of penetration (P_d), HAZ width (W_{HAZ}) and area of fusion (A_F) with the support of image analyzer software.

| (a) | (b) |
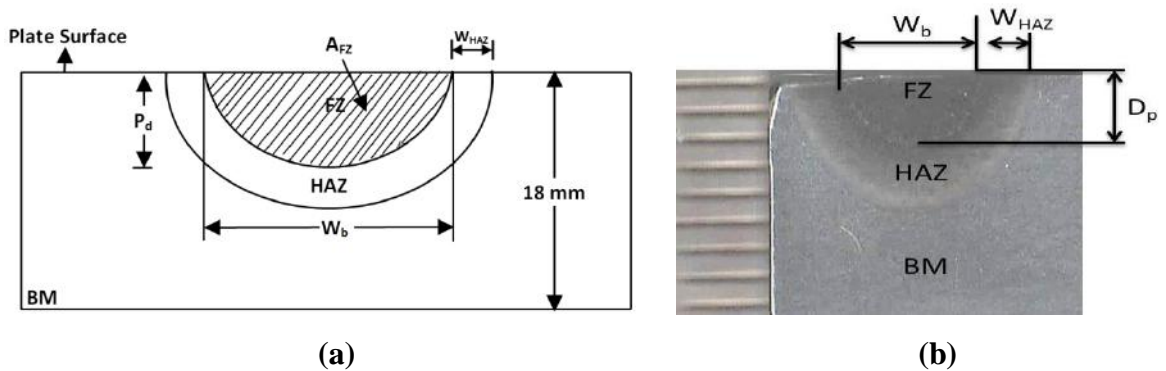
Fig. 4.8 (a) Schematic diagram showing geometrical aspects of modified zone and (b) typical macrograph of modified bead geometry.

4.5.4.2 Metallographic studies

Metallographic studies include the study of morphology of the FZ and HAZ with respect to its microstructure.

Studies on FZ and HAZ

The microstructures of FZ and HAZ at different arcing parameters were studied on the metallographically prepared transverse section etched in 4% nital solution. It was studied qualitatively with respect to phase transformation as revealed under Leica make optical microscope (Fig.4.9) primarily at centre of the FZ. The specific features of the microstructure were recorded in the computer using Leica Application Suit software.

Fig. 4.9   Photograph of the Leica optical microscope used for recording microstructure.

The HAZ of modified zone near to the fusion contour was studied using metallographically prepared and etched specimens of the modified zone at different C-TIG and P-TIG arcing parameters. The different zones of a modified area have been shown in Fig. 4.10. The width of HAZ (W_{HAZ}) perpendicular to the fusion line was measured at several locations along it. The adobe photoshop 7.0 and "image J" was used to analysis the captured images. The accuracy of the measurements was also confirmed by studying the same under optical microscope at suitable magnifications. Average of all the values of the width of HAZ measured on several specimens prepared at a given arcing parameter has been reported as its characteristic feature.
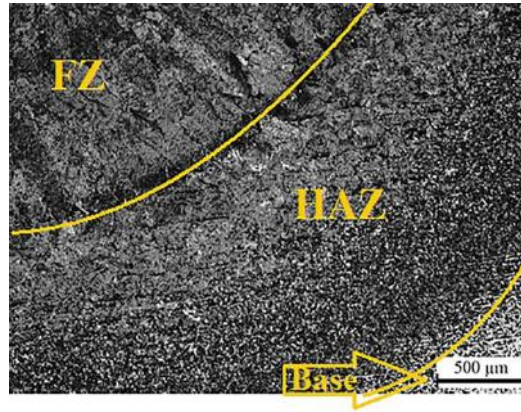
Fig. 4.10   Schematic diagram showing HAZ at both sides of fusion zone.

4.5.4.3 XRD studies

The XRD analysis was carried out with Cu Kα radiation at voltage of 40 kV and current of 30 mA with 1°/min scan rate within the scan angle of $30^o \leq 2\theta \geq 110^o$ .The Fig. 4.11 shows the instrument used for XRD analysis made by Rigaku smartlab. Prior to XRD analysis the substrate surface was polished upto 1000 grit paper and properly cleaned by chemical (acetone) to remove any dust and corrosion particle.

Fig. 4.11   Photograph of the X-ray Diffractometer used for analysis of phases.

4.5.5 Hardness measurement

The Vickers microhardness of C-TIG and P-TIG arcing has been studied at different locations of their etched transverse section revealing the FZ and HAZ. The Vickers microhardness of base metal, FZ and HAZ was measured by diamond indentation using a load of 300 gm and 30 s dwell time. A photograph of the hardness testing machine used for measurement of hardness has been shown in Fig. 4.12. The hardness of FZ was taken at different location and HAZ hardness was measured at 0.30 mm from the fusion line.The

hardness profile was measures from top surface to substrate of single-pass TIG arcing process. The average hardness observed in FZ and HAZ for the given set of parameters were found out for both C-TIG and P-TIG arcing process. The average hardness was correlated with heat input heat input and Arcing current (I) in case of C-TIG arcing.
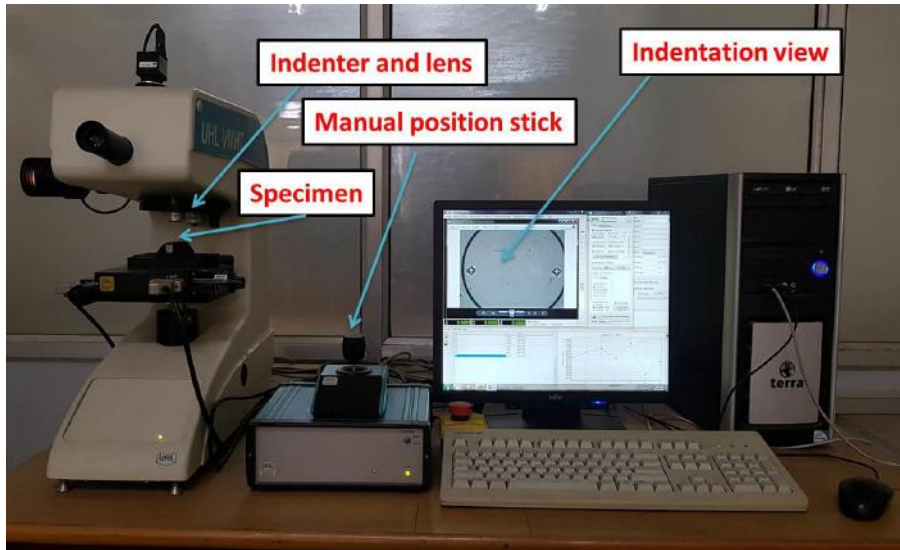
Fig. 4.12   Photograph of the hardness testing machine used for measurement of hardness.

4.6 Multi-pass TIG arcing process

The arcing parameters for optimum modified surface properties obtained in a single-pass TIG arcing process were used for multi-pass arcing with 50% overlap to maintain a uniform depth of modification. The multipass TIG arcing process is applied over a substrate surface in reference to commercial perspective. The effect of multipass treatment by both the processes (C-TIG and P-TIG arcing process) are studied and compared in terms of microstructural features and hardness distribution in its different thermally affected regions.

4.6.1 Preparation of multi-pass treatment

The controlled rolled AISI 4340 steel of 10 mm thick plate of size 75 x 150 mm has been used in preparation of multi-pass treatment. Multi-pass treatment of surface with 50% overlapping of fusion zone as shown in fig. 4.13 (a and b) was carried out at optimum arcing parameters of single-pass fusion, which was found to create maximum penetration nd a width of fusion in both of the processes (C-TIG and P-TIG arcing). Every pass has been done in continuous to and fro manner. The schematic diagram (Fig. 4.13 (a)) is representing the modified surface after multi-pass treatment. The multi-pass treatment was carried out by direct current electrode negative polarity as stated earlier. Prior to multi-pass treatment, the base plate was carefully scrubbed to remove the extra oxide film and any corrosion product adhering to the faying surface. The arcing parameters used during multi-pass treatment under C-TIG and P-TIG arcing processes is shown in Tables 4.4 and 4.5 respectively.
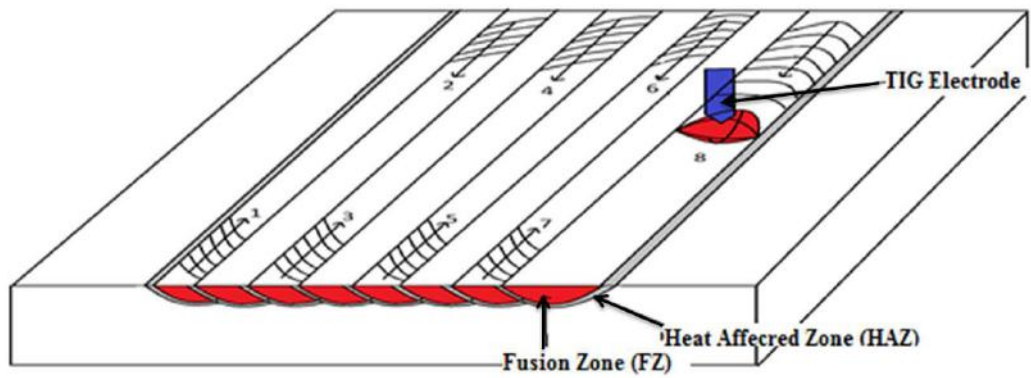
(a)
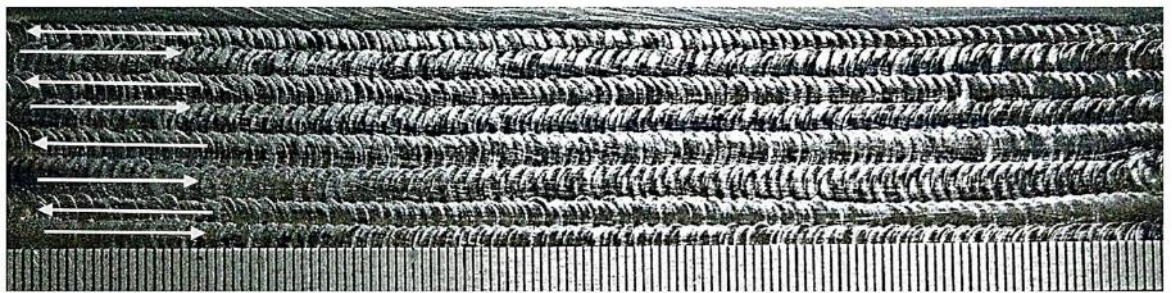
(b)

Fig. 4.13 Multi-pass TIG arcing process, (a) Schematic diagram and (b) photograph of top surface modified by multi-pass TIG arcing process.

Table 4.4 Arcing parameters used in multipass treatment using C-TIG arcing process

Arc Voltage (V)	Travel speed (S) (cm/min)	Arc Current (I) A	Heat Input (kJ/mm)
10.5 ± 1.0	12	80	0.30
		100	0.39
		120	0.50
		140	0.60
10.5 ± 1.0	15	80	0.24
		100	0.32
		120	0.40
		140	0.48

65

Table 4.5   Arcing parameters used in multi-pass treatment using P-TIG arcing process

Arc Voltage (V)	Travel speed (cm/min)	Heat Input (kJ/cm)	I_m (A)	I_{eff} (A)	ϕ	Pulse Parameters				
						I_P	I_b	t_P (sec)	t_b (sec)	f (Hz)
10.5 ± 1.0	12	0.39	100	108	0.21	141	59	0.034	0.034	15
		0.60	140	151	0.21	197	84	0.034	0.034	15

4.6.2 Metallographic studies on multi-pass modified zone

The transverse sections of the modified region prepared by using the multi-pass C-TIG and P-TIG arcing processes were prepared for microstructural studies by standard metallographic technique and etched with 4% chemical (Nital) solution. Metallographic studies under optical microscope were carried out on the different thermally affected regions produced at multi-pass treated modified zone. The thermally affected regions are divided into five zones as shown in fig. 4.14.
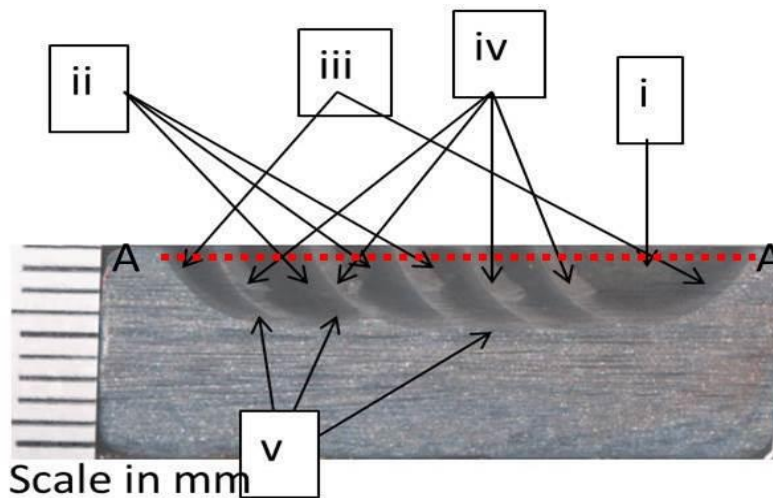
Fig. 4.14   Typical appearance of transverse section (A-A), representing (i) original FZ, (ii) reheat refined FZ, (iii) original HAZ of base metal, (iv) double reheat refined fusion zone and (v) reheat refined HAZ of base metal of the Multi-pass TIG arcing processed surface.

4.6.3 Hardness Studies

The distribution of hardness along the line A-A as shown in Fig. 4.14 was measured by Vickers micro hardness testing (Fig. 4.12) of UHL VMHT Microhardness Tester at a load of 300 grams having provision of magnification of image up to X500. Prior to carrying out testing the machine was calibrated by measuring the hardness of a standard sample at the same load.

4.7 Mechanical characterization

Mechanical characterization i.e. axial Tensile test, three point bend test and fatigue test was performed at room temperature on INSTRON 8802 servo hydraulic machine having $\pm$ 50 KN and $\pm$ 250 KN dynamic load cell and $\pm$ 75 mm working length. The fig. 4.15 (a) an (b) shows the Photograph of INSTRON 8802 servo hydraulic machine a) testing Section b) controlling section.

(a)   (b)
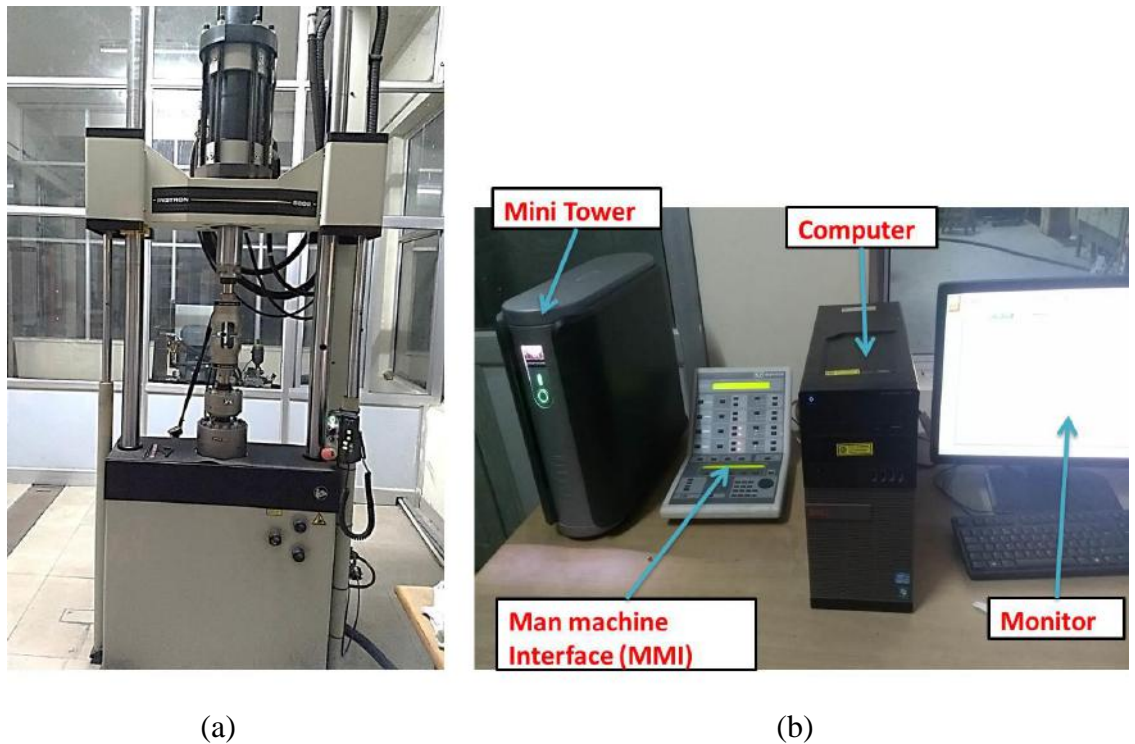
Fig. 4.15   Photograph of INSTRON 8802 servo hydraulic machine a) testing Section b) controlling section

4.7.1 Tensile test

The axial tensile testing has been done on same machine of three point bend test, the setup for tensile test on INSTRON 8802 was shown in fig. 4.16, sample was prepared according to ASTM E8 standard "Standard Test Methods for Tension Testing of Metallic Materials" and the sample size is shown in Fig. 4.17 (a) and (b) for single and multi-pass TIG arcing process. The gauge length portion of each sample was polished by silicon carbide paper up to grid size of 600 to minimize any mechanical effect of surface roughness on the test. The tensile test was carried out by loading at a cross head speed of 0.5 mm/min. At least three samples were tested for each condition and the average is reported for the tensile properties. Matrix toughness was estimated from area under the stress strain curve of the tensile test.
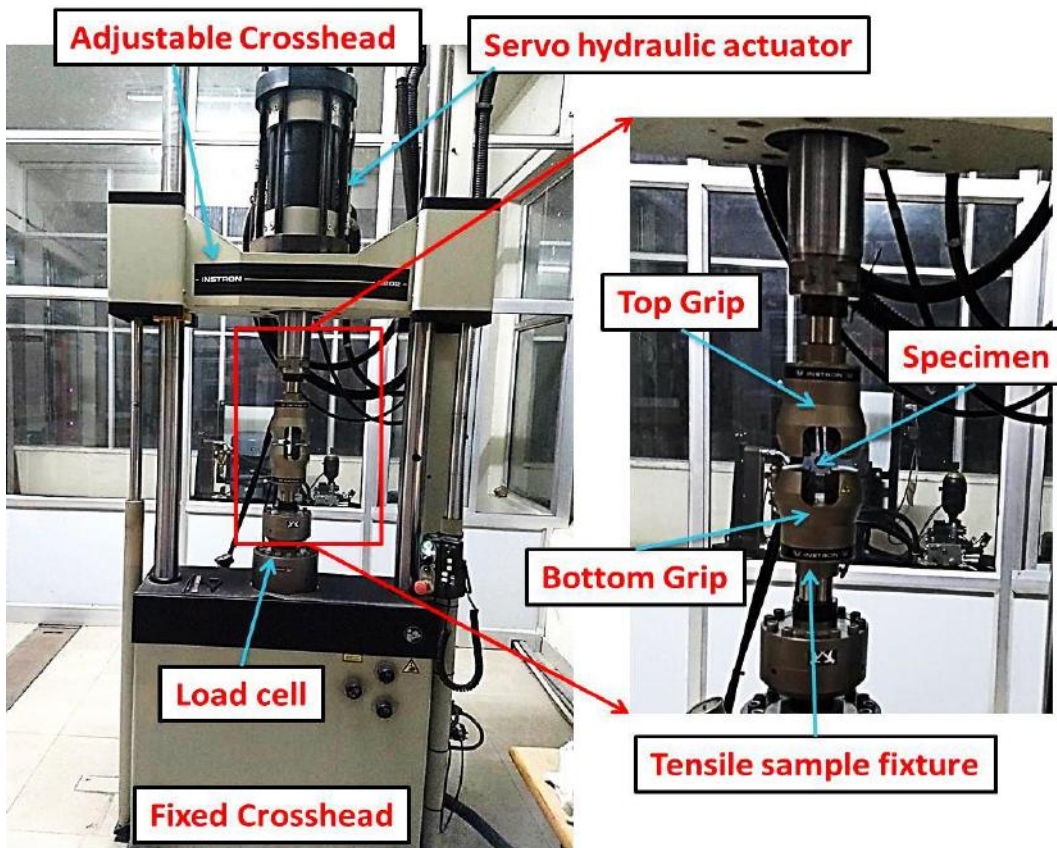
Fig. 4.16 Photograph of the test setup of axial tensile test on INSTRON 8802.
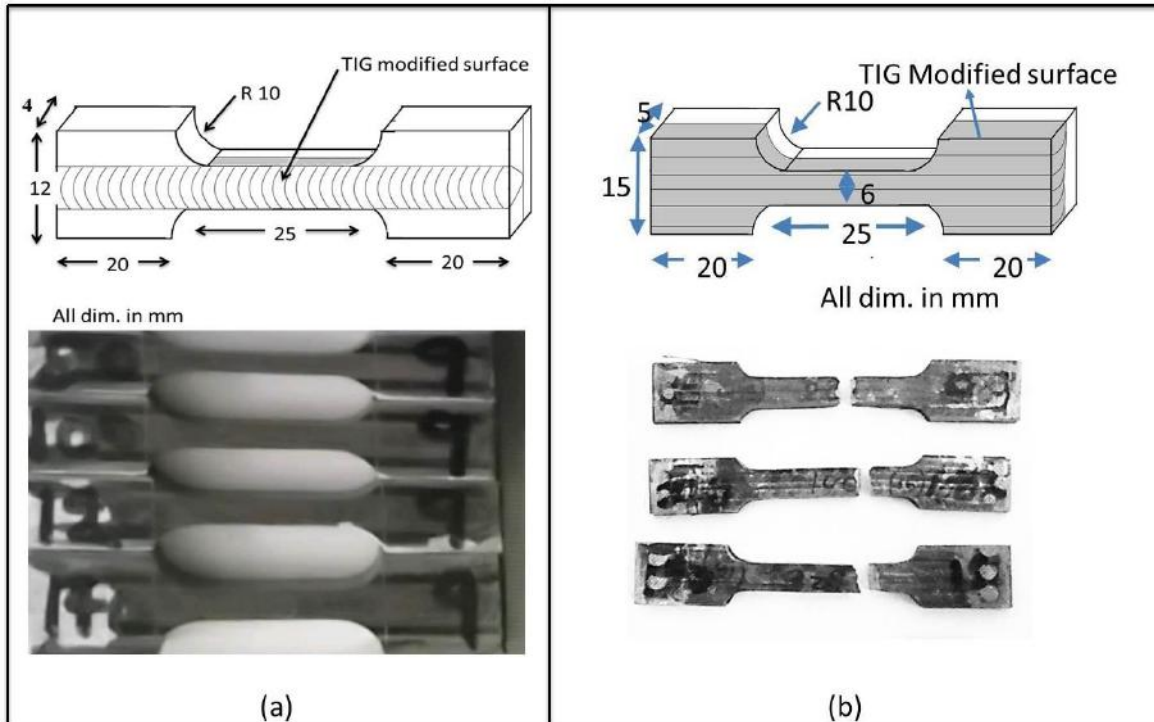
Fig. 4.17 Schematic view and typical appearance of tensile test sample for a) Single-pass surface modification b) multi-pass surface modification.

68

4.7.2 Three point bend test

The setup of three-point bend test has been shown in fig. 4.18 of INSTRON 8800 testing machine at room temperature. Symmetric diagram of the three-point bend test is shown in Fig. 4.19 (a) and (b) for single and multi-pass three point bend test, in which modified zone was kept as lower fibre so that it is experiencing maximum tensile stresses and cross head speed was taken as 1.0 mm/min. Five samples were tested for each condition taking sample size as 140 x 14 x 9.5 mm^3. Three-point bend test was carried out according to the ASTM E855. Flexural stress (σ) in MPa was estimated using eq. no. 4.9, where M is bending moment at midpoint (Nmm), y is the perpendicular distance to the neutral axis (mm) and I is the moment of inertia (mm^4).

$$\sigma = M*Y/I \quad \text{…………………………………. (4.9)}$$

Where,

$$M = F*L/4 \quad \text{…………………………………(4.10)}$$

$$I = W*T^3/12 \quad \text{…………………………………(4.11)}$$

Where, F= force applied (N) and L, W, and T are length (mm), width (mm) and thickness (mm) respectively as shown in fig. 4.19.
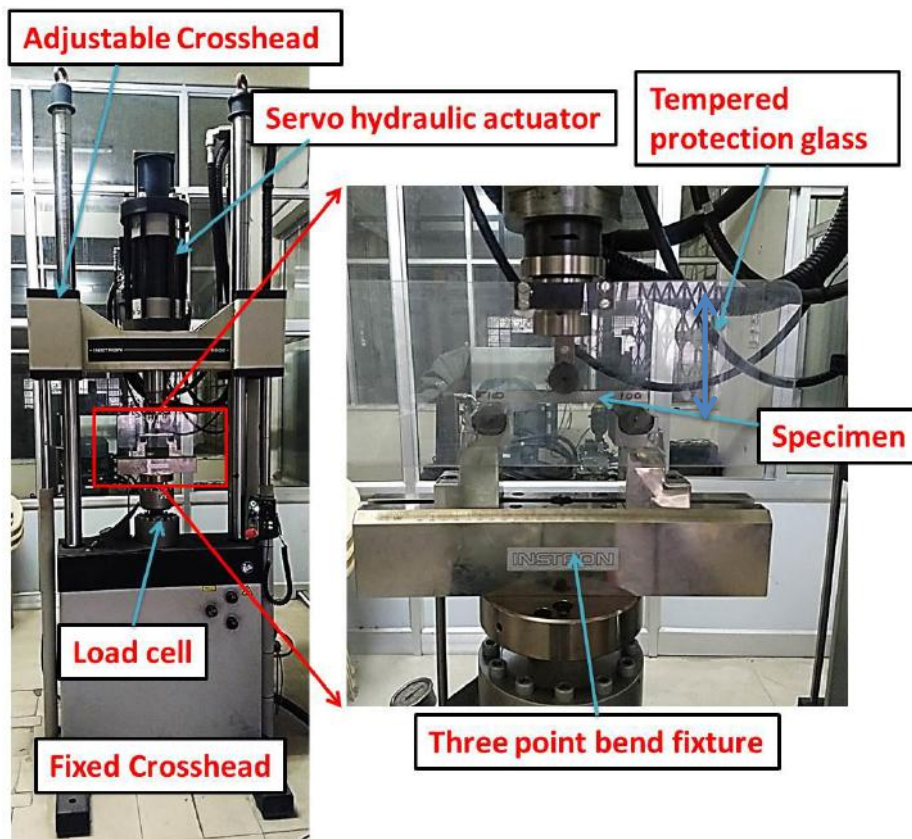
Fig. 4.18   Photograph of the test setup of three point bend test on INSTRON 8802.
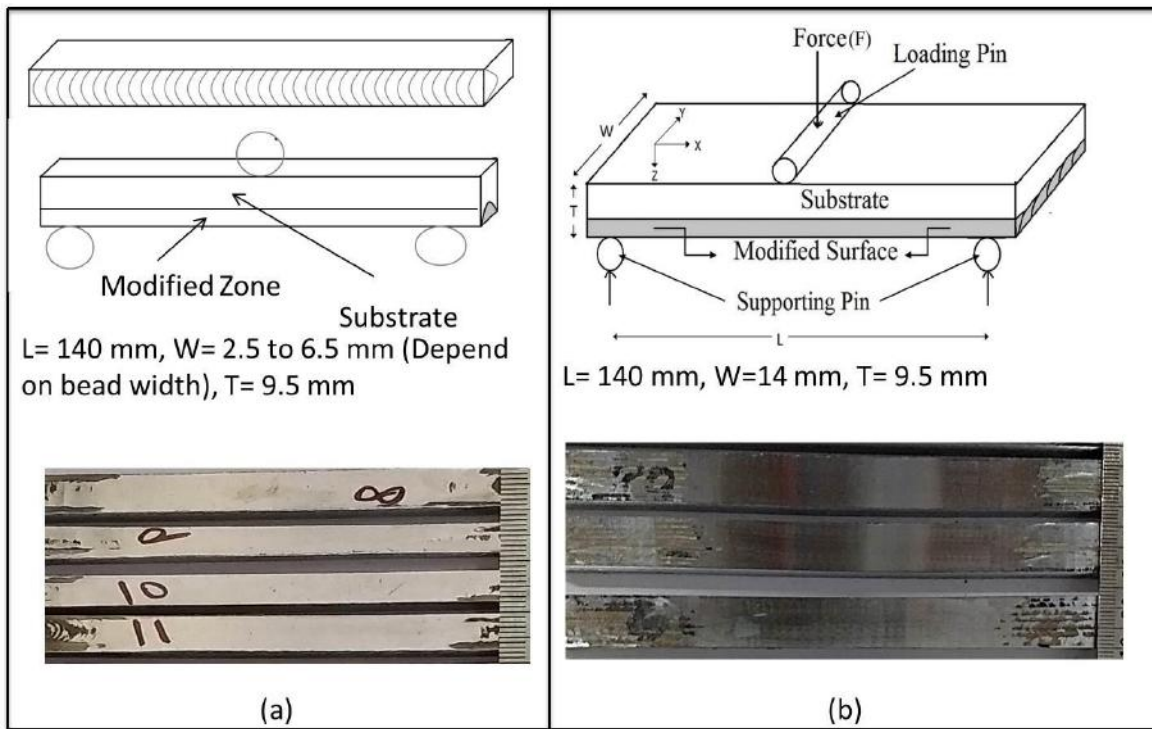
Fig. 4.19 Schematic view and typical appearance of three point bend test sample for a) Single-pass surface modification b) multi-pass surface modification.

4.7.3 Fatigue test under tensile loading

Single-pass modified surface by C-TIG and P-TIG arcing process, the test sample of the sub size samples were prepared according to the ASTM E466 standard "Standard Practice for Conducting Force Controlled Constant Amplitude Axial Fatigue Tests of Metallic Materials" for uniaxial tensile loading of fatigue test whereas the sample was prepared according to standared ASTM E466 for multi-pass modified surface by C-TIG and P-TIG arcing process. The change in sample size was did due to limitation of bead width in single-pass modified surface whereas multi-pass surface modification are not having such limitation. The sample size is shown in Fig. 4.20 (a) and (b) and the test was performed on same apparatus as tensile test shown in fig. 4.16. The samples for fatigue testing were also fine polished by silicon carbide paper up to grid size of 1200 to ensure that there is no stress concentration point on the surface. The fatigue test was carried out by operating the machine under load control mode. The test was performed at 25 Hz frequency of cyclic loading at stress ratio (R) of 0.1, where $R = \sigma_{min}/\sigma_{max}$ and σ_{min} and σ_{max} are the minimum and maximum applied stresses respectively. In order to get a relatively faster testing period in comparative studies, the maximum stress of cyclic loading was kept at around 0.5-0.6 fraction of their respective UTS during fatigue testing of differently modified test samples. The test was performed until the specimen is failed, or if test life exceeds 1×10^6 cycle then the experiment was suspended.
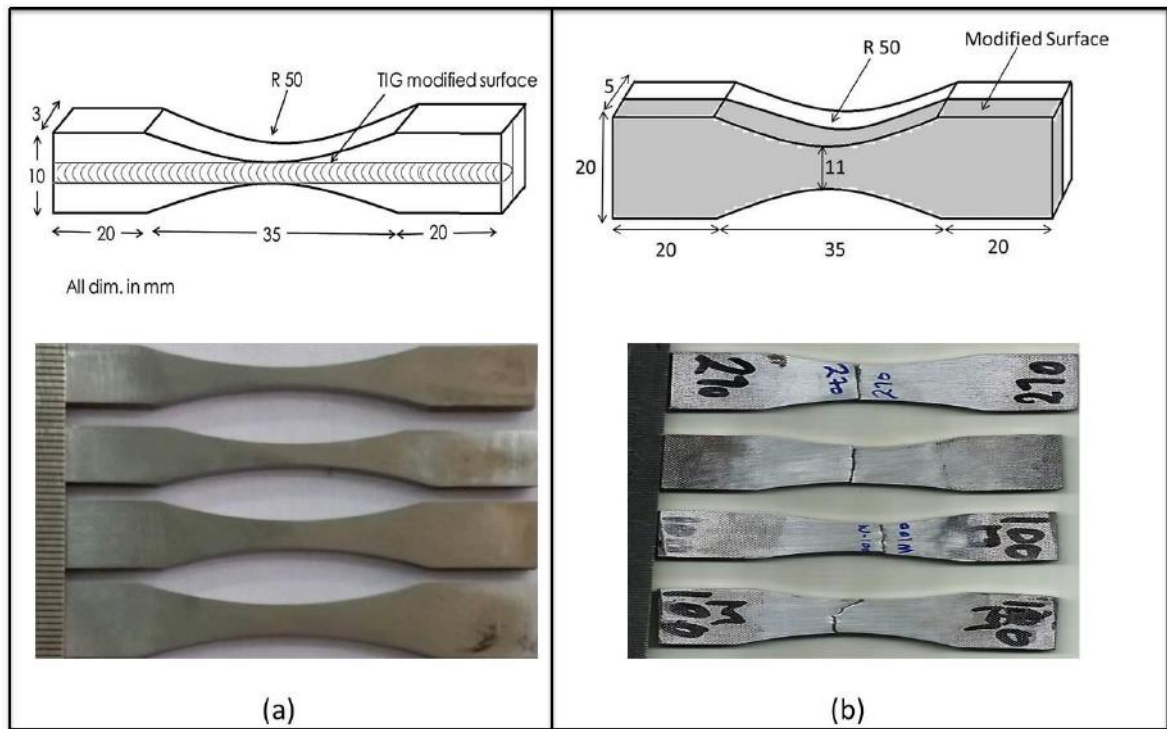
Fig. 4.20   Schematic view and typical appearance of tensile fatifue test sample for a) Single-pass surface modification b) multi-pass surface modification.

4.7.4 Fatigue test under bending load

Fatigue test under bending load was done on same apparatus of three point bend test (shown in fig. 4.18) with same sample size as shown in fig. 4.18. The test was performed at 10 Hz frequency and stress ratio (R) of 0.1, where $R = \sigma_{min}/\sigma_{max}$ and σ_{min} and σ_{max} are the minimum and maximum applied stresses, respectively. The test was performed until it failed, or the sample life exceed 1×10^{6} cycle than experiment was suspended. Representation of fatigue test results was compliance with ASTM E-739-91 "Standard Practice for Statistical Analysis of Linearized Stress-Life (S-N) Fatigue Data".

4.8 Scanning Electron Microscopy (SEM)

The morphological characteristics of AISI 4340 structural after different test like tensile, three point bend and fatigue test has been examined by scanning electron microscopy (SEM). The broken samples were cleaned in ultrasonic bath before fracture studies in SEM in order to remove the contaminants from the fractured surface.

Fig. 4.21   Photograph of the Zeiss Scanning Electron Microscope.

5.9 Residual Stress and distortion studies

Residual stress has been measured at centre of the TIG arcing modified surface by using hole drill method as describe in ASTM E-837 "Standard Test Method for Determining Residual Stresses by the Hole-Drilling Strain Gage Method". A TML strain gauge rosette of type FRS-2-17, supplied by M/s Tokyo Sokki Kenkyujo Co. Ltd., Japan, has been used for this study which is generally recommended for residual stress measurement of mild steel as shown in Fig. 4.22 (a) and (b). Prior to fixing strain gauge, the modified surface was properly cleaned by silicon carbide paper up to 2000 grid followed by chemical etching by 4% Nital solution to find the exact location of its placement on modified zone. In one strain gauge rosette, three gauges are placed there at 0, 90 and 225° in radial direction to find the strain. Drill hole at the centre was made using a standard device according to VISHAY PRICISION GROUP tech note TN-503 as shown in Fig. 4.23.

Longitudinal and transverse direction residual stresses were calculated by using eqs. 4.12 and 4.13.

Longitudinal Residual Stress = P – Q   …………………………..(4.12)

Transverse Residual Stress = P + Q   …………………………..(4.13)

P and Q are the two combination stresses corresponding to the three measured strains. P and Q were calculated by the eqs. 4.14 and 4.15:

$$\sigma_2 = \frac{E(\varepsilon_1 - \varepsilon_3)}{4\bar{b}(1+\nu)} \qquad \text{................................(4.14)}$$

$$\sigma_3 = \frac{E(\varepsilon_1 - \varepsilon_3)}{4\bar{a}} \qquad \text{................................(4.15)}$$

Where, ε_1, ε_2 and ε_3 are the measured strain from the strain rosette during hole drilling, E is Modulus of Elasticity and ν is Poisson's ratio. E and ν are the material constants considered as 210 GPa and 0.29 respectively. The $\bar{a}$ and $\bar{b}$ are the calibration coefficients and the values have been taken as corresponding to hole diameter (Do) and gage circle diameter (D).
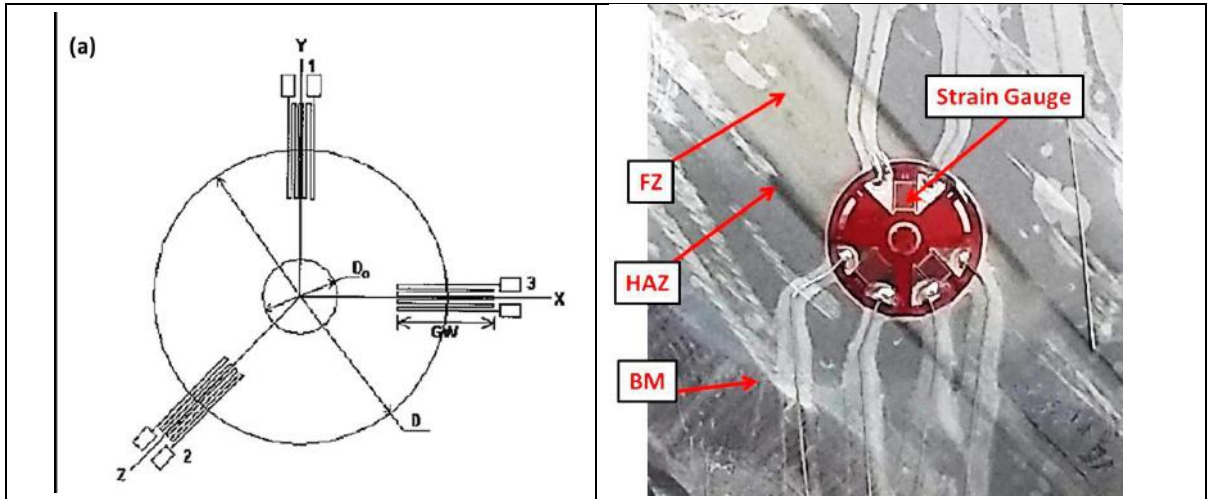
Fig. 4.22 (a) Schematic arrangement of strain gages placed at different directions of measuring and (b) Typical view of a three strain gage rosette at a fusion zone.
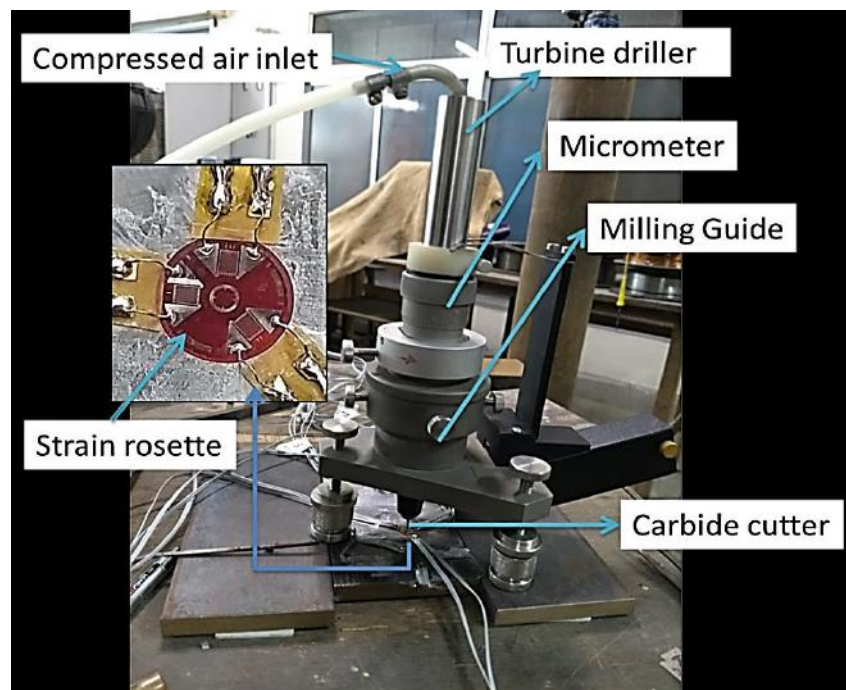
Fig. 4.23 Arrangement of residual stress measurement setup and strain gauge rosette.

This chapter presents detailed discussions of the results obtained in the present work for preparation of a tough core substrate using Continuous current TIG arcing process. The chapter deals with the results of various experiments, details of which are described in the chapter 5, and examine them in order to understand the influence of C-TIG arcing process, parameters and procedure on modification of AISI 4340 steel substrate. Analyzing the mechanical and metallurgical characteristics and residual stresses of the modified zone, the relevant control of the operating parameters and procedure has been established to improve the surface properties. The necessary control of operating parameters to improve the surface properties is analyzed in the light of a prescribed model.

5.1 Characteristics of AISI 4340 steel

The base material of 10 mm thick plate of HSLA steel has been characterized with respect to its chemistry, microstructure, hardness, tensile and 3-point bending properties as well as fatigue properties under the bending and tensile loading, which may be subsequently influenced by the thermal characteristics of TIG arc processing. These observations have been used as a reference point to study the variation in characteristics of base metal at FZ and HAZ with a change in arc processing conditions.

5.1.1 Chemical Composition

Chemistry of the HSLA (4340 structural steel) steel base material used in this work for surface modification by autogenous TIG arcing process is given in table 5.1. The results primarily show that the chemical composition of base material are in agreement to those prescribed in standard and the test certificate given by the supplier.

Table 5.1   Chemical composition of AISI 4340 structural steel.

	Chemical composition (wt. %)								
	C	Cr	Ni	Mo	Mn	S	P	Si	Fe
ASTM A29	0.38-0.43	0.7-0.9	1.65-2.0	0.2-0.3	0.6-0.8	0.04	0.035	0.15-0.35	remaining
Test Certificate	0.39	0.8	1.69	0.23	0.69	0.04	0.04	0.22	remaining
*	0.39	0.79	1.65	0.22	0.71	0.04	0.04	0.21	remaining

* Indicates testing by spark emission optical microscopy

5.1.2 Microstructure

The typical microstructures of the transverse and longitudinal sections of the AISI 4340 low alloy steel base plate having homogeneously distributed grains in the matrix has been shown in fig. 5.1 (a-b) respectively. The microstructures consist of uniformly distributed proeutectoid ferrite and pearlite in the matrix. Average grain size in the transverse and longitudinal direction has been found to be of the order of 9.5 ± 1 μm and 9 ± 1 μm respectively.

(a)

(b)
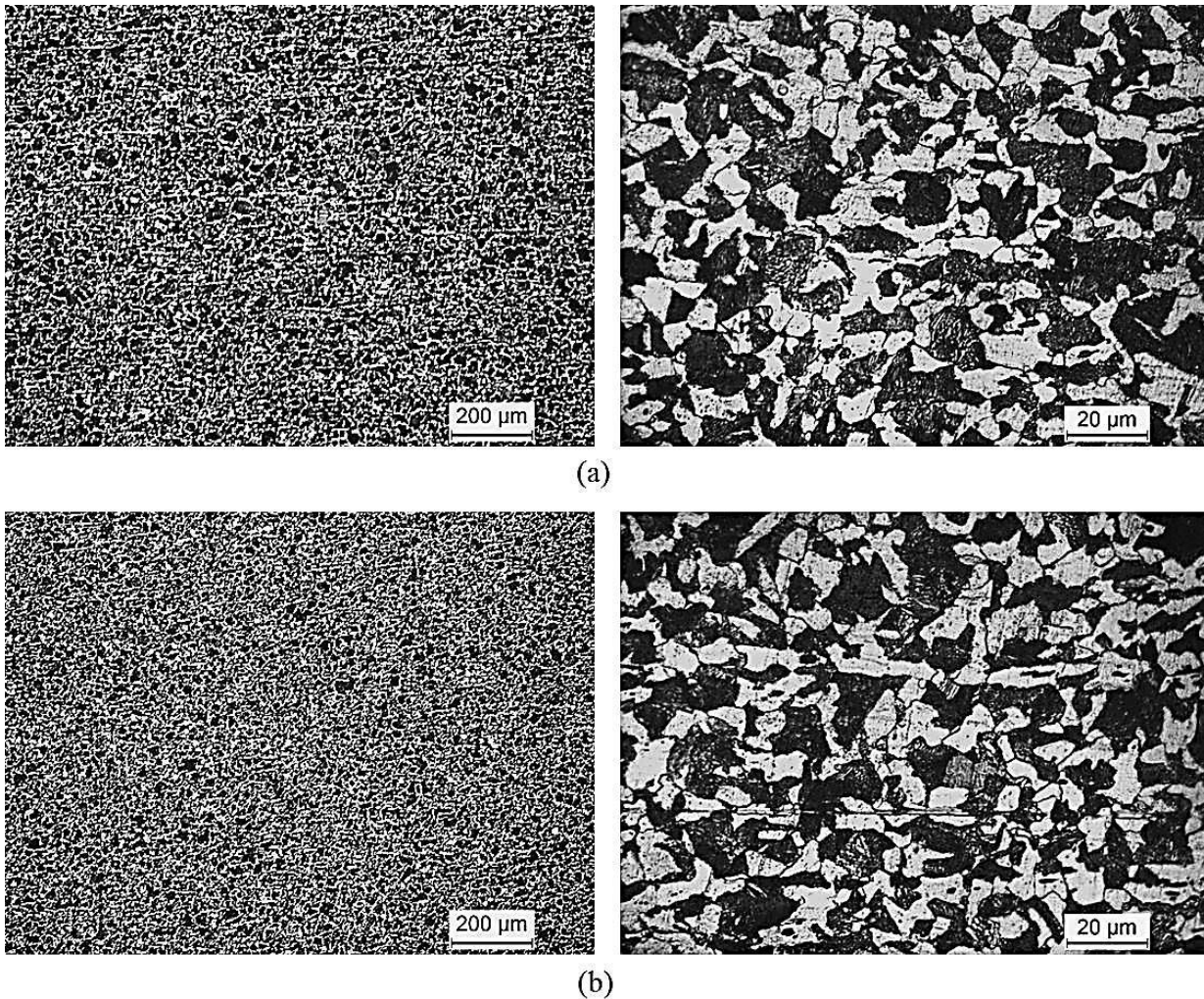
Fig. 5.1   Typical microstructure of AISI 4340 steel in its (a) transverse section and (b) longitudinal section**.**

5.1.3 Mechanical properties
5.1.3.1Tensile Properties

Three samples were tested to find out the average properties of base material under uniaxial tensile testing. Tensile stress-strain curve of the AISI 4340 steel plate is shown in fig. 5.2. In agreement to the fig. 5.2, the average yield strength and ultimate strength of the base

76

material have been found of the order of 395 MPa and 705 MPa respectively and the ductility (% strain) and toughness is found as 19.24 mm/mm and 119 J/mm^3 respectively as shown in table 5.2.
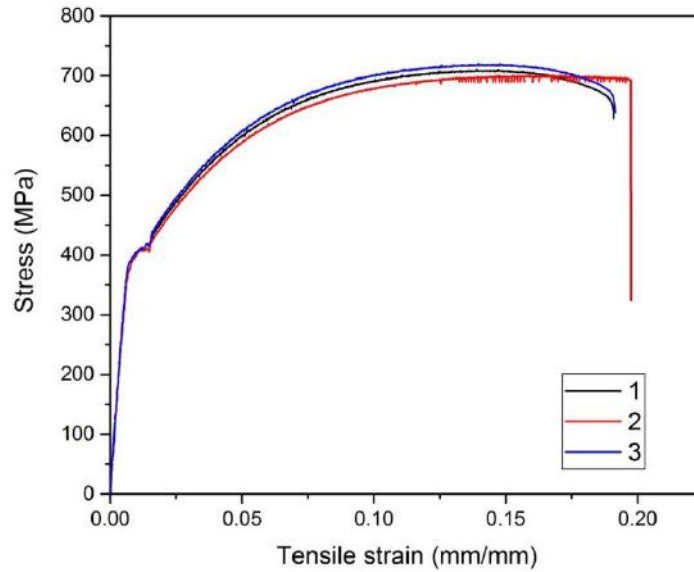
Fig. 5.2   Stress versus strain plot under tensile test of base material

Table 5.2   Tensile properties of base material.

Sr. No.	Yield Strength		Ultimate Strength		% Strain		Toughness	
	(MPa)		(MPa)		mm/mm		J/mm^3	
1	395		705		19.01		116	
2	395	395	714	705	19.10	19.24	119	119
3	398		693		19.74		121	

5.1.3.2 Three point bend Properties

The flexural yield strength and flexural maximum strength of the as received base material were found as 540 and 1160 MPa respectively under the three-point bend test. The flexural stress versus extension characteristics of the base metal is shown in fig. 5.3. The stress versus extension curve becomes practically flat after a flexural extension of about 15 to 18 mm (bending up to an angle of about 80°) and as such the test was withdrawn at this stage.
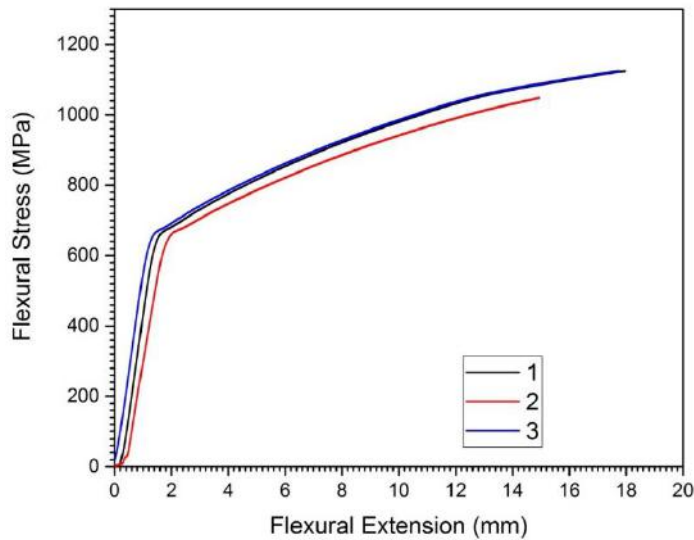
Fig. 5.3 Flexural stress versus extension plot under three point bend test of base material

5.1.4 Fatigue properties

5.1.4.1 Under tensile loading

The study on fatigue characteristics (S-N curves) under uniaxial tensile loading of AISI 4340 structural steel as base metal is shown in fig. 5.4. The figure shows that at maximum cyclic stress (σ_{max}) of 570 MPa, the base material has been failed at about 13.6×10^3 cycles, when it shows the endurance limit at the σ_{max} of 400 MPa, which is approximately 0.56% of its ultimate strength. The S-N curve has been drawn with coefficient of correlation more than 95 % as per ASTM standard for fatigue test.
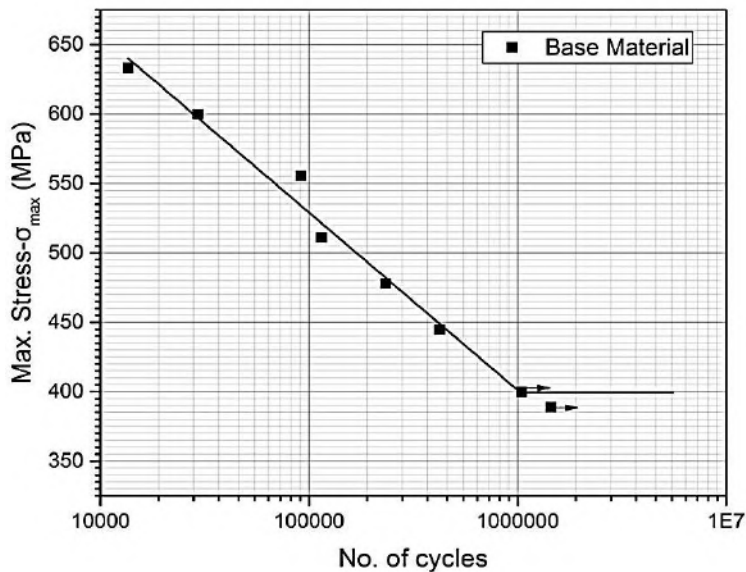
Fig. 5.4 S-N curve of base material under uniaxial tensile loading.

78

5.1.4.2 Under bending load

Fatigue behaviour (S-N curve) of the base material under uniaxial bending load has been shown in fig. 5.5. The figure shows that the endurance limit lies at σ_{max} of about 477 MPa. The base material was failed in 8.01×10^4 cycles at the σ_{max} of 711 MPa. Here also the curve has been drawn with coefficient of correlation more than 95 % as per ASTM standard for fatigue test.

.
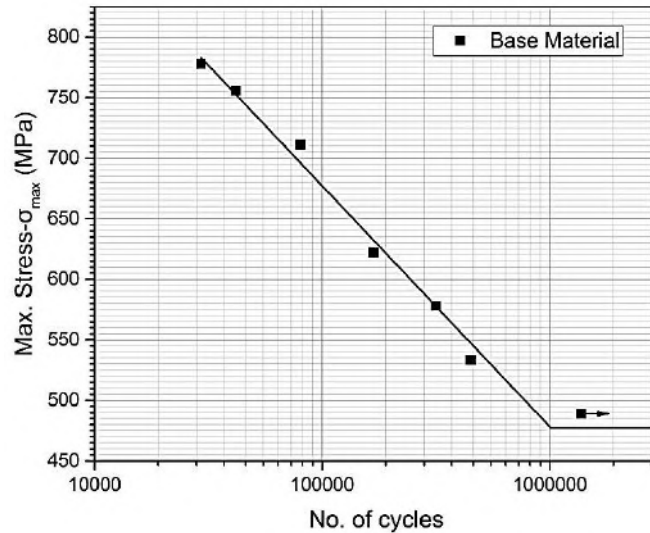
Fig. 5.5   S-N curve of base material under uniaxial bending load.

5.1.5 Effect of heating on microstructure

The thermal effect on base metal microstructure and intercritical temperature range of the steel were estimated by the computational alloy thermodynamic software Thermocalc. The observed thermodynamically stable phases and their critical temperatures of formation are summarized in fig. 5.6. The thermodynamically stable phases like bcc (ferrite), fcc (austenite), cementite and M_3C, $M_{23}C_6$, M_7C_3, M_3C_2 and M_5C_2 carbides that can form in this system were chosen where M in these carbides could be any of the metallic elements (Fe, Cr, Mn or Ni) present in the alloy.

The fig. 5.6 depicts the critical temperature of transformation line Ae1 and Ae3 representing transformation temperatures of 680 and 760^{0}C respectively. In this temperature range the ferrite phase is transformed to austenite phase. It is noted that the initial stable phases are ferrite and the M_7C_3 carbide. The M_7C_3 phase is completely dissolved at 565^{0}C. Thus, the observed carbides in the starting microstructure of the steel are more likely to consist of cementite (M_3C), rather than the equilibrium M_7C_3 carbide.
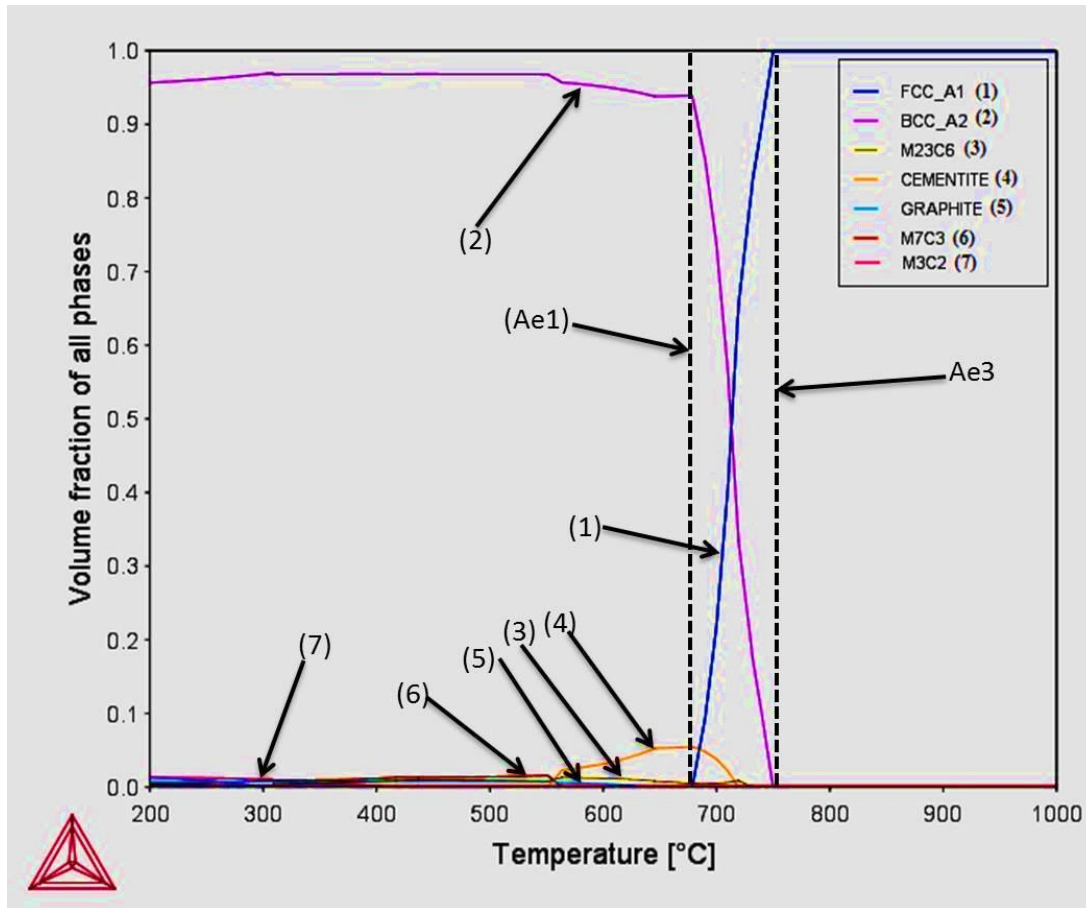
Fig. 5.6   Effect of temperature on the volume fraction of phase transformation in AISI 4340 steel.

5.2. Single-pass C-TIG arcing process

5.2.1 Geometric studies

The studies on thermal and geometrical aspects of the modified zone as a function of arcing parameters provide the knowledge to understand and analyze the effect of C-TIG arcing parameters on bead geometry, temperature of the weld pool and heat input (Ú) on modification of matrix characteristics. This may play a leading role in deciding the parameters for multi-pass modification of extended surface of AISI 4340 steel. In addition to this the detail knowledge of single-pass C-TIG arcing process also helps in optimization of single-pass P-TIG arcing process parameters especially in terms of the depth of modified zone. At a given arc voltage (V) the geometrical characteristics have been studied at varying arcing current of 80 to 140 A and travel speed (S) of 6 to 15 cm/min. The C-TIG arcing parameters used for single-pass study have already been shown in Tables- 4.2 (chap. 4).

5.2.1.1 Thermal aspects of fusion pool of C-TIG arcing process

At a given arc voltage of 10.5 ± 1.0 V, the influence of arcing current on theoretically estimated energy transfer (Q_T) has been depicted in fig. 5.7. The figure shows that total energy transferred to weld pool almost linearly increases with the increment of arcing current. The empirical correlation of Q_T with the arcing current (I) at the given arc voltage has been worked out as follows.

$$Q_T = 12.22 \times I - 53.21 \qquad\qquad \text{.............................(5.1)}$$
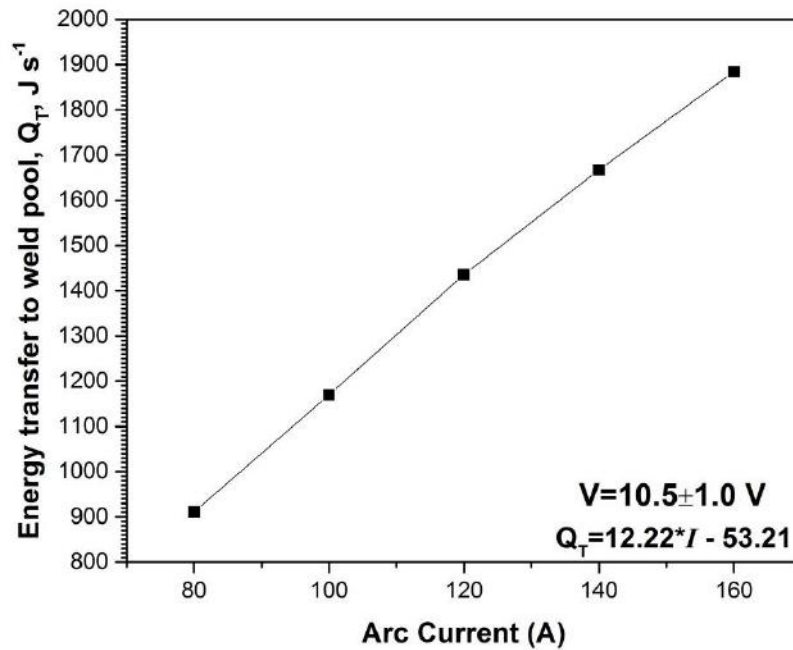
Fig. 5.7   Effect of arcing current on energy transfer to fusion pool at given arc voltage of 10.5 ± 1.0 V.

The amply verified [B.P. Aggrawal, 2010; Goyal et al 2008 (b)] mathematical expression (Chap-4, eq.4.3) for estimation of weld pool temperature has been used for estimation of weld pool temperature. At a given arc voltage of 10.5 ± 1.0 V, the effect of arcing current on theoretically estimated weld pool temperature (T_{WP}) at a depth of about 1.5 mm from its surface and about 1.5 mm from the arc center under different travel speed has been shown in fig. 5.8. It has been observed that at a given arc voltage and travel speed (S), the T_{WP} increases significantly with the increase of arcing current. The figure also depicts that the T_{WP} decreases with the increase in travel speed (S) from 6 to 15 cm/min at a given arcing current (I) and arc voltage (V). The empirical correlation of T_{WP} with I and S has been worked out as follows.

$$T_{WP} = -25.10 \ S + 10.73 \ I - 0.0625 \ SI + 1242 \qquad \text{...............................(5.2)}$$
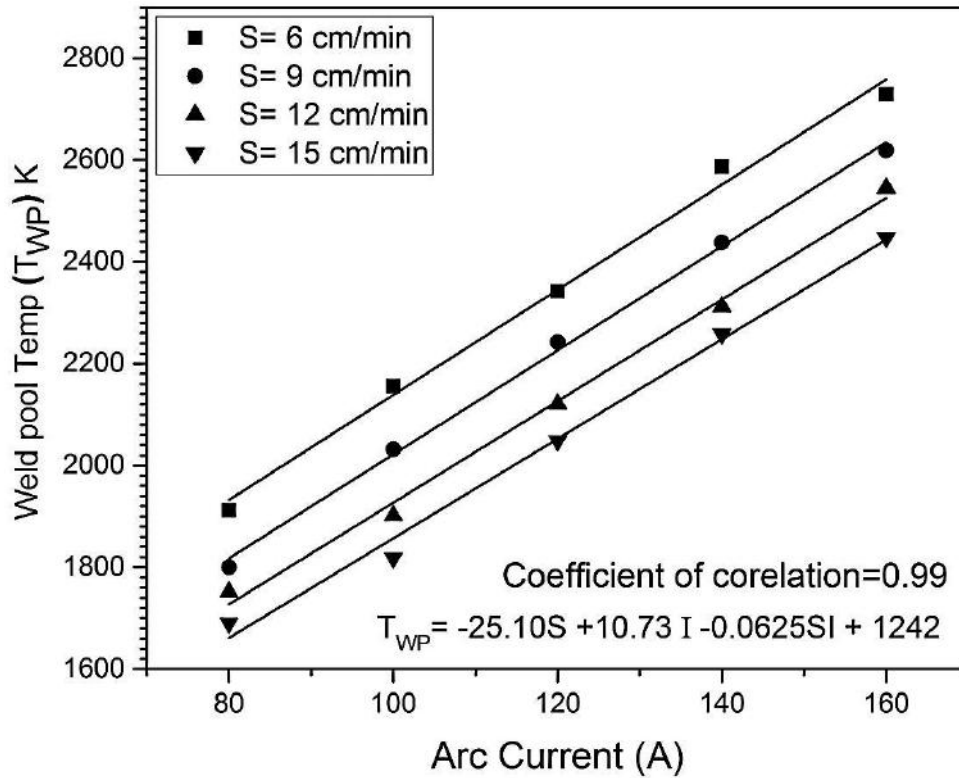
Fig. 5.8   At a given arc voltage of 10.5 ± 1.0 V, the effect of I and S on weld pool temperature.

5.2.1.2 Geometric studies during single-pass C-TIG arcing process

The typical appearance of surface and transverse sections of the single-pass C–TIG arc modification at varying arcing current from 80 to 140 A at arc travel speed of 6 and 12 cm/min is shown in figs. 6.9 and 6.10 respectively. The figures show that at a given arc voltage, the increase of arcing current and decrease of travel speed significantly affect the geometry of fusion zone. The figure further depicts that the increase in arcing current from 80 to 140 A and decrease in travel speed from 12 to 6 cm/min increases the heat input into the work piece. The increase in heat input (Ω) significantly affects the geometrical aspect of fusion zone, such as bead width (W_b), Depth of penetration (P_d), HAZ width (W_{HAZ}) and area of fusion zone (A_{FZ}). It is well-known that the increase of heat content in the work piece is obtained through reduction in arc travel speed (S) and increment in arcing current (I). The net increase in heat input increases the temperature of the fused pool and its fluidity [Fan and Kovacevic, 2004].

Arcing Current (A)	Heat input (kJ/mm)	Top surface appearance (scale in mm)	Transverse Section (scale in mm)
80	0.60		
100	0.79		
120	0.99		
140	1.21		

Fig. 5.9   Typical appearance of modified surface and its transverse section prepared by single-pass TIG arcing at different currents with given arc voltage and arc travel speed of 10.5 ± 1.0 V and 6 cm/min respectively.
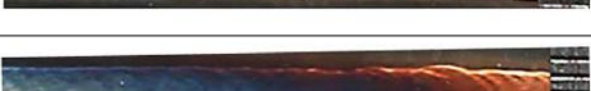
Arcing Current (A)	Heat input (kJ/mm)	Surface appearance (Scale in mm)	transverse section (Scale in mm)
80	0.30		
100	0.39		
120	0.50		
140	0.60		

Fig. 5.10   Typical appearance of modified surface and its transverse section prepared by single-pass TIG arcing at different currents with given arc voltage and arc travel speed of 10.5 ± 1.0 V and 12 cm/min respectively.

At a given arc voltage of 10.5 ± 1.0 V the effect of variation in arcing current (I) and arc travel speed (S) on the bead width, depth of penetration, width of HAZ and area of fusion zone has been shown in figs. 5.11 (a-d) respectively. The figures show that the increase in arcing current from 80 to 160A significantly increases the W_b, P_d, W_{haz} and A_{FZ}. It has been further observed that the W_B, P_d, W_{haz} and A_{FZ} increase appreciably with the reduction of arc travel speed. Such a variation in W_B, P_d, W_{haz} and A_{FZ} as a function of arcing current and arc travel speed may be primarily attributed to the variation in heat transfer to the fusion zone governing its pool size and fluidity [Robert W Messler, 1999]. The empirical correlations of W_B, P_d, W_{haz} and A_{FZ} as a function of I and S depicted in Figs 5.11 (a-d) respectively have been given below.

$$W_B = -0.12213S + 0.04532I + 9.17 \times 10^{-5} SI + 0.5204 \quad \dots\dots\dots\dots(5.3)$$

$$P_d = -0.0172S + 0.02617I - 5.48 \times 10^{-4} SI - 0.2314 \quad \dots\dots\dots\dots(5.4)$$

$$W_{haz} = -0.71S + 1.04 \times 10^{-2} I + 7.33 \times 10^{-6} IS + 0.956 \quad \dots\dots\dots\dots(5.5)$$

$$A_{FZ} = 0.496S + 0.252I - 1.09 \times 10^{-2} IS - 13.11 \quad \dots\dots\dots\dots(5.6)$$
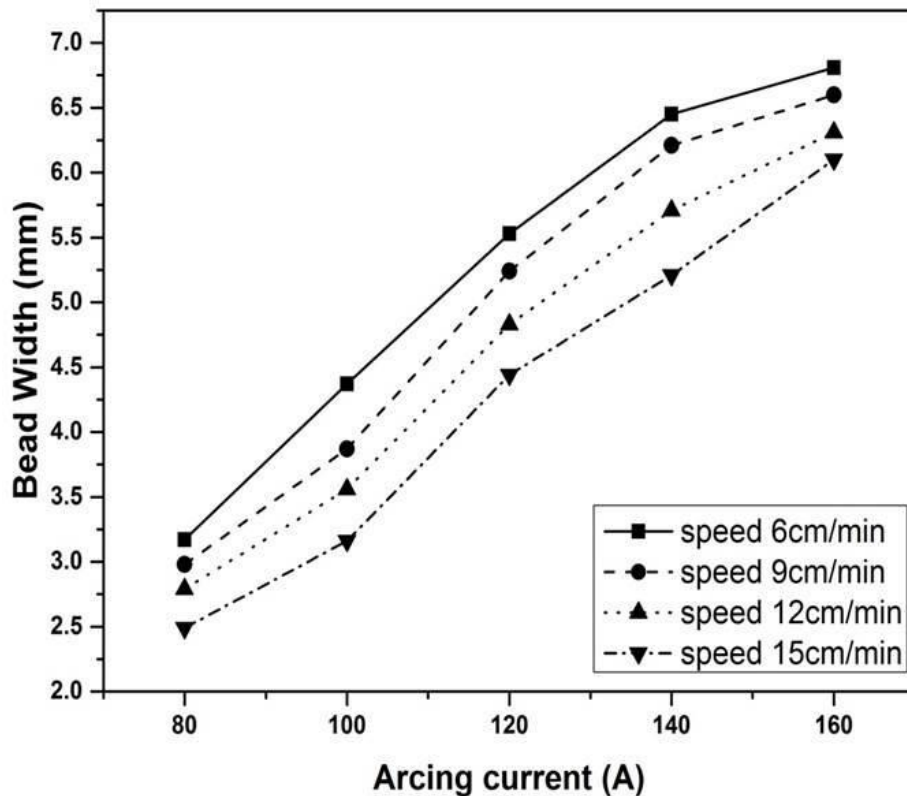
(a)
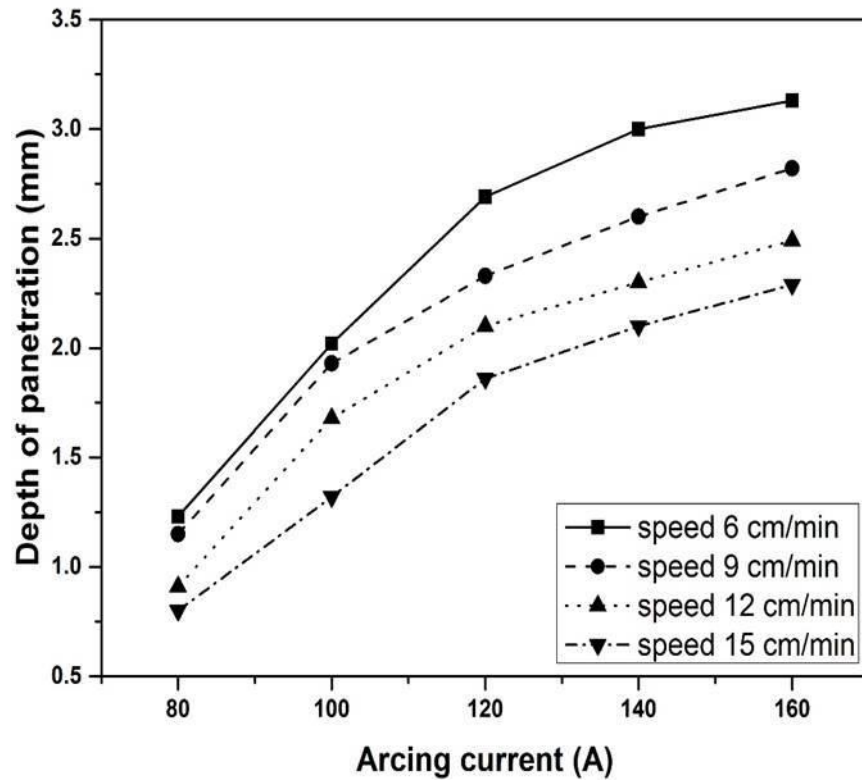
(b)
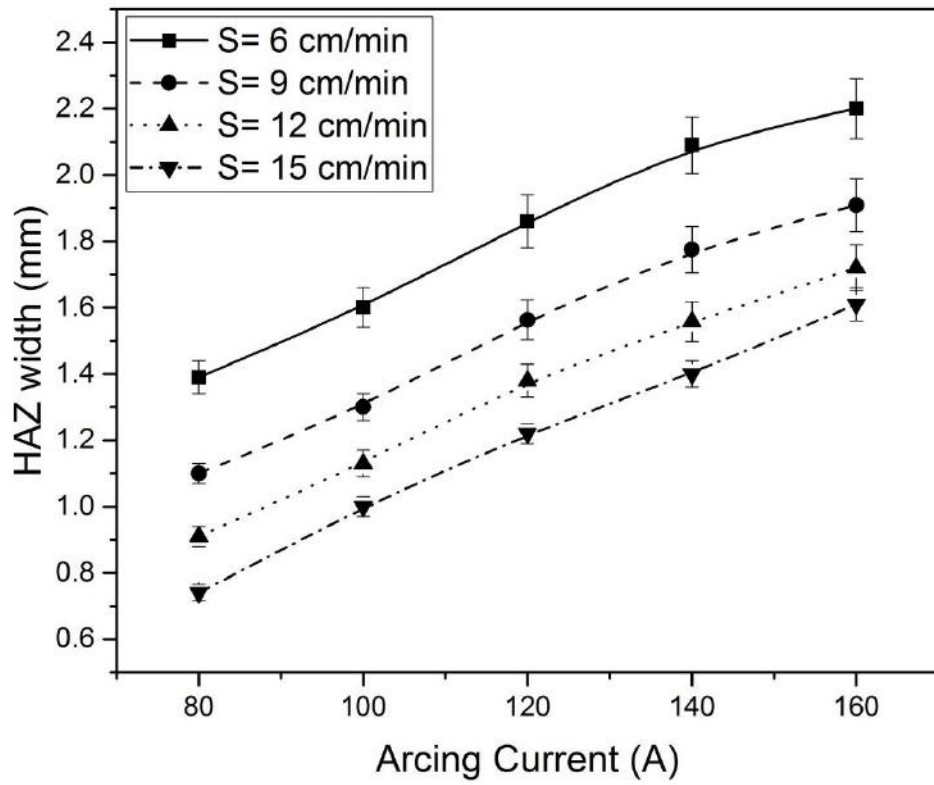
(c)
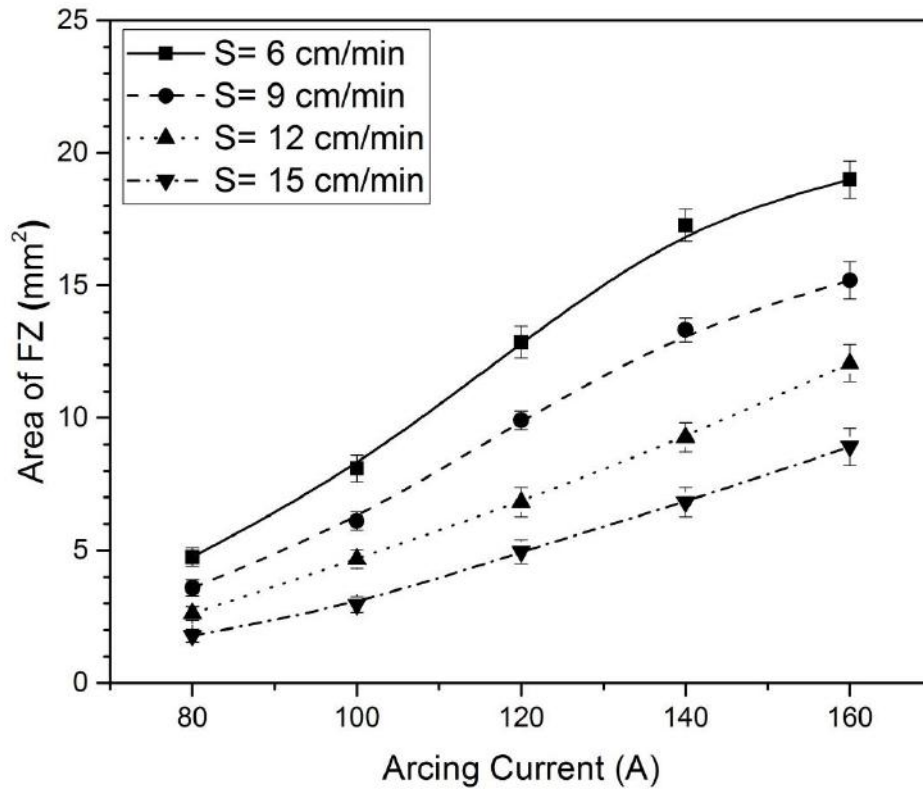
(d)

Fig. 5.11   Effect of arcing current and travel speed on (a) bead width (b) depth of penetration (c) width of HAZ and (d) area of fusion zone at an arc voltage of 10.5 ± 1.0 V.

5.2.2 Analytical estimation of thermal characteristics

The size and shape of fusion zone in the TIG arcing process affect the mechanism and kinetics of solidification and thus, the microstructure and properties of the modified zone. The size and shape of the fusion zone along with the size and shape of its heat affected zone also affects the thermally introduced stresses that act on the modified zone leading to formation of residual stresses and distortion. In C-TIG arcing process, the size of fusion zone is controlled by the arcing current, arc travel speed and heat input. However, C-TIG arcing process is governed by the isotherms and thermal cycle that may be predicted out of solutions of the heat flow equations. Thus, it is very much necessary to study the effect of these arcing parameters on isotherm and thermal cycle in order to critically understand, predict and ultimately control the final modified zone to a maximum extent for desired properties of substrate surface to perform under given service conditions.

5.2.2.1 Analytical estimation of thermal characteristics for single-pass C-TIG arcing process

The size of fused pool and HAZ is dictated by the isotherm produced in the substrate by the heat input as a function of operating current, arc voltage and travel speed of the C-TIG

arcing process. The isothermal curves in both the planes of x-y and y-z, thermal cycle and cooling rate are estimated by the expression of heat flow as stated in chapter 4.

5.2.2.1.1 Isothermal curve in x-y and y-z plane

At a given arc voltage of 10.5 ± 1.0 V the variation in arcing current and travel speed from 80 to 140 A and 6 to 15 cm/min, respectively, on fusion isotherm at the XY plane on the surface and YZ plane of the cross section have been shown in figs. 5.12 (a-b) and 5.13 (a-b) respectively. It is observed from fig. 5.12 (a) that the width and length of the isotherm increases with the increase of arcing current at a given travel speed and the fig. 5.12 (b) shows that there is a decrease in width and length of the isotherm significantly with the increase in arc travel speed at a constant arcing current and arc voltage. Similarly the fig. 5.13 (a-b) depicts that the width and depth of modified zone increases with the increase in arcing current at a given arc travel speed. This is primarily attributed to the increment in heat transferred to the fusion pool with the increase of arcing current at a given arc travel speed. It has also been observed from the figures that the increase of travel speed at a given arcing current and arc voltage, reduces the width, length and depth of the isotherm. This is attributed to the reduction of heat transferred to the fusion zone with the reduction of heat input (Ω). It is further observed that increase of Ω at a given arcing current, which is achieved through the reduction of welding speed, increases the length of the fusion pool and depth of modified zone. This may have primarily happened because of its ability to cool the molten fusion pool to a relatively higher extent due to availability of comparatively more time at lower arc travel speed and higher Ω. The increment in arc travel speed at a constant arcing current reduces the energy input per unit length, which is responsible for distribution of energy into the work piece. The increment in travel speed reduces the distribution of energy into the system. The fig. 5.13 (a-b) also shows a comparison between the predicted and measured geometry of the modified zone at arcing current and arc travel speed of 80 to 140 A and 6 to 15 cm/min respectively. The figure shows that the predicted geometry of modified zone is quite close to their experimental observations with accuracy of 4 ± 2 %.
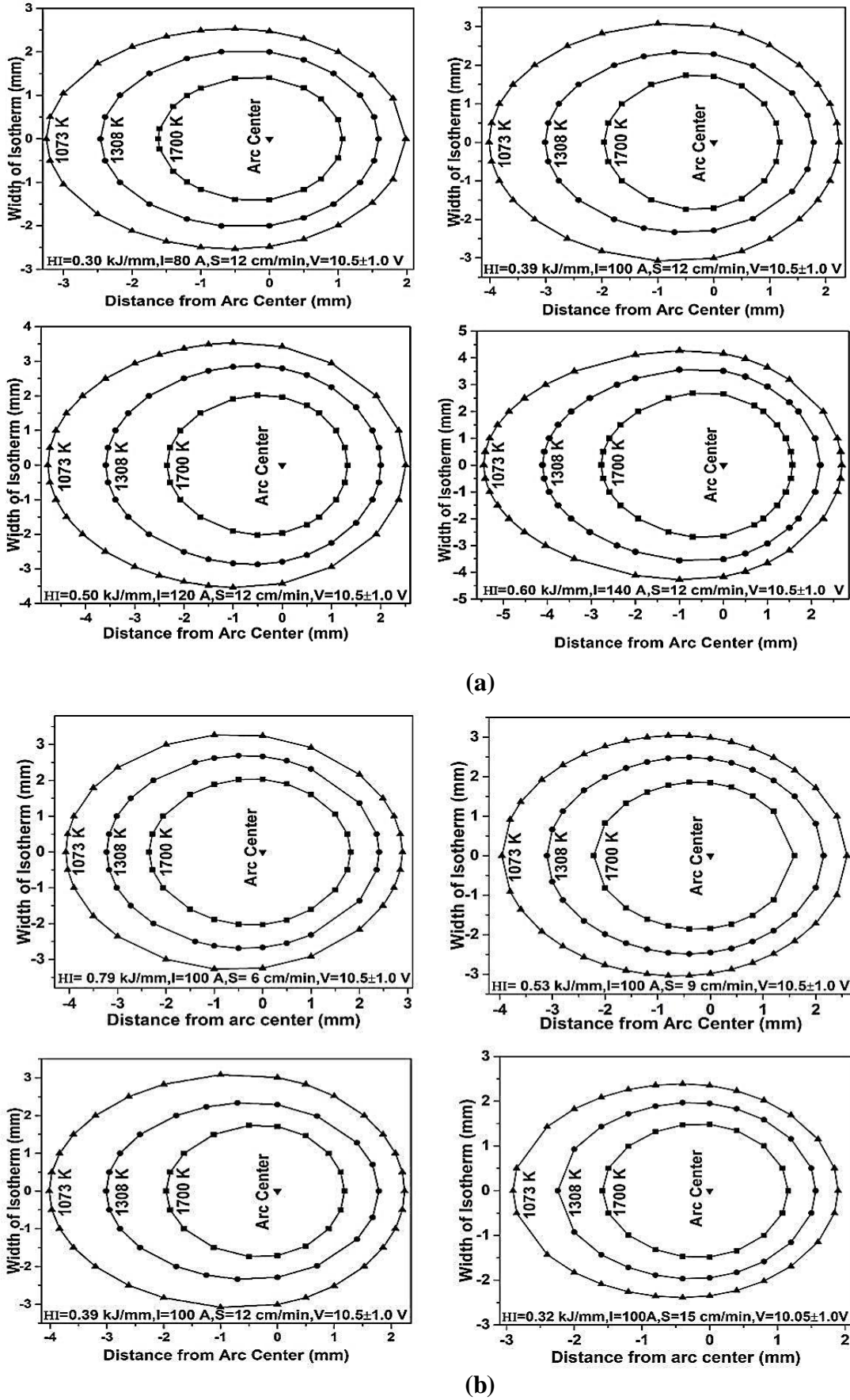
Fig. 5.12 Effect of arcing current and heat input on estimated isotherms in XY plane at given arc voltage 10.5 ± 1.0 V and varied arc travel speed of (a) 6, (b) 9, (c) 12 and (d) 15 cm/min.

88
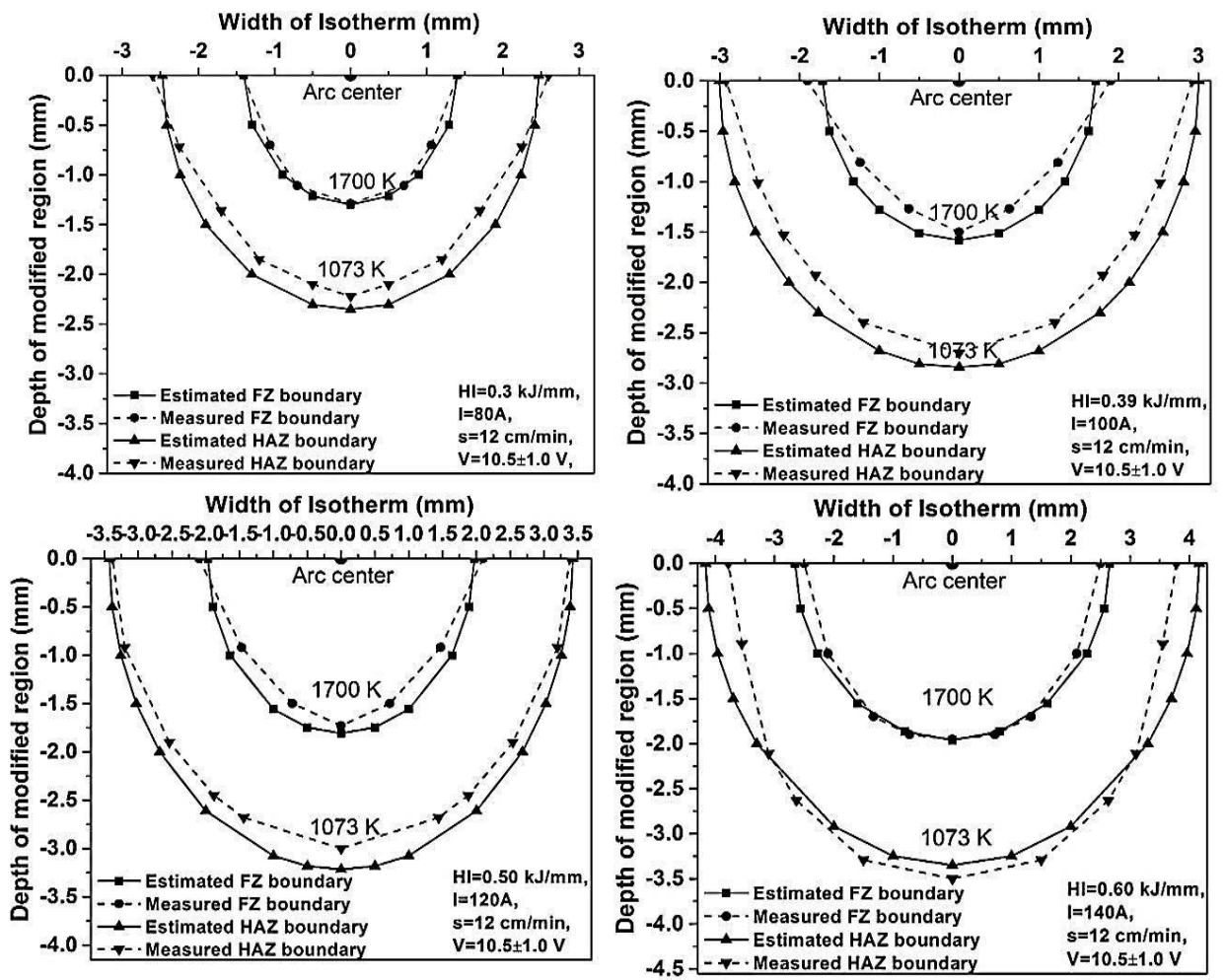
(a)
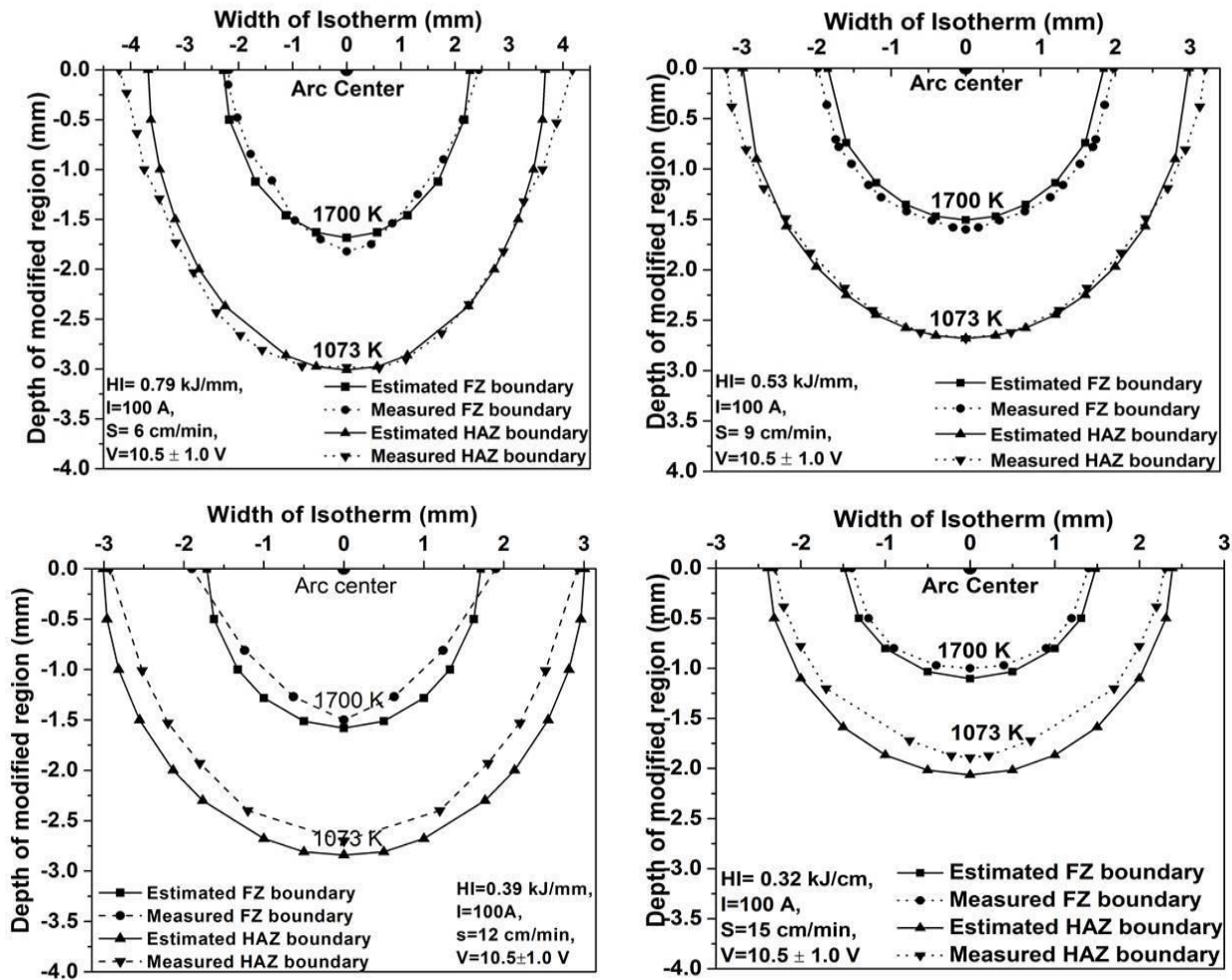
(b)

Fig. 5.13 Effect of arcing current and heat input on estimated and measured isotherms in YZ plane at given arc voltage of 10.5 ± 1.0 V and varied arc travel speed of (a) 6, (b) 9, (c) 12 and (d) 15 cm/min.

5.2.2.1.2 Thermal Cycle

Thermal cycle shows the nature of variation in temperature during heating and cooling with respect to time of a location inside and adjacent to the fused zone. At a given arc voltage and arc travel speed of 10.5 ± 1.0 V and 12 cm/min respectively, the effect of arcing current and Ú, lying in the range of 80-140 A and 0.3 − 0.60 kJ/mm respectively, on estimated and measured thermal cycle of the fused zone and HAZ of adjacent matrix is shown in fig. 5.14 (a-b). The measured thermal cycle represents the characteristics of a point at a depth of Z axis corresponding to close approximation of its estimated value. It is observed that the increase in Ú with the increase of arcing current reduces the cooling rate (CR). At higher heat input a lower area of the heat sink is available for heat transfer from the FZ to the surrounding matrix of base metal which may cause a lower CR at the intercritical temperature range (800–500°C). But when the heat input is reduced from 0.60 to 0.30 kJ/mm due to lowering of arcing current from 140 to 80 A, a relatively larger area of the available heat sink for heat transfer may cause

90

a higher CR in the intercritical temperature range. This is attributed to increase in size of the fused pool at higher heat input that enhances the temperature of wider area of surrounding base metal and reduces its temperature gradient from the effective heat sink leading to lowering of CR.
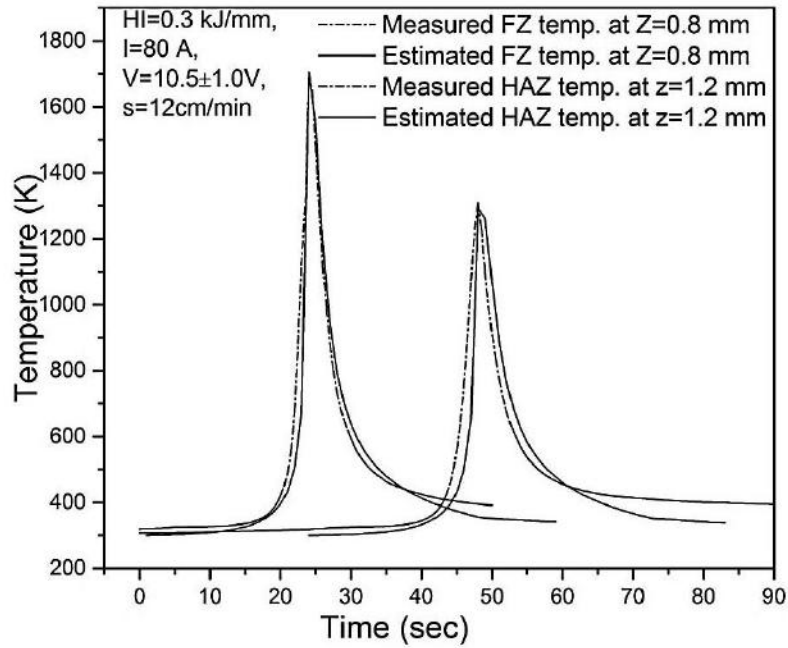
(a)
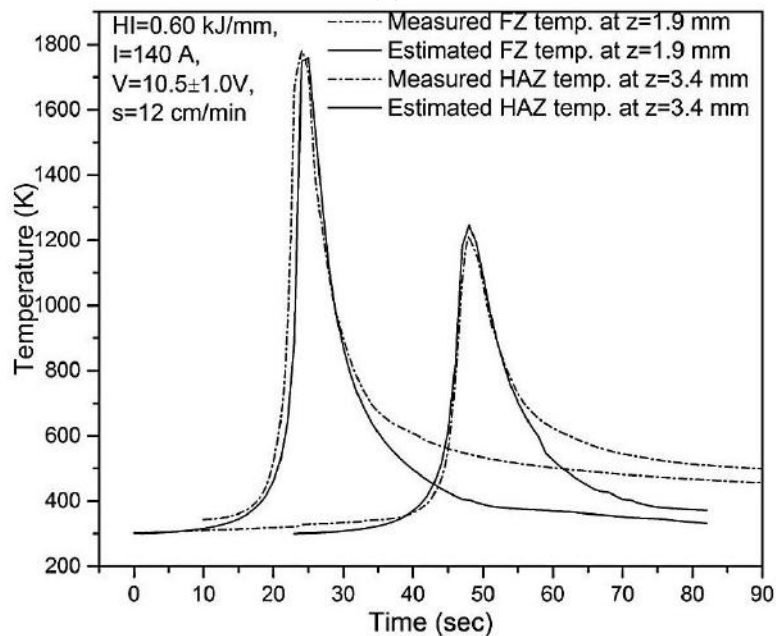
(b)

Fig. 5.14   Comparison of the estimated and measured weld thermal cycle at different combination of arcing current and heat input of (a) 100 A; 0.30 kJ/mm and (b) 140 A; 0.60 kJ/cm at a given arc voltage and travel speed of 10.5 ± 1.5 V and 12 cm/min respectively.
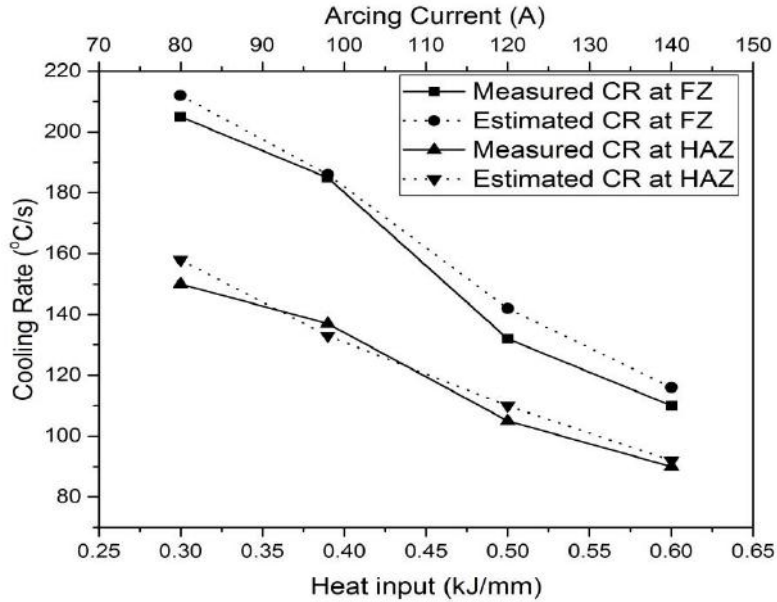
Fig. 5.15 Comparison of estimated and measured cooling rate at intercritical temperature range (800-500^{0}C).

The fig. 5.15 shows the estimated and measured CR at the intercritical temperature range (800-500^{0}C) evaluated from the respective thermal cycle plots. The figure shows that CR decreases with the increase in heat input on variation in arcing current from 80 to 140 A. The figure also shows that the estimated magnitude of CR is similar to its measured value with an accuracy of average variation 4 ± 1%. The variation of isotherm and CR from the peak temperature dictates the final phase transformation of the fused zone and HAZ.

5.2.3 Microstructural studies for single-pass C-TIG arcing process

The microstructure of a metallic material strongly influences its mechanical and chemical properties such as strength, toughness, ductility, hardness, corrosion resistance and wears resistance, which in turn governs the application of materials in industrial practices. However, the properties of any material not only depend upon the microstructure, but also on the type, morphology and proportionate amount of different phases present in the matrix. In this regard the control of heating rate, peak temperature and cooling rate along with the reheating temperature and time, in case of multi-pass arc heating, all factors play important role in governing the desired phase transformation at any location of the matrix.

During surface modification of AISI 4340 steel by single-pass C-TIG arcing arcing process, the phase transformation is primarily dictated by the isotherms and thermal cycle of arc heating zone as a function of arcing parameters. Thus, it is very much necessary to study the effect of these parameters on phase transformation in this steel in order to critically

understand, predict and ultimately control the final microstructure of matrix for desired service conditions.

Microstructure of the C-TIG arcing processed AISI 4340 steel is analyzed in reference to Ú, arcing current (I) and travel speed (S). The detailed discussions of the microstructure of the modified zone with respect to the arc parameters have been given below.

5.2.3.1 Effect of arcing parameters on microstructure of fusion zone

At a given arc voltage (V) and arc travel speed (S) of 10.5 ± 1.0 V and 12 cm/min the overall appearance of microstructure of fusion zone using single-pass C-TIG arcing process at arcing current of 100 and 140 A has been typically shown in figs. 5.16 (a) and (b) respectively. The FZ microstructure at different arcing current reveals the cast dendritic morphology along with acicular ferrite. The figures further reveal that the increase of arcing current that enhances the Ú coarsens the dendritic growth in the matrix. Similarly, at a given V and S of 10.5 ± 1.0 V and 12 cm/min respectively the detail microstructures of fusion zone using single-pass C-TIG arcing process at varying arcing current of 80, 100, 120 and 140 A have been shown in figs. 5.17 (a), (b), (c) and (d) respectively. It is observed from the figures that at a relatively low heat input of 0.30 kJ/mm (I= 80 A) needle shape martensite predominantly forms in the matrix with some amount of bainite. However, with the increase of arcing current from 100 to 140A, the microstructure of FZ is found to have relative coarsening of martensite to lath shape with increased amount of bainite and pro eutectoid ferrite. This is in agreement to the increase of cooling rate with the decrease of arcing current (section 5.2.2) promoting transformation of martensite whereas, a slower cooling rate at higher arcing current indulges the formation of lath martensite along with bainite. Similarly, the micro structures shown in fig. 5.18 (a-d) reveal that at the arc travel speed of 6 cm/min the increase of heat input from 0.60 to 1.21 kJ/mm with the increase of acing current from 80 to 140 A, completely suppresses the formation of needle shape martensite and enhances the amount of ferrite and bainite transformation in the matrix. The X-ray diffraction profile of the fusion zone of TIG arc processed substrate at varying I from 80 to 140 A is shown in fig. 5.19. The figure confirms the presence of characteristic peaks of martensitic phase present in the fused matrix [S. Bhattacharya et. Al., 2011]. This is also in agreement to the similar identification of martensite in low alloy steel as described by Tewary et al. (2014).

(a)   **(b)**
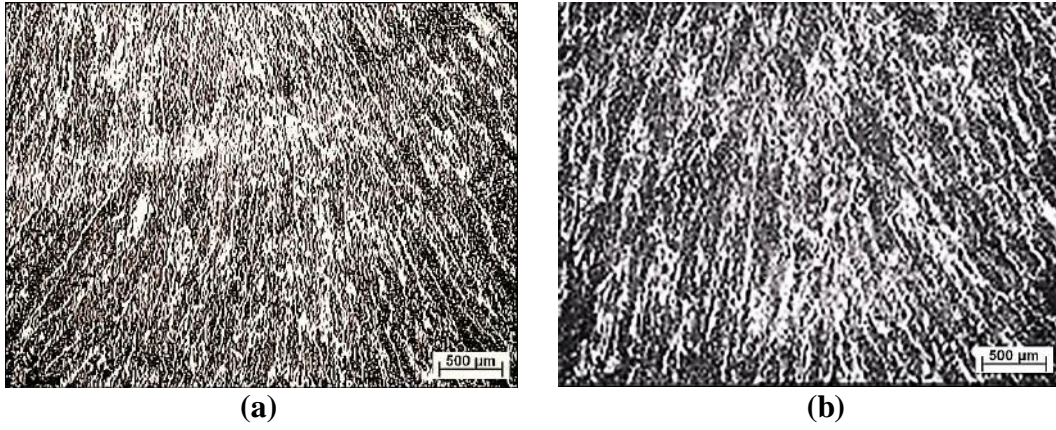
Fig. 5.16   Typical microstructure of FZ at different I of (a) 100 and (b) 140 A, where the V and S are kept constant at 10.5 ± 1.0 V and 12 cm/min respectively.
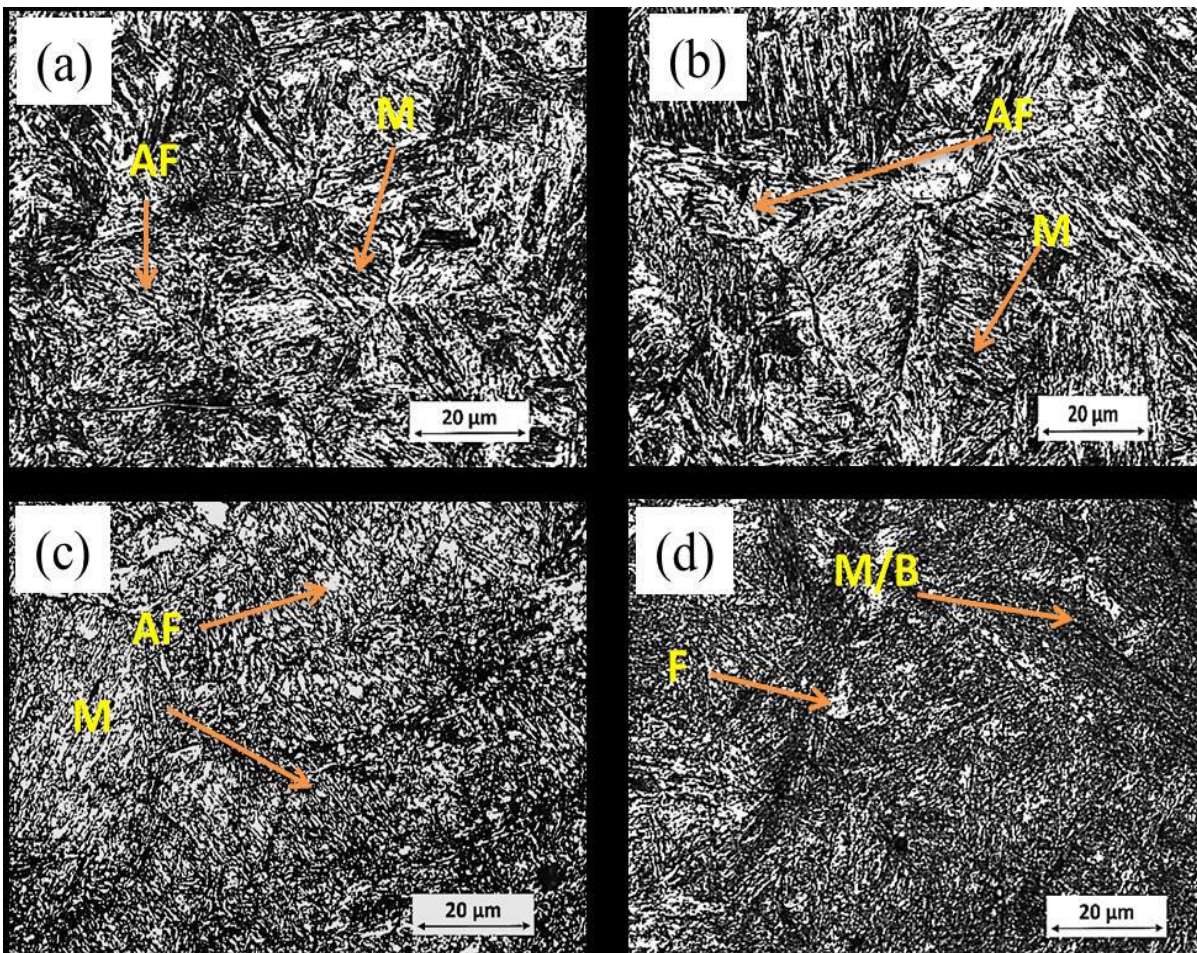
Fig. 5.17   Typical microstructure of fusion zone in single-pass C-TIG arcing process under different arcing current of (a) 80 (b) 100 (c) 120 and (d) 140A where the V and S are kept constant at 10.5 ± 1.0 and 12 cm/min respectively.
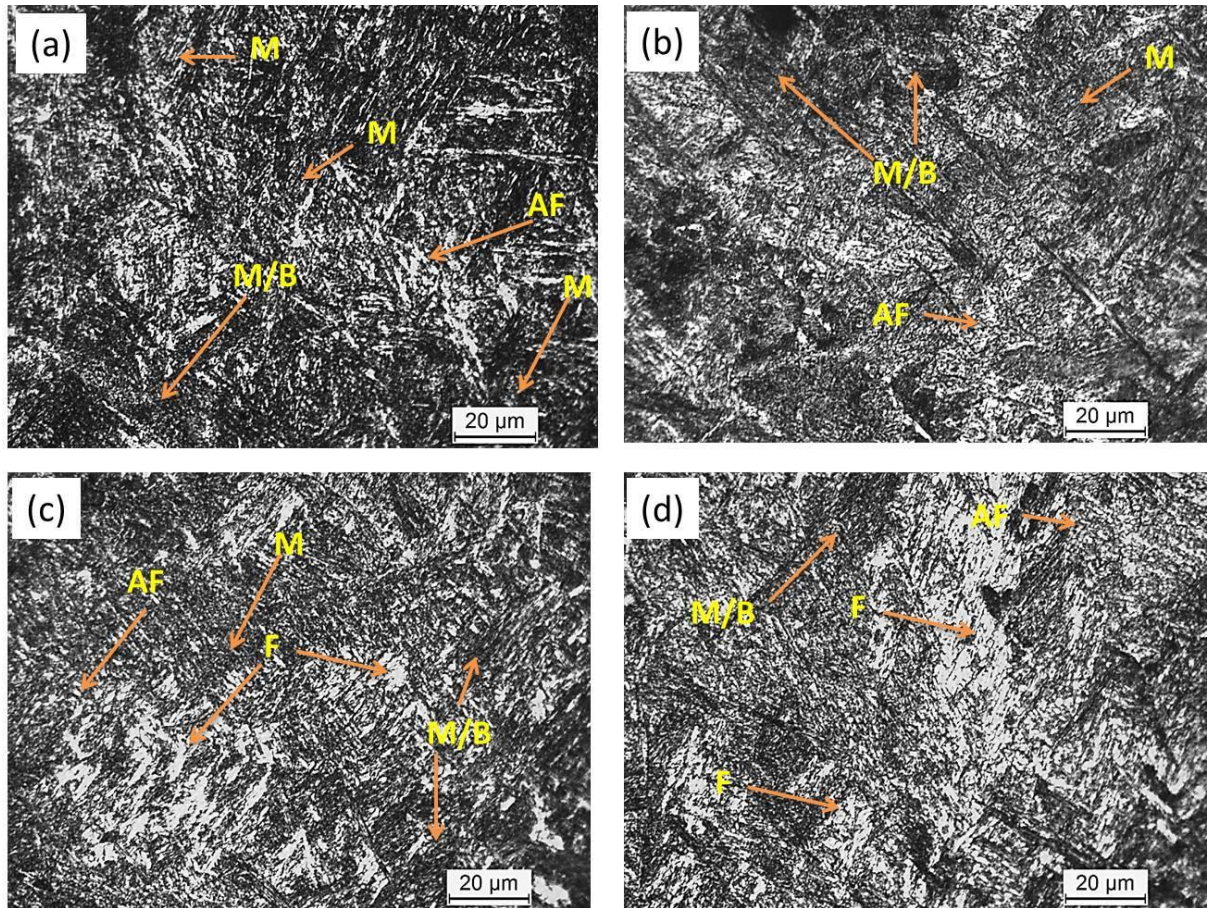
Fig. 5.18   Typical microstructure of fusion zone in single-pass C-TIG arcing process under different arcing current of (a) 80 (b) 100 (c) 120 and (d) 140A where the V and S are kept constant at 10.5 ± 1.0 and 6 cm/min respectively.
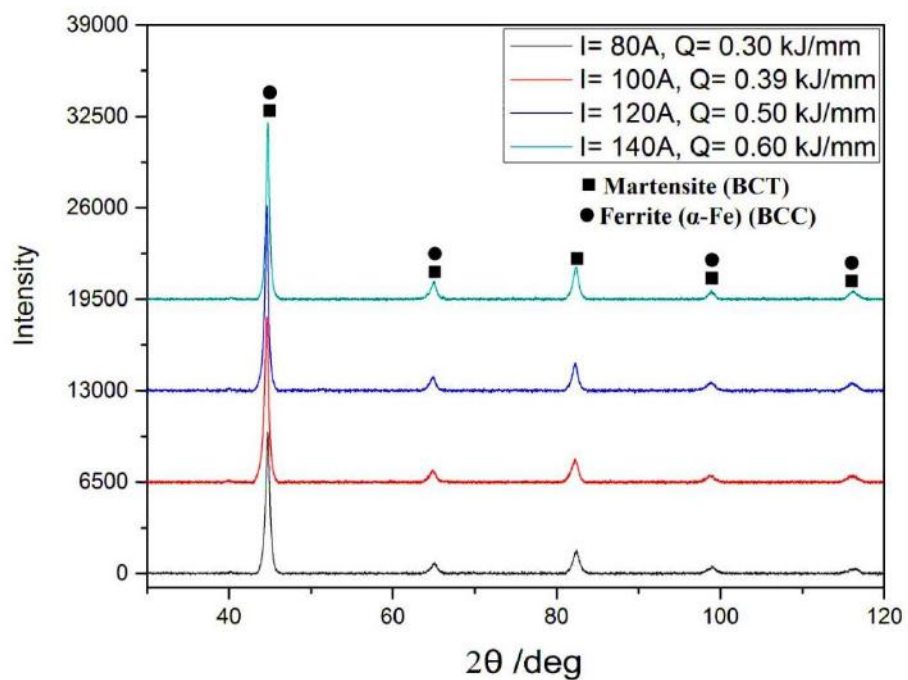
Fig. 5.19   XRD analysis of the modified surface at S and V of 12 cm/min and 10.5 ± 1.0 V respectively.

5.2.3.2 Effect of arcing parameters on microstructure of HAZ

At a given arc voltage and travel speed, the overall and detail studies on microstructure of HAZ adjacent to fusion line (0.3 mm) formed during using single-pass C-TIG arcing process at varied arcing current from 80 to 140 A have been typically shown in figs. 5.20 and 5.21, respectively. The microstructure of base metal (fig. 5.1) in HAZ adjacent to fusion line is thoroughly modified at the peak temperature (fig. 5.14) raised to the range of 1000–1200 K (700-950 ^{0}C). It is transformed to relatively finer grain with respect to that of the base metal along with transformation to martensite combined with bainite and allotriomorphic ferrite at its comparatively high CR (fig. 5.15). At the relatively higher cooling rate of low arcing current of 80A and 100 A the HAZ consists of a higher proportion of martensite and that is compensated by formation of more bainite and ferrite due to reduction of CR at the higher arcing current of 120, and 140 A. It is noted that at the higher arcing current the transformation of HAZ is having more proeutectoid ferrite than that observed in case of the lower arcing current.
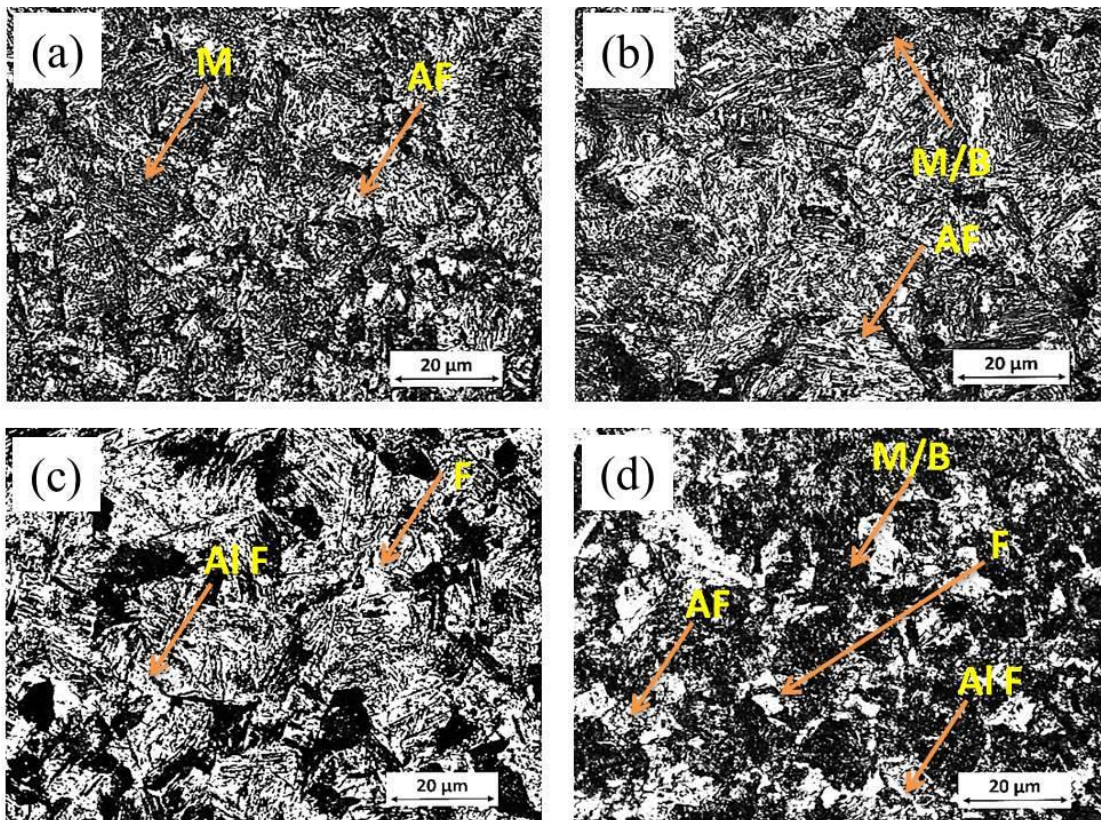
Fig. 5.20 Typical microstructure at HAZ using single-pass C-TIG arcing process under different arcing current of (a) 80 (b) 100 (c) 120 and (d) 140A, where the V and S are kept constant at 10.5 ± 1.0 and 12 cm/min respectively.
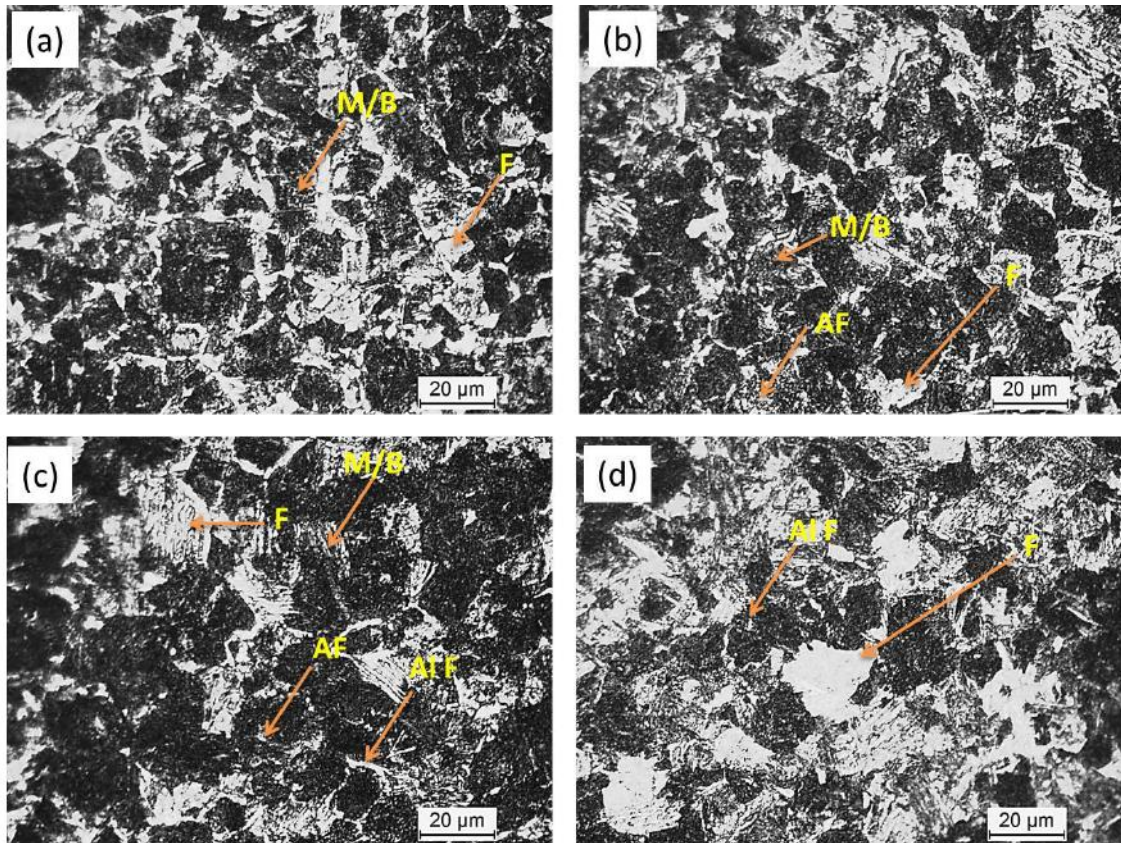
Fig. 5.21   Typical microstructure at HAZ using single-pass C-TIG arcing process under different arcing current of (a) 80 (b) 100 (c) 120 and (d) 140A, where the V and S are kept constant at 10.5 ± 1.0 and 6 cm/min respectively.

At a given V and S, the increase of arcing current increases the Ω which reduces the cooling rate of modified zone because of comparatively lower temperature gradient between different locations within the fused pool [Robert W. Messler 1999]. But it increases fluid flow velocity and thus enhances the dendrite growth significantly. This has primarily happened due to increase of the fusion zone area as well as weld pool temperature with the increase of Ω.

5.2.4 Hardness Study

The hardness and its distribution in the matrix play an important role to affect the toughness and fatigue properties of a high strength low alloy structural steel. The hardness of AISI 4340 steel is primarily dictated by the isotherms and thermal cycle (heating and cooling rate) of the TIG arcing process. The present study involves understanding the effect of TIG arcing parameters of single-pass C-TIG arcing process on the hardness and its distribution in this steel. The hardness of base material (AISI 4340 steel) used in this study has been found as 256 ± 10 HV.

5.2.4.1 Effect of single-pass C-TIG arcing process on Hardness of FZ and HAZ

At a given arc voltage of 10.5 ± 1.0 V, the effects of variation in arcing current (I) and arc travel speed (S) on the hardness of fusion zone and HAZ have been shown in figs. 6.22 ((a)

and (b)) respectively. The figures show that the increase in arcing current from 80 to 140 A significantly decreases the hardness of fusion zone and its HAZ. It has been further observed that the hardness of FZ and HAZ increases appreciably with the increase of arc travel speed. The figures also reveal that the hardness of the FZ and HAZ at any I and S is much more than that of the base metal (256 ± 10 VHN), which might have largely happened due to favourable phase transformation as discussed earlier. In HAZ it has happened primarily through a process of re-crystallization and phase transformation as a function of heating and cooling rate which are largely governed by the heat input and temperature gradient in the fusion pool dictated by the arcing parameters [Ghosh et al 2009]. The decrease in arcing current at a given arc travel speed and the increase in travel speed at a given arcing current reduces the heat input that reduces the size of fusion pool and consequently enhances its cooling rate. The high cooling rate is primarily responsible for the fully lath martensitic structure (refer to sec. 5.2.3) which is relatively hard as clearly reflected in the figure. Finally the presence of varied amount of different phases in the fused and heat affected zones as discussed in section 5.2.3.2 is reflected in their matrix hardness. The empirical correlations of hardness of FZ and HAZ with I and S have been worked out as follows.

At V=10.5 ± 1.0 V

$$H_{FZ} = 905.1 - 5.32 \times S - 2.69 \times I + 0.122 \times I \times S \qquad \text{…….…………..(5.7)}$$

$$H_{HAZ} = 526.1 + 3.79 \times S - 1.924 \times I + 8 \times 10^{-3} \times I \times S \quad \text{………………..(5.8)}$$

At different arcing currents of 80, 100, 120 and 140 A, the distribution of hardness across the region starting from the fusion zone through HAZ to base material is shown in fig. 5.23 (a-d) respectively. The figure shows that as one proceeds from the fused modified zone to HAZ the hardness falls till it reaches the stable hardness (256 ± 10 HV) of base metal. It is observed that with the increase of arcing current from 80 to 140 A at constant arc travel speed of 12 cm/min, the fusion zone of hardness varied from about 730 to 690 HV extends from about 0.8 to 2.7 mm respectively. It was having a backup of relatively lower hardness HAZ lying in the range from about 420 to 340 HV respectively as shown in fig. 5.23 (c). At an appropriate arcing current giving fine grain in HAZ may have relatively low hardness as compared to FZ and a tougher HAZ backup due to formation of lath martensite is found to be extended up to about 1.5 and 2.5 mm followed by base metal. In view of the above it may be assumed that the use of TIG arcing processing is effective to produce high surface hardness with tougher inner core.
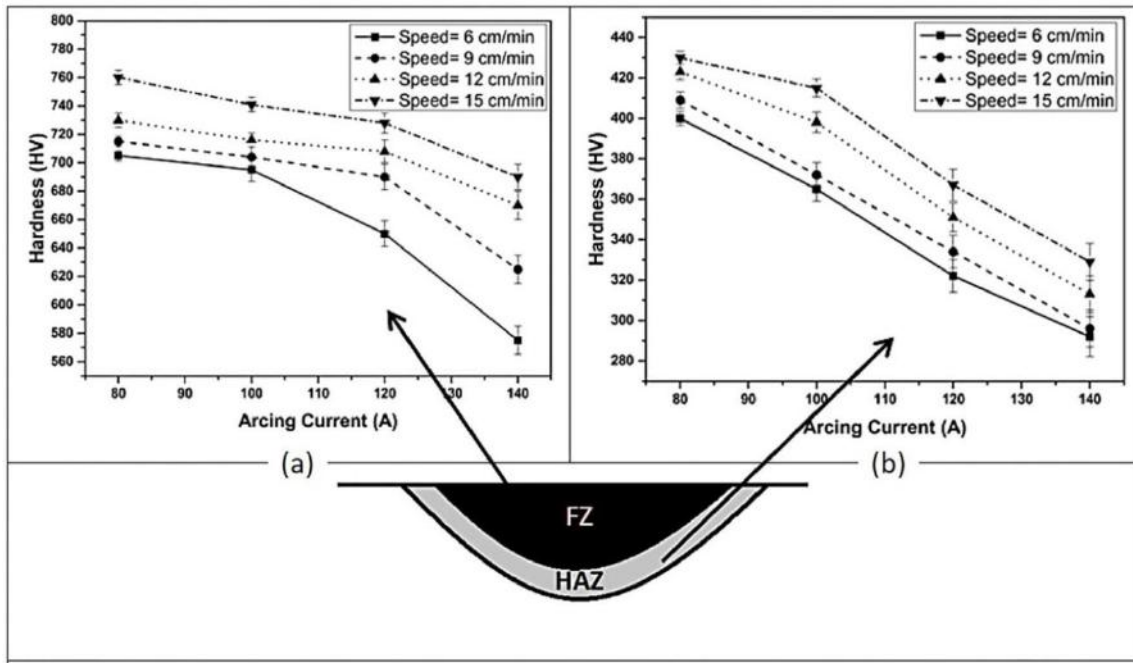
Fig. 5.22   The effect of arcing current and arc travel speed on hardness of (a) FZ and (b) HAZ at an arc voltage of 10.5 ± 1.0 V.
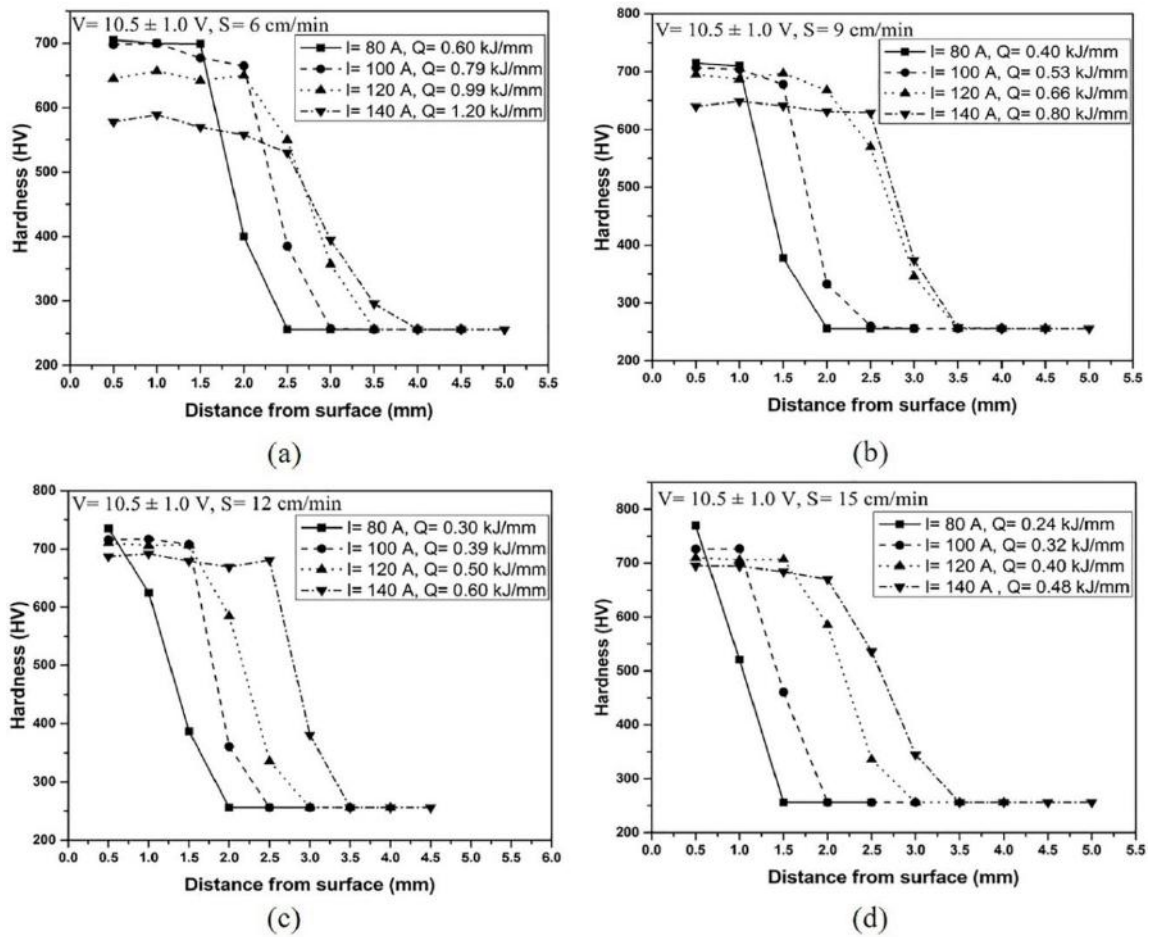
Fig. 5.23   At different arcing currents the distribution of hardness across the modified region starting from the fusion zone through HAZ to base metal observed at arc travel speed (a) 6, (b) 9, (c) 12 and (d) 15 cm/min.

5.2.5 Tensile properties

The yield strength (YS), ultimate tensile strength (UTS), toughness and ductility (strain%) of the as received AISI 4340 structural steel are found as about 395 MPa, 705 MPa, 119 J/mm^3 and 19.24% respectively. The engineering stress-strain curve of the surface modified substrate prepared by arc travel speed of 6, 9, 12 and 15 cm/min has been shown in figs. 5.24 (a-d) respectively, where the heat input was duly varied from 0.24 to 1.21 kJ/mm due to change in arcing current from 80 to 140 A at a given arc voltage of 10.5 ± 1.0 V. Under such conditions of surface modification, the effect of arcing current at different arcing speeds on the YS, UTS, toughness and percentage strain of the surface modified substrate is illustrated in figs. 5.25 (a-d). From the stress-strain curves depicted in figs. 5.24 (a-d) it was clearly understood that surface modification using TIG arcing significantly affects the tensile properties of base material, where the YS and UTS are considerably improved along with some reduction of strain and toughness (fig. 5.25 (a-d)). This is in agreement to the hard phase transformation in the matrix as discussed above which is functional in governing its mechanical properties based on the processing parameters. Here, the decrease of arcing current or increase of arc travel speed reduces the heat input and consequently enhances the cooling rate favouring hard phase transformation in the matrix. However, it is interestingly observed that at a given arcing current, the decrease of heat input with the increase of arc travel speed beyond 12 cm/min in general adversely affect the tensile properties of the surface modified AISI 4340 steel (fig. 5.25) and it is relatively more prominent at higher arcing current. Thus, it may be understood that there may be a critical requirement of heat input with appropriate heat distribution (controlled by arc travel speed) governing the thermal cycle for desired phase transformation in the fusion modified matrix.
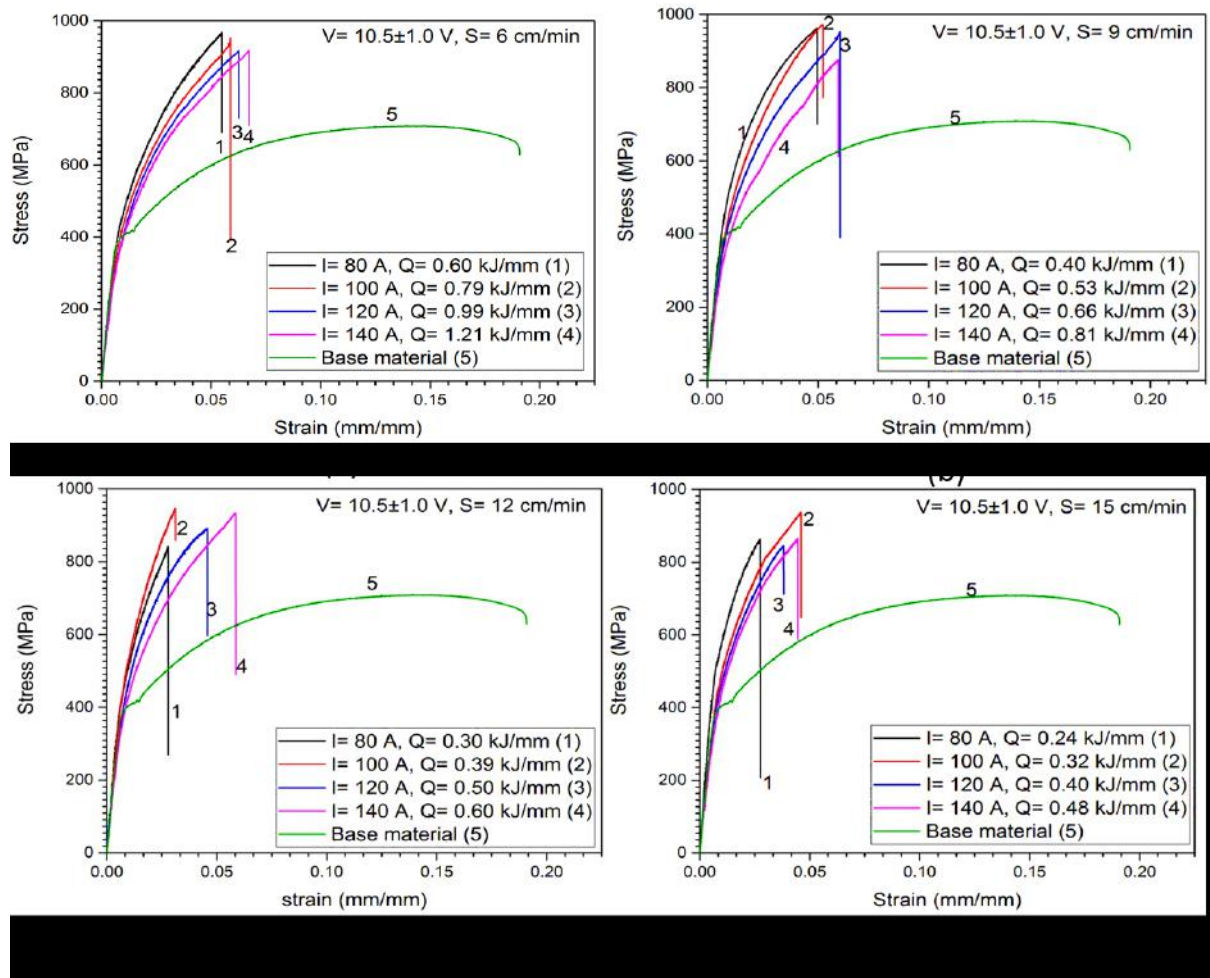
Fig. 5.24   Tensile stress-strain diagram of surface modified AISI 4340 structural steel produced at different heat input obtained by varying arc current (I) at different arc travel speeds (S) of (a) 6, (b) 9, (c) 12 and (d) 15 cm/min, where the arc voltage of 10.5±1.0 V is kept constant.

In this context it is also observed that at a given close range of heat input the increase of arc travel speed beyond 12 cm/min significantly affects the mechanical properties of the matrix by reducing the YS along with relative increase in strain and toughness. In consideration of the results presented in figs. 5.25 and 5.26, it appears that an optimum combination of tensile properties assumed as relatively high YS, UTS, ductility (strain%) and toughness can be achieved by TIG arcing processing of AISI 4340 steel using the arc travel speed at 9-12 cm/min giving heat input in the range of 0.6-0.81 kJ/mm. At a given arc voltage of 10.5 ± 1.0 V, keeping the arc travel speed at 9-12 cm/min with heat input maintained in the range of 0.6 to 0.81 kJ/mm by adjusting the arcing current within 120 to 140 A gives the YS, UTS, ductility and toughness in the range of about 570-642 MPa, 875-952 MPa, 5.85-6.0% and 35.1-39.3 J/mm^3 respectively as shown in fig. 5.26 (a-d) respectively. Such changes in tensile properties give a strong agreement of formation of needle shape martensite, lath martensite and banitic structure in the modified surface of AISI 4340 steel produced by TIG arcing process.

101
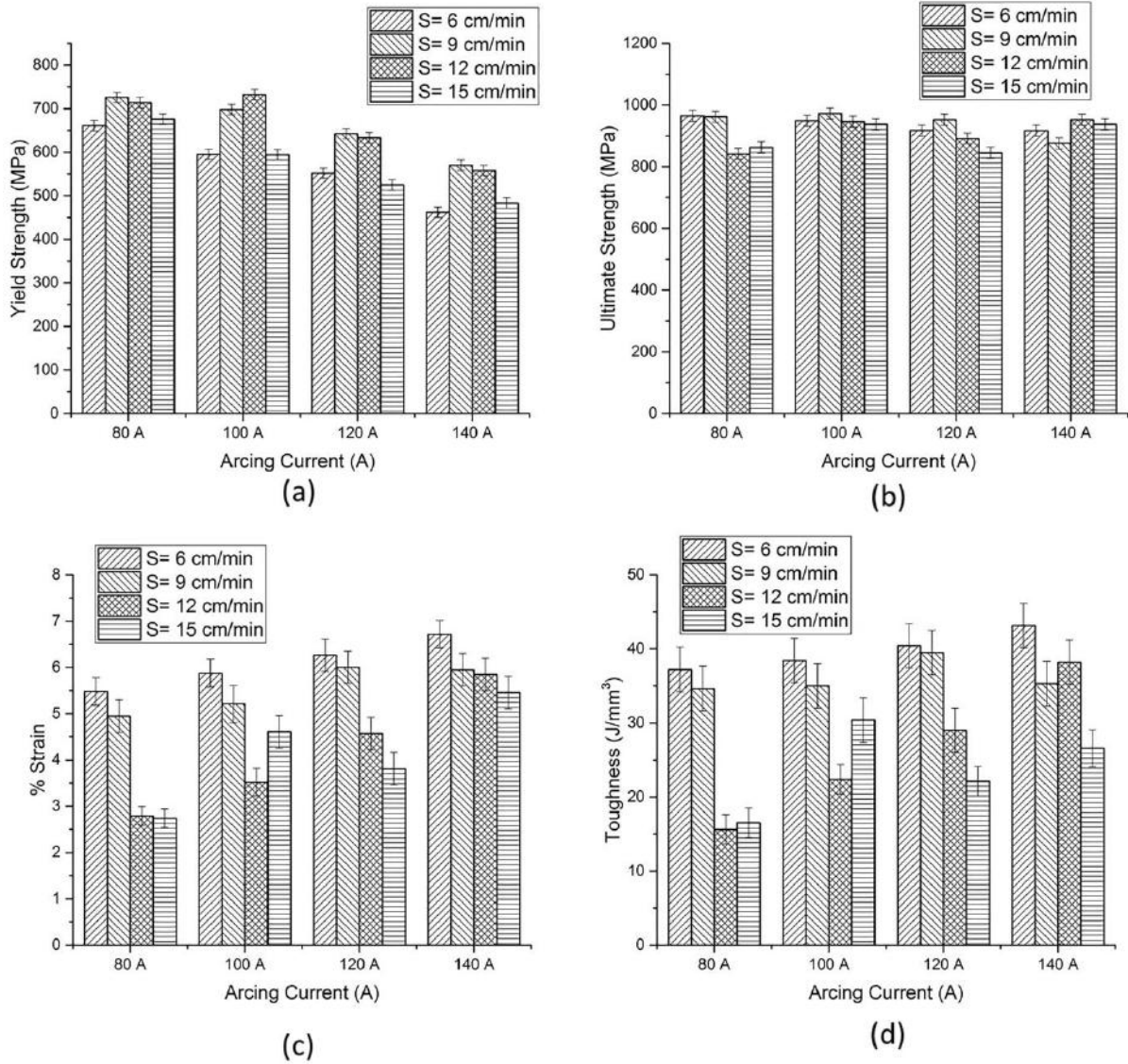
Fig. 5.25 At different arcing currents effect of arc travel speed on a) Yield strength, b) ultimate tensile strength, c) strain and d) toughness observed during tensile test of the surface modified steel.
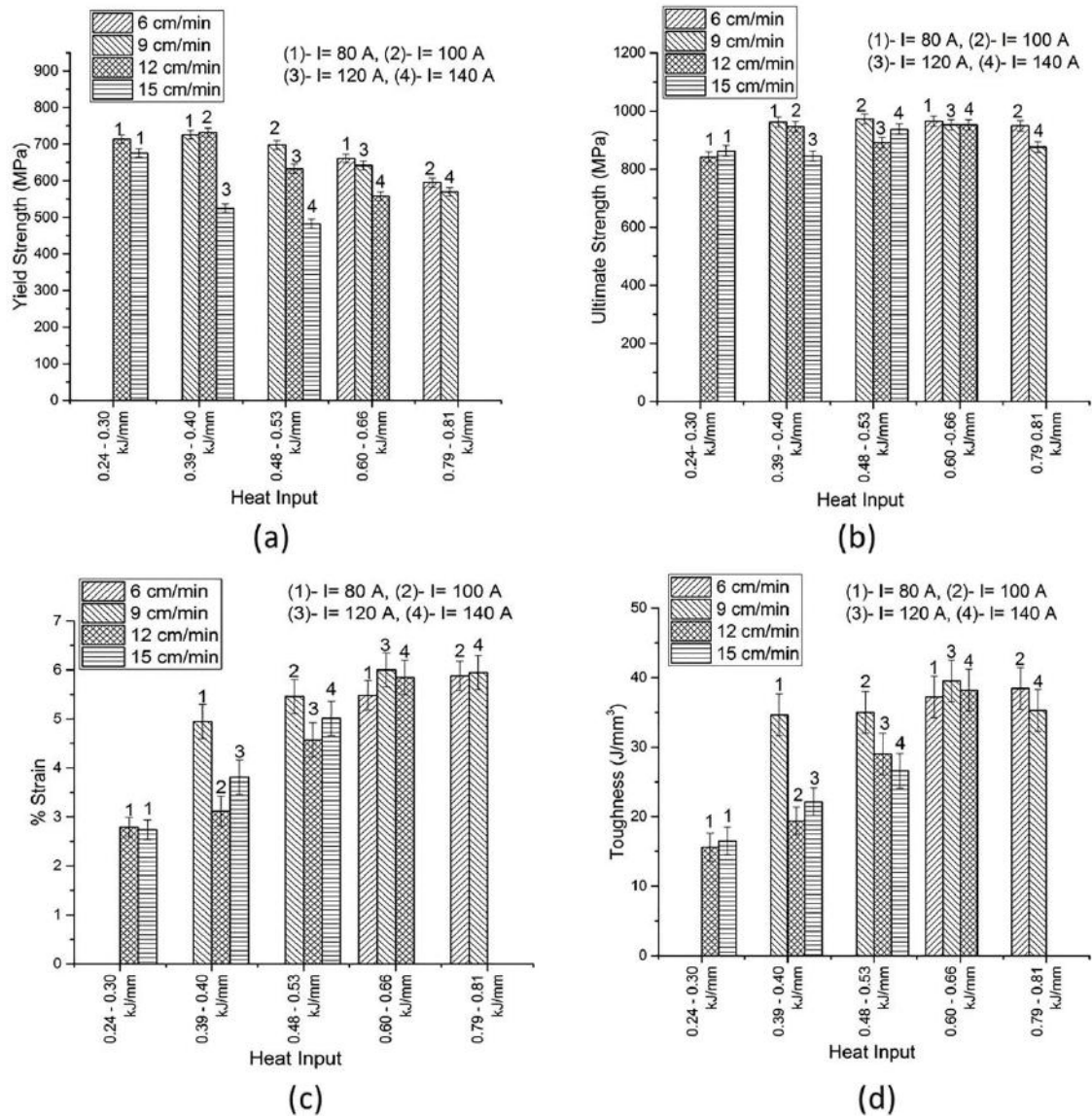
Fig. 5.26 At a given close range of heat input effect of arc travel speed on a) yield strength, b) ultimate tensile strength, c) strain and d) toughness observed during tensile test of the surface modified steel.

Fractograph of the base material fractured under uniaxial tensile test has been shown in fig. 5.27 (a). The figure shows the presence of tear ridges, transgranular ductile dimple and cleavage facets in the matrix, which is primarily attributed to mixed mode of failure. However, under the same test condition, the fractograph of the region modified at heat input of 0.79 kJ/mm depicts the presence of appreciable transganular cleavage facets with some amount of ductile tear ridges in the matrix as shown in fig. 5.27 (b). The predomination of cleavage fracture confirms the tensile failure with relatively higher strength but appreciable reduction in strain as stated earlier.
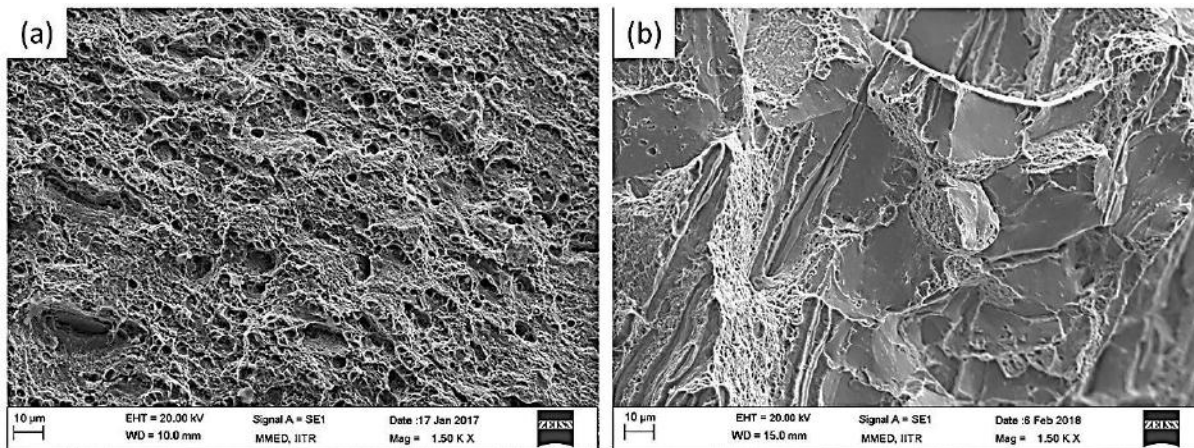
Fig. 5.27   Fractographs of a) base material and b) region modified at heat input of 0.79 kJ/mm failed under tensile test.

5.2.6 Bending properties

The flexural yield strength and the maximum strength of as received AISI 4340 structural steel are found as about 540 MPa and 1160 MPa respectively. At a given arc voltage of 10.5 ± 1.0 V, the flexural stress-extension curve has been shown figs. 5.28 (a-d), where heat input was duly varied from 0.24 to 1.21 kJ/mm due to change in arcing current at different arc travel speed of 6, 9, 12 and 15 cm/min respectively. It is observed that the single-pass TIG arc surfacing significantly affects the bend properties such as flexural yield strength and maximum flexural strength of a component as shown in figs. 5.29 (a-d). The figures reveal that a low heat input below about 0.4 kJ/ mm often shows a tendency to maximum lowering of the flexural properties as compare to those of the base metal. This has happened due to increase of cooling rate at low heat input of weld pool, prompting hard phase transformation in it. This is found as formation of needle shape matensite in the matrix as discussed in (section 5.2.3), which has significantly low ductility attributed to sudden failure. Formation of residual stress due to such hard phase transformation may have also put an adverse effect on flexural yield strength. Further, it was observed that as heat input is increased by decreasing arc travel speed from 12 cm/min to 6 cm/min, there was an appreciable increase in flexural yield strength as well as flexural maximum stress and flexural extension as shown in fig. 5.28 (a-c). Such behaviour has happened primarily due to formation of relatively softer lath matensite and banite transformation in the matrix due to relatively slower cooling rate at higher heat input. Fig. 5.29 (a) shows that at the arc travel speed of 6 cm/min, there is maximum improvement in flexural yield strength of the order of 25 to 35 % at approximately similar maximum flexural stress with respect to that of the base metal. Maximum reduction in flexural properties is observed at an arcing current and arc travel speed of 80 A and 15 cm/min respectively.

104
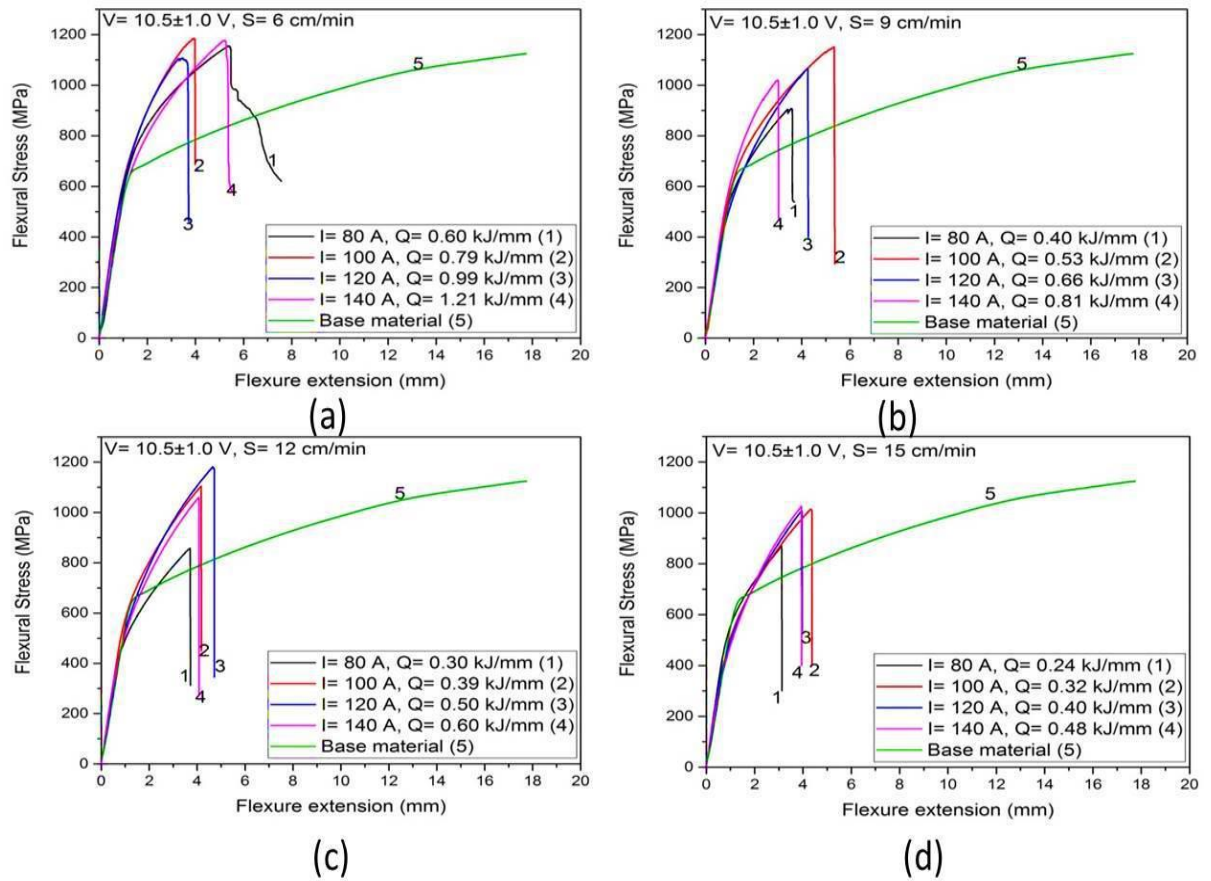
Fig. 5.28   Flexural stress-extension diagram of surface modified AISI 4340 structural steel produced at different heat input obtained by varying arc current (I) at different arc speeds (S) of (a) 6, (b) 9, (c) 12 and (d) 15 cm/min, where the arc voltage of 10.5±1.0 V is kept constant.

Typical fracture surface of the three point bend test has been shown in fig. 5.30. The fracture surface reveals the occurrence of brittle fracture in the modified zone followed by ductile fracture in base material primarily due to presence of relatively brittle phase in the fusion modified matrix. At higher magnification the modified surface reveals the presence of some micro cracks at the centre of modified zone, which may have generated by the presence of residual stresses in the matrix. The modified surface was failed in the direction parallel to that of the applied load.
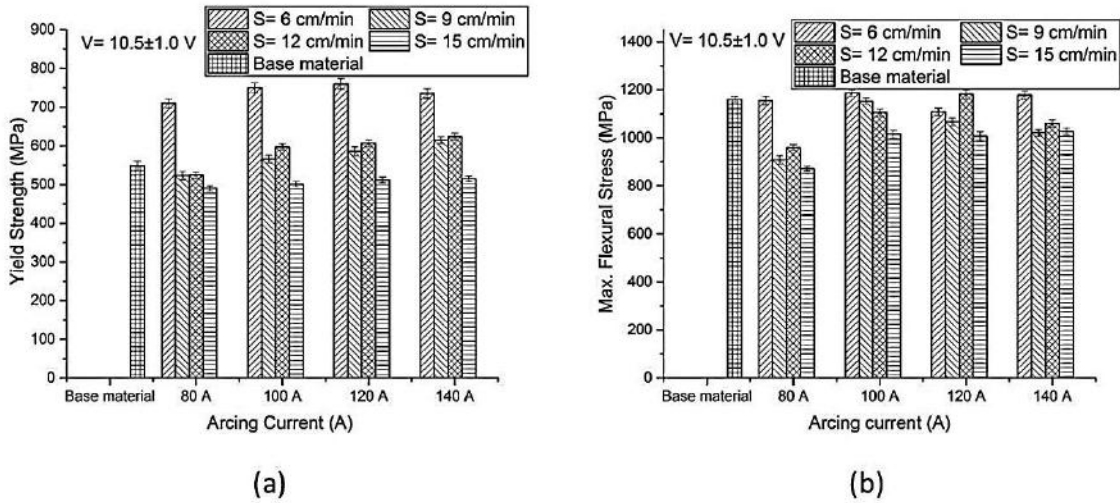
Fig. 5.29 At different arcing currents effect of arc travel speed on a) Flexural yield strength, b) flexural maximum strength, observed during three point bend test of the surface modified steel.
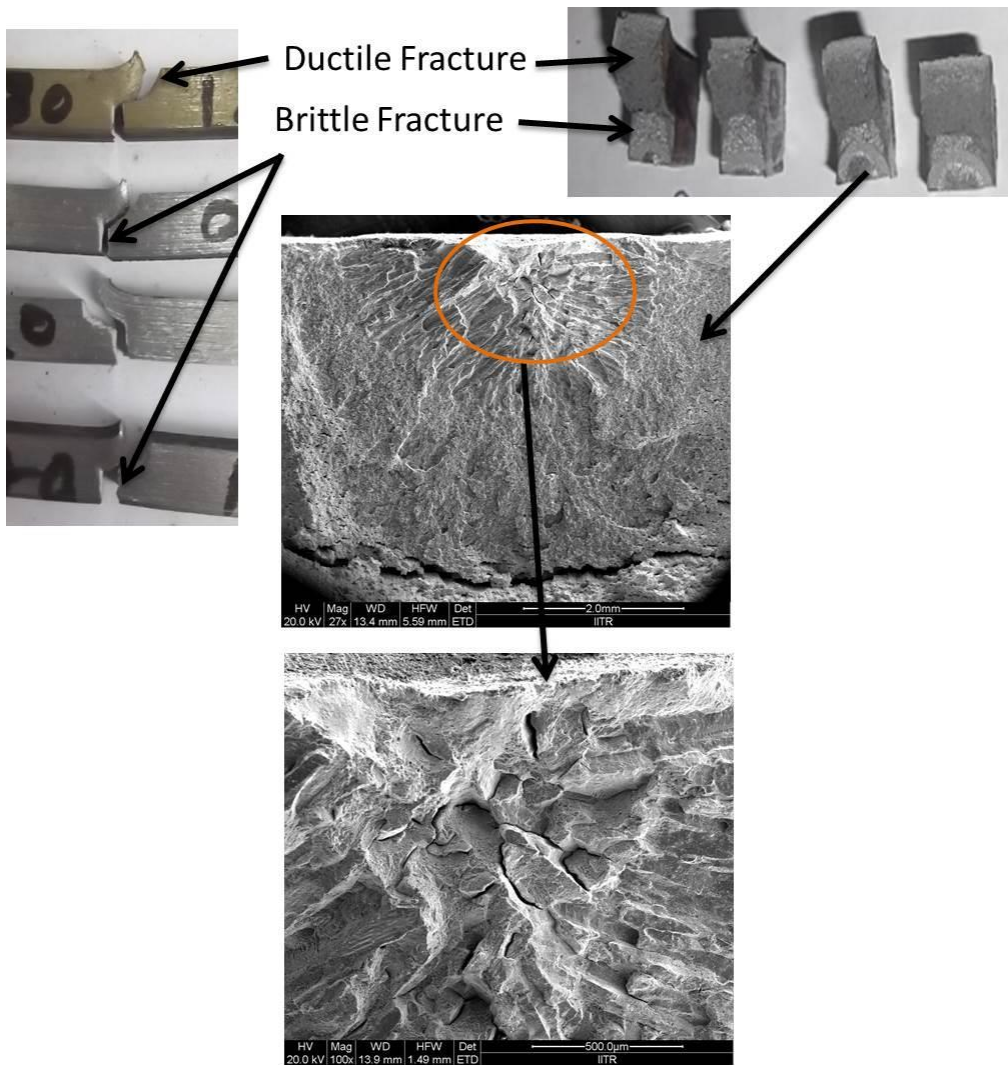
Fig. 5.30 Macro and micro fractographs of flexural test failed under bending load.

5.2.7 Residual stresses

Mechanical properties of a component can be significantly affected by the presence of residual stresses in the matrix, where tensile stress may promote premature failure and compressive residual stresses can delay failure, resisting crack opening [Bendeich et. Al., 2006]. At a given arc voltage of 10.5 ± 1.0 V, the longitudinal and transverse residual stresses at the centre of FZ of the TIG arc modified surface has been shown in figs. 5.31 (a) and (b) respectively. It is observed that as the heat input increases from 0.39 to 1.21 kJ/mm there is a significant reduction in compressive residual stress from 200 to 25 MPa but, an appreciable increase in tensile stress from 130 to 165 MPa in longitudinal direction of surface modification as shown in fig. 5.31 (a). However, in case of transverse direction of surface modification there is significantly more increase in tensile stress from 153 to 265 MPa as shown in fig. 5.31 (b). In longitudinal direction of modification the tensile residual stress was found at the upper surface up to a depth of 0.23 mm from the top followed by compressive stress in the matrix distributed up to a fairly larger depth of 0.2 - 1.0 mm. These have possibly a significant positive contribution on improvement of fatigue life of the surface modified base material under uniaxial tensile fatigue. But in case of fatigue under bending load the top surface having tensile residual stresses may give an adverse effect. These stresses are primarily attributed to differential thermal expansion-contraction and phase (martensite) transformation in the modified region [Hidekazu et. Al., 2008]. The FZ and HAZ have experienced heating in the temperature range of 1440-1900 ^{o}C and 700- 1200 ^{o}C respectively as discussed above. The behaviours of residual stresses observed in the matrix are largely in agreement to the phase transformation under different conditions of surface modifications as discussed above.
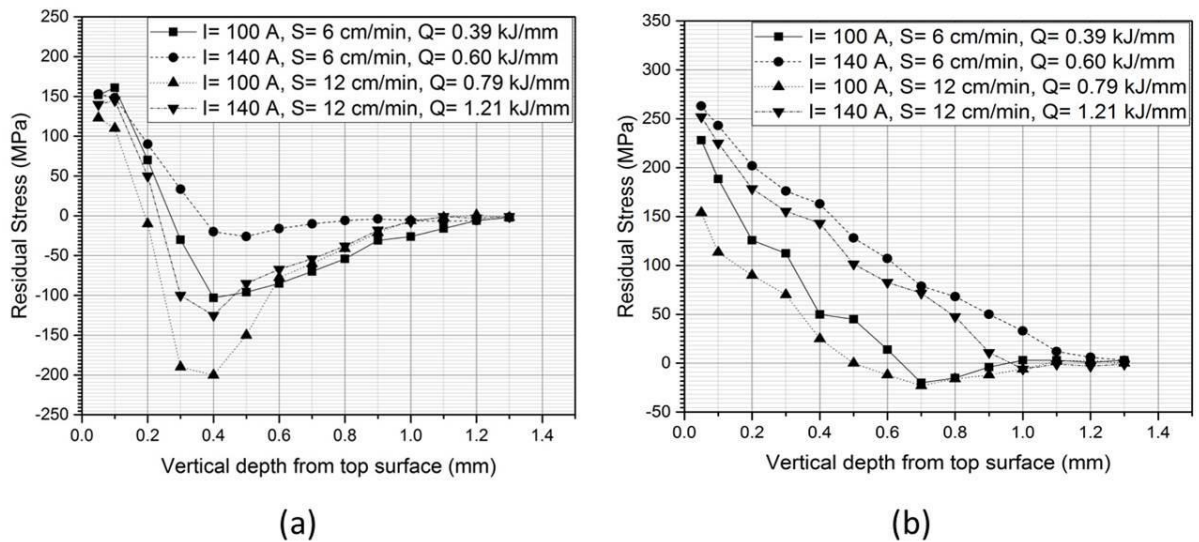
Fig. 5.31   Different components of residual stresses in the matrix modified at different heat input a) longitudinal and b) transverse directions.

The resolved stresses were calculated to understand the stress level in the sample during testing. Resolved stresses for uniaxial tensile test were calculated by the eq. 6.9.

$$\sigma_{resolved} = \sum_{i=0}^{i=4} \sigma_{a_i} + \sigma_{r_i}$$

....6.9

Where σ_a is applied stress due to load, σ_r is residual stresses due to surface modification and I is thickness of the tensile sample (about 4 mm). Possible resolved stress during tensile test of single-pass C-TIG arc modified sample prepared at the heat input of 0.39 kJ/mm (I= 100 A and S= 12 cm/min) is shown in fig. 5.32. the figure reveals that the resolved stress was reached to about 525 MPa up to a depth of 0.15mm followed by a sudden reduction to about 200 MPa, when applied stress was 400 MPa by the tensile machine.

The resolved stresses for three point flexural bend stresses were calculated by the eq. 6.10.

$$\sigma_{resolved} = \sum_{i=-5}^{i=5} \sigma_{a_i} + \sigma_{r_i}$$

.... 6.10

Where σ_a is applied stress due to load, σ_r is residual stresses due to surface modification and i is thickness of the flexural sample (about 10 mm thickness). Here i=0 mm means neutral axis of the sample. The modified surface was kept as lower fibre, thus resolved stress at lower fibre during the flexural test of single-pass C-TIG arc modified sample prepared at the heat input of 0.39 kJ/mm (I= 100 A and S= 12 cm/min) is shown in fig. 5.33. The figure reveals that the resolved stress was reached about 725 MPa up to the depth of 0.15mm followed by a sudden reduction up to 370 MPa, when applied stress was 600 MPa by the tensile machine. In the case of flexural test, availability of tensile residual stresses is relatively more prominent for the crack initiation and propagation that adversely affects the flexural test in static as well as dynamic loading.
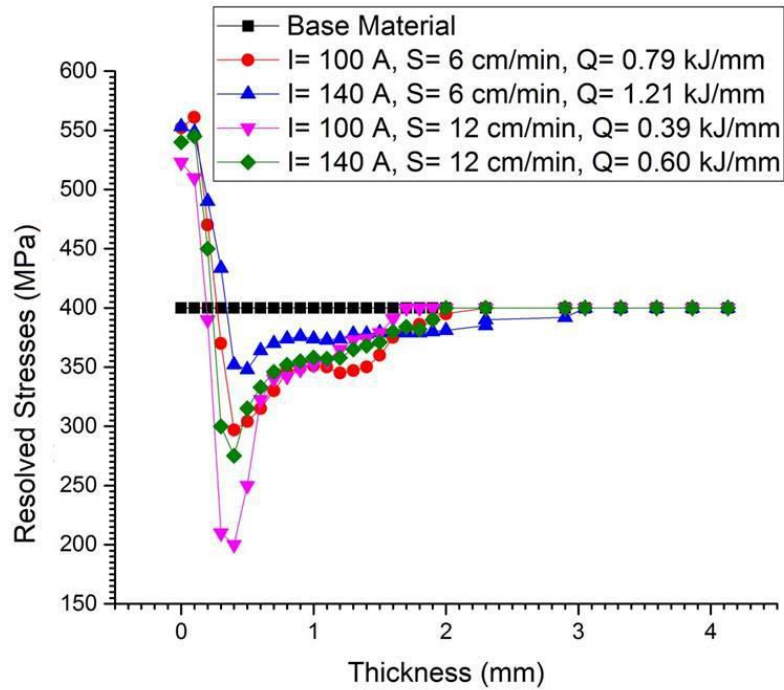
Fig. 5.32 The amount of resolved stresses within sample under tensile loading of 400 MPa stress by the machine.
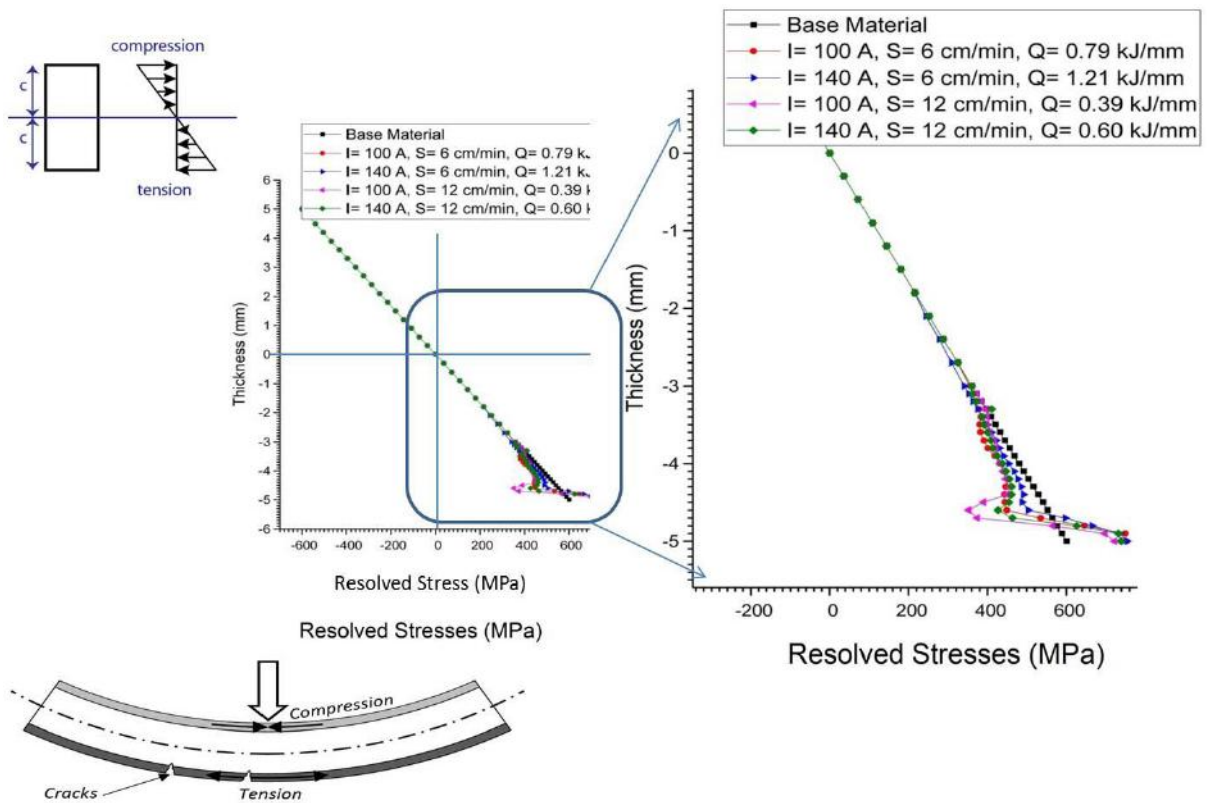
Fig. 5.33 The amount of resolved stresses within sample under bending stress of 600 MPa at lower fiber applied by the machine.

5.2.8 Fatigue Test

5.2.8.1 Under uniaxial tensile load

The studies on fatigue characteristics (S-N curves) of the AISI 4340 structural steel as base metal and the surface modified base metal prepared at various heat input resulting from varying arcing current and arc travel speed in the range of 80 to 140 A and 6 to 15 cm/min respectively at a given arc voltage of 10.5 ± 1.0 V are shown in figs. 5.34 (a-d). At the maximum cyclic stress (σ_{max}) of 570 MPa the base material has been failed at about 13.6×10^3 cycles, when it shows the endurance limit at the σ_{max} of 400 MPa, which is approximately 0.56% of its ultimate strength. The figs. 5.34 (a-d) depict that the surface modification of AISI 4340 steel can significantly improve the endurance limit of its fatigue failure up to σ_{max} in the range of about 530 - 577 MPa depending upon the TIG arcing process parameters. It indicates that the surface modification by TIG arcing process can improve fatigue performance of the base material of the order of 32 - 45 % as compared to that of the base material.

At a given arc voltage and arc travel speed of 10.5 ± 1.0 V and 6 cm/min, respectively, the increase of arcing current from 80 - 140 A decreases the endurance limit to σ_{max} from 577 to 533 MPa respectively as shown in fig. 5.34 (a), where the heat input is enhanced from 0.60 to 1.21 kJ/mm respectively. At the relatively higher arc travel speed of 9, 12 and 15 cm/min a similar behaviour of reduction in σ_{max} of the endurance limit with the increase of arcing current was observed, where the arc voltage was kept again at 10.5 ± 1.0 V, as shown in figs. 5.34 (b-d) respectively. At this juncture if it is considered that the fatigue life of surface modified AISI 4340 steel is broadly a function of heat input then it may be interesting to know that at a given arc voltage, out of arcing current and arc travel speed which one will be having predominant effect. In this regard it appears that the effect of arc travel speed varied in the range of 6 to 15 cm/min is relatively more significant as compared to the effect of arcing current. Thus it may be inferred that in case of instant fusion by arc heating the heat distribution predominated by the arc travel speed primarily governs the desired phase transformation especially by dictating the cooling rate. It may be understood from the slope of the S-N curves in their finite life region which maintains relatively higher σ_{max} of endurance limit. In case of the surface modified steel the S-N curves are found to be relatively flatter than that of the base metal when it is treated by the TIG arcing process at the arc travel speed of 9 and 12 cm/mm. At a given σ_{max} the surface modified AISI 4340 steel has always been found to give considerably higher fatigue life than that of the untreated base metal. Maximum improvement in the fatigue life under uniaxial tensile loading was observed at the relatively low heat input of 0.40 kJ/mm where, the arcing current, arc voltage and arc travel speed is kept as 80 A, 10.5 ± 1.0 V and 9 cm/min

respectively, as shown in fig. 5.34 (b). However, optimum improved fatigue performance of the surface modified AISI 4340 steel over that of the base material has been noticed in case of the modification carried out at the heat input in the range 0.4-0.6 kJ/mm with arc travel speed of 9-12 cm/min having suitably varied arcing current at the arc voltage of 10.5 ± 1.0 V. The observed fatigue characteristics are in agreement to the microstructure, hardness, strength and toughness of the modified material as a function of the processing parameters as discussed above.

(a)

(b)

(c)

112
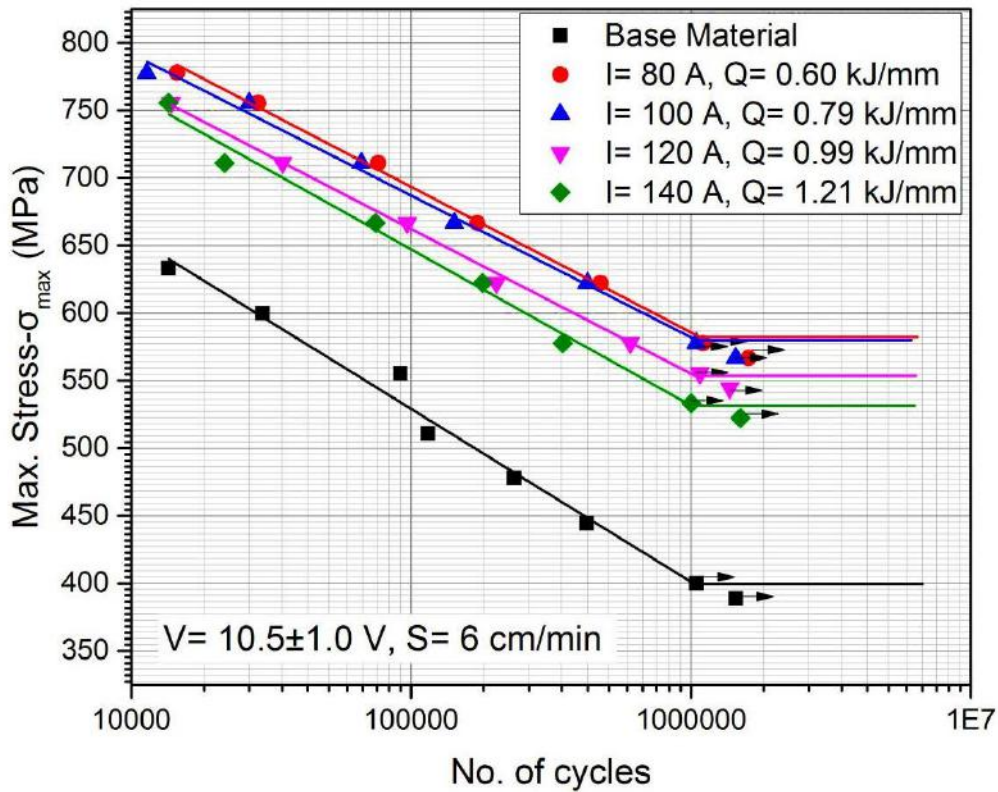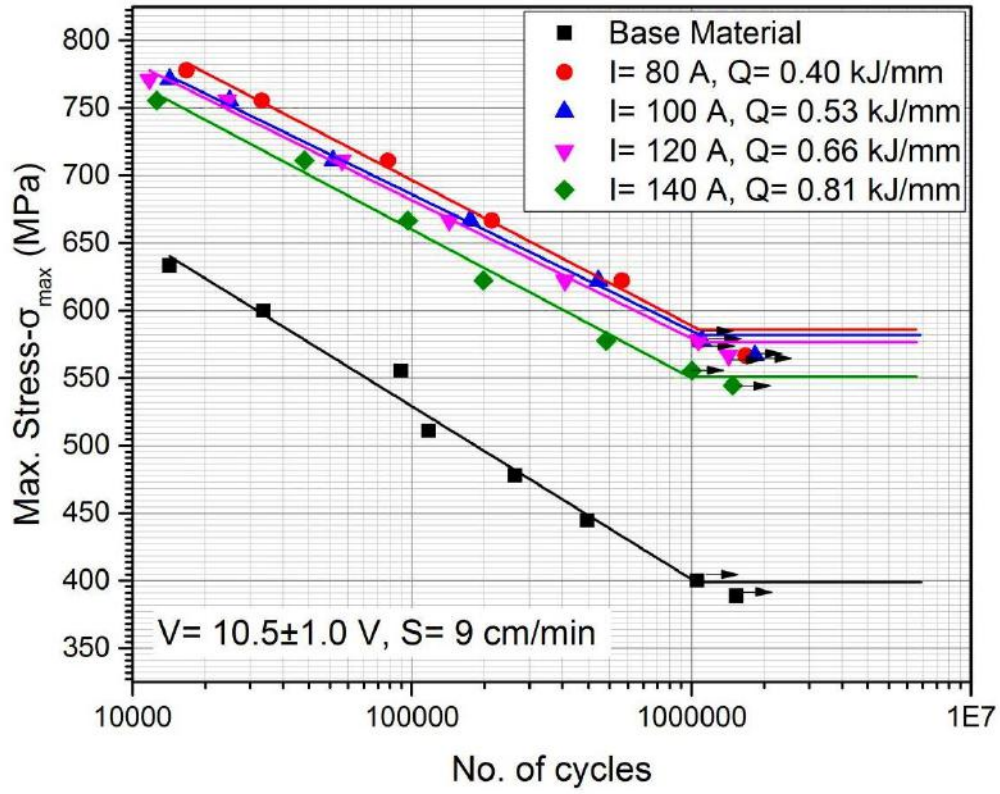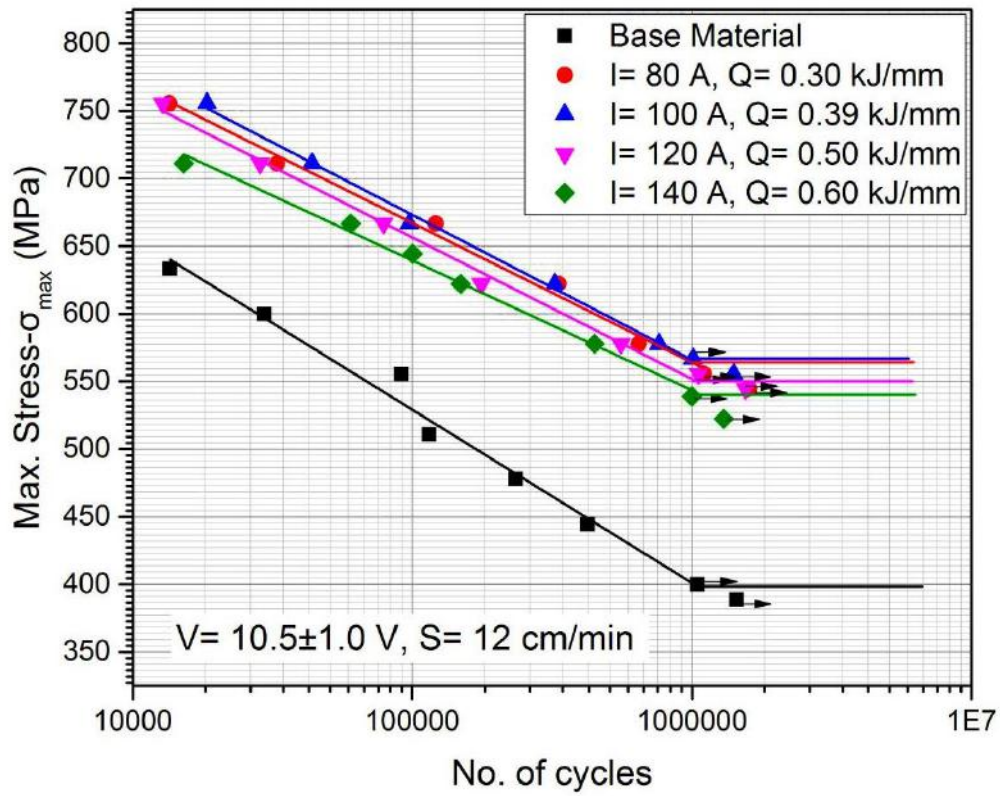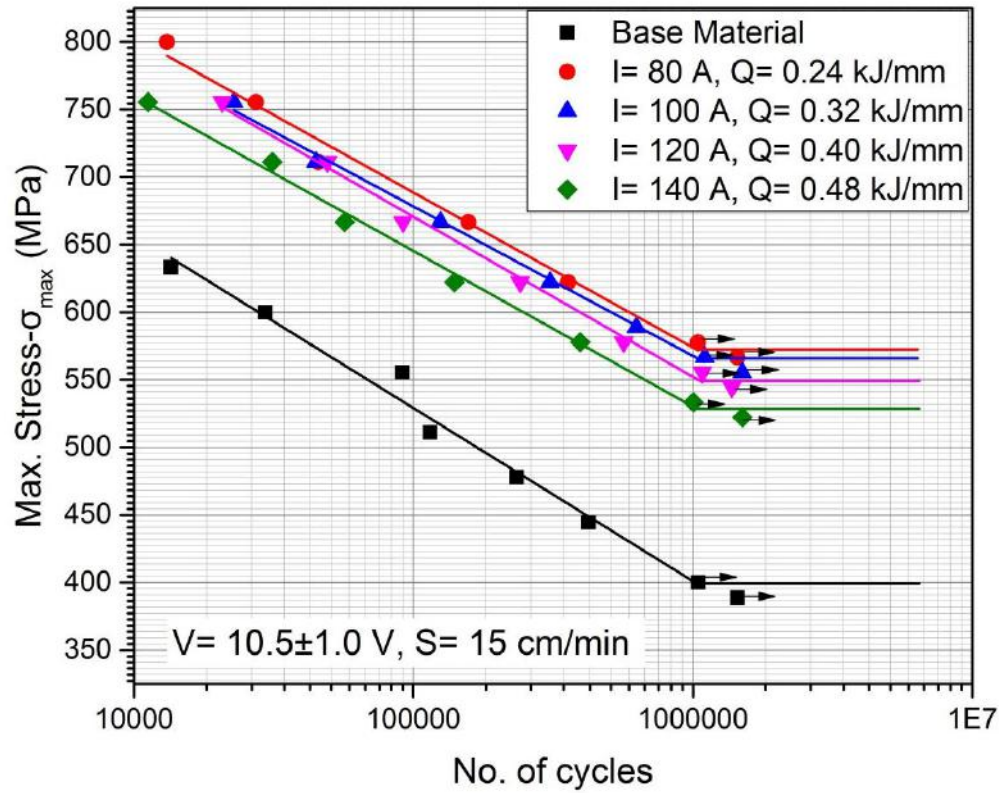
(d)

Fig. 5.34 At given arc travel speed of (a) 6, (b) 9, (c) 12 and (d) 15 cm/min the nature of S-N curve of surface modified steel prepared at different heat inputs varied by changing the arcing current compared to the same of unmodified base metal.

5.2.8.2 Under bending load

The fatigue life of the base material and modified surface under bending load has been shown in figs. 5.35 (a-d). The figure shows that the fatigue life of modified surface has been significantly decreased under bending load. It is observed that at the heat input in the range of 0.24 to 0.32 kJ/mm the endurance limit decreases from σ_{max} of 480 to 405 ± 5 MPa as compared to that of the base metal. Fig. 5.35 (a-d) also depicts that with the increase in heat input from 0.24 kJ/mm to 1.21 kJ/mm, there is an improvement in fatigue life of the substrate from σ_{max} of 400 MPa to 500 MPa. Such improvement is in agreement to the flexural strength and microstructural changes under the surface modification as previously discussed. At a constant arc voltage and arc travel speed of 10.5 ± 1.0 V and 6 cm/min respectively, an approximately same endurance limit with respect to the base material of σ_{max} of 480 MPa is observed when the heat input lies in the range of 0.99 - 1.21 kJ/mm, but there is reduction in finite fatigue life as shown in fig. 5.35 (a). Hard phase transformation in the matrix is attributed to change in slope of S-N curve, which is reduced from that of the base metal. Investigation on residual stresses states that the tensile nature of residual stress is present in the modified surface

113

upto a depth of about 0.20 mm. This stress is attributed to increase in the resolved stress of tensile nature which may initiate premature cracking and forms a critical crack.

(a)

(b)

114
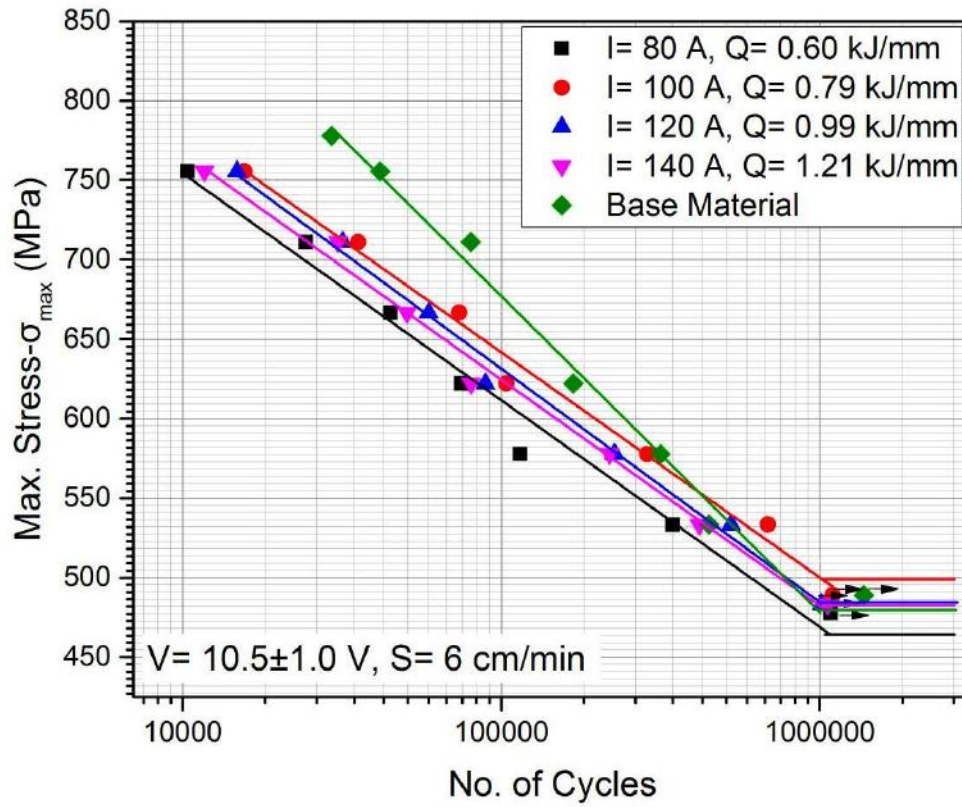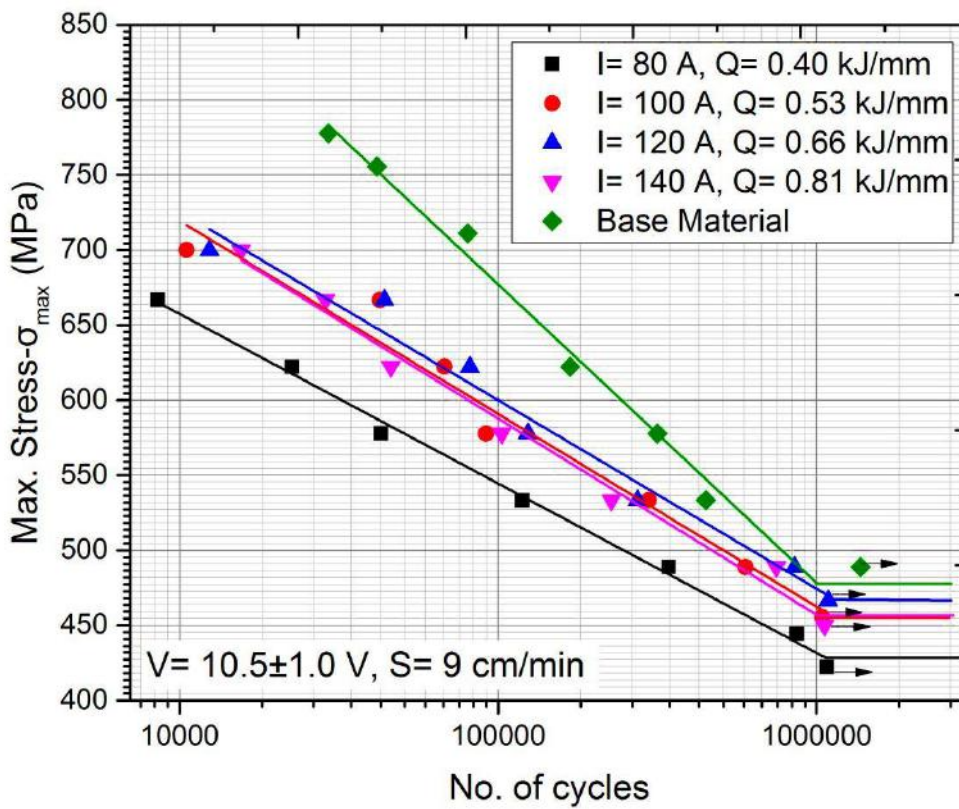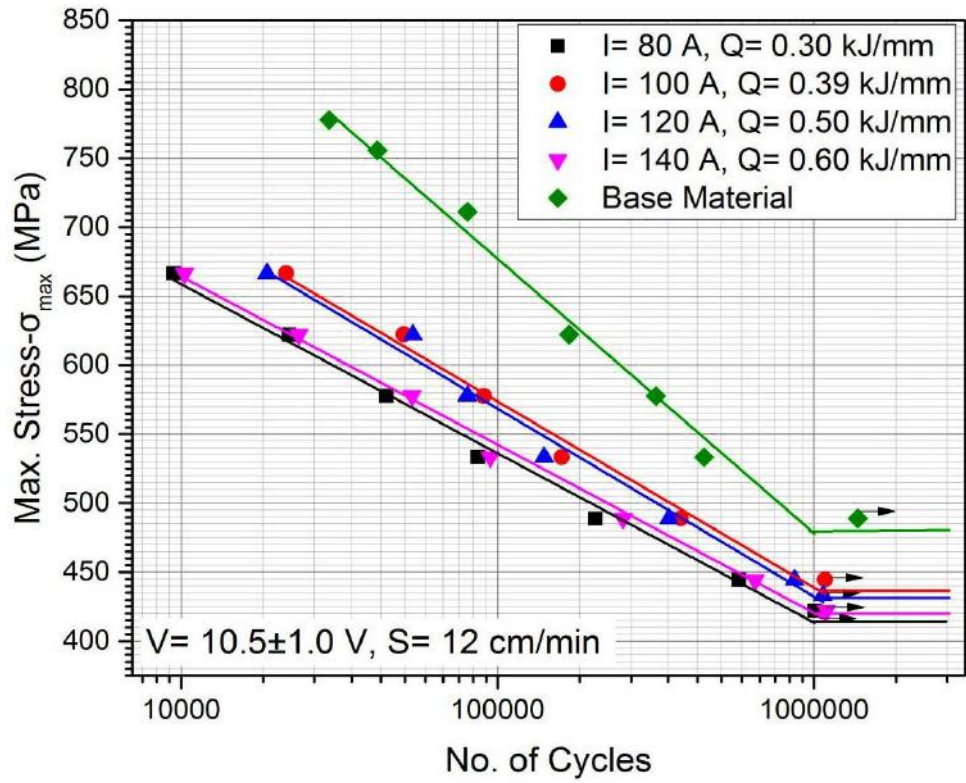
(c)
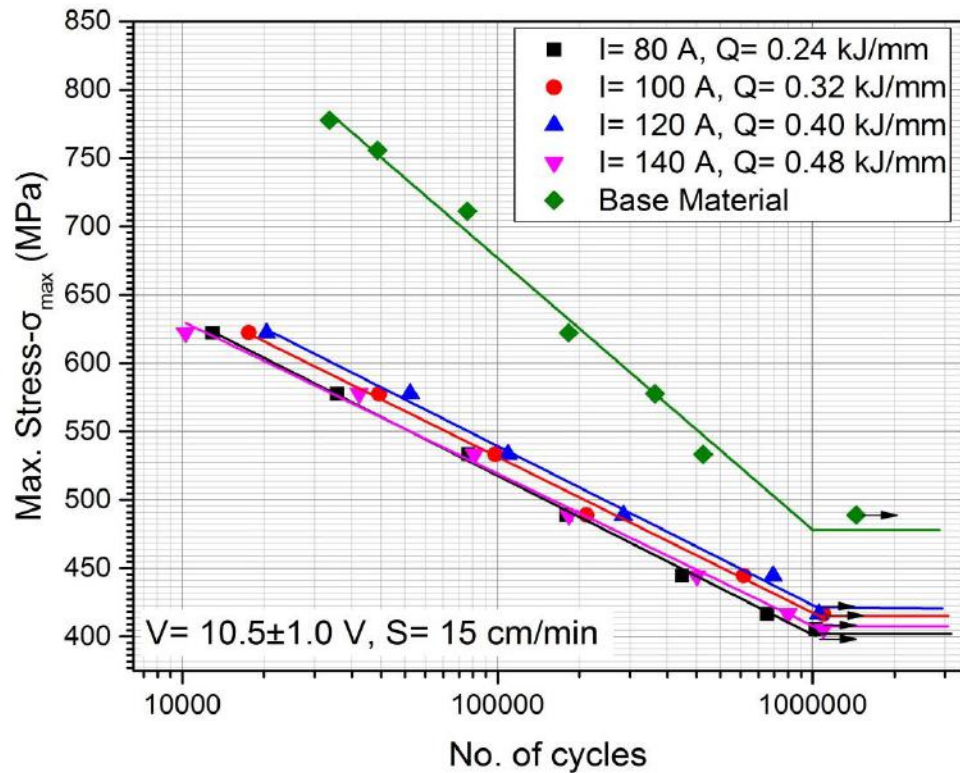
(d)

Fig. 5.35   At given arc travel speed of (a) 6, (b) 9, (c) 12 and (d) 15 cm/min the nature of S-N curve under bending load of surface modified steel prepared at varied heat inputs obtained by changing the arcing current as compared to the same of unmodified base metal.

115

5.2.9 Summary

Basic understandings of the effect of single-pass C-TIG arcing process have been revealed in this study in terms of modified zone geometry like depth of penetration, width of fusion zone, width of HAZ and the fusion zone area. The studies on characteristics of the variation in arcing parameters (Arcing current and travel speed) and their effect on heat input provides the effective utilization of the C-TIG arcing process for surface modification of materials The precise control of heat developed in fused zone by using appropriate I and S in C-TIG arcing process effectively increases the depth of penetration, bead width and fusion zone area.

The effect of arcing parameters of single-pass C-TIG arcing process on isotherms and thermal cycle is predicted and analyzed. Analytical estimation of thermal characteristics of surface modification by TIG arcing process can provide effective control of desired properties of surface modified substrate. Analytical approximation of the depth of the fused modified zone and intercritical cooling rate lies well within 3–5% variation from the measured value.

The microstructure of FZ and HAZ can be varied significantly with respect to Ω and operating parameters in single-pass C-TIG arcing process. The microstructure of the FZ and HAZ is primarily dictated by the isotherm, heating and cooling rate. The metallurgical characteristics of the modified fused and heat affected zones of the base metal are governed by the proportionate transformation of martensite, bainite and pro eutectoid ferrite in the matrix.

The effect of single-pass C-TIG arcing process has been revealed in this study in terms of hardness of FZ and HAZ along with the distribution of hardness within them. It is observed that the variation of arcing and travel speed (I and S) in C-TIG arcing process significantly improves the hardness of the surface (FZ) with a backup of refined and comparatively lower hardness of HAZ. However, it is interestingly observed that the use of C-TIG arcing process gives relatively higher hardness in the fusion zone and heat affected zone at relatively lower Ω. The precise control of heat development in fused zone by using appropriate process parameter of C-TIG arcing process effectively increases the hardness of FZ and HAZ along with increase in area of modified zone. As compared to base material the hardness of the FZ and HAZ is increased up to 175 ± 20 % and 50 ± 25 % respectively.

Tensile and flexural properties can be significantly affected by the applying of single-pass C-TIG arcing process over the AISI 4340 steel substrate. At an appropriate heat input of TIG arcing process can improve the tensile properties such as yield strength and ultimate strength in the order of 600 and 900 MPa respectively, but the ductility and toughness was decreased to 6 % and 38 J/mm^3 respectively. These tensile properties significantly affect the

fatigue properties under tensile loading. The fatigue properties are significantly improved by enhancement of the endurance limit of its fatigue failure raising σ_{max} from about 530 to 577 MPa depending upon the TIG arcing process parameters. It indicates that the surface modification by TIG arcing processing can improve fatigue performance of the base material of the order of 32 - 45 % as compared to that of the base material. Similarly, in the case of flexural test of the modified surface, it was observed that the flexural yield and maximum strength can be improved by using high heat input above 0.60 kJ/mm. However, in case of low heat input below 0.60 kJ/mm the flexural properties are decreased. Thus, the fatigue properties of modified surface under bending load were reduced at low heat input and it may be recovered by increasing the heat input.

5.3 Multi-pass C-TIG arcing process

This section presents the observation on multi-pass surface modification of AISI 4340 steel plate using C-TIG arcing process over a relatively large surface area of the substrate in order to analyze the effectiveness of the process for industrial applications. The optimum TIG arcing parameters for improvement of surface properties obtained in single-pass TIG arcing process were used for multi-pass processing with 50% overlap to maintain a uniform depth of modification. A similar extent of overlap was also described by [Lakhkar et al., 2008] for laser surface modification. During multi-pass arcing, the inter-pass temperature was kept at 140 – 180 ^{o}C. The effect of multi-pass treatment using C-TIG arcing process is studied and compared in terms of microstructural features and hardness distribution in its different thermally affected regions. Further mechanical properties such as tensile and three point bend test are examined at various process parameters. The effect of microstructural modification and residual stress on fatigue properties under uniaxial tensile loading and bending load are studied.

Optical macrograph of modified surface and its cross section prepared by applying multi-pass C-TIG arcing processes at the different heat input raised by changing arcing current from 80 A to 140 A, at constant arc voltage and arc travel speed of 10.5 ± 1.0 V and 12 cm/min, respectively, is shown in fig. 5.36, Thermal behaviour of the multi-pass C-TIG arcing processes and their influence on the respective geometrical, microstructural and mechanical characteristics of the modified surface are discussed below.

Arcing Current (A)	Heat Input (kJ/mm)	Surface appearance (Scale in mm)	Macro photograph of transverse section (Scale in mm)
80 A	0.30		
100 A	0.39		
120 A	0.50		
140 A	0.60		

Fig. 5.36   Typical appearance of modified surface and its transverse section prepared by multi-pass C-TIG arcing at different currents at given arc voltage and arc travel speed of 10.5 ± 1.0 V and 12 cm/min respectively.

5.3.1 Thermal Cycle

Typical thermal cycle of FZ and HAZ of modified surface of the multi-pass C-TIG arcing carried out at the heat input of 0.39 and 0.60 kJ/mm (at I= 100 and 140 A, respectively) has been shown in figs. 5.37 (a) and (b), respectively, where the arc voltage and arc travel speed were kept constant as 10.5 ± 1.0 V and 12 cm/min respectively. The thermocouple was inserted at the third pass of the process so that it can show the back tempering effect of the subsequent passes no. 4, 5, 6 and 7 on FZ and HAZ as shown in figs. 5.37 (a) and (b). The figures depict that the third pass of C-TIG arcing rise the temperature of the FZ and HAZ in the range of 1400 to 1700 ^{o}C and 900 to 1150 ^{o}C respectively. Whereas the forth pass rise the temperature of these zones in the range of 800 to 1000 ^{o}C which confirms the back tempering effect during multi-pass C-TIG arcing process. Thermal characteristics of the subsequent FZ and HAZ of multi-pass arcing introduces back-tempering up to certain extent in the relevant

zones (typically shown in fig. 5.37 (b)) of the former modified matrix lying in the temperature range of 800-1000 °C [Cordovilla et al., 2016]..
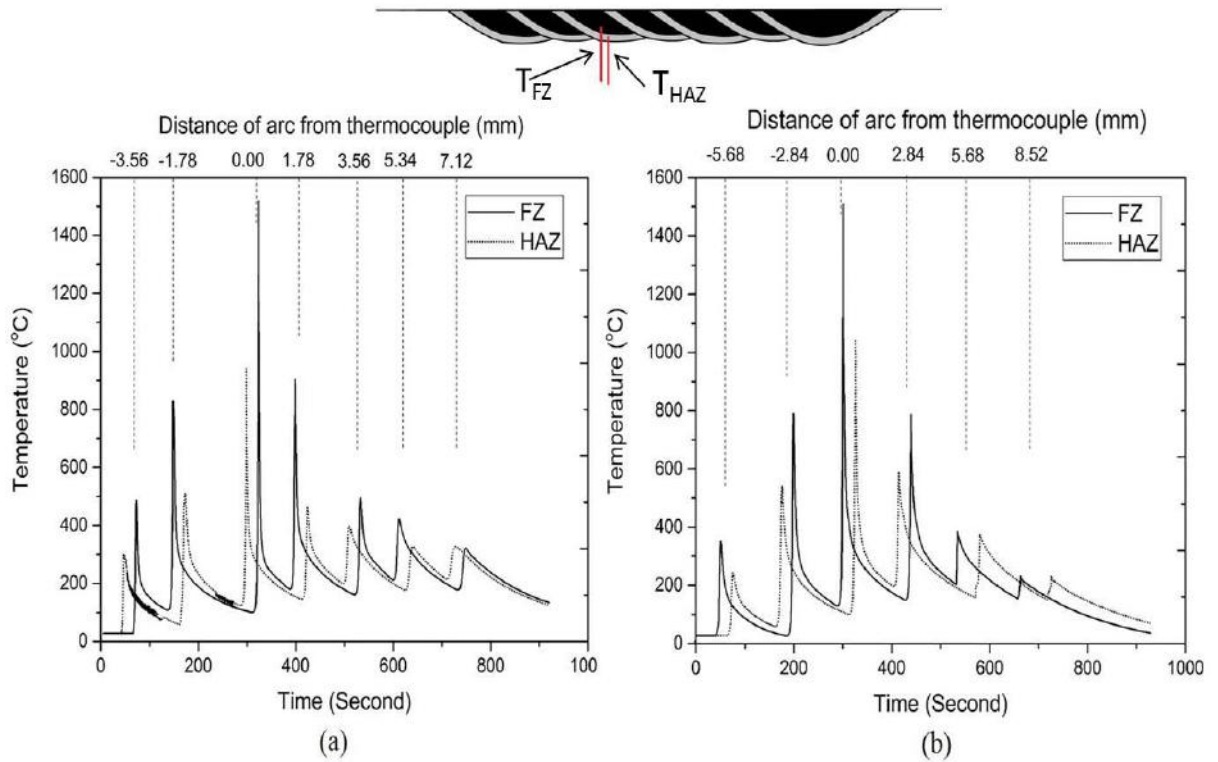
Fig. 5.37   Thermal cycle of FZ and HAZ during multi-pass C-TIG arcing at (a) 0.39 kJ/mm (I=100 A), and (b) 0.60 kJ/mm (I= 140 A).

5.3.2 Microstructural Studies

The observation under optical microscopy on the microstructure of the modified matrix prepared by multi-pass C-TIG arcing clearly reveals five different zones as shown in figs. 5.38 (i-v) and 5.39 (i-v), where the process was operated at the heat inputs of 0.39 (at I= 100 A) and 0.60 kJ/mm (at I= 140 A), respectively, at a given arc travel speed and arc voltage of 12 cm/min and 10.5 ± 1.0 V, respectively. The notations (i) to (v) in the figures show distinctly different microstructures of different zones of the modified matrix as follows (i) original FZ, (ii) reheat refined FZ, (iii) initial HAZ of base metal, (iv) double reheat refined fusion zone and (v) reheat refined HAZ of base metal, respectively. The last pass of TIG arcing shows the microstructure of the initial fused matrix and its HAZ while all areas of the FZ and HAZ of previous passes are suitably tempered by the subsequent passes of TIG arcing. This has exposed the matrix in the temperature range of 700 – 1300° C of AC1 and AC3 austenitizing temperature range respectively, as shown in fig. 5.37. In agreement to this phenomenon, the relatively large patches of martensite of the initial fusion zone (figs. 5.38 (i) and 5.39 (i)) becomes significantly refined by tempering (figs. 5.38 (ii) and 5.39 (ii)) followed by double reheat refined (figs. 5.38 (iv) and 5.39 (iv)) due to reheating by the subsequent arcing passes. It

119

was also noted that the microstructure of the double reheat refined FZ is comparatively coarser (figs. 5.38 (iv) and 5.39 (iv)) than that of the FZ initially refined by tempering (figs. 5.38 (ii) and 5.39 (ii)). The microstructure of the initial HAZ primarily reveals the presence of bainite and fine pearlite along with patches of proeutectoid ferrite (figs. 5.38 (iii) and fig. 5.39 (iii)) where the predominance of bainite is relatively more pronounced at the lower heat input of 0.39 kJ/mm (Fig. 5.38 (iii)) due to its higher cooling rate (fig. 5.15). The morphology of the proeutectoid ferrite patches becomes relatively coarser at the higher heat input of 0.60 kJ/mm (fig. 5.39 (iii)) resulting from a slower cooling rate. Irrespective of the magnitude of arcing current, the morphology of various phases of the HAZ becomes considerably refined in the reheated HAZ, as shown in figs. 5.38 (v) and 5.39 (v). However, the morphology of various phases of the FZ and HAZ was found to be significantly coarser in the microstructures presented in fig. 5.39 compared to those shown in fig. 5.38, primarily due to the use of higher heat input at a higher arcing current (140 A) in the former case.
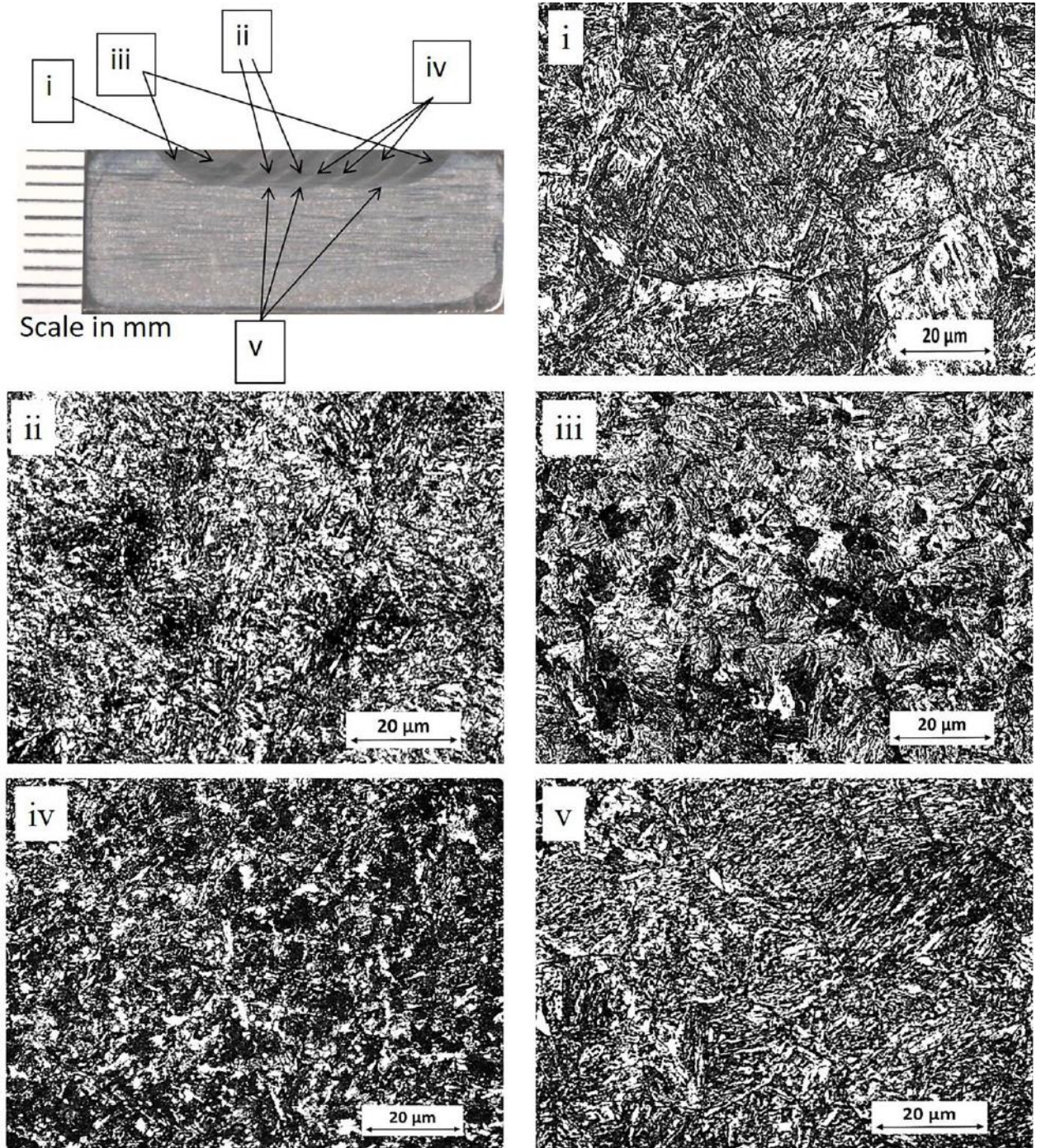
Fig. 5.38 Microstructure of different locations of modification at a given heat input of 0.39 kJ/mm, where arc travel speed, voltage and current are kept at 12 cm/min, 10.5 ± 1.0 V and 100 A respectively (i) initial FZ, (ii) reheat refined FZ, (iii) initial HAZ of base metal, (iv) double reheat refined fusion zone and (v) reheat refined HAZ of base metal in modified surface prepared by multi-pass TIG arcing.
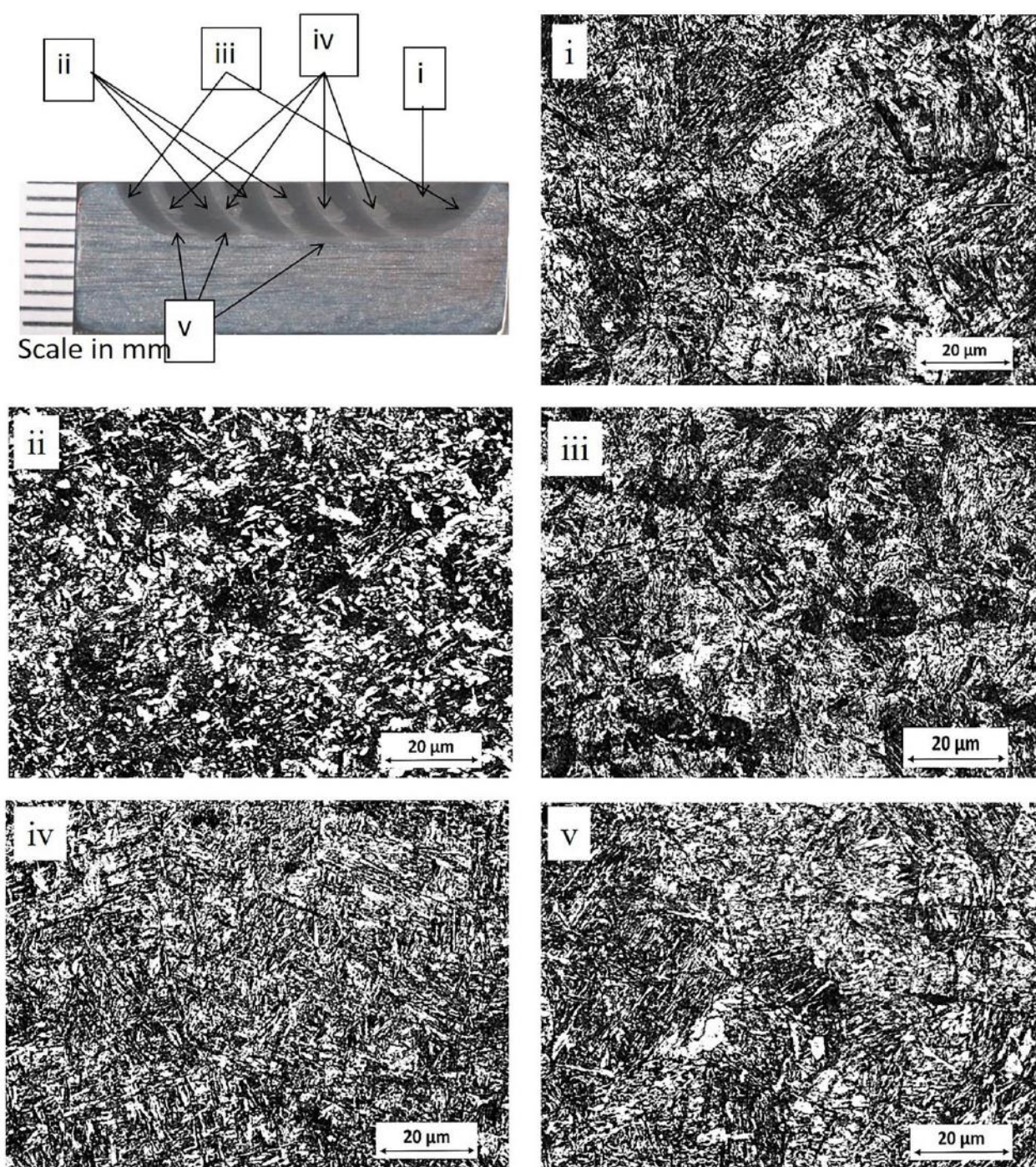
Fig. 5.39 Microstructure of different locations of modification at a given heat input of 0.60 kJ/mm, where arc travel speed, voltage and current are kept at 12 cm/min, 10.5 ± 1.0 V and 140 A respectively (i) initial FZ, (ii) reheat refined FZ, (iii) initial HAZ of base metal, (iv) double reheat refined fusion zone and (v) reheat refined HAZ of base metal in modified surface prepared by multi-pass TIG arcing.

5.3.3 Hardness Study

At a given arc voltage of 10.5 ± 1.0 V, the effect of varying arc speed and arcing current from 12 to 15 cm/min and 80 A to 140 A respectively, on the hardness of stabilized (tempered) and non-stabilized zone in the modified region produced by multi-pass arcing is shown in figs. 5.40 and 5.41 respectively. Hardness of the modified surface raised by multi-pass TIG arcing is found to be relatively low as compared to the hardness observed in the surface modified by the single-pass arcing. This is primarily happened due to the tempering of microstructure of the previous pass by the distribution of isotherm and thermal cycle at certain location established by the subsequent passes of arcing. Only the last pass contains untendered zone which can be realized from the microstructure as shown in figs. 5.38 and 5.39 and discussed above.

At the arcing current and arc travel speed of 80 A and 15 cm/min, with respect to maximum effect of multi-pass C-TIG arcing process on matrix hardness, its distribution in the matrix is shown in fig. 5.41. The figure shows the typical distribution of hardness at different thermally affected zones of the matrix as typically referred in fig. 5.38. The second pass changes the characteristics of FZ and HAZ of the first pass due to tempering effect. The second pass creates the reheated and reheats refined FZ over the FZ of the first pass. The similar zones are created by the third, fourth and so on passes in the FZ and HAZ of the previous passes and the hardness of this zone was observed as 553 ± 8 HV. Further double reheat refined zone was observed as discussed in the microstructural analysis and the hardness of this zone was observed as 525 ± 8 HV. So the area under the first, second, third and up to second last passes may be recognized as stabilized modified zone and area under the last pass as unstabelized region. The hardness of the unstabelized regions is observed as 745 ± 10 HV which is similar to the hardness of single-pass C-TIG arcing.
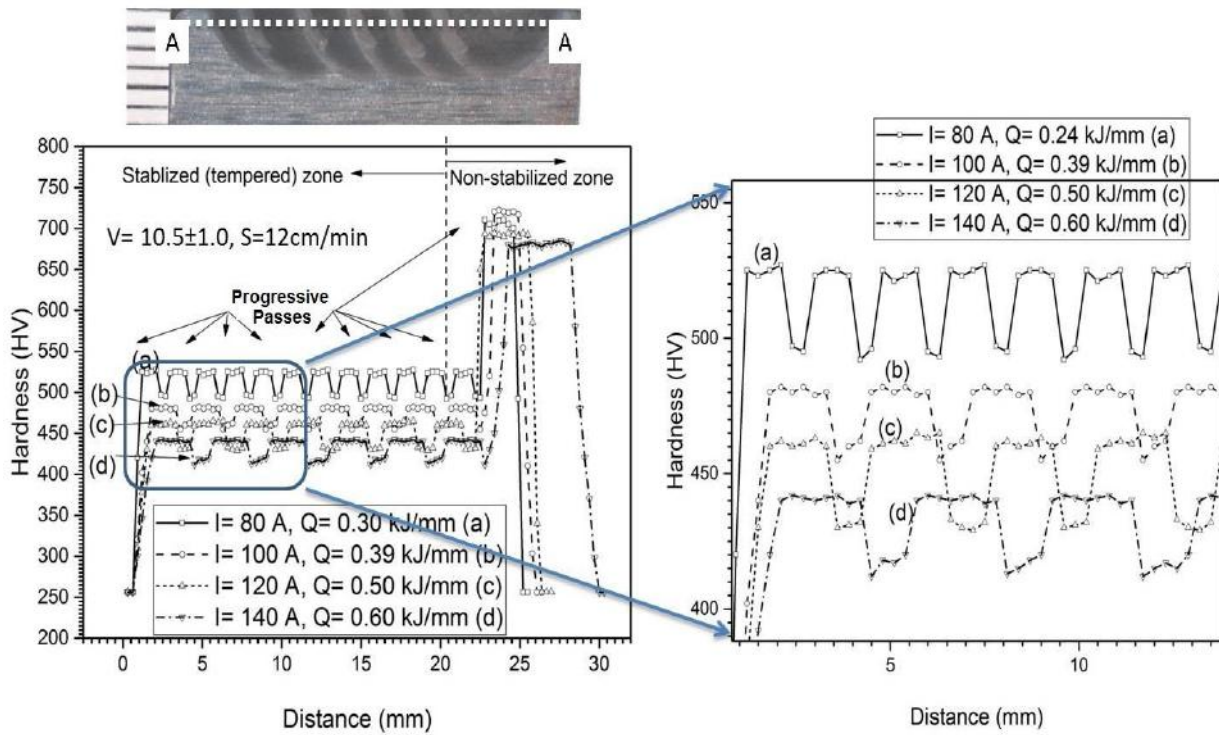
Fig. 5.40   Hardness distribution in multi-pass C-TIG modified surface prepared at heat input varied from 0.30 to 0.60 kJ/mm by changing arcing current from 80 to 140 A, at constant arc voltage and arc travel speed of 10.5±1.0 V and 12 cm/min, respectively.
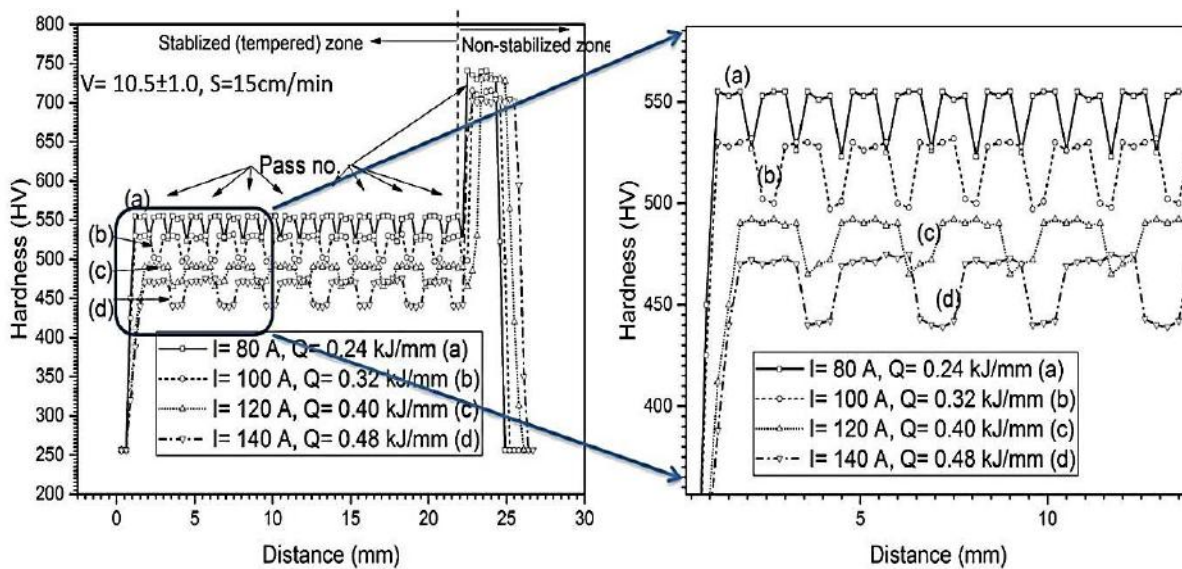
Fig. 5.41   Hardness distribution in multi-pass C-TIG modified surface prepared at heat input varied from 0.24 to 0.48 kJ/mm by changing arcing current from 80 to 140 A, at constant arc voltage and arc travel speed of 10.5±1.0 V and 15 cm/min, respectively.

124

5.3.4 Tensile properties

The average stress versus strain characteristics of the base metal and the surface modified substrate prepared at the arcing currents varying in the range of 80-140 A employed at the arc travel speeds of 12 and 15 cm/min is shown in figs. 5.42 (a) and (b), respectively, where the arc voltage is kept constant at 10.5 ± 1.0 V. The figures have illustrated that a significant improvement with respect to base metal was observed in yield strength and maximum strength of the order of 725 ± 45 MPa (70 to 110% improvement) and 960 ± 65 MPa (22 to 47% improvement) after multi-pass surface modification. However, toughness and ductility of the modified surface was relatively decreased with respect to those of the base metal due to hard phase transformation. Surface modification at an arcing current, arc voltage and arc travel speed of 100 A, 10.5 ± 1.0 V and 15 cm/mm respectively, gives maximum enhancement of tensile yield and ultimate strength of about 110 % and 47 % respectively as compared to that of the base metal as shown in fig. 5.42 (b). This may have primarily happened because the microstructure of the matrix of optimum reheat-refined modified zone is primarily consisting of lath martensite, which results the significant increase in tensile properties. The fig 5.42 (a) shows that the tensile yield strength and ultimate tensile strength of the modified surface increases with the increase of arcing current up to 100 A (heat input of 0.39 kJ/mm) followed by a decrease with further increase of arcing current or heat input at constant arc voltage and arc travel speed. Thus, it may be assumed that it is basically a function of heat input, which gives rise to a criticality in favourable phase transformation, which controls the tensile properties of the matrix.

Such behaviour is also clearly revealed in figs. 5.43 (a-d) where the yield strength, ultimate tensile strength, toughness and ductility (% strain) of the surface modified substrate are found to be significantly affected as a function of arcing current and travel speed. The figs. 5.43 (a) and (b) depict that the yield strength and ultimate tensile strength are significantly increased due to decrease in heat input by increasing travel speed instead of decrease of arcing current. At this juncture, toughness and ductility was decreased significantly by increasing arc travel speed from 12 to 15 cm/min, where other parameters such as arcing current and voltage are kept as shown in figs. 5.43 (c) and (d).
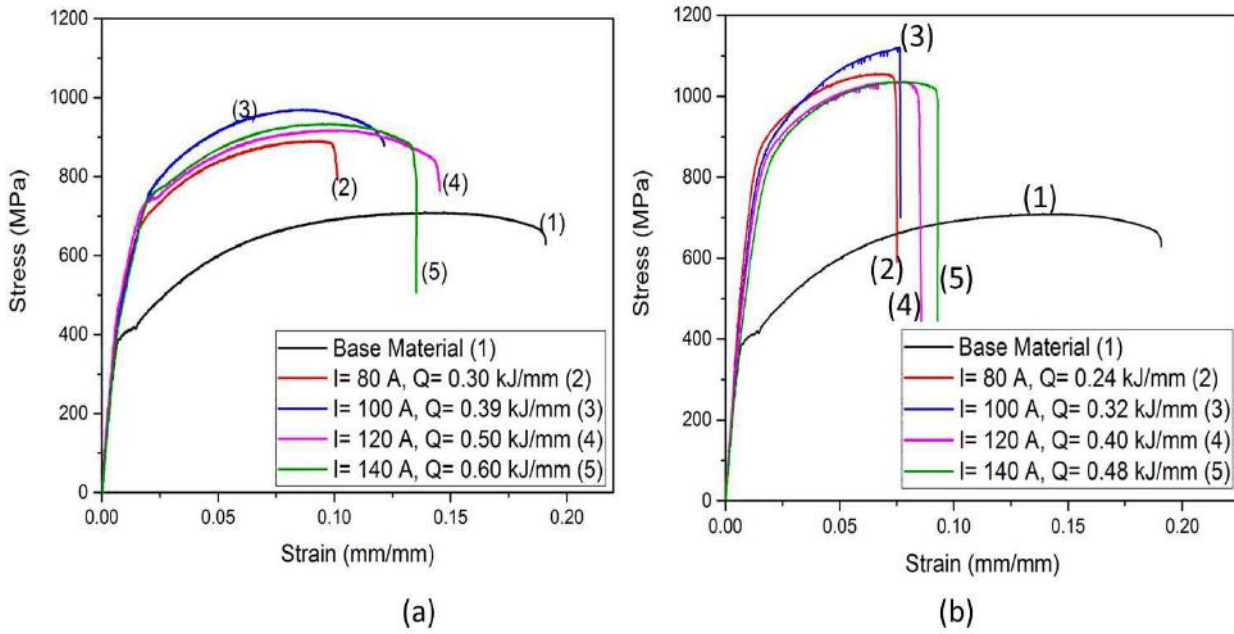
Fig. 5.42   Tensile stress-strain curve of surface modified AISI 4340 structural steel produced at different heat input obtained by varying arc current (I) at different arc speeds (S) of (a) 12 and (b) 15 cm/min, where the arc voltage of 10.5±1.0 V is kept constant.
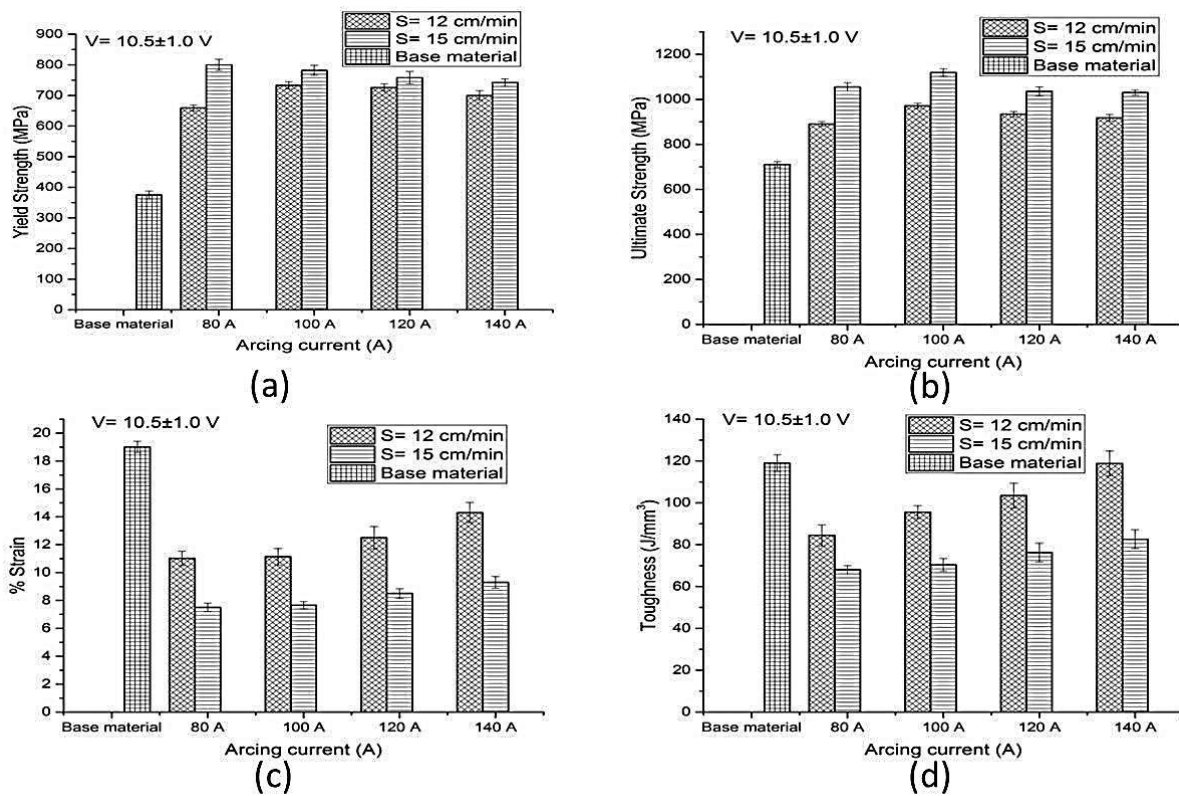
Fig. 5.43   At different arcing currents effect of arc travel speed on a) yield strength, b) ultimate tensile strength, c) strain and d) toughness observed during tensile test of the surface modified AISI 4340 structural steel produced by multi-pass C-TIG arcing.

126

In this context it is observed that at a given close range of heat input the increase of arc travel speed beyond 12 cm/min significantly affects the mechanical properties of the matrix by increasing the yield strength and UTS along with relative decrease in strain and toughness as shown in figs. 5.44 (a-d). In consideration of the results presented in figs. 5.42 and 5.43, it appears that the heat input in the range of 0.30 – 0.32 kJ/mm gives an optimum combination of tensile properties assumed as relatively high YS, UTS, ductility (strain%) and toughness that can be achieved by C-TIG arcing process of AISI 4340 steel. At a given arc voltage of 10.5 ± 1.0 V, keeping the arc travel speed at 12-15 cm/min with the heat input maintained in the range of 0.3 to 0.32 kJ/mm by adjusting the arcing current within 80 to 100 A gives the YS, UTS, ductility and toughness in the range of about 670 - 742 MPa, 925 - 1122 MPa, 7.5 - 11.2% and 70 - 82 J/mm3 respectively as shown in figs. 5.44 (a-d). Such changes in tensile properties show a strong agreement to formation of lath martensite along with banite and fine pearlite with patches of proeutectoid ferrite in the modified matrix of the AISI 4340 steel produced by multipass C-TIG arcing process.

(a)

(b)

127
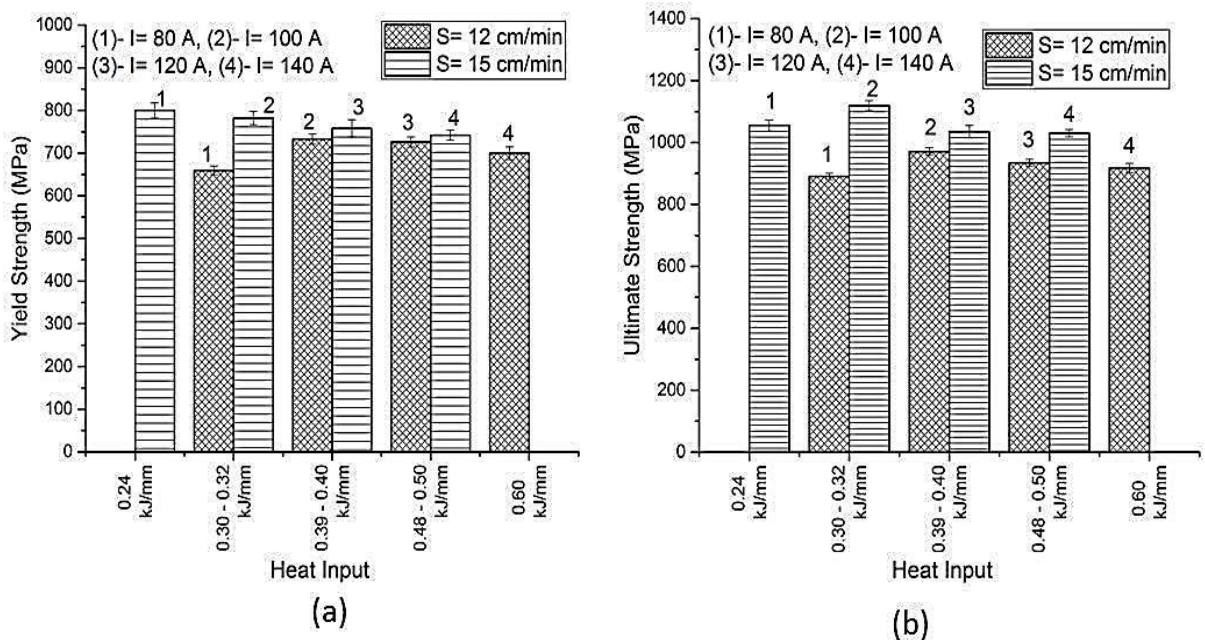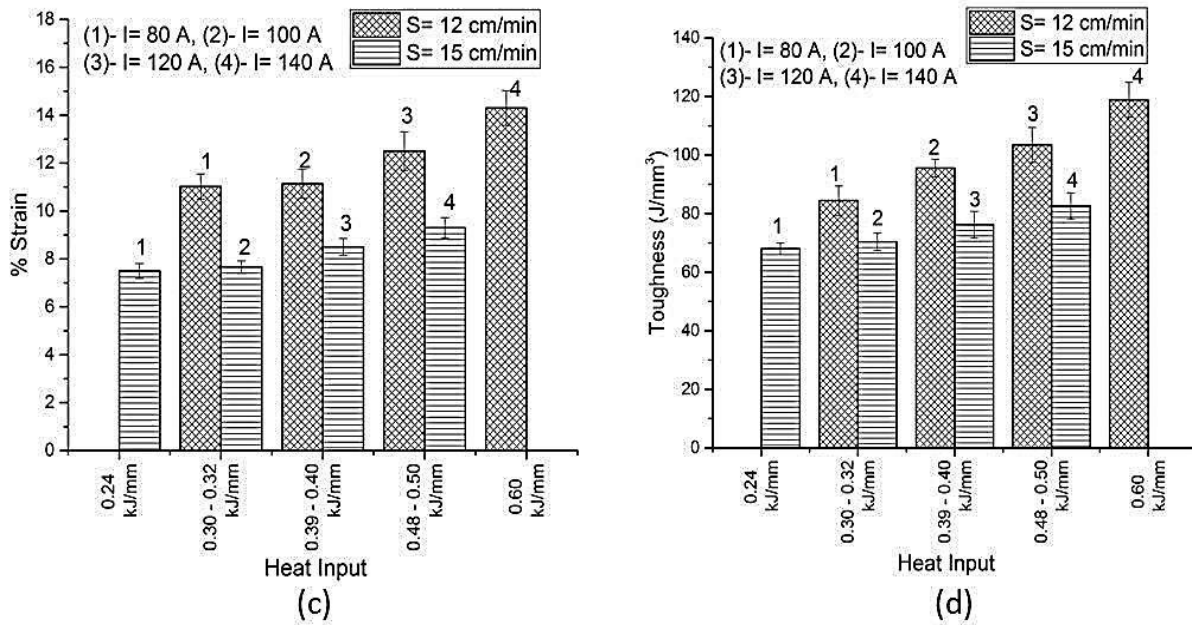
Fig. 5.44   At a given close range of heat input effect of arc travel speed on a) yield strength, b) ultimate tensile strength, c) strain and d) toughness observed during tensile test of the multi-pass C-TIG arcing modified steel.

5.3.5 Three point bend properties

The average flexural stress versus extension characteristics of the base metal and the modified surface prepared at different arcing current varying in the range of 80 - 140 A employed at the arc travel speeds of 12 and 15 cm/min is shown in figs. 5.45 (a) and (b), respectively, where the arc voltage is kept constant at 10.5 ± 1.0 V. It is also noted in fig. 5.45 (a) and (b) that the stress versus extension curve becomes practically flat after bending up to an angle of about 80° and as such the test was withdrawn at this stage. The fig. 5.45 (a) illustrates that the increase in heat input from 0.30 to 0.39 kJ/mm by changing arcing current from 80 to 100 A significantly increases the flexural characteristics (flexural yield strength, maximum strength and extension) of the modified matrix. However, the further increase of heat input to 0.50 and 0.60 kJ/mm by changing the arcing current to 120 and 140 A respectively reduces the flexural extension considerably. Similar behaviour was observed in case of arcing speed of 15 cm/min, where increase in arcing current beyond 100 A reduce the flexural extension as shown in fig. 5.45 (b). So, it may be concluded that the use of a low arcing current (< 120 A) or a lower arc travel speed at a given arcing current appreciably increases the extension and deformation with a greater bending angle. Thus, it is assumed that the bend properties of the matrix are basically a function of heat input, which gives rise to a criticality based upon favourable phase transformation.

Such behaviour is also clearly revealed in figs. 5.46 (a) and (b) where the yield strength and flexural stress respectively of the modified surface are found to vary significantly

as a function of arcing current and arc travel speed. In consideration of the results presented in figs. 5.45 and 5.46, it appears that maintaining the heat input in the range of 0.24 – 0.39 kJ/mm of C-TIG arcing process gives an optimum combination of flexural properties as relatively high YS, max strength and flexural extension of AISI 4340 steel as clearly presented in fig. 5.47 (a) and (b). At a given arc voltage of 10.5 ± 1.0 V keeping the arc travel speed at 12 - 15 cm/min with heat input maintained in the range of 0.24 to 0.39 kJ/mm by adjusting the arcing current within 80 to 100 A gives the YS, max strength and flexural extension in the range of about 700 - 872 MPa, 1390 - 1522 MPa and 35 mm respectively as shown in fig. 5.47 (a) and (b).
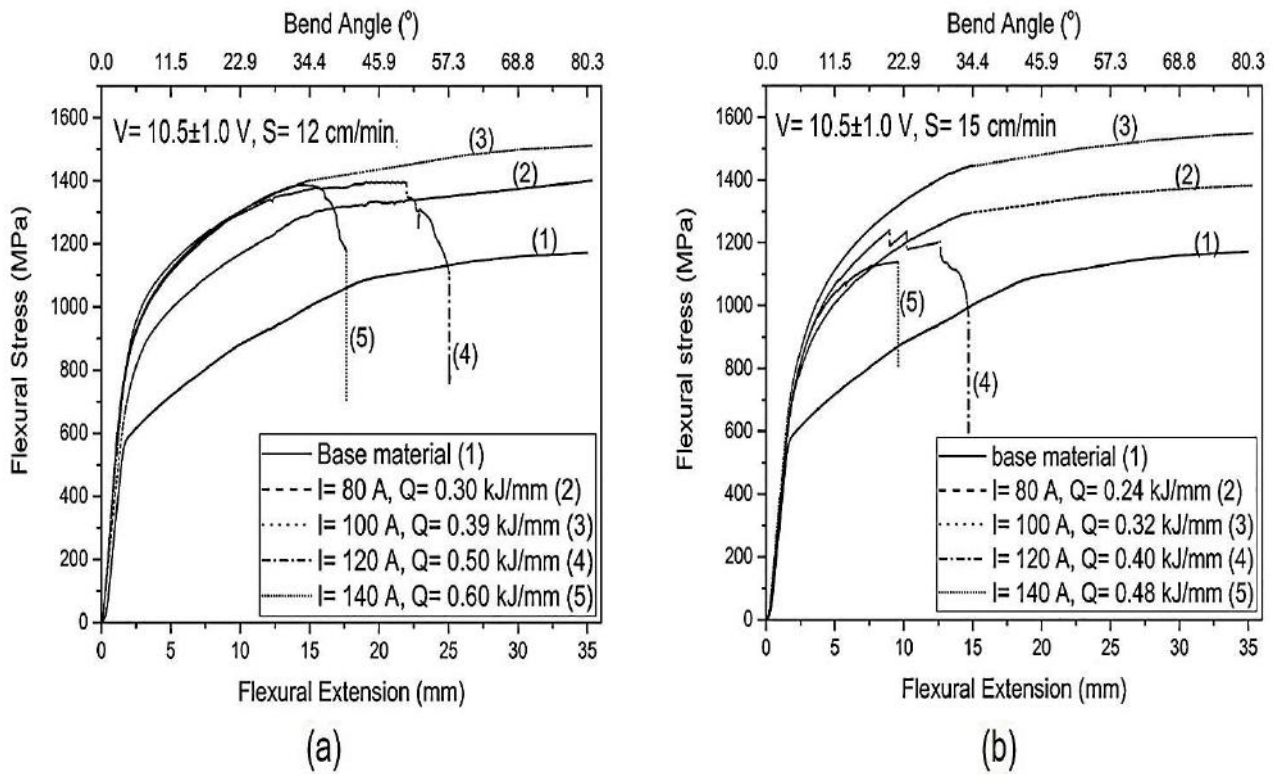
Fig. 5.45 Flexural stress-extension diagram of surface modified AISI 4340 structural steel produced at different heat inputs obtained by varying arc current (I) at different arc speeds (S) of (a) 12 and (b) 15 cm/min, where the arc voltage of 10.5 ± 1.0 V is kept constant.
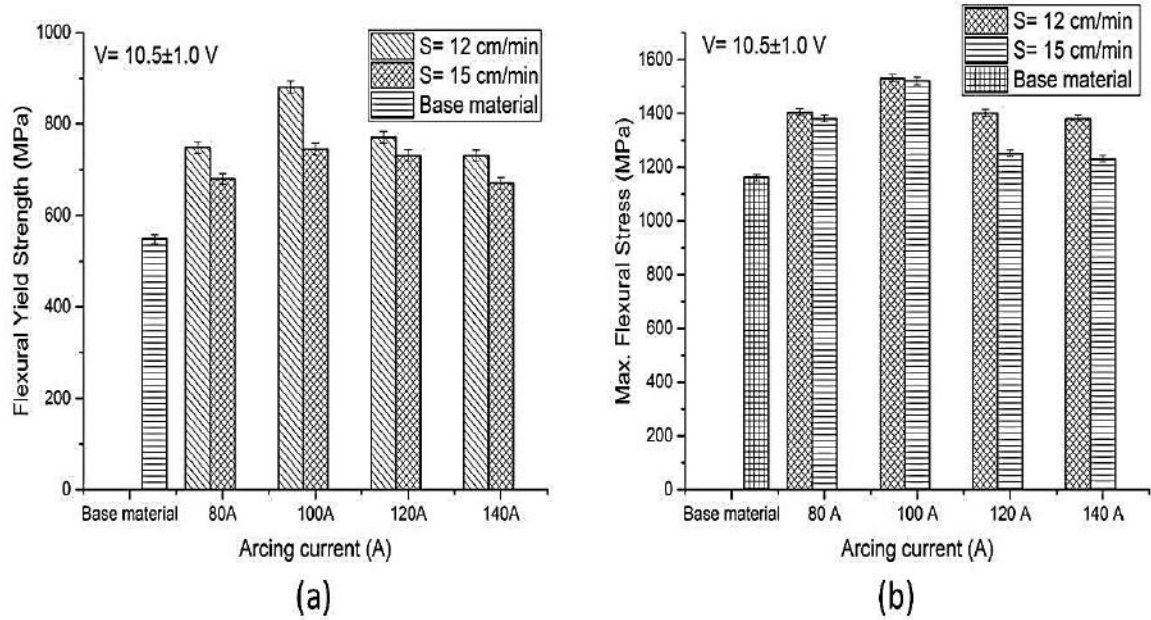
Fig. 5.46   At different arcing currents effect of arc travel speed on (a) flexural yield strength, and (b) flexural maximum stress observed during three point bend test of the modified steel surface.
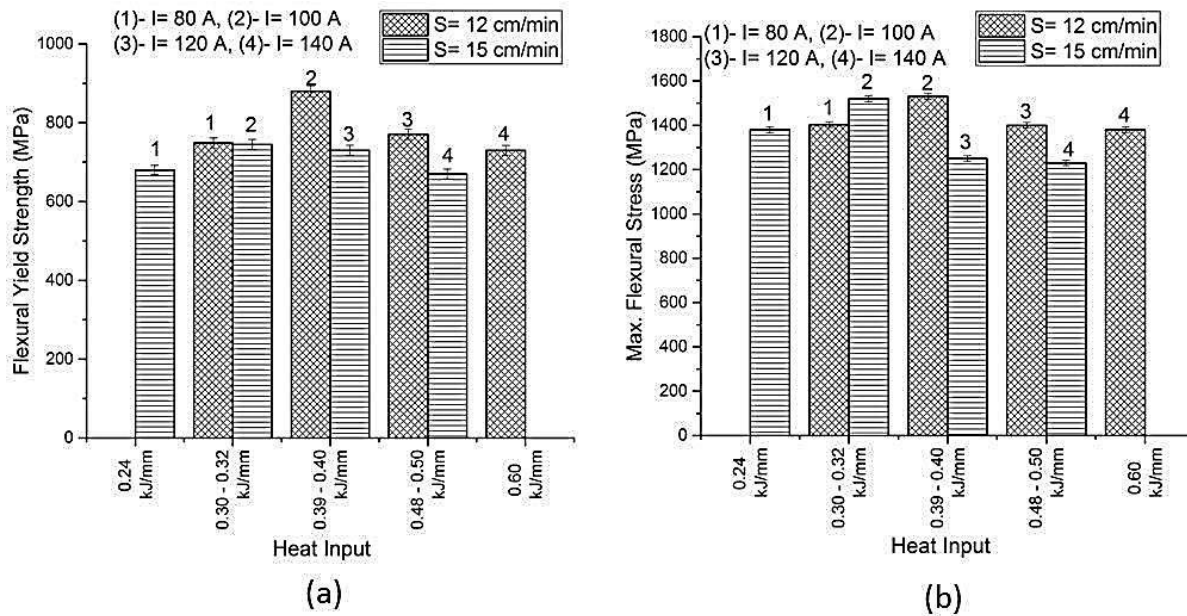
Fig. 5.47   At a given close range of heat input effect of arc travel speed on (a) yield strength, (b) ultimate tensile strength, (c) strain and (d) toughness observed during bend test of the modified steel surface prepared by multi-pass C-TIG arcing process.

The SEM studies on the fractured surface of the samples failed under three-point bend test are shown in the fractographs presented in figs. 5.48 (a-e). The fig. 5.48 (a) shows the top view of fracture surface, which is characterized by the locations of crack initiation and final fracture. The detailed view of crack initiation zone is shown in fig. 5.48(b). The fracture is characterized

130

by mixed mode of failure. Both the cleavage facets and fine dimples were noticed in the crack initiation zone. The cleavage facets zone was further characterized at higher magnification, as shown in fig. 5.48 (c). The ductile dimples besides the smooth inter-crystalline area are clearly noticed in fig. 5.48 (c). Fig. 5.48 (b) shows mainly quasi-cleavage and intergranular (IG) fracture along the prior austenite grain boundary with regions of tearing topology surface (TTS). The similar pattern of fractographs was also reported by Sun et al. (2014). According to Liu (2005), the IG embrittlement (fig. 5.48 (c)) due to fracture along the prior austenite grain boundaries largely happens due to segregation of manganese sulphide (MnS) on it. Feature of the IG fracture is generally observed in low alloy cast steel identified by (Bhadeshia and Honeycombe, 2005). TTS is primarily due to micro-plastic tearing and encountered by overload stresses which was explained by (Thompson and Chesnutt, 1979). The detailed features of the final fracture surface observed at both the relatively lower and higher magnifications are shown in figs. 5.48 (d) and (e) respectively. The fractographs reveal the presence of fine and shallow ductile dimples with negligible amount of cleavage facets. In agreement to an work reported (Sun et al., 2014) earlier, the evidence of quasi-cleavage as a result of tear ridges formed by cleavage facets followed by micro-void coalescence (MVC) is clearly revealed in figs. 5.48 (d) and (e).

1= MVC   2= TTS   3= IG
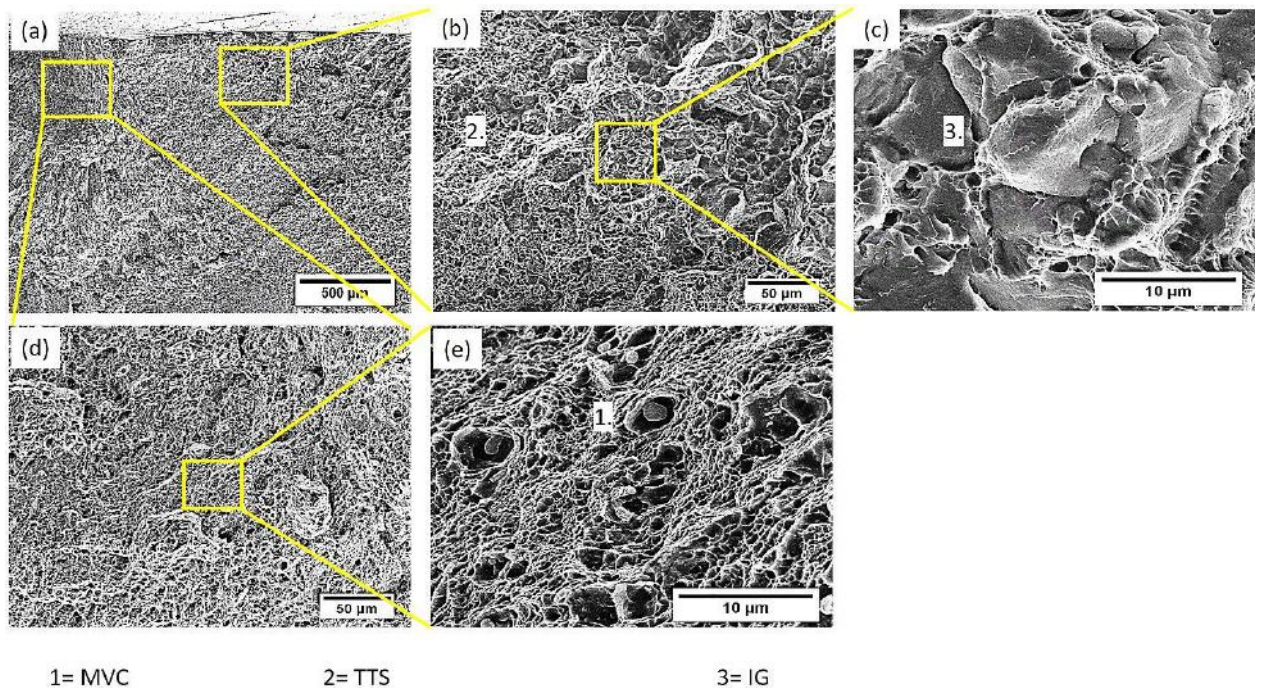
Fig. 5.48   SEM images of fractured surface of modified zone of AISI 4340 steel after three-point bend test: (a) Top view of fracture surface, (b) detailed view of crack initiation zone, (c) presence of cleavage facets in crack initiation zone, (d) detailed view of final fracture zone at low magnification, (e) detailed view at higher magnification (MVC= micro-void coalescence, TTS= tearing topology surface and IG= intergranular).

5.3.6 Residual stresses

At a given arc voltage of 10.5 ± 1.0 V, the longitudinal and transverse residual stresses in the modified surface of substrate developed under the multi-pass C-TIG arc processing has been shown in figs. 5.49 (a) and (b) respectively. The figures illustrate that a considerable amount of compressive nature of residual stress was developed in the longitudinal as well as in transverse direction of the modified surface. It is observed that as the heat input increases up to 0.39 kJ/mm, there is a significant increase in the compressive residual stress from 251 to 289 MPa at a depth of 0.1 mm. Whereas at further increase of heat input to 0.60 kJ/mm, it was noticed that the compressive residual stress is reduced from 289 to 163 MPa at the depth of 0.1 mm in the longitudinal direction as shown in fig. 5.49 (a). At favourable orientation these residual stresses are active to improve tensile and bending properties in static as well as dynamic loading condition. However, in case of transverse residual stress at a depth of 0.1 mm, there is a significant reduction in compressive stress from 110 to 45 MPa during increase of heat input as shown in fig. 5.49 (b). The intensity of these stresses decreases up to the depth of 0.4 to 0.7 mm depending upon C-TIG parameter. In longitudinal direction, the maximum compressive stresses were found at the top surface and followed by a reduction of the compressive stress up to a depth of 1.5 mm. These residual stresses have most probably a significant positive contribution to improvement of fatigue life of the surface modified base material under uniaxial tensile fatigue as well as three point bend flexural fatigue life. These stresses are primarily attributed to differential thermal expansion-contraction and phase (martensite) transformation in the modified region [Hidekazu et. Al., 2008]. The behaviour of residual stresses observed in the matrix are largely in agreement to the phase transformation under different conditions of surface modifications as discussed above.
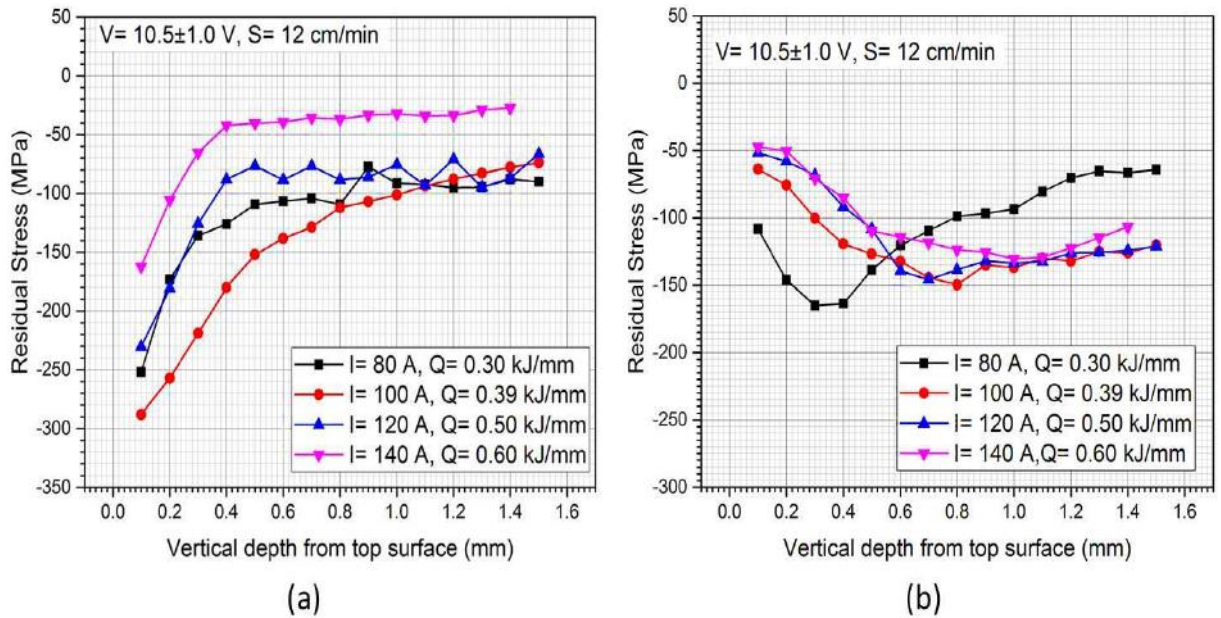
Fig. 5.49　　Distribution of different components of residual stresses in depth of the matrix modified by multi-pass C-TIG at different heat inputs (a) longitudinal and (b) transverse directions.

Resolved stresses for uniaxial tensile test were calculated by the eq. 5.11 where, σ_a is applied stress due to load, σ_r is residual stresses due to surface modification and i is thickness of the tensile sample, which is about 4 mm.

$$\sigma_{resolved} = \sum_{i=0}^{i=4} \sigma_{a_i} + \sigma_{r_i} \qquad\qquad \text{……………..………………} \text{5.11}$$

The resolved stress possibly present in the specimen during tensile test is shown in fig. 5.50. In the multi-pass surface modified sample prepared by C-TIG process operated at the heat input of 0.39 kJ/mm (I= 100 A and S= 12 cm/min) the resolved stress reached approximately to 105 MPa at the depth of 0.1 mm. This was followed by a continuous increase up to 400 MPa to the depth of 2.0 mm when 400 MPa stresses were applied by the tensile machine. Such reduction is primarily happened due to presence of residual stresses.
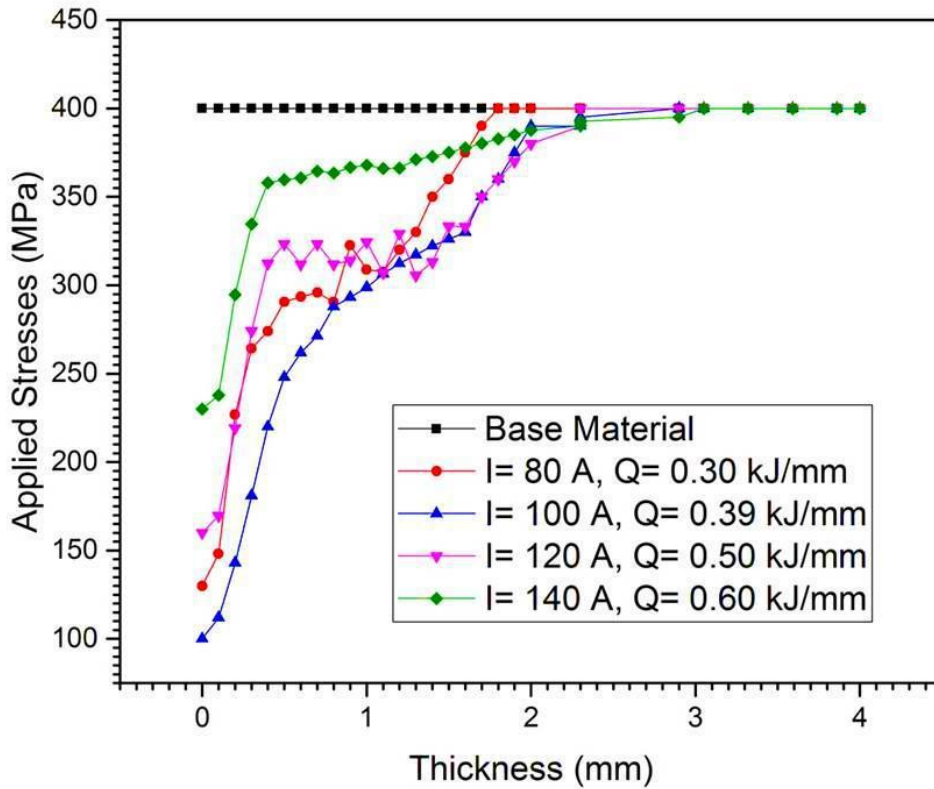
Fig. 5.50   The amount of resolved stresses present across the depth from the surface under tensile test loading of 400 MPa.

Resolved stresses for three point flexural stresses were calculated by the eq. 5.12 where, σ_a is applied stress due to load, σ_r is residual stresses due to surface modification and i is thickness of the flexural sample, which is about 10 mm thickness. Here i=0 mm means the neutral axis of the sample.

$$\sigma_{resolved} = \sum_{i=-5}^{i=5} \sigma_{a_i} + \sigma_{r_i}$$

………………………………………………….……. 5.12

The modified surface was kept as lower fibre, so that possible resolved stress at lower fibre during the flexural test may present as shown in fig. 5.51. In the multi-pass C-TIG processed modified sample prepared at the heat input of 0.39 kJ/mm (I= 100 A and S= 12 cm/min), the resolved stress reached approximately to 295 MPa at the depth of 0.1mm. It was followed by an increase up to 370 MPa when a stress of 600 MPa was applied at lower fibre by the testing machine as shown in fig. 5.51. In the case of flexural test, availability of compressive residual stresses is relatively more prominent for supressing the crack initiation and propagation, this favour to improve flexural properties in static as well as dynamic loading.

134
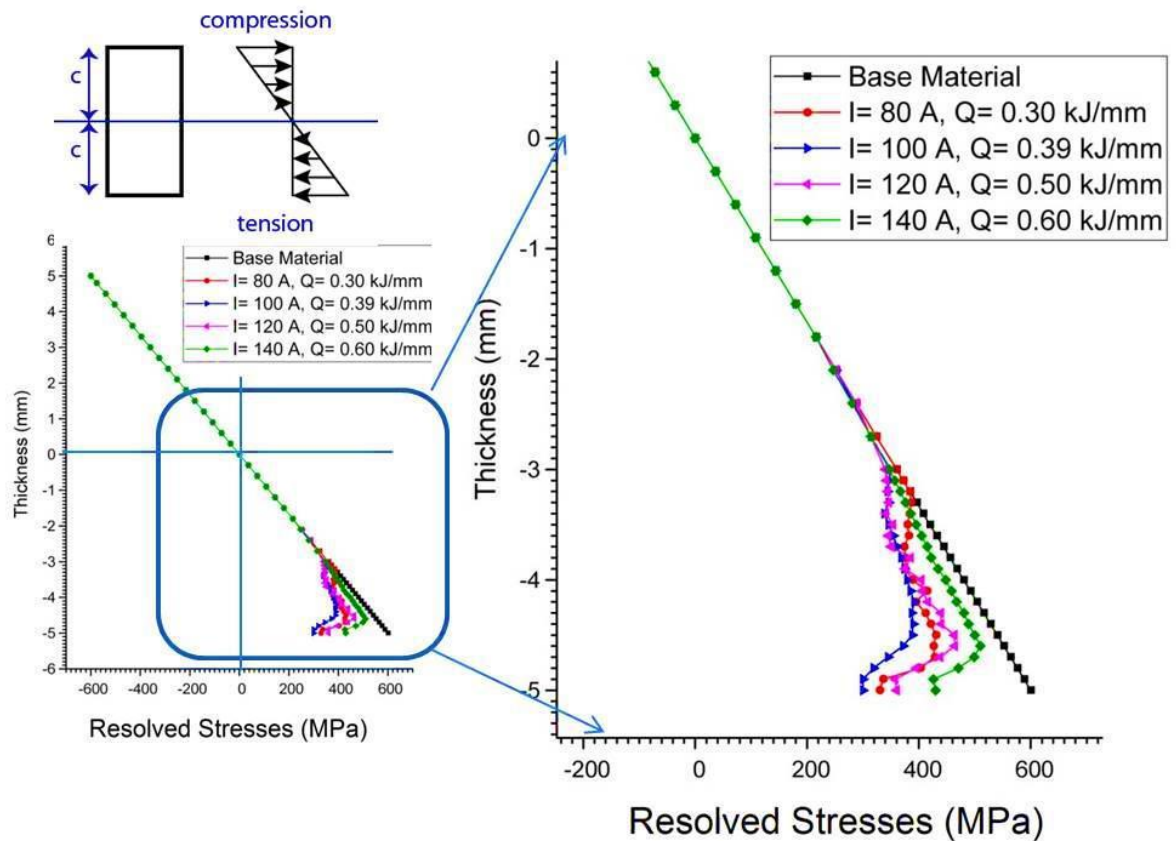
Fig. 5.51   The amount of resolved stresses present across the depth from the surface under bend test loading of 600 MPa.

5.3.7 Fatigue Test

5.3.7.1 Under uniaxial tensile loading

The studies on fatigue characteristics (S-N curves) under uniaxial tensile loading of the surface modified AISI 4340 structural steel produced by multi-pass TIG surfacing at various heat input resulting from varying arc current in the range of 80 to 140 A at the arc travel speed of 12 to 15 cm/min are shown in figs. 5.52 (a) and (b) respectively where the arc voltage is kept as 10.5 ± 1.0 V. The fig. 5.52 (a) and (b) depicts that the surface modification of AISI 4340 steel can significantly improve the endurance limit of its fatigue life up to σ_{max} in the range of about 510 - 550 MPa depending upon the TIG arcing process parameters. It indicates that the surface modification by multi-pass C-TIG arcing process can improve fatigue performance of the order of $25 - 37.5$ % as compared to that of the base material.

At a given arc voltage and travel speed of 10.5 ± 1.0 V and 12 cm/min, respectively, the increase of arcing current from 80 to 140 A decreases the endurance limit to σ_{max} from 550 to 510 MPa respectively, as shown in fig. 5.52 (a), where the heat input is enhanced from 0.30 to 0.60 kJ/mm respectively. At this juncture if the heat input is consider as the main criterion of surface modification of AISI 4340 steel using multi-pass C- TIG surfacing, it may be noted that

135

the slope of the S-N curve decreases as the heat input is less than 0.30 kJ/mm (I= 80 A, S= 15 cm/min). It may have happened due to the presence of needle martensite in the matrix of the modified region, which provides an easy path for the crack movement. Similarly it is noticed that the slope of the S-N curve is almost constant at any heat input within 0.30 - 0.60 kJ/mm. Thus it may be inferred that in case of the multi-pass surface modification by C-TIG at the heat input more than 0.30 kJ/mm, the subsequent passes have significantly tempered the needle shape matensite and form the lath matensite or bainite along with ferrite in the matrix.

At a given σ_{max}, the surface modified AISI 4340 steel has always been found to give considerably higher fatigue life than that of the untreated base metal. Maximum improvement in the fatigue life under uniaxial tensile loading was observed at the relatively low heat input of 0.30 kJ/mm where, the arcing current, arc voltage and arc travel speed is kept as 80 A, 10.5 $\pm$ 1.0 V and 12 cm/min respectively, as shown in fig. 5.52 (a). However, optimum improved fatigue performance of the surface modified AISI 4340 steel over that of the base material has been noticed in case of the modification carried out at the heat input in the range 0.30 - 0.40 kJ/mm with arc travel speed of 12 - 15 cm/min having suitably varied arcing current at the arc voltage of 10.5 $\pm$ 1.0 V. The observed fatigue characteristics are in agreement to the microstructure, hardness, strength and toughness of the modified material as a function of the processing parameters as discussed above. It is also observed that the residual stresses present in the matrix of the multi-pass surface modified substrate are of compressive nature as discussed earlier in section 5.3.6.
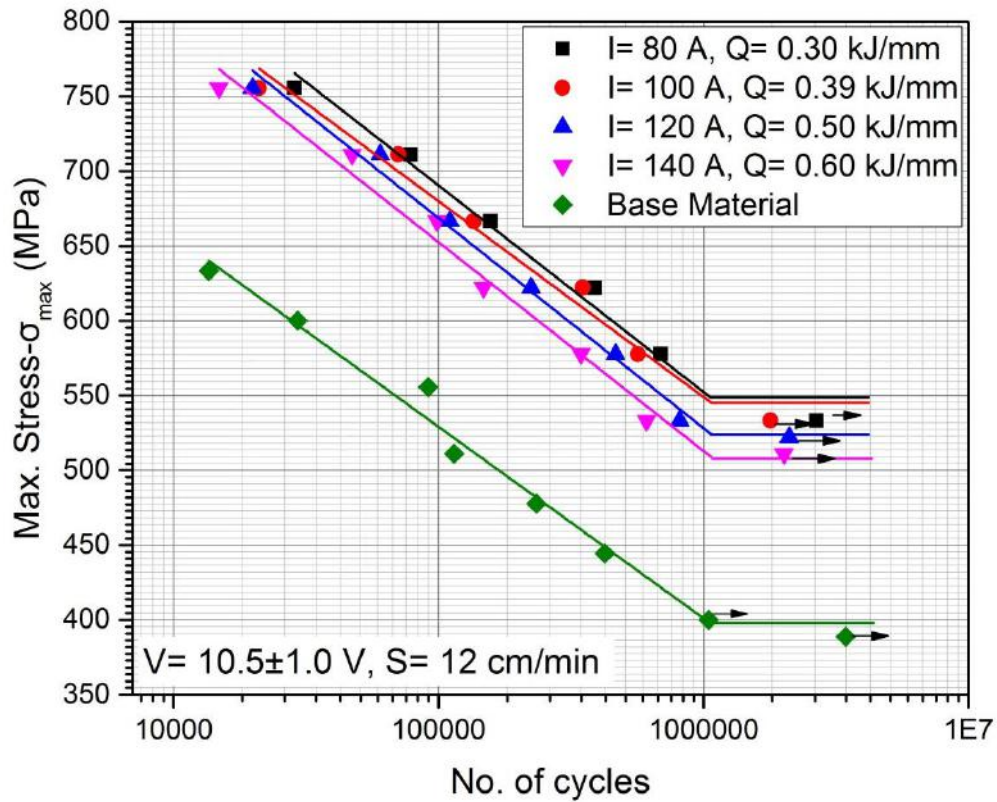
(a)
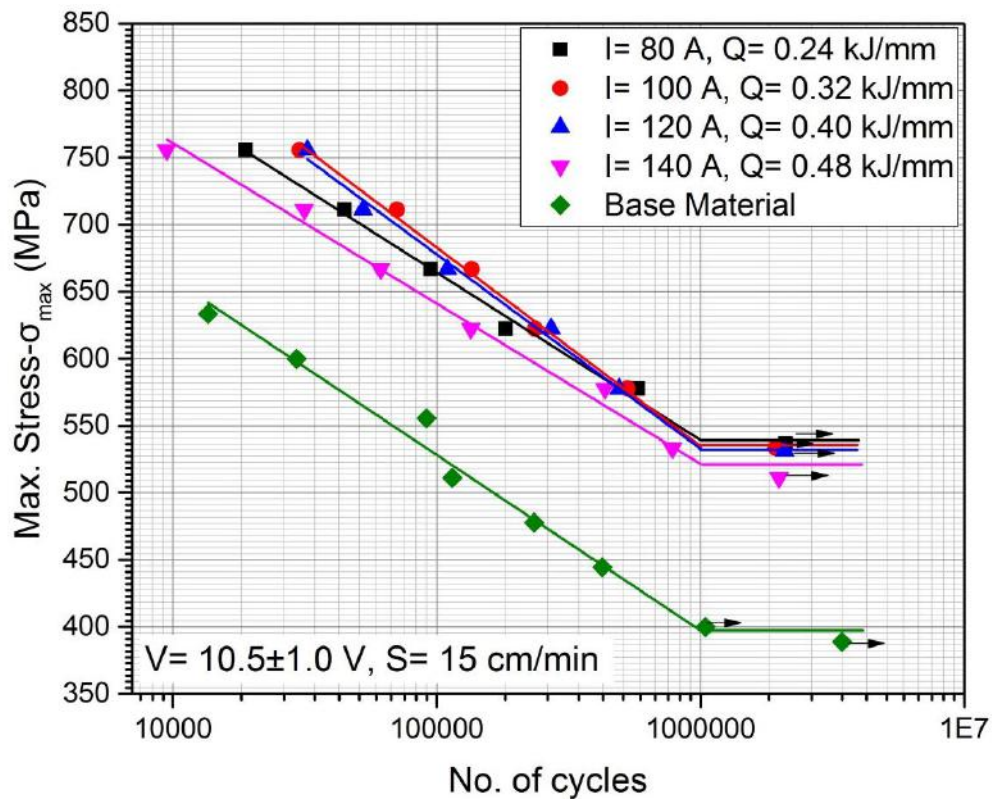
(b)

Fig. 5.52   At given arc travel speed of (a) 12 cm/min and (b) 15 cm/min the nature of S-N curve of surface modified AISI 4340 steel prepared at different heat inputs varied by changing the arcing current compared to the same of unmodified base metal.

137

5.3.7.2 Under bending load

Typical S-N curve of fatigue behaviour under bending load on the surface modified AISI 4340 structural steel prepared by multi-pass TIG surfacing at various heat input resulting from varying arc current in the range of 80 to 140 A at the arc travel speed of 12 and 15 cm/min is shown in figs. 5.53 (a) and (b) respectively where the arc voltage is kept at 10.5 ± 1.0 V. The fig. 5.53 (a) and (b) depicts that the surface modification of AISI 4340 steel can significantly improve the endurance limit of its fatigue life up to σ_{max} in the range of about 545 - 625 MPa depending upon the C-TIG arcing parameters. It indicates that the surface modification by C-TIG arcing process can improve fatigue performance of the order of $13 - 30$ % as compared to that of the base material. In case of the multi-pass surface modified steel the S-N curves are found to be relatively flatter in finite life region than that of the base metal when it is treated by the multi-pass C-TIG arcing process at both the arc travel speed of 12 and 15 cm/min. But it is more prominent in case of using the lower arc travel speed of 12 cm/min. Thus it may be inferred that in case of instant fusion by arc heating the heat distribution predominated by the arc travel speed largely governs the desired phase transformation by dictating the cooling rate affecting the fatigue characteristics of the modified matrix.

At a given arc voltage and arc travel speed of 10.5 ± 1.0 V and 12 cm/min respectively, the maximum improvement is revealed at the heat input of 0.39 kJ/mm, where endurance limit was observed at σ_{max} of 625 MPa and failure was occurred in 1.46×10^5 cycles at the σ_{max} of 711 MPa. As the heat input increases or decreases from 0.39 to 0.60 or 0.39 to 0.30 kJ/mm respectively by changing the arcing current, there is a reduction in fatigue life of endurance limit as well as finite life. Similarly in case of arc travel speed of 15 cm/min, with the increase in arcing current from 100 A there is an appreciable reduction in fatigue properties of the modified matrix under bending load. In this context it is also interesting to note that the multi-pass surface modification improves the endurance limit but the fatigue strength in the finite life range of $10^3 - 3 \times 10^4$ cycles is appreciably reduced under bending load especially in case of the surface modification made at the arc travel speed of 15 cm/min.
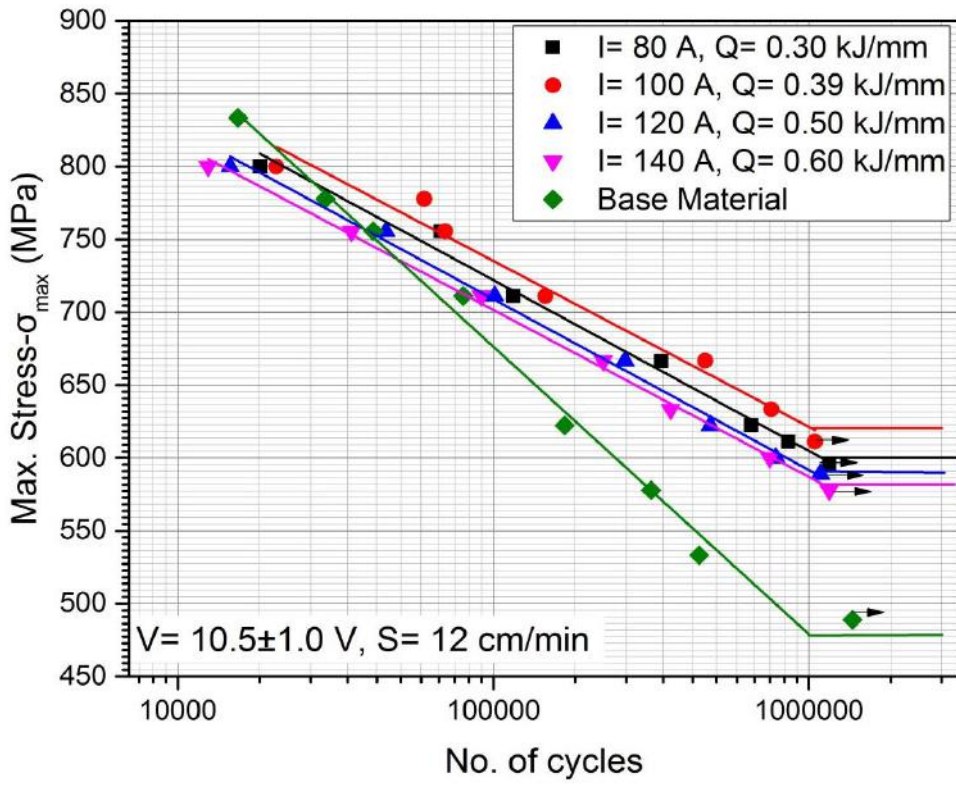
(a)
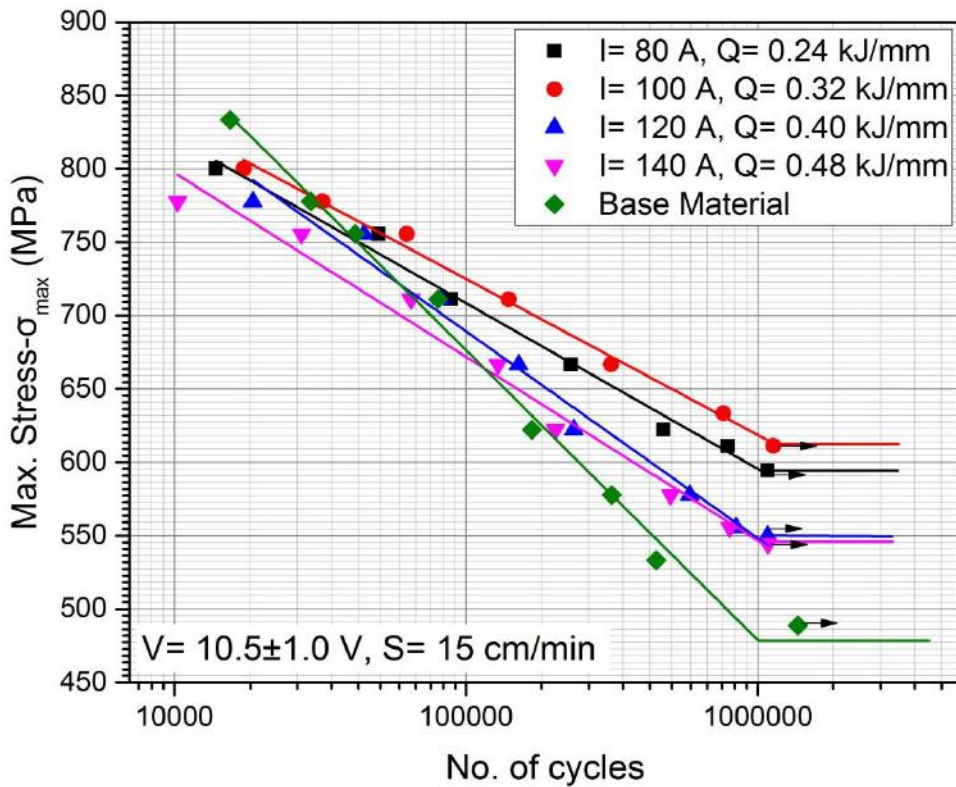
(b)

Fig. 5.53   At a given arc travel speed of (a) 12 and (b) 15 cm/min the nature of S-N curve under bending load of surface modified AISI 4340 steel prepared at different heat inputs varied by changing the arcing current compared to the same of unmodified base metal.

139

5.3.8 Summary

The multi-pass C-TIG arcing processes with 50% overlap are successfully employed over larger surface area to match the needs of industrial applications. Thermal cycle of on FZ has been analyzed and it illustrate that the single and double reheat and microstructure refinement was occurred during multi-pass C-TIG arcing process. Further HAZ zone also become heat treated by the subsequent passes. The microstructures of stabilized zone primarily consist of tempered lath martensite followed by bainite and proeutectoid ferrite. The microstructure of different zones primarily depends upon the C-TIG arcing parameters. The effect of tempering is clearly observed in the distribution of the hardness in the modified zone. The hardness in the stabilized zone is found as 90 ± 20 % more than the base metal. However, the hardness of the modified zone using multi-pass C-TIG arcing process is reduced by 15 ± 9 HV due to effect of tempering as compared to the single-pass C-TIG arcing process.

A significant improvement was observed in the tensile properties such as yield strength, UTS, ductility and toughness of the multi-pass modified matrix as compared to those of the single-pass C-TIG modified surface. The yield strength and UTS has been improved in the range of 90 ± 20 % and 35 ± 12 %, respectively on the other hand, toughness and ductility is decreased as compared to the base material. Similarly, the flexural properties are significantly increased in case of the surface modification by multi-pass C-TIG arcing process at a given heat input. The maximum improvement is observed in flexural yield strength and maximum flexural stress in the range of 872 and 1522 MPa respectively at the heat input of 0.32 kJ/mm.

The characteristics of S-N curve are analyzed under tensile and bending load on multi-pass surface modified AISI 4340 steel. It shows that the fatigue endurance limit under tensile loading of the surface modified substrate can be improved up to σ_{max} of 550 MPa at the heat input of 0.30 kJ/mm where the arcing current, arc voltage and arc travel speed is kept as 80 A, 10.5 ± 1.0 V and 12 cm/min respectively. Whereas endurance limit of surface modified matrix under bending load is improved up to σ_{max} of 625 MPa at the heat input of 0.39 kJ/mm where arcing current, arc voltage and arc travel speed is kept at 100 A, 10.5 ± 1.0 V and 12 cm/min respectively. Thus, it is concluded that the arc travel speed of 12 cm/min and heat input in the range of 0.30 – 0.39 kJ/mm gives the maximum improvement in fatigue life under tensile and bending load. This is primarily happened due to desired phase transformation and favorable residual stress development in the modified surface. Compressive residual stresses are observed to develop in the longitudinal and transverse directions of the modified surface up to a magnitude of 289 and 110 MPa respectively under variation of heat input. These compressive

stresses are relatively more prominent for the improvement in mechanical properties under static and dynamic tensile and bending load.

5.4 Characteristics of surface modification by single-pass P-TIG arcing process

The acceptability of the hardened region in TIG arcing process is largely governed by its required depth of penetration at an optimum thermal exposure giving rise to a minimum heat affected zone (HAZ) of undesirable phase transformation. The extent of modification of the base metal largely depends upon nature of energy transfer and thermal behavior of the fusion zone dictating the shape and size of the molten pool and its temperature. The heat content of weld pool is largely governed by its molten mass per unit length and temperature. The shape and size of weld pool affect the properties of the fusion zone and HAZ. Achieving all these aspects can be more precisely addressed by using pulse TIG (P-TIG) arcing process controlled by the summarized influence of pulse parameters. The summarized influence of pulse parameters defined by a dimensionless hypothetical factor ϕ derived on the basis of an energy balance concept of the system is proposed earlier [Ghosh et al., 2000, Ghosh and Kumar,2014]. This is because, it more thoroughly facilitates controlling the fusion characteristics including its microstructure [Ghosh 1996, Ghosh et al., 2006, Ghosh et al., 2008, Goyal et al., 2008 (b), Hussian et al., 1996, Randhawa et al., 1998, Randhawa et al., 2000]. The thermal behavior of fusion has been studied considering heat transfer to the fusion zone by the arc, heat input (Ω), temperature of weld pool (T_{WP}) and weld isotherm governing the shape and size of fusion pool [Goyal et al., 2008 (b), Ghosh et al., 2006].

5.4.1 Geometrical aspects of the modified zone

The parameters I_m, T_{WP} and fusion isotherm, which to a great extent dictate the geometrical aspects of fusion pool, are largely dictated by various pulse parameters of the P-TIG arcing process. Thus, the geometrical aspects of fusion zone (FZ) with respect to its bead width (W_b), depth of penetration (P_d), area of fusion (A_F) and HAZ width (W_{HAZ}) have been studied as a function of pulse parameters. This is to facilitate optimization of pulse parameters to ensure the characteristics of the modified zone as per the requirement of industrial applications. At a given arc voltage and travel speed of 10.5 ± 1.0 V and 12 cm/min respectively, the typical photographs of the surface appearance of the bead geometry of the fused zone observed during using P-TIG arcing process at heat input of 0.39 and 0.60 kJ/mm obtained from I_m as 100 A and 140 A respectively at ϕ=0.21 and f =15 Hz has been shown in fig. 5.54. The fig. 5.54 also shows the macrograph of transverse section of the modified zone observed under the same conditions of the P-TIG arcing process.

Heat Input (kJ/cm)	I_m (A)	Surface appearance (Scale in mm)	Transverse section (Scale in mm)
0.39	100		
0.60	140		

Fig. 5.54   Typical appearance of modified surface and its transverse section prepared by single-pass P-TIG arcing at different heat inputs of 0.39 and 0.60 kJ/mm using the I_m of 100 and 140 A respectively.

The geometrical features of the modified zone in the substrate as revealed in the fig. 5.54 clearly show that at given heat input the use of pulse current arcing has significant influence on bead width, depth of penetration and area of fusion and width of HAZ in the substrate in comparison to that observed in case of the C-TIG arcing process (Fig. 5.10). At given heat input of 0.39 and 0.60 kJ/mm a comparative study on the effect of single-pass P-TIG and C-TIG on the FZ width, depth of penetration, FZ area and HAZ width has been shown in fig. 5.55 (a-d) respectively where the arc voltage and arc travel speed are kept at 10.5 ± 1.0 V and 12 cm/min respectively.

The figure illustrates comparative increase in the geometry of FZ considered as its width, depth of penetration and area along with appreciable reduction in width of HAZ. Such improvement is primarily governed by energy distribution in the system primarily as a function of the peak current (I_p), ϕ and f [Goyal et al., 2008 (b), Ghosh et al., 2006, Goyal et al., 2008 (b), Hussian et al., 1996, Randhawa et al., Ghosh., 2017]. The observations on variation in geometry of modified zone as a function of I_p, ϕ and f is largely attributed to increase of heat buildup in molten pool [Pal and Pal, 2011, Ghosh., 2017] enhancing its size and fluidity.
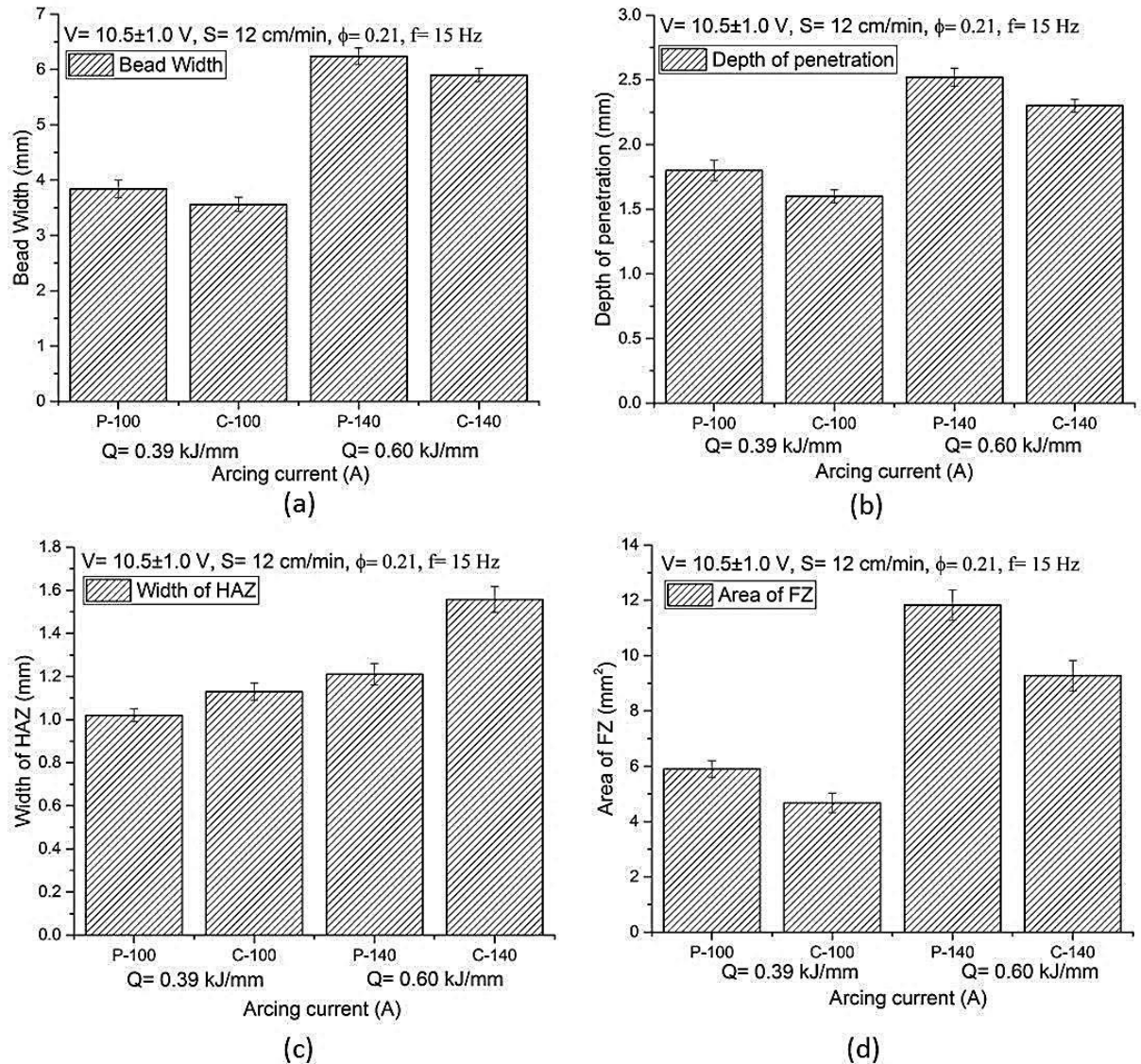
Fig. 5.55   At given heat input a comparative effect of single-pass P-TIG and C-TIG on (a) bead width (b) depth of penetration (c) HAZ width and (d) fusion zone area.

The fig. 5.56 shows the cooling rate of FZ and HAZ observed during P-TIG and C-TIG arcing processes at given heat inputs of 0.39 and 0.60 kJ/mm obtained by changing the arcing current to 100 and 140 A respectively where the other parameter such as arc voltage, arc travel speed, ϕ and f are kept constant as 10.5 ± 1.0 V, 12 cm/min, 0.21 and 15 Hz respectively. The fig. 5.56 depicts that the cooling rate of FZ and HAZ is increased from 187 to 218 and 145 to 178 ^{o}C/min, respectively by employing P-TIG instead of C-TIG at the same heat input of 0.39 kJ/mm, such an increase in cooling rate was primarily associated with the reduction in width of HAZ and thermal distribution in the system as a function of pulse parameters.

143
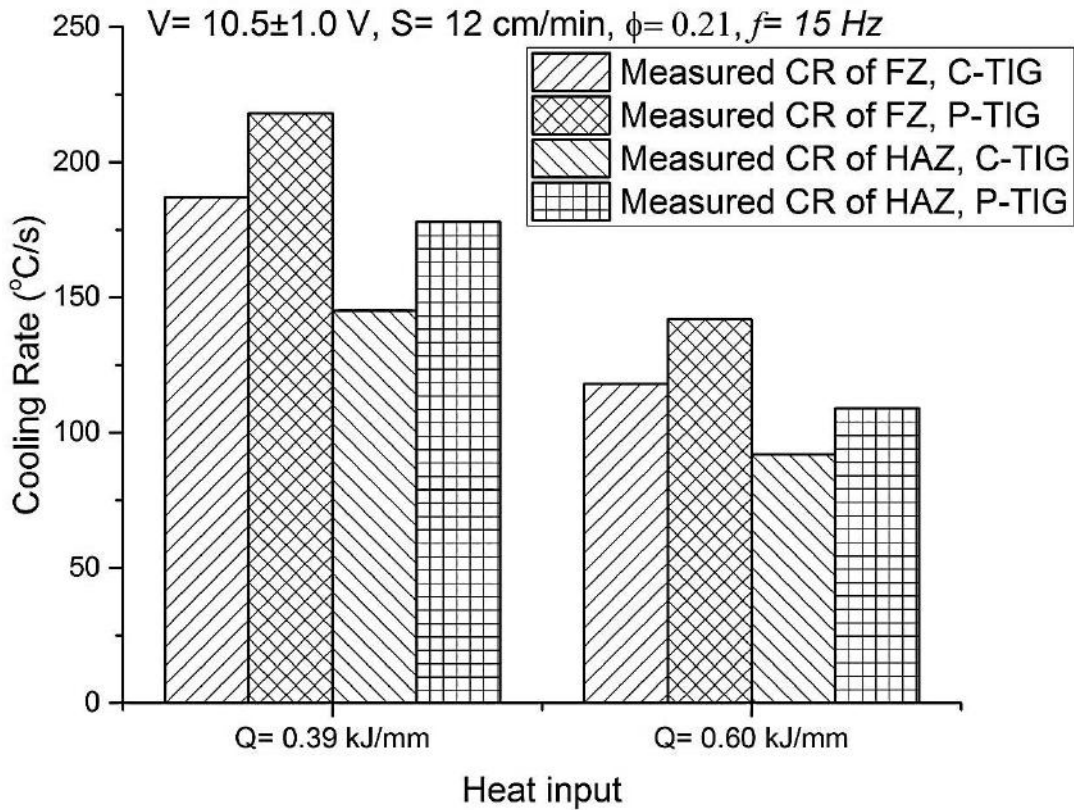
Fig. 5.56   **Comparison of single-pass P-TIG and C-TIG arcing on measured cooling rate at inter-critical temperature range (800-500⁰C).**

5.4.2 Effect on microstructure of FZ and HAZ

At a given arc voltage and arc travel speed of 10.5 ± 1.0 V and 12 cm/min, the typical variation in the microstructure of FZ at I_m of 100 and 140 A has been shown in fig. 5.57 (a) and (b) respectively, where ϕ and f are kept constant as 0.21 and 15 Hz respectively. The fusion zone has been found to have cast dendritic morphology. The fig. 5.57 (a) also reveals that the microstructure of FZ primarily consist of needle martensite with proportionate amount of bainite and proeutectoid ferrite. The proportion of bainite and proeutectoid ferrite reduces with the increase of I_m from 100 to 140 A at the same ϕ and f as shown in fig. 5.57 (b). This is largely attributed to increase of fusion pool temperature and size of isotherm (relatively wider HAZ) with the increase of I_m resulting in reduction of cooling rate due to comparatively lower temperature gradient. It was also observed from the fig. 5.57 that with the increase in heat input at a given ϕ and f, the microstructure of fusion zones becomes relatively coarser. The change of microstructure is primarily attributed to the change in cooling rate as shown in fig. 5.56.
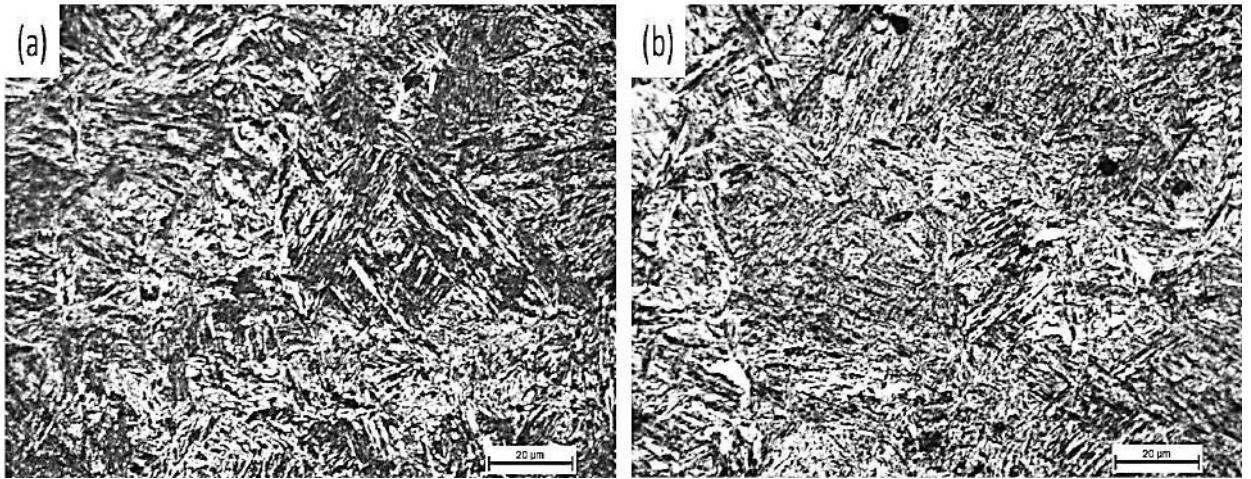
Fig. 5.57   Typical microstructure of fusion zone in single-pass P-TIG arcing process under different I_m of (a) 100 (b) 140 A where the V, S, ϕ and f are kept constant at 10.5 $\pm$ 1.0 V, 12 cm/min, 0.21 and 15 Hz respectively.

At a given arc voltage and travel speed of 10.5 $\pm$ 1.0 V and 12 cm/min respectively, the typical variation in microstructure of HAZ with variation of I_m from 100 to 140 A has been shown in fig. 5.58 (a) and (b) respectively. It has been observed that the reduction in heat input from 0.60 to 0.39 kJ/mm by changing I_m from 140 to 100 A at a given ϕ and f, the microstructure of HAZ becomes relatively finer that consists of uniformly distributed lath martensitic with some proportion of bainite, proeutectoid ferrite and retained austenite.
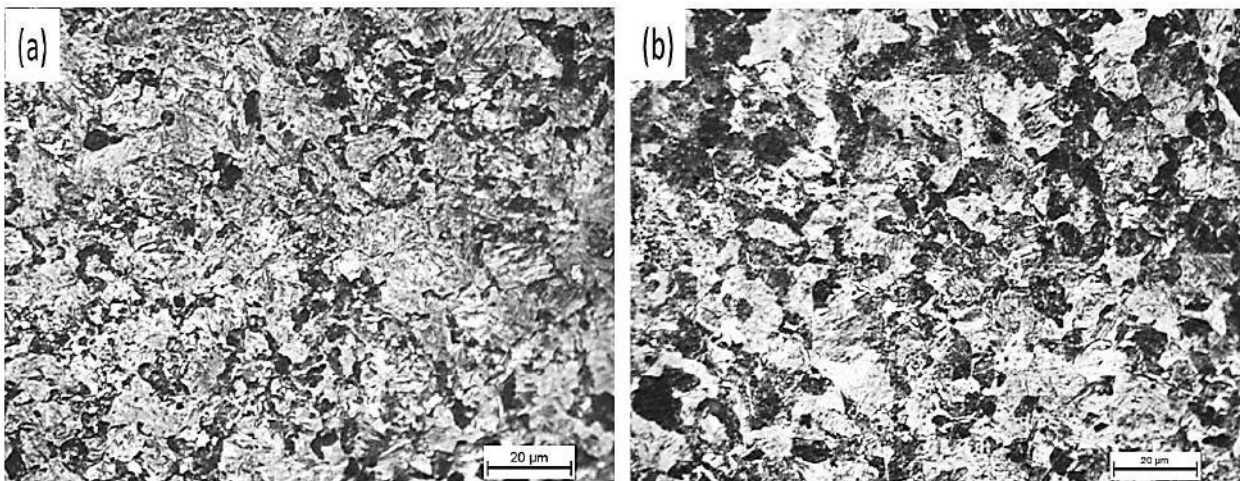
Fig. 5.58   Typical microstructure of HAZ in single-pass P-TIG arcing process under different I_m of (a) 100 and (b) 140 A where the V, S, ϕ and f are kept constant at 10.5 $\pm$ 1.0 V, 12 cm/min, 0.21 and 15 Hz respectively.

5.4.3 Effect on hardness of FZ and HAZ

At a given I_m of 100 and 140 A, the effect of P-TIG on the distribution of hardness across the region starting from the fusion zone through HAZ to base material is shown in fig. 5.59. The figure show that as one proceeds from the fused modified zone to HAZ the hardness

falls till it reaches the stable hardness (256±10 HV) of base metal. The fig. 5.59 depicts that hardness of FZ and HAZ significantly increases with the application of P-TIG in comparison to that of C-TIG. The fig. 5.59 illustrates that the hardness of FZ is increased by 30 ± 10 HV with employing the P-TIG instead of C-TIG at a given heat input of 0.39 kJ/mm. Similarly the hardness was also increased in case of the heat input of 0.60 kJ/mm in P-TIG arcing process, while arcing parameters ϕ and f were kept as 0.21 and 15 Hz. The increase of hardness by employing P-TIG may be primarily attributed to enhancement of cooling rate which controls the microstructure of the modified zone as discussed in section 5.4.2.
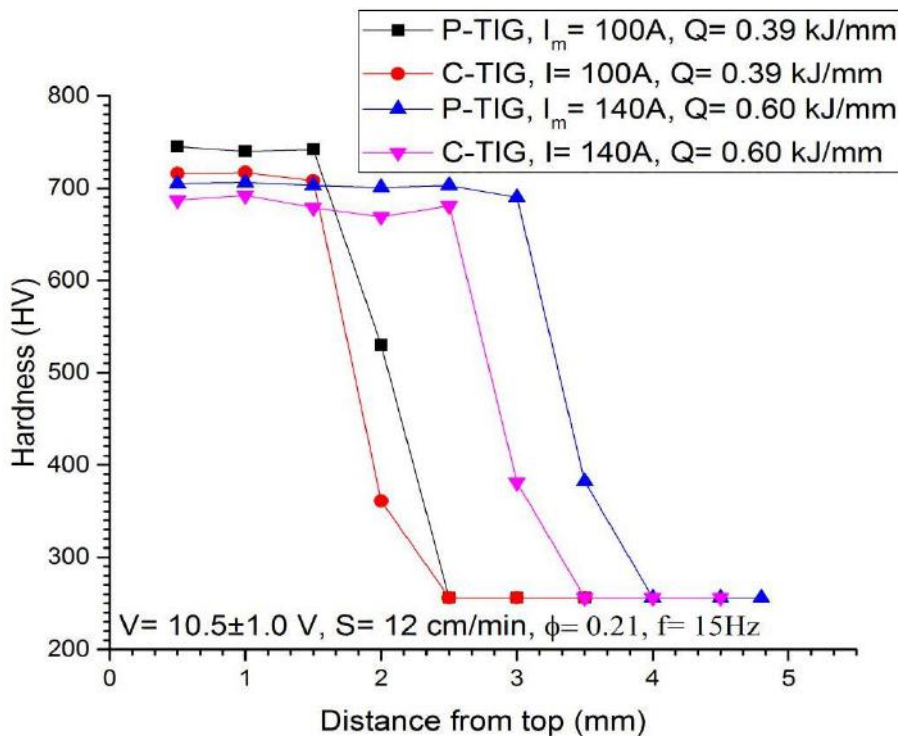
Fig. 5.59   Distribution of hardness across the single-pass P-TIG and C-TIG modified region starting from the fusion zone through HAZ to base metal at different heat inputs.

5.4.4 Effect on tensile Properties

The engineering stress-strain curve of the surface modified substrate prepared by P-TIG and C-TIG arcing processes at the heat input of 0.39 and 0.60 kJ/mm by changing arcing current has been shown in fig. 5.60, where arc voltage and arc travel speed is kept as 10.5 ± 1.0 V and 12 cm/min. Under such condition of surface modification, a comparative study of P-TIG with C-TIG arcing process at different arcing mean current on the YS, UTS, toughness and percentage strain of the surface modified substrate is illustrated in figs. 5.61 (a-d) respectively. The stress-strain curve shown in fig. 5.60 depicts clearly that the surface modification using P-TIG arcing significantly affects the tensile properties of base material, where the YS and UTS are considerably improved along with some reduction of strain and toughness (Fig. 5.25 (a-d))

146

in comparison to those of C-TIG modified substrate and the base material. This is in agreement to the hard phase transformation in the matrix as discussed above which is functional in governing its mechanical properties based on the processing parameters. Thus, it may be understood that there may be a critical requirement of heat input with appropriate heat distribution (controlled by arc stability) governing the thermal cycle for desired phase transformation in the fusion modified matrix.
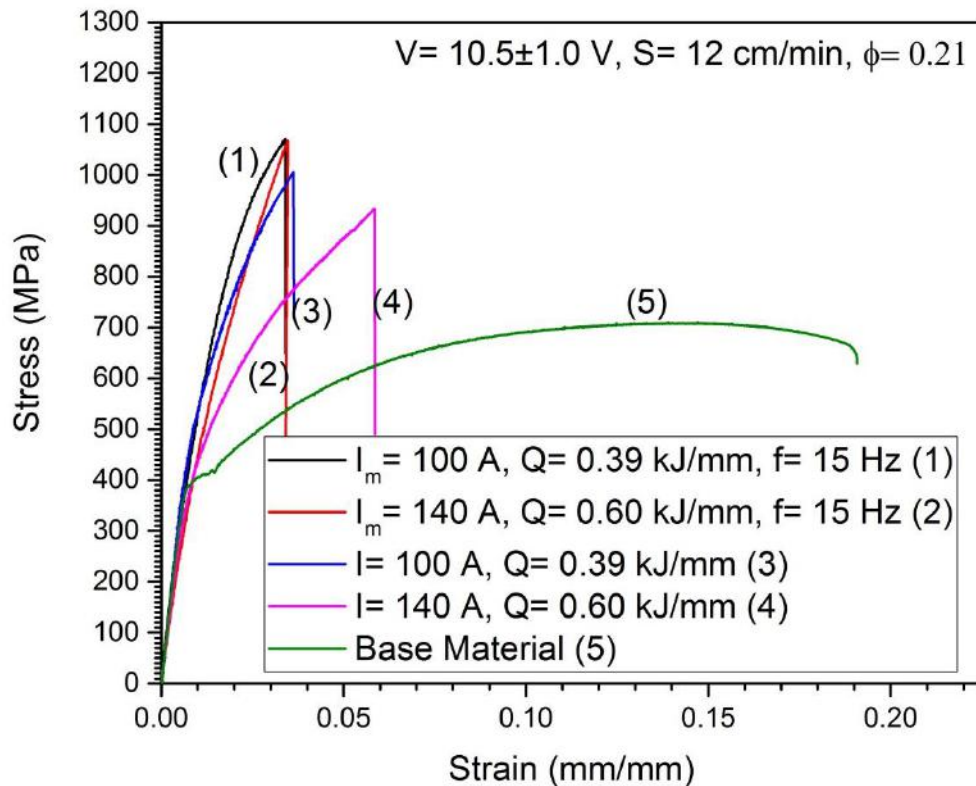
Fig. 5.60   Tensile stress-strain diagram of surface modified AISI 4340 structural steel produced by single-pass P-TIG and C-TIG arcing at different heat input obtained by varying arc current (I or I_m), where the V, S, ϕ and f are kept constant at 10.5 ± 1.0 V, 12 cm/min, 0.21 and 15 Hz respectively.

In this context it is also observed that at a given arc voltage and arc travel speed of 10.5 $\pm$ 1.0 V and 12 cm/min respectively, the increase in heat input from 0.39 to 0.60 kJ/mm by adjusting the I_m to 100 to 140 A respectively, shows (Fig. 5.61 (a-d)) the tensile properties such as YS, UTS, ductility and toughness are lying in the range of about 770 ± 15 MPa, 1060 ± 15 MPa, 3.33 ± 0.2 % and 22 ± 1.0 J/mm^3 respectively. Such changes in tensile properties gives a strong agreement of formation of needle shape martensite, lath martensite and banitic structure in the modified surface of AISI 4340 steel produced by P-TIG arcing process.
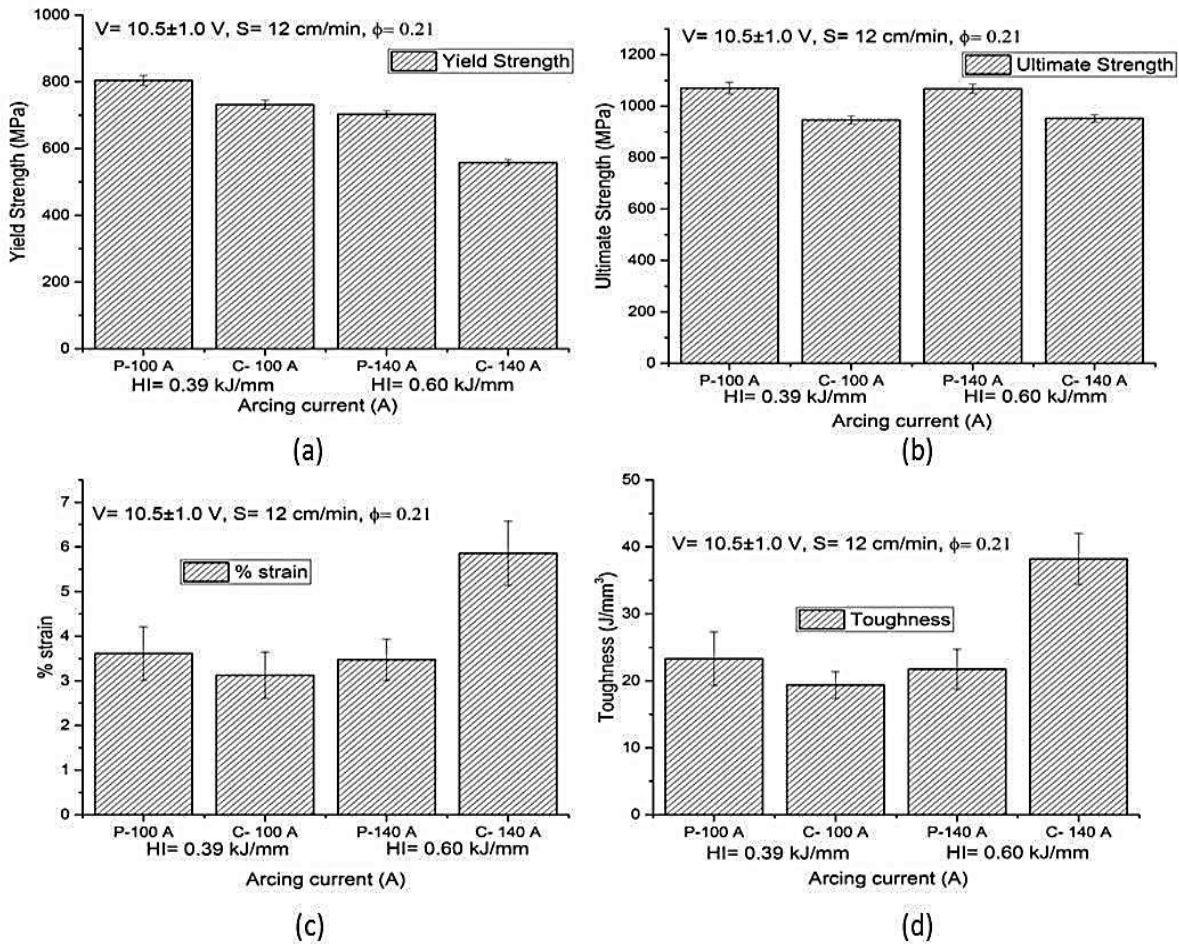
Fig. 5.61 Effect of different heat inputs of varying arcing currents of single-pass P-TIG and C-TIG arcing processes on (a) Yield strength, (b) ultimate tensile strength, (c) strain and (d) toughness observed during tensile test of the surface modified steel.

5.4.5 Effect on three point bend properties

Flexural behavior of modified surface employed by P-TIG and C-TIG arcing processes at the heat input of 0.39 kJ/mm and 0.60 kJ/mm has been shown in fig. 5.62, where heat input was increased by changing I_m or I respectively to 100 and 140 A. Here the arcing parameter such as arc voltage, arc travel speed, ϕ and f are kept constant as 10.5 ± 1.0 V, 12 cm/min, 0.21 and 15 Hz respectively. It is observed that the surface modification by single-pass P-TIG arcing process has almost similar bending properties in comparison to those observed in case of employing the C-TIG arcing such as flexural yield strength and maximum flexural stress of a component as shown in fig. 5.63 (a-b) respectively. The flexural stress verses extension curve shown in fig. 5.62 depicts relatively more brittle nature by reduction of flexural extension in surface modified by single-pass P-TIG arcing process with respect to that observed in case of using C-TIG arcing at given heat input of 0.39 to 0.60 kJ/mm. This has happened because of relatively higher cooling rate of weld pool of P-TIG arcing as compare to that of C-TIG arcing

at the given heat input of 0.39 and 0.60 kJ/mm as discussed earlier. Increase in cooling rate favors hard phase transformation in the matrix which is having relatively low ductility, on the other hand presence of a tensile nature of residual stress (discussed latter) may put an adverse effect on flexural strength.
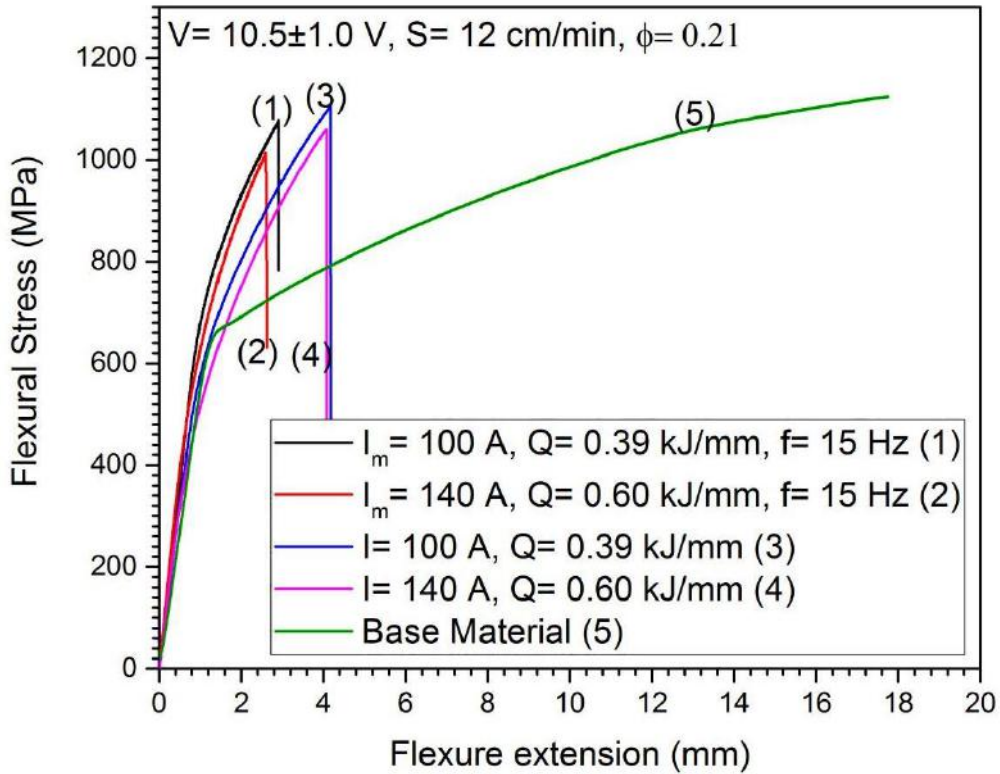
Fig. 5.62　　Flexural stress-extension diagram of surface modified AISI 4340 structural steel by single-pass P-TIG and C-TIG arcing processes at different heat inputs.
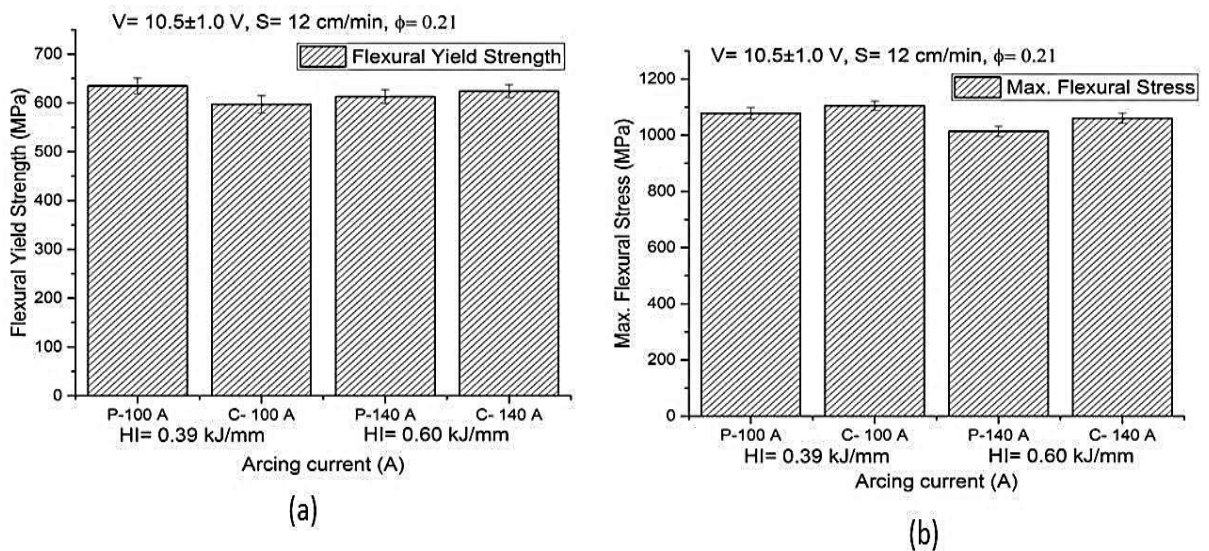
Fig. 5.63　　At different arcing currents effect of single-pass P-TIG and C-TIG arcing processes on (a) flexural yield strength and (b) flexural maximum stress of the modified surface.

149

5.4.6 Effect on residual stresses

At a given arc voltage and arc travel speed of 10.5 ± 1.0 V and 12 cm/min respectively, the longitudinal and transverse residual stresses at the centre of FZ of modified surface prepared by the single-pass P-TIG and C-TIG arcing process at the heat inputs of 0.39 to 0.60 kJ/mm has been shown in figs. 5.64 (a) and (b) respectively. It is observed that in case of both the P-TIG and C-TIG arcing the modified surface develops similar trends of distribution of residual stresses across the depth in the substrate. Here in longitudinal component the tensile residual stress from surface reduces to a compressive stress at certain depth followed by an increase in it to reach at neutral stress with further increase of depth to about 1.0 mm in the substrate. Whereas, in the transverse component the tensile residual stress from surface continuously reduces to a practically neutral stress at depth of about 1.0 mm in the substrate. However, in case of both the process the increase of heat input from 0.39 to 0.60 kJ/mm enhances the magnitude of residual stresses in the matrix, when at a given heat input the use of P-TIG in place of C-TIG arcing process develops relatively higher residual stresses in the matrix especially in case of employing the higher heat input of 0.6 kJ/mm. In longitudinal component the modified surface gets a tensile residual stress of about 125-150 MPa irrespective of using any of the arcing process. Whereas in case of transverse component the modified surface gets a tensile residual stress of about 160-190 MPa and 240-250 MPa at the lower and higher heat input respectively during modification by any arcing process. Such change in residual stress may considerably influence the fatigue life of the surface modified base material under uniaxial tensile loading and the same of the modified surface under tensile bending load.
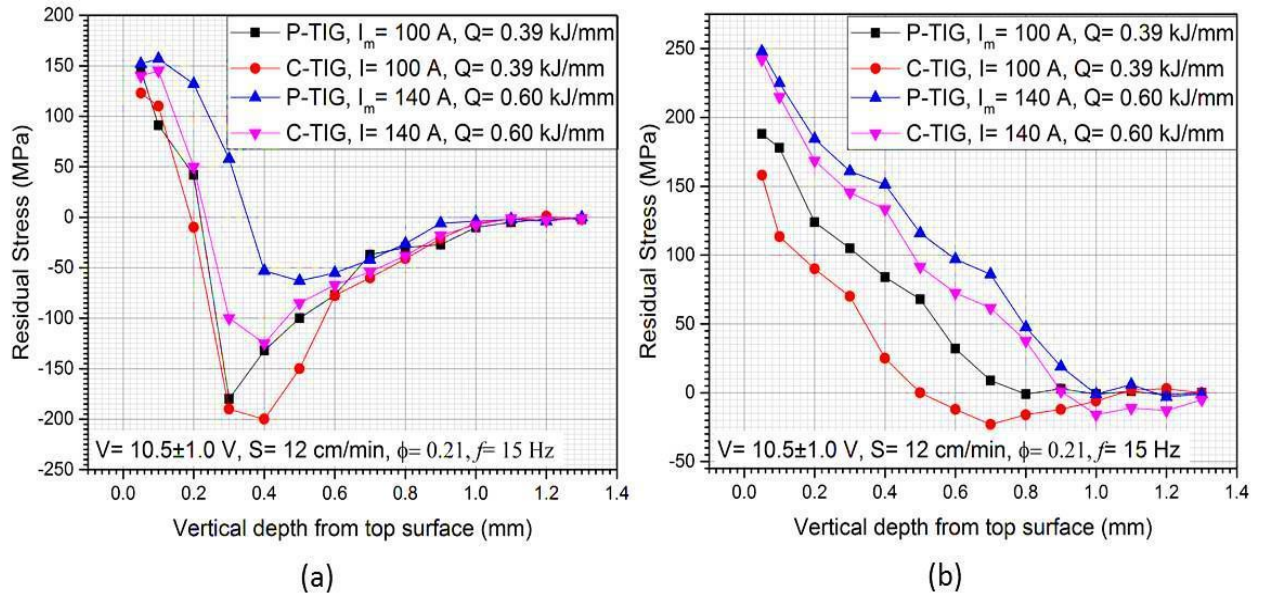
Fig. 5.64 In different components distribution of residual stresses in depth of the matrix modified by single-pass P-TIG and C-TIG arcing processes at heat inputs of 0.39 to 0.60 kJ/mm (a) longitudinal and (b) transverse components.

5.4.7 Effect on fatigue properties

5.4.7.1 Under Tensile loading

The effect of surface modification of the AISI 4340 structural steel by P-TIG arcing processes on fatigue characteristics (S-N curves) has been studied and compared to that of the base metal processed by C-TIG arcing as shown in fig. 5.65. Here the heat input was varied to 0.39 and 0.60 kJ/mm by changing respectively the I_m or I to 100 to 140 A at other arcing parameter such as arc voltage, arc travel speed, ϕ and f are kept constant as 10.5 ± 1.0 V, 12 cm/min, 0.21 and 15 Hz respectively. The fig. 5.65 depicts that the surface modification by P-TIG arcing process at both the heat inputs significantly reduces (16 - 20 %) the endurance limit of its fatigue life in comparison to that observed in case of surface modification by C-TIG arcing process. However, in case of surface modification by both the arcing processes the fatigue life of the substrate has been found to be higher than that of the base metal. The fatigue performance of the surface modified base metal has always been found relatively better when it is done at the lower heat input. Such behaviour of fatigue life of the surface modified AISI 4340 structural steel can be easily understood in light of its microstructure transformation as discussed above.
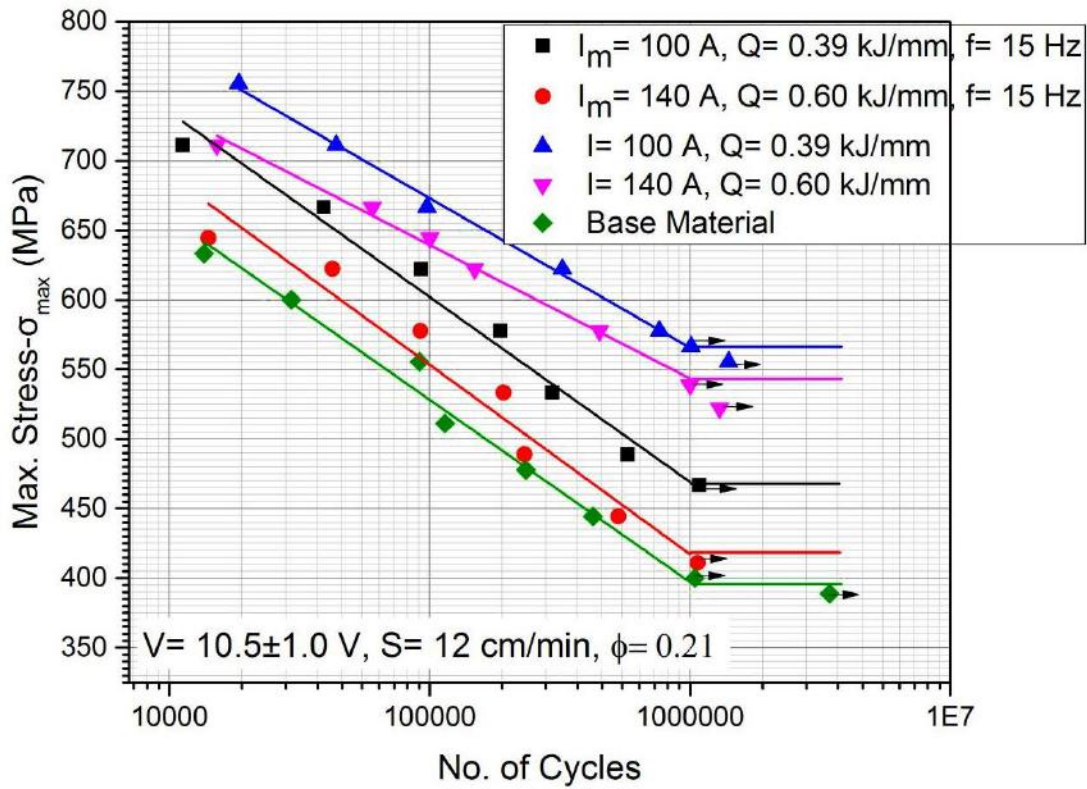
Fig. 5.65 The nature of S-N curve under tensile loading of surface modified AISI 4340 steel prepared by single-pass P-TIG and C-TIG at different heat inputs varied by changing the arcing current compared to the same of unmodified base metal.

5.4.7.2 under bending load

Fatigue life under bending load on the base material and the modified surface, prepared by P-TIG and C-TIG arcing processes has been compared in fig. 5.35. It is observed that the surface modification by C-TIG arcing process at the relatively low and high heat input of 0.39 and 0.60 kJ/mm respectively obtained by keeping arcing current at 100 and 140 A respectively at a given arc voltage and arc travel speed as 10.5 ± 1.0 V and 12 cm/min respectively reduces the endurance limit σ_{max} from 437 to 415 MPa. This is always appreciably lower than the endurance limit of base material having σ_{max} of 477 MPa. The fatigue performance of the modified surface prepared by the P-TIG arcing at the same heat input of 0.39 and 0.60 kJ/mm, obtained by changing I_m to 100 to 140 A respectively at given arc voltage, arc travel speed, ϕ and f as 10.5 ± 1.0 V, 12 cm/min, 0.21 and 15 Hz respectively, has been found further lower than observed in case of the surface modified by C-TIG arcing process. In this case the endurance limit was not even found up to σ_{max} of 375 MPa when the test was abandoned because at this stress level the applied load and amplitude was reaching in the error range of the testing machine. However at this juncture it can be concluded that the fatigue property of the modified surface of AISI 4340 structural steel drastically reduces in case of applying the P-TIG arcing process. This may have primarily attributed to non-compatible hard phase

152

transformation and development of excessive tensile residual stress (Fig. 5.64) in the matrix with respect to that observed in case of using the C-TIG arcing process.
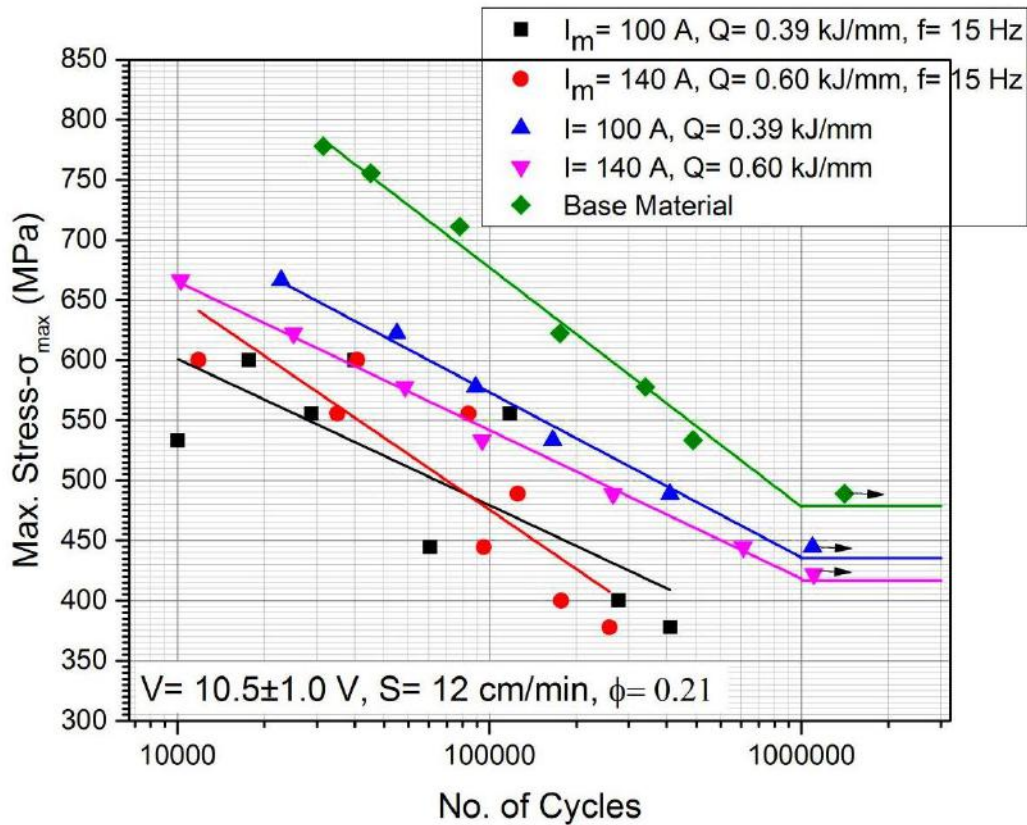
Fig. 5.66   The nature of S-N curve under bending load of surface modified steel prepared by single-pass P-TIG and C-TIG processes at different heat inputs varied by changing the arcing current and compared to the same of unmodified base metal.

5.4.8 Summary

It is observed that the surface modification by using P-TIG arcing process significantly improves the geometrical characteristics of modified zone by increasing the depth of penetration, width of fusion and area of fusion zone and lowering the width of HAZ as compared to that observed in case of surface modification at a given heat input by the C-TIG arcing process. It is clear that application of P-TIG arcing in surface modification increases its cooling rate (Figs. 5.56) which favors more formation of needle shape martensite phase along with some volume fraction of bainite and ferrite. At a given ϕ and f the increase in I_m reduces the fraction of needle martensite and increases the amount of lath martensite, bainite and proeutectoid ferrite in the matrix. It may have primarily happened due to additional heat buildup which retards the cooling rate and promotes the proportion of refined lath martensite.

Variation of arcing current significantly affects the improved hardness of the substrate surface (FZ) with a backup of refined and comparatively lower hardness of HAZ. The use of P-TIG arcing process gives relatively higher hardness in the fusion zone and heat affected zone as

compared to that observed in the C-TIG arcing process performed at a given heat input. The precise control of heat buildup in fused zone in P-TIG arcing process effectively increases the hardness of FZ and HAZ more than 30±10 HV as compared to the hardness obtained in case of the C-TIG arcing process at the same arc current and heat input. As compared to base material the hardness of the FZ and HAZ is increased up to 180 ± 20 % and 60 ± 25 % respectively by employing single-pass P-TIG arcing process.

Tensile and flexural properties are significantly affected by employing the single-pass P-TIG arcing in comparison to those observed in case of surface modification of AISI 4340 steel substrate by single-pass C-TIG arcing process. At appropriate heat input use of P-TIG arcing process significantly enhances the yield strength and ultimate strength to 770 ± 15 and 1060 ± 15 MPa respectively, but reduces the ductility and toughness to 3.3 ± 0.2 % and 22 ± 1 J/mm^3 respectively of the surface modified AISI 4340 steel substrate. Similarly, in the case of flexural test of the modified surface of the AISI 4340 steel substrate prepared by P-TIG arcing, it is observed that the flexural yield and maximum strength is improved, but in-spite of these improvement the flexural extension is decreased in comparison to those observed in case of using the C-TIG arcing process at same heat input of 0.39 and 0.60 kJ/mm.

The residual stresses of tensile nature at the modified surface have always been found relatively higher during arcing at higher heat input of 0.60 kJ/mm than that observed in case of lower heat input of 0.39 kJ/mm. It is gradually reduced to a compressive stress followed by neutral at larger depth in the substrate. Due to it's relatively higher cooling rate and larger transformation of hard phase transformation the use of P-TIG arcing gives relatively higher residual stresses at the modified surface than that observed in case of using the C-TIG arcing process which gives adverse effect on fatigue life.

But in-spite of significant improvement in yield strength and ultimate strength, the reduction in ductility and toughness gave on adverse effect on the fatigue properties under uniaxial tensile loading. Further it is also observed that the fatigue properties are significantly reduced by the application of P-TIG arcing as compared to C-TIG arcing at a given heat input. The endurance limit of its fatigue life was observed at σ_{max} of 475-420 MPa depending upon the I_m of P-TIG arcing process. The fatigue properties of modified surface under bending load are also reduced on employing the P-TIG arcing.

5.5 Characteristics of surface modification by multi-pass P-TIG arcing process

The multi-pass P-TIG arcing process applied over the AISI 4340 steel substrate surface at optimized parameters is discussed in chapter 4. The effect of multi-pass treatment using P-TIG arcing process operated at optimum pulse parameters is studied in terms of microstructural

features and hardness distribution in its different thermally affected regions and compared to those of the similar substrate prepared under the C-TIG arcing process. At a given arc voltage and travel speed of 10.5 ± 1.0 V and 12 cm/min respectively, the typical photographs of the surface appearance of the bead geometry of the fused zone observed during using P-TIG arcing process at heat input of 0.39 and 0.60 kJ/mm obtained from I_m as 100 A and 140 A respectively at ϕ=0.21 and f =15 Hz has been shown in fig. 5.67. The fig. 5.67 also shows the macrograph of transverse section of the modified zone observed under the same conditions of the P-TIG arcing process.

Heat Input (kJ/cm)	I_m (A)	Surface appearance (Scale in mm)	Transverse section (Scale in mm)
0.39	100		
0.60	140		

Fig. 5.67   Typical appearance of modified surface and its transverse section prepared by multi-pass P-TIG arcing at different heat inputs of 0.39 and 0.60 kJ/mm using the I_m of 100 and 140 A respectively.

5.5.1 Microstructural studies

At a given arc voltage and travel speed of 10.5 ± 1.0 V and 12 cm/min respectively, the microstructures of different locations of the zones modified at the heat input of 0.39 and 0.60 kJ/mm by varying I_m of 100 and 140 A have been shown in figs. 5.68 and 5.69, where ϕ and f are 0.21 and 15 Hz respectively. It is observed from the figure that the multi-pass P-TIG arcing also changes the characteristics and morphology of the fused and HAZ of the previous pass through tempering by the subsequent passes. The multi-pass P-TIG arcing also clearly reveals five different zones of microstructure as shown in figs. 5.68 (i-v) and 5.69 (i-v), where the process was operated at the heat inputs of 0.39 (at I_m= 100 A) and 0.60 kJ/mm (at I_m =140 A) respectively, at a given arc travel speed and arc voltage of 12 cm/min and 10.5 ± 1.0 V, respectively. Microstructures of the five different zones of the modified matrix revealed in both the figures (i-v) are defined as follows (i) Initial FZ, (ii) reheat refined FZ, (iii) initial HAZ of base metal, (iv) double reheat refined fusion zone and (v) reheat refined HAZ of base metal respectively. Microstructures of the initial FZ formed at the relatively low and high heat inputs

of 0.39 and 0.60 kJ/mm as shown in figs. 5.68(i) and 5.69 (i) respectively reveal the presence of cast dendritic structure with extensive content of martensite phase in the matrix. However, the morphology of martensite is found relatively coarser in the later one due to comparatively slower cooling at higher heat input. The figs. 5.68 (ii and iv) and 5.69 (ii and iv) show the effect of subsequent passes as ii[nd], iii[rd] and iv[ih] pass respectively on the microstructure of FZ. It is observed from the figures that the microstructure of reheated FZ (Figs 5.68 (ii) and 5.69 (ii)) contains refined and smaller patches of tempered lath martensite along with lower and upper bainite, whereas the microstructure of the double reheated zone (Figs. 5.68 (iv) and 5.69 (iv)) is having uniformly distributed refined martensite plates. The figs. 5.68 (iii and v) and 5.69 (iii and v) show the microstructures of HAZ and reheated refined HAZ of the multi-pass modified zones. The bainite and proeutectoid ferrite with some retained austenite are visible in the microstructure shown in figs. 5.68 (iii) and 5.69 (iii). The refinement of grains is observed in figs. 5.68 (v) and 5.69 (v) with absence of martensite and bainite phases in the matrix.
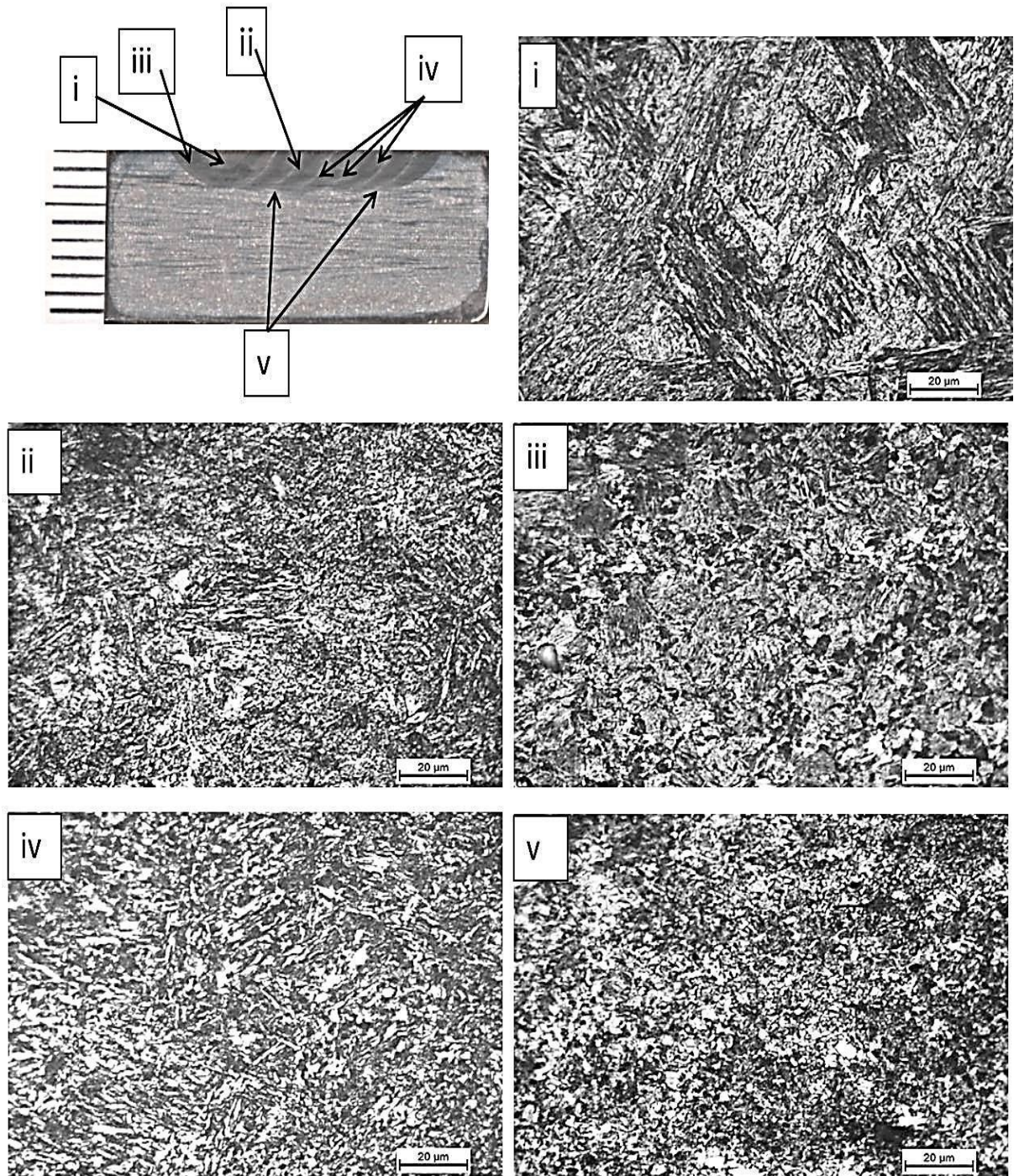
Fig. 5.68 Microstructures of different zones in the multi-pass modified matrix created by P-TIG arcing at a heat input of 0.39 kJ/mm, where arc travel speed, voltage, current, ϕ and f are kept at 12 cm/min, 10.5 ± 1.0 V, 100 A, 0.21 and 15 Hz respectively (i) initial FZ, (ii) reheat refined FZ, (iii) initial HAZ of base metal, (iv) double reheat refined FZ and (v) reheat refined HAZ of base metal.
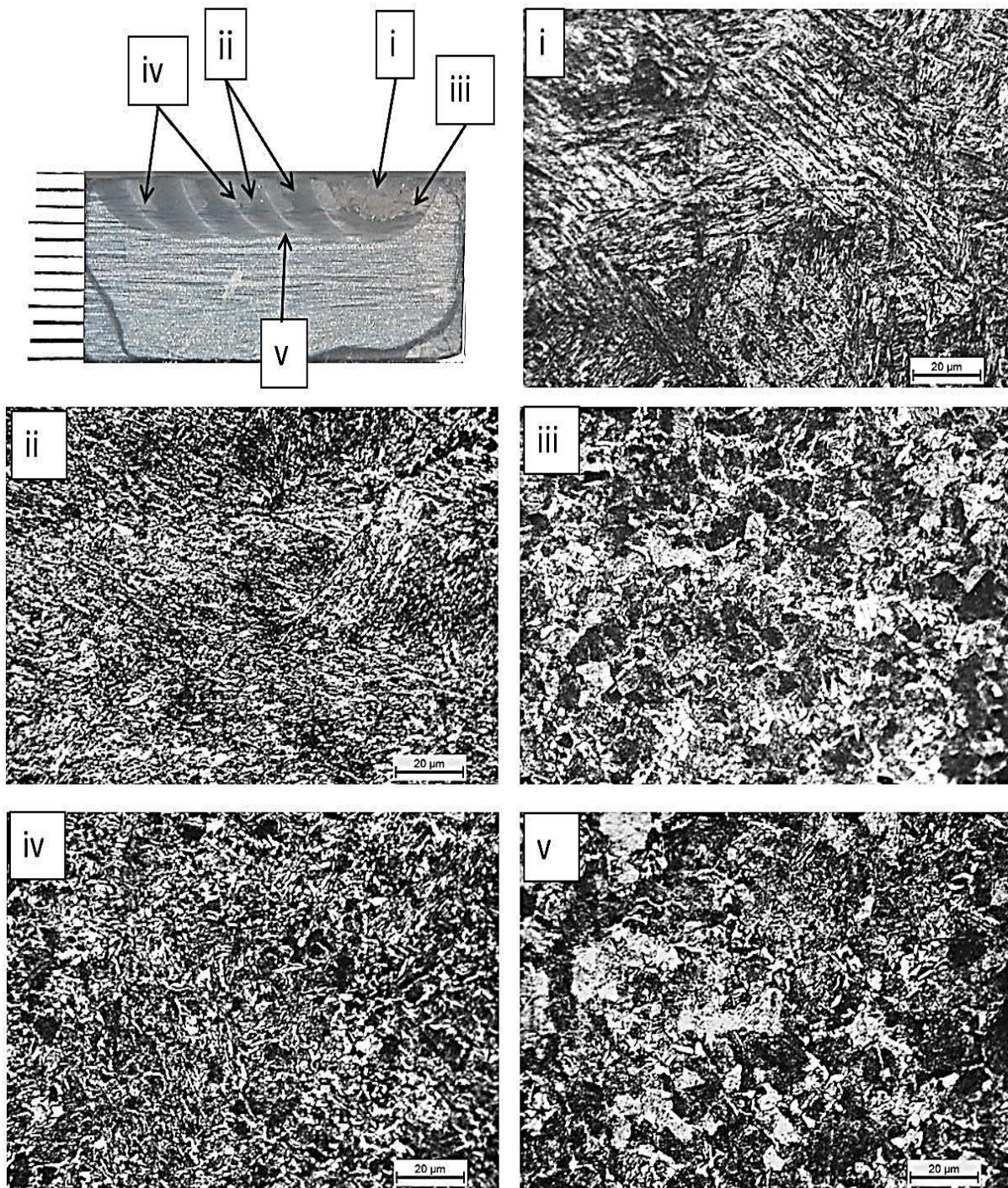
Fig. 5.69   Microstructures of different zones in the multi-pass modified matrix created by P-TIG arcing at a heat input of 0.60 kJ/mm, where arc travel speed, voltage, current, ϕ and f are kept at 12 cm/min, 10.5 ± 1.0 V, 100 A, 0.21 and 15 Hz respectively (i) initial FZ, (ii) reheat refined FZ, (iii) initial HAZ of base metal, (iv) double reheat refined FZ and (v) reheat refined HAZ of base metal.

5.5.2 Hardness Study

At a given arc voltage and travel speed of 10.5 ± 1.0 V and 12 cm/min respectively, the hardness distribution in the surface of the AISI 4340 steel modified by P-TIG and C-TIG arcing process at the heat input of 0.39 and 0.60 kJ/mm obtained by varying I or I_m to 100 and 140 A

158

has been shown and compared in fig. 5.70, where the φ and *f* of 0.21 and 15 Hz respectively. The figure shows that the hardness of the stabilized region (explained in the section 5.3.3) is varied in the range of 486 ± 9 and 460 ± 10 HV at the heat input of 0.39 kJ/mm. Similarly, at the heat input of 0.60 kJ/mm hardness of the stabilized region is found to vary in the range of 438±10 and 457±10 HV. The fig. 5.70 shows that the hardness in stabilized zone of the multi-pass P-TIG arcing process is higher of the order of 35 ± 10 HV as compared to that of the same of the C-TIG arcing process. It is further observed that employing the P-TIG arcing process enhances the width of the modified zone. The variation in hardness is attributed to the characteristics of phase transformation in different location of the modified matrix during using different TIG arcing parameters as discussed earlier.
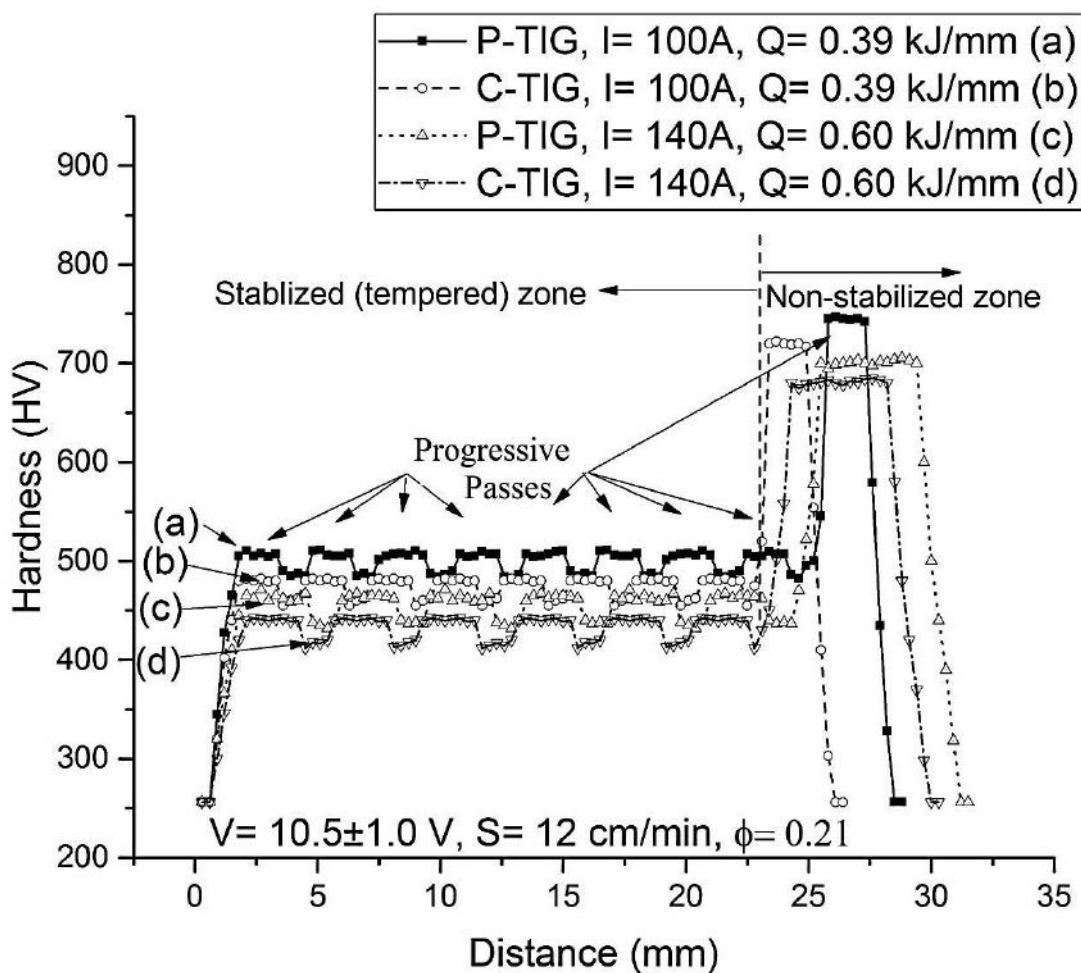
Fig. 5.70   Typical comparative hardness profile in different zones of multi-pass P-TIG and C-TIG arcing modified surface obtained at heat input of 0.39 to 0.60 kJ/mm by changing arcing current to 100 to 140 A.

159

5.5.3 Tensile properties

The average engineering stress versus strain characteristics of the AISI 4340 steel base metal and its modified surface prepared by multi-pass P-TIG and C-TIG arcing at different heat inputs of 0.39 and 0.60 kJ/mm obtained by varying arcing current to 100 and 140 A respectively is shown in fig. 6.71. Here the other parameters such as arc voltage and arc travel speed and the pulse parameters as ϕ and f are kept constant at 10.5 ± 1.0 V and 12 cm/min, 0.21 and 15 Hz respectively. The figure shows that at a given heat input the use of P-TIG arcing process improves the tensile properties in comparison to that of the base material except ductility. Whereas in a comparison to the tensile properties of modified surface prepared by C-TIG arcing process the yield strength is found to be reduced from 725 to 582 MPa when other UTS, toughness and ductility was improved. This may have primarily happened because the microstructure in matrix of the modified zone prepared by P-TIG arcing is transformed relatively more to lath martensite with better optimum reheat refinement in comparison to that observed in case of multipass surface modification by C-TIG arcing process. Thus, it may be inferred that the use of P-TIG arcing process for surface modification of the AISI 4340 structural steel at a given heat input, that gives favourable phase transformations may improve overall tensile properties of the matrix.

Such behaviour is also clearly revealed in fig. 5.72 (a-d), where the yield strength, ultimate tensile strength, toughness and ductility (% strain) respectively of the modified surface are found to be significantly affected by the choice of application of the P-TIG and C-TIG processes at a given heat input. The fig. 5.72 (a) depicts that the yield strength significantly decreases due to employing the P-TIG arcing instead of C-TIG arcing for surface modification at a given heat input and arc travel speed. However, under the similar condition the UTS, toughness and ductility of the modified surface increases significantly due to application of P-TIG arcing instead of C-TIG arcing process as shown in figs. 5.72 (b), (c) and (d) respectively.

160
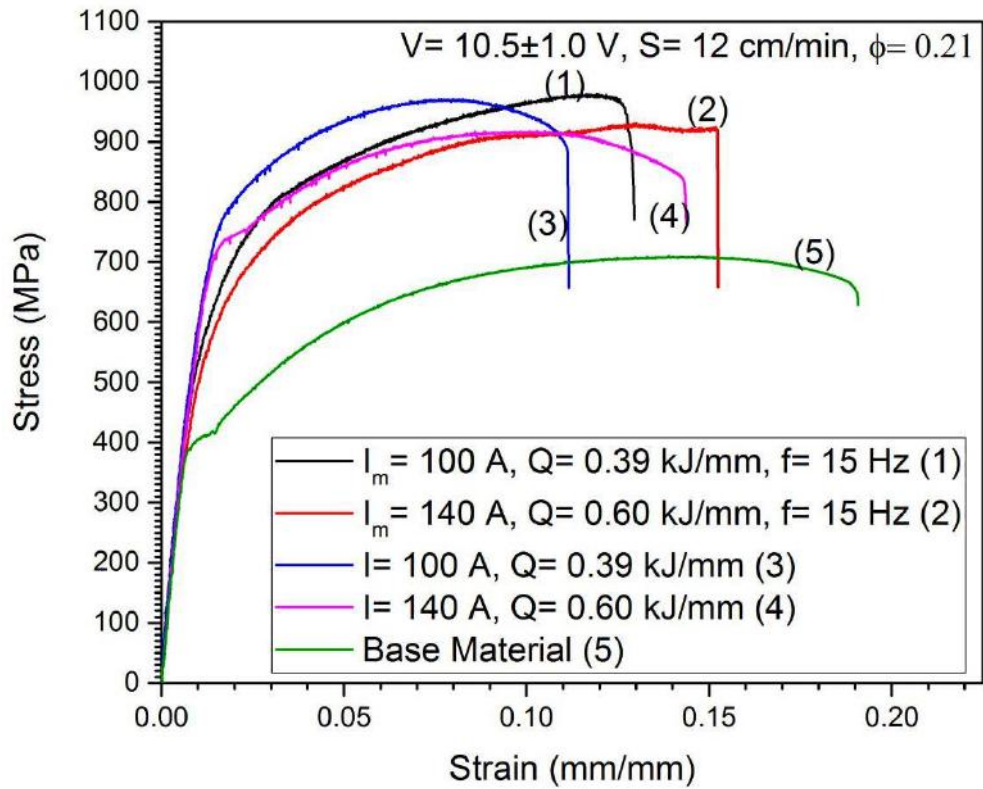
Fig. 5.71   Tensile stress-strain diagram of surface modified AISI 4340 structural steel produced by multi-pass P-TIG and C-TIG arcing at different heat input obtained by varying arc current, where the V, S, ϕ and f are kept constant at 10.5 ± 1.0 V, 12 cm/min, 0.21 and 15 Hz respectively.
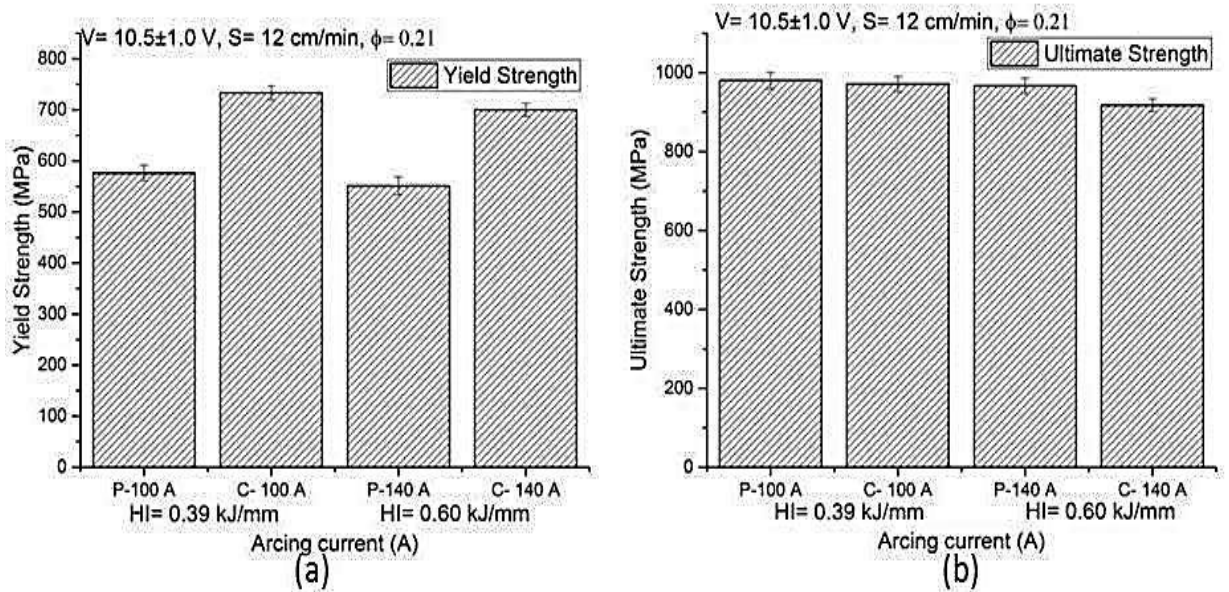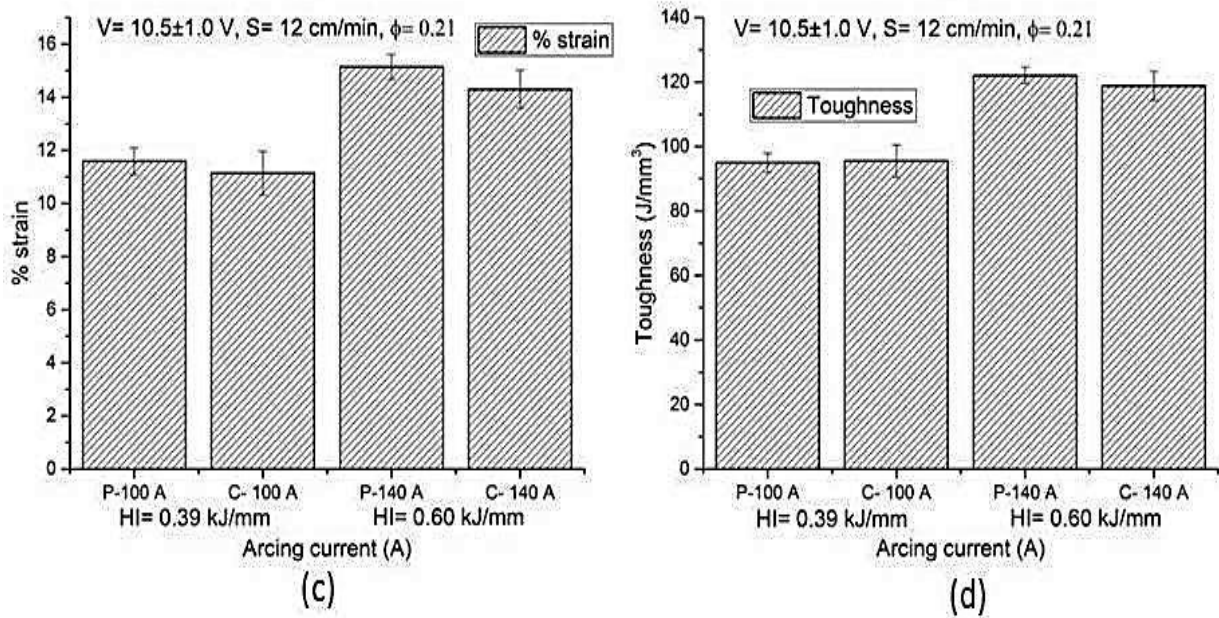
Fig. 5.72   Comparative study on effect of different arcing currents and heat input of multi-pass P-TIG and C-TIG arcing on (a) yield strength, (b) ultimate tensile strength, (c) strain and (d) toughness observed during tensile test of the surface modified AISI 4340 steel substrate.

5.5.4 Three point bend properties

The effect of P-TIG arcing on average flexural stress versus extension characteristics of the modified surface of the AISI 4340 steel substrate and its comparison to that prepared by C-TIG arcing at given heat input of 0.39 and 0.60 kJ/mm has been shown in fig. 5.73. The figure shows that at the heat inputs of 0.39 kJ/mm (I_m = 100 A) and 0.60 kJ/mm (I_m = 140 A), the maximum flexural stress was observed as 1343 and 1246 MPa respectively at the flexural extension of 11.74 and 5.97 mm respectively in case of the surface modified by P-TIG arcing process. Whereas at same heat inputs, the surface modified by C-TIG arcing gives the maximum flexural stress as 1511 and 1387 MPa respectively at the flexural extension of 35 and 14.71 mm respectively. Thus, it is concluded that at a given heat input and arc travel speed the failure has been occurred at relatively low flexural extension in case of P-TIG modified surface than that observed in C-TIG arc modified surface. The extent of hard phase transformation in the matrix of the modified surface is attributed to such change in the flexural properties. The hard phase transformation was generally governed by the increase in cooling rate. This gives an agreement for the surface modification by P-TIG arcing process as discussed earlier. The figure also shows that the surface hardening significantly improves the matrix strength compare to that of the base metal. The flexural yield and ultimate stress has been shown in figs. 5.74 (a) and (b) respectively, where the properties were compared for the substrate surface modified by P-TIG and C-TIG arcing processes. The figs. 5.74 (a) and (b) illustrate that the flexural

properties are reduced by increasing heat input from 0.39 to 0.60 kJ/mm for both the P-TIG and C-TIG arcing process.
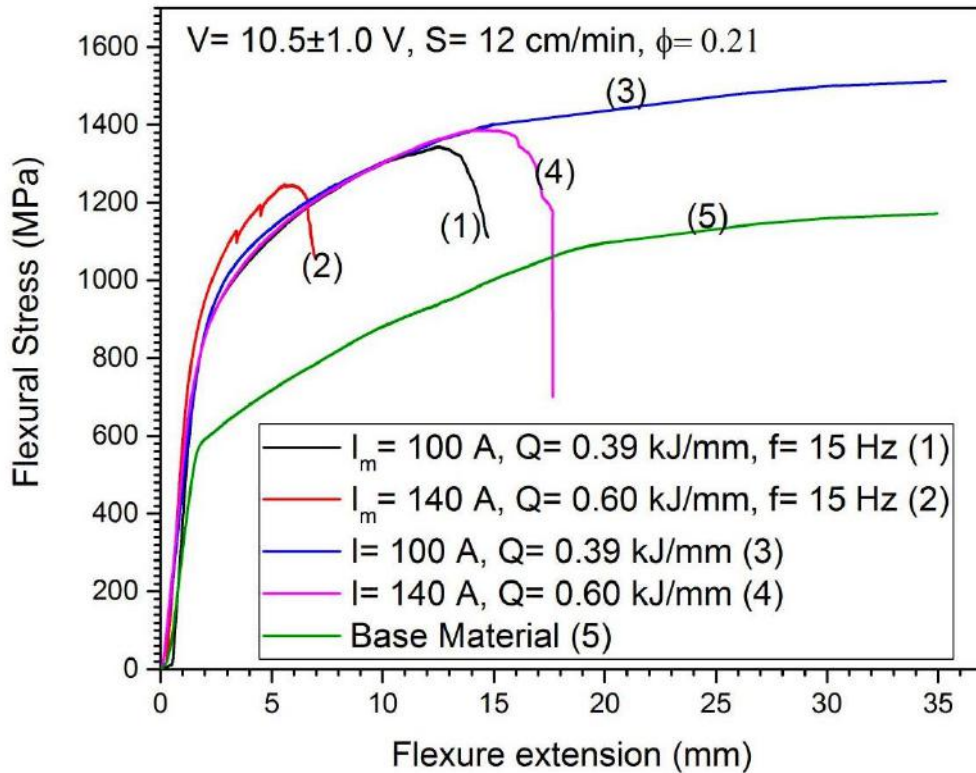
Fig. 5.73   Flexural stress-extension diagram of the modified surface of AISI 4340 structural steel substrate produced by multi-pass P-TIG and C-TIG arcing processes.
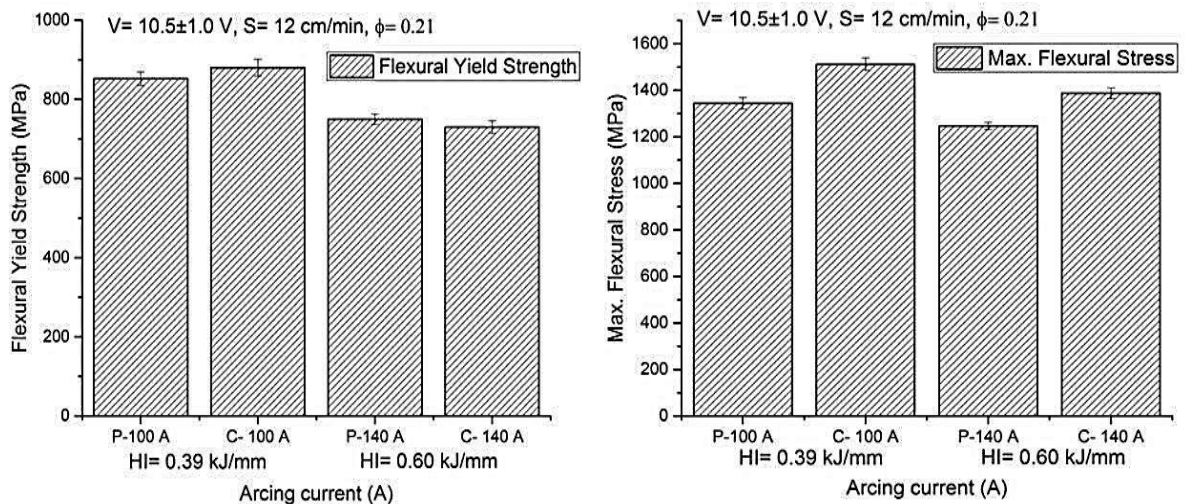
Fig. 5.74   At different arcing currents effect of multi-pass P-TIG (P) and C-TIG (C) arcing on (a) Flexural yield strength and (b) flexural maximum stress of the modified surface of AISI 4340 structural steel substrate.

5.5.5 Residual stress

At a given arc voltage and arc travel speed of 10.5 ± 1.0 V and 12 cm/min respectively, the longitudinal and transverse residual stresses developed in the modified surface of the AISI

4340 structural steel prepared by multi-pass P-TIG and C-TIG arcing process operated at the heat inputs of 0.39 and 0.60 kJ/mm has been shown and compared in figs. 5.75 (a) and (b) respectively. The figures depict that both the multi-pass TIG arcing processes introduce compressive residual stresses at the surface which is appreciably lower in case of using the higher heat input especially at longitudinal component in the matrix. Such compressive stresses gradually decrease and increase respectively in case of the longitudinal and transverse components up to a depth of about 0.4-0.8 mm depending upon heat input and direction stresses. However, it is clearly noticed that at a given heat input the use of multi-pass P-TIG arcing introduces appreciably less residual stresses in the matrix than that observed in case of surface modification by the C-TIG arcing process. It may be further noted that the use of multi-pass surface modification by TIG arcing always maintains a distribution of compressive residual stresses at depth in the substrate which is in contrast to that observed (Fig. 5.64) in case of single-pass surface modification using both the TIG arcing process. Such characteristics of distribution of residual stresses in the surface modified substrate, in agreement to the change in microstructural transformation in the matrix, may give a positive influence on improvement of its fatigue life under dynamic loading.
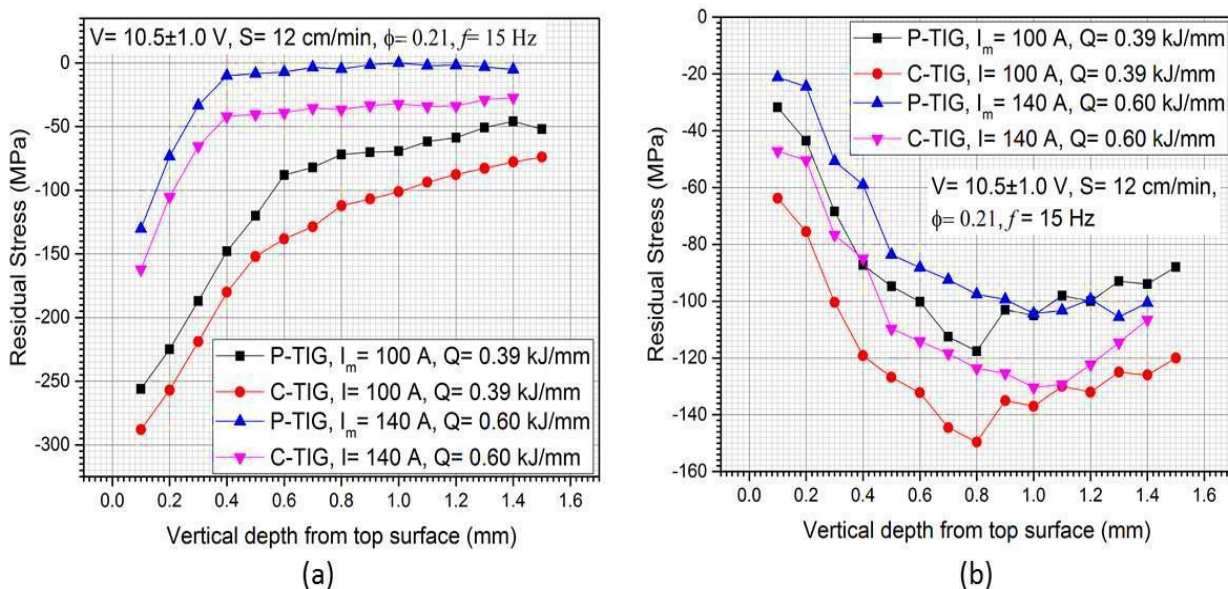
Fig. 5.75   In different components distribution of residual stresses in depth of the matrix modified by multi-pass P-TIG and C-TIG arcing processes at heat inputs of 0.39 to 0.60 kJ/mm (a) longitudinal and (b) transverse components.

5.5.6 Fatigue properties

5.5.6.1 Under Tensile loading

The studies on fatigue characteristics (S-N curves) under uniaxial tensile loading of the surface modified AISI 4340 structural steel produced by multi-pass P-TIG and C-TIG arcing at the heat input of 0.39 and 0.60 kJ/mm, resulting from varying arc current of 100 and 140 A

respectively, is shown in fig. 6.76. Here also the arc voltage and arc travel speed as well as the pulse parameters as ϕ and f are relevantly kept constant at 10.5 ± 1.0 V and 12 cm/min and 0.21 and 15 Hz respectively. The fig. 5.76 depicts that the surface modified by P-TIG arcing at the heat input of 039 kJ/mm has significantly improved the endurance limit as σ_{max} of 500 MPa as compared to that of the base metal. But as compared to the endurance limit (σ_{max} =550 MPa) of the surface modified by C-TIG arcing process, it is found relatively less. However, as the heat input is increased from 0.39 kJ/mm to 0.60 kJ/mm, the finite life as well as endurance limit of S-N curve is decreased during use of both the surface modification processes, where it is found relatively more damaging in case of using the P-TIG arcing process bringing down the endurance limit σ_{max} to 377 MPa which is lower than that of the base metal. The observed improvement and variation in fatigue characteristics of the modified surface prepared by using P-TIG arcing process is largely in agreement to the development and change of compressive residual stress in the matrix as discussed above.
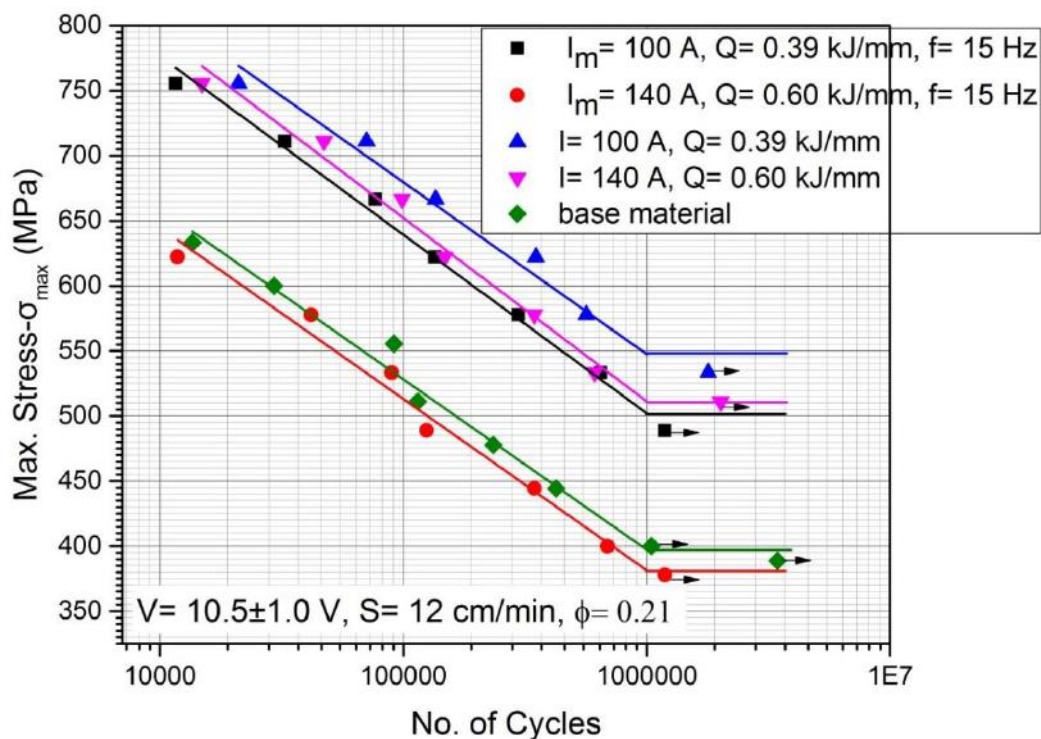
Fig. 5.76   The nature of S-N curve under tensile loading of surface modified AISI 4340 steel prepared by multi-pass P-TIG and C-TIG at different heat inputs varied by changing the arcing current compared to the same of unmodified base metal.

5.5.6.2 under bending load

The typical S-N curve of fatigue behaviour under uniaxial bending load on the modified surface of the AISI 4340 structural steel prepared by multi-pass P-TIG and C-TIG arcing at the heat input of 0.39 and 0.60 kJ/mm, resulting from varying arc current of 100 and 140 A

respectively, is shown in fig. 5.77. The figure depicts that the surface modification by multi-pass P-TIG arcing can significantly improve the endurance limit of the matrix up to σ_{max} in the range of about 560-605 MPa depending upon heat input. It indicates that the surface modification by P-TIG arcing process can improve fatigue performance of the base material of the order of 17–25 % as compared to that of the base metal. The fig 5.77 also depicts that the slope of S-N curve in finite zone is significantly reduced due to surface modification with respect to that of the base metal. sample is failed in less no of cycle at the σ_{max} of 800 MPa. At this juncture, it is understood that at high σ_{max} of about 800 MPa the fatigue life of multi-pass P-TIG arcing is marginally lower, but it is improved considerably to be significantly higher at σ_{max} below about 700 MPa than that of the base metal. Here also it is noticed that surface modification at lower heat input of 0.39 kJ/mm gives relatively higher σ_{max} of the endurance limit than that observed in case of the same produced by using higher heat input of 0.60 kJ/mm. However, the fatigue properties of modified surface prepared by using multi-pass P-TIG arcing is found to be reduced by about 4 to 10 % as compared to the same of the C-TIG arc modified matrix.
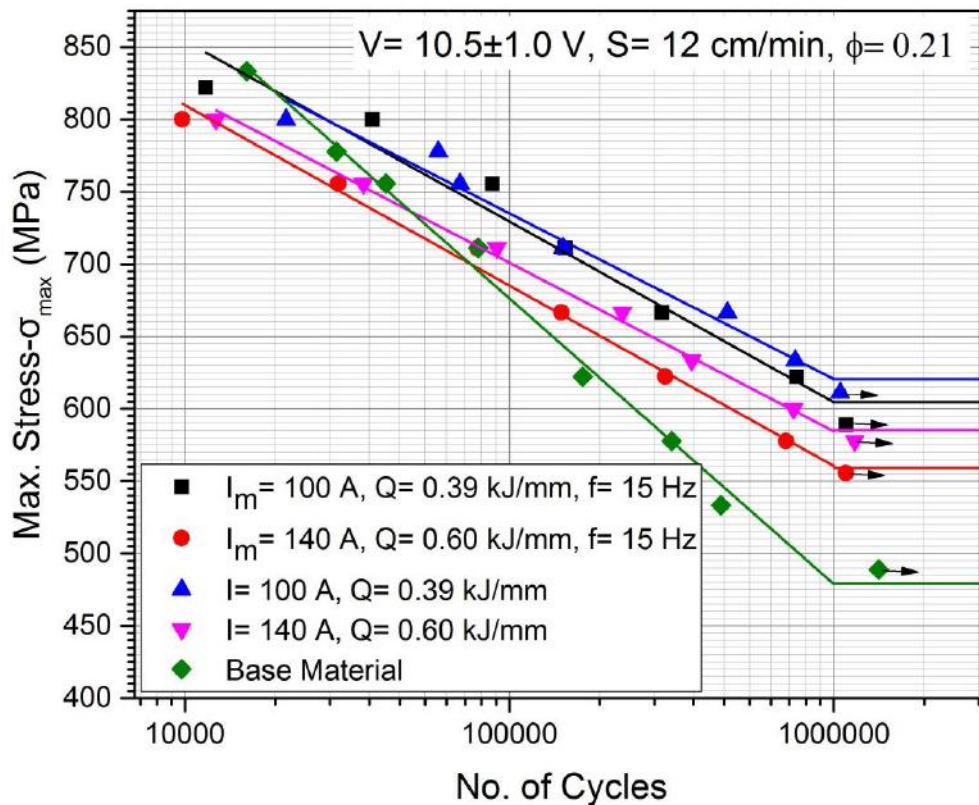
Fig. 5.77   The nature of S-N curve under bending load on the modified surface of the AISI 4340 steel prepared by multi-pass P-TIG and C-TIG processes at different heat inputs varied by changing the arcing current and compared to the same of unmodified base metal.

5.5.7 Summary

The multi-pass P-TIG arcing process for modification of larger surface area can significantly improve the desired mechanical properties of AISI 4340 structural steel. The microstructure of stabilized zone of multi-pass modification primarily consists of tempered lath martensite, bainite and proeutectoid ferrite in different proportions primarily as function of heat input varied by changing the mean current I_m. The effect of tempering is clearly justified by distribution of hardness in the modified zone. The hardness in the stabilized zone is found as 80 ± 10 % more than that of the base metal. The hardness and width of the stabilized zone are found more during the use of multi-pass P-TIG arcing process as compared to that in case of using C-TIG arcing process at a given arcing current. Such behavior is primarily associated with the higher cooling rate of FZ and HAZ, which governs the hard phase transformation in the modified matrix followed by its tempering during multi-pass P-TIG arcing.

Surface modification by the multi-pass P-TIG arcing process shows the reduction in yield strength of the substrate under tensile loading with respect to that observed in case of using multi-pass C-TIG arcing process at a given heat input of 0.39 kJ/mm. Similarly under bending load the multi-pass P-TIG arc modified surface shows the reduction in flexural extension as compared to that of the multi-pass C-TIG arc modified one. It is observed that the increase in heat input to 0.60 kJ/mm gives an adverse effect on the mechanical properties of modified surface under the tensile and three-point bend test. The multi-pass P-TIG arcing process significantly affects the fatigue properties under tensile and bending load depending on heat input where the lower one is preferable. The S-N curve under tensile and bending load shows the reduction in endurance limit by 10 to 30 % and 5 to 10 % respectively in case of employing multi-pass P-TIG and C-TIG arcing process respectively. The observed variation in fatigue properties of the multi-pass TIG arc modified surface is largely in agreement to the development and in depth distribution of compressive stress in the matrix.

5.6 Characteristics of Fatigue Fracture

Characteristics of fatigue fracture of the base material (AISI 4340 steel) happened at σ_{max} of 477 MPa showing a fatigue life of about 23.4×10^4 cycles has been typically presented in figs. 5.78 (a-b). The fig. 5.78 (a) shows the typical feature of intergranular fracture with tear topology. At higher magnification the fracture surface reveals (fig. 5.78 (b)) the presence of fatigue striations in the matrix having average spacing of about 0.09 μm. Similarly, the fractographs of the modified surface prepared at relatively low and high heat inputs precisely of 0.4 and 0.79 kJ/mm have been revealed in figs. 5.78 (c-d) and (e-f) respectively, while the fracture took place showing a fatigue life respectively of about 19.3×10^4 and 14.2×10^4 cycles at

a given σ_{max} of 666 MPa. The different heat inputs of 0.4 and 0.79 kJ/mm were obtained by using different combinations of TIG arcing process parameters as (arcing current= 80 A, arc travel speed= 9 cm/min) and (arcing current=100 A and arc travel speed= 6 cm/min) while the arc voltage is kept constant as 10.5 ± 1.0 V. For fractographic studies of fatigue fracture the samples of surface modification having relatively larger variation of heat input has been chosen in order to facilitate to study the difference in characteristic features affecting the fatigue failure more distinctively. In both the cases of modification at relatively low and high heat inputs the fractured matrix is found to have locations of micro void formation and coalescence along with cleavage facets. However, the amount of cleavage facets present in the matrix is found to be relatively more in case of surface modification at the lower heat input (fig. 5.78 (c)) than that of the other one produced at higher heat input (Fig. 5.78 (e)). This is primarily attributed to the possibility of more hard phase transformation at faster cooling rate of lower heat input (0.40 kJ/mm) as discussed above, which gives comparatively higher matrix strength due more hard phase transformation and thus fails at longer life cycles (19.3×10^4) than that (14.2×10^4) observed in case of the matrix modified at higher heat input (0.79 kJ/mm). In a comparison of matrix morphology of fatigue fracture of the modified surface prepared at the relatively low and high heat input studied at the higher magnification it reveals that both the fractographs contain typical feature of fatigue striation. But the inter striation spacing is found relatively finer (0.15 ± 0.03 μm) in case of using the lower heat input than that observed (0.22 ± 0.03 μm) in case of the surface modified at higher heat input. This is well in agreement to the formation of relatively harder phase transformation in the matrix modified at comparatively lower heat input, which provides the observed higher fatigue life of the specimen than that of the specimen having surface modification at higher heat input. The relatively higher inter striation spacing (0.15 ± 0.03 μm) found in multipass modified matrix than that (0.09 μm) observed in case of fatigue fracture of base metal may have primarily attributed to tempering of microstructure in the modified matrix.

In view of the morphology of fracture surface the possible mechanism of the crack propagation may be realised as the interaction between propagating cracks and interaction of the crack front with relatively tougher phase that restricts crack movement resulting in their reduced growth and increase of striation width. However, in spite of appreciably low inter striation spacing (0.09 ± 0.025 μm) the considerably low fatigue life at a given σ_{max} observed in case of the base material than that of the surface modified one may have largely attributed to significant presence of micro crack formation in the matrix of the former one. The grain boundaries (GBs) are also found to act as a topological obstacle to the propagating crack, where

some sliding may have lead to void formation along it as seen in the matrix [Joshi et. al., 2017]. But in the context of improvement of fatigue life of the surface modified AISI 4340 structural steel the influence of formation of compressive residual stresses in the matrix during the TIG arcing process also cannot be ignored.
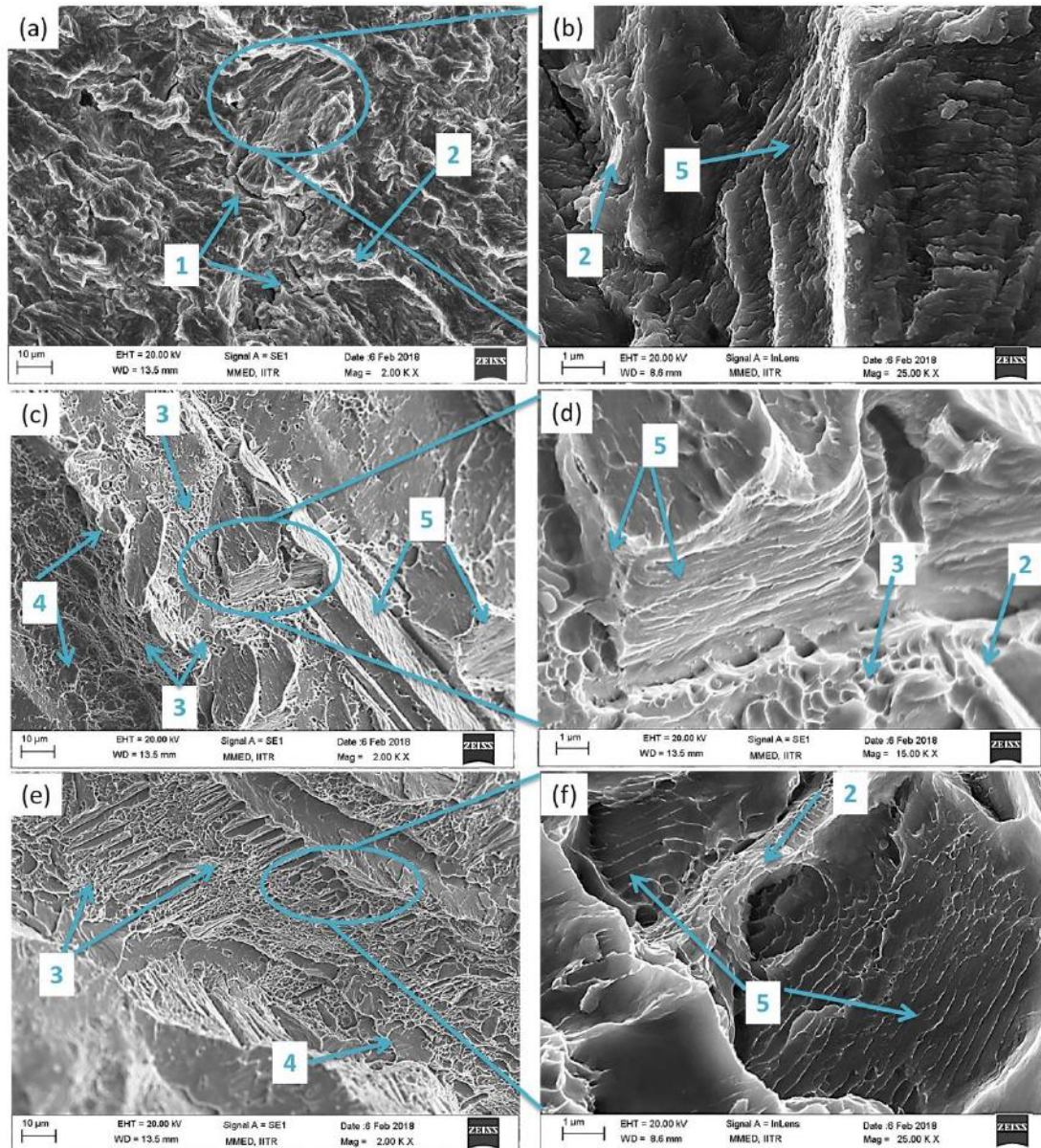
1= Micro Cracks, 2= Tear topology, 3= Micro void coalescence, 4= cleavage facets, 5= Fatigue striation

Fig. 5.78   At relatively low and high magnifications typical appearance of fatigue fracture of (a-b) base metal and surface modified at different heat inputs (c-d) 0.4 kJ/mm and (e-f) 0.79 kJ/mm.

5.7 Basquin Equation

Basquin equation is primarily associated with the finite life of S-N curve, where, at a given σ_{max}, life of a component is calculated or vice versa. Basquin equation known as

$$\sigma_{max} = AN^B \qquad \text{..................................... 6.11}$$

169

where, σ_{max} =maximum cyclic stress, N= Fatigue life, A and B are material based constants.
The mathematical expression to represent the part of the S-N curve for the region $N < 10^6$ may be realised as shown in fig. 5.79.
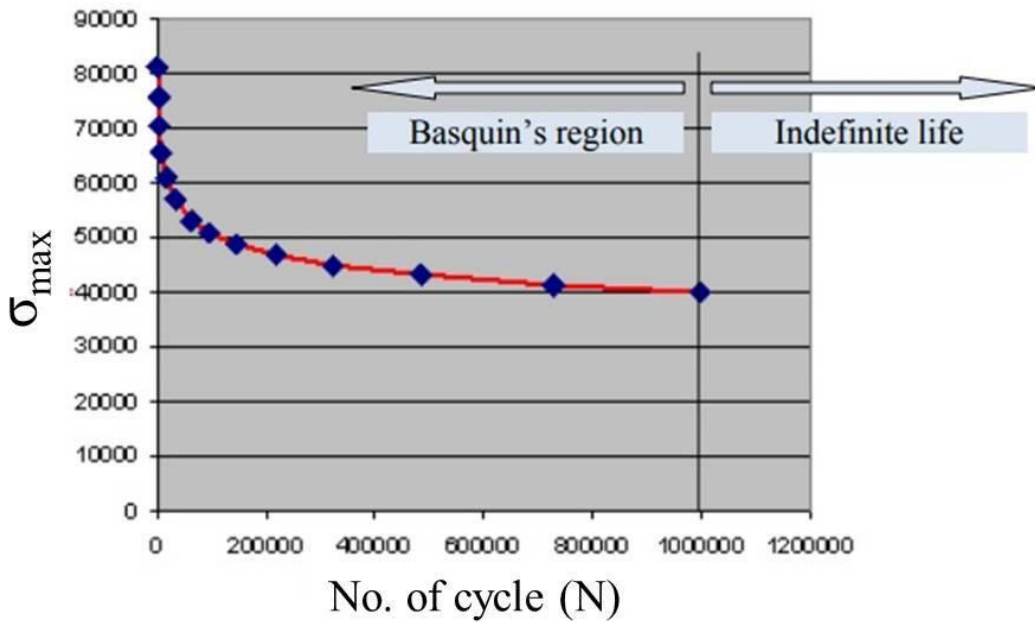
Fig. 5.79   Basquin's equation region on S-N curve

Once the constants A & B are known, then one can determine the maximum fully reversing stress (σ_{max}) for any value of N (less than 10^6) using the Basquin's equation. Alternatively, for a given fully reversing stress σ_{max} greater than endurance limit, we can determine the number of stress reversals (N) after which fatigue failure may occur:

$$N = \left(\frac{\sigma_{max}}{A} \right)^{\frac{1}{B}} \qquad \ldots\ldots\ldots\ldots\ldots\ldots\ldots\ldots\ldots\ldots..6.12$$

The values of the constants A and B of the Basquin's equation has been calculated from the S-N curves (Fig. 6.34, 6.35, 6.52 and 6.53) of surface modified AISI 4340 structural steel produced by single and multi-pass C-TIG arcing process at different arcing parameters, as shown in Table 6.3 to 6.6. The constants A and B for P-TIG arcing process has been shown in table 6.7.

Table 5.3   Constants A and B for fatigue test under uniaxial tensile loading of surface modified AISI 4340 steel substrate produced by single-pass C-TIG arcing.

Fatigue under uniaxial tensile loading		
C-TIG parameter	A	B
Base Material	1725.295	-1.06E-01
I= 80 A,S= 6 cm/min, Q= 0.60 kJ/mm	1492.208	-0.06868

C-TIG parameter	A	B
I= 100 A, S= 6 cm/min, Q= 0.79 kJ/mm	1432.654	-0.06573
I= 120 A, S= 6 cm/min, Q= 0.99 kJ/mm	1474.631	-0.07066
I= 140 A, S= 6 cm/min, Q= 1.21 kJ/mm	1632.904	-0.08099
I= 80 A, S= 9 cm/min, Q= 0.40 kJ/mm	1528.549	-0.07042
I= 100 A, S= 9 cm/min, Q= 0.53 kJ/mm	1434.379	-0.06582
I= 120 A, S= 9 cm/min, Q= 0.66 kJ/mm	1395.26	-0.06382
I= 140 A, S= 9 cm/min, Q= 0.81 kJ/mm	1456.492	-0.06976
I= 80 A, S= 12 cm/min, Q= 0.30 kJ/mm	1459.372	-0.06991
I= 100 A, S= 12 cm/min, Q= 0.39 kJ/mm	1529.772	-0.07188
I= 120 A, S= 12 cm/min, Q= 0.50 kJ/mm	1454.95	-0.06969
I= 140 A, S= 12 cm/min, Q= 0.60 kJ/mm	1346.011	-0.06626
I= 80 A, S= 15 cm/min, Q= 0.24 kJ/mm	1613.28	-0.07432
I= 100 A, S= 15 cm/min, Q= 0.32 kJ/mm	1577.738	-0.07412
I= 120 A, S= 15 cm/min, Q= 0.40 kJ/mm	1626.649	-0.07776
I= 140 A, S= 15 cm/min, Q= 0.48 kJ/mm	1556.526	-0.07753

Table 5.4   Constants A and B for fatigue test under bending load on modified surface of AISI 4340 steel substrate produced by single-pass C-TIG arcing.

Fatigue under bending load		
C-TIG parameter	A	B
Base Material	2590.737	-0.1207
I= 80 A, S= 6 cm/min, Q= 0.60 kJ/mm	1865.676	-0.0986
I= 100 A, S= 6 cm/min, Q= 0.79 kJ/mm	2010.373	-0.10234
I= 120 A, S= 6 cm/min, Q= 0.99 kJ/mm	2082.264	-0.10571
I= 140 A, S= 6 cm/min, Q= 1.21 kJ/mm	1902.05	-0.09916
I= 80 A, S= 9 cm/min, Q= 0.40 kJ/mm	1557.294	-0.09447
I= 100 A, S= 9 cm/min, Q= 0.53 kJ/mm	1657.094	-0.09347
I= 120 A, S= 9 cm/min, Q= 0.66 kJ/mm	1632.122	-0.09062
I= 140 A, S= 9 cm/min, Q= 0.81 kJ/mm	1912.737	-0.10474
I= 80 A, S= 12 cm/min, Q= 0.30 kJ/mm	1633.778	-0.09794
I= 100 A, S= 12 cm/min, Q= 0.39 kJ/mm	1854.206	-0.10339

I= 120 A, S= 12 cm/min, Q= 0.50 kJ/mm	1885.236	-0.10642
I= 140 A, S= 12 cm/min, Q= 0.60 kJ/mm	1630.104	-0.09778
I= 80 A, S= 15 cm/min, Q= 0.24 kJ/mm	1551.117	-0.0971
I= 100 A, S= 15 cm/min, Q= 0.32 kJ/mm	1558.74	-0.0955
I= 120 A, S= 15 cm/min, Q= 0.40 kJ/mm	1644.827	-0.09939
I= 140 A, S= 15 cm/min, Q= 0.48 kJ/mm	1442.655	-0.09185

Table 5.5   Constants A and B for fatigue test under uniaxial tensile loading of surface modified AISI 4340 steel substrate produced by multi-pass C-TIG arcing.

Fatigue under uniaxial tensile loading		
C-TIG parameter	A	B
I= 80 A, S= 12 cm/min, Q= 0.30 kJ/mm	1884.00683	-0.08911996
I= 100 A, S= 12 cm/min, Q= 0.39 kJ/mm	1764.62099	-0.0853086
I= 120 A, S= 12 cm/min, Q= 0.50 kJ/mm	1828.41812	-0.08936065
I= 140 A, S= 12 cm/min, Q= 0.60 kJ/mm	1755.51628	-0.08778906
I= 80 A, S= 15 cm/min, Q= 0.24 kJ/mm	1673.89426	-0.08082458
I= 100 A, S= 15 cm/min, Q= 0.32 kJ/mm	1997.4173	-0.09427816
I= 120 A, S= 15 cm/min, Q= 0.40 kJ/mm	2095.36867	-0.09827861
I= 140 A, S= 15 cm/min, Q= 0.48 kJ/mm	1560.22044	-0.07925258

Table 5.6   Constants A and B for fatigue test under bending load on modified surface of AISI 4340 steel substrate produced by multi-pass C-TIG arcing.

Fatigue under bending load		
C-TIG parameter	A	B
I= 80 A, S= 12 cm/min, Q= 0.30 kJ/mm	1595.943	-0.07148
I= 100 A, S= 12 cm/min, Q= 0.39 kJ/mm	1574.341	-0.0685
I= 120 A, S= 12 cm/min, Q= 0.50 kJ/mm	1573.513	-0.07114
I= 140 A, S= 12 cm/min, Q= 0.60 kJ/mm	1557.604	-0.07178

I= 80 A, S= 15 cm/min, Q= 0.24 kJ/mm	1524.132	-0.06815
I= 100 A, S= 15 cm/min, Q= 0.32 kJ/mm	1487.24	-0.06438
I= 120 A, S= 15 cm/min, Q= 0.40 kJ/mm	1785.686	-0.08524
I= 140 A, S= 15 cm/min, Q= 0.48 kJ/mm	1566.689	-0.0765

Table 5.7 Constants A and B for fatigue test under uniaxial tensile loading of surface modified substrate and bending load on modified surface of AISI 4340 steel substrate produced by single-pass and multi-pass P-TIG arcing.

Fatigue under uniaxial tensile loading		
P-TIG parameter (Single-pass)	**A**	**B**
I= 100 A,S= 12 cm/min, Q= 0.39 kJ/mm, f=15 Hz	1667.727	-0.09219
I= 140 A, S= 12 cm/min, Q= 0.60 kJ/mm , f=15 Hz	1726.29	-0.10386
Fatigue under uniaxial Bending load		
P-TIG parameter (Single-pass)	**A**	**B**
I= 100 A,S= 12 cm/min, Q= 0.39 kJ/mm, f=15 Hz	2053.27	-0.11334
I= 140 A, S= 12 cm/min, Q= 0.60 kJ/mm , f=15 Hz	1927.683	-0.10993
Fatigue under uniaxial tensile loading		
P-TIG parameter (multi-pass)	**A**	**B**
I= 100 A, S= 12 cm/min, Q= 0.39 kJ/mm, f=15 Hz	1848.745	-0.09567
I= 140 A, S= 12 cm/min, Q= 0.60 kJ/mm , f=15 Hz	1739.694	-0.10973
Fatigue under bending load		
P-TIG parameter (multi-pass)	**A**	**B**
I= 100 A, S= 12 cm/min, Q= 0.39 kJ/mm, f=15 Hz	1619.48	-0.07346
I= 140 A, S= 12 cm/min, Q= 0.60 kJ/mm , f=15 Hz	1574.341	-0.07744

The empirical equations generated from the result shown in table 6.3 to 6.66 for Single and multi-pass C-TIG arcing process, with the coefficient of correction is more than 0.95, have been shown below.

Single-pass C-TIG arcing : Empirical equations for uniaxial tensile fatigue of surface modified substrate.

$$A = 1089.36 + 43.64 \times S + 2.94 \times I - 0.3193 \times S \times I \qquad \text{...................6.13}$$

$$B = -0.04222 - 0.00225 \times S - 2.13863 \times 10 - 4 \times I + 1.5843 \times 10 - 5 \times S \times I \quad \text{.............6.14}$$

Single-pass C-TIG arcing : Empirical equations for fatigue under bending load on modified surface of the substrate.

$$A = 1576 - 2.30 \times S + 5.2479 \times I - 0.3803 \times S \times I \qquad \text{...................6.15}$$

$$B = -0.08457 - 1.03 \times 10 - 3 \times S - 1.6286 \times 10 - 4 \times I + 1.26879 \times 10 - 5 \times S \times I \quad \text{.............6.16}$$

Multi-pass C-TIG arcing : Empirical equations for uniaxial tensile fatigue of surface modified substrate.

$$A = 2063.65 - 6.549 \times S - 3.18 \times I + 0.131 \times S \times I \qquad \text{...................6.17}$$

$$B = -0.0851 - 2.3 \times 10 - 4 \times S - 1.5794 \times 10 - 5 \times I + 1.2915 \times 10 - 6 \times S \times I \quad \text{...................6.18}$$

Multi-pass C-TIG arcing : Empirical equations for fatigue under bending load on modified surface of the substrate.

$$A = 2769.05 - 94.165 \times S - 11.4186 \times I + 0.9033 \times S \times I \qquad \text{...................6.19}$$

$$B = -0.1566 + 682 \times 10 - 5 \times S + 83 \times 10 - 5 \times I - 7.064 \times 10 - 5 \times S \times I \quad \text{...................6.20}$$
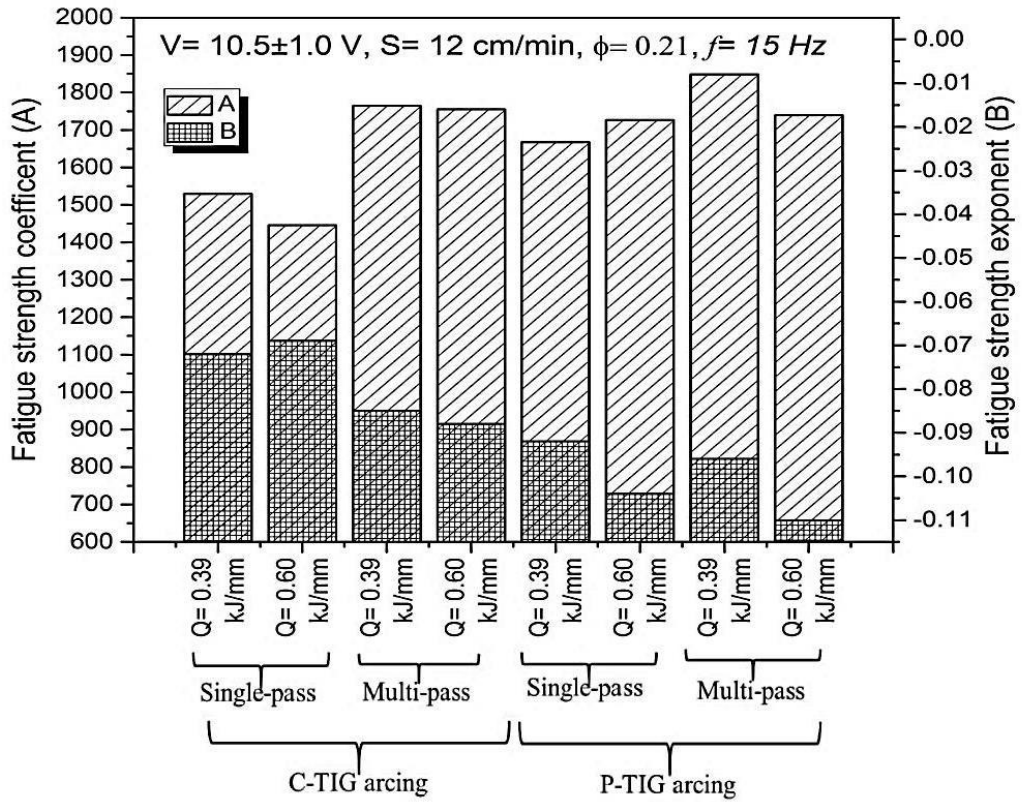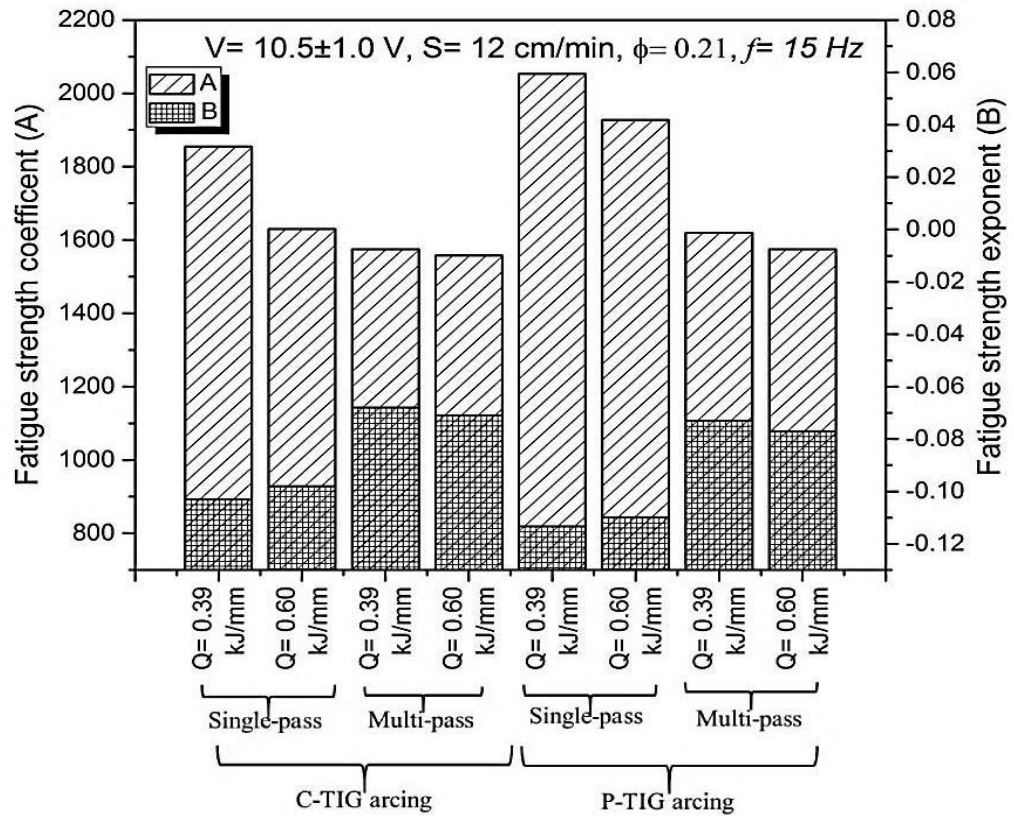
Fig. 5.80 Basquin equation constants 'A' & 'B' at the heat input of 0.39 and 0.60 kJ/mm under single and multi-pass using C-TIG and P-TIG arcing process under (a) tensile loading and (b) bending load.

Basquin equation constants 'A' and 'B' is known as the fatigue strength coefficient and fatigue strength exponent, respectively. The fatigue strength coefficient (A) is closely related to the strength of material and the fatigue strength exponent (B) mainly reflects the cumulative fatigue damage rate of the material [Qiu et. al., 2013]. The fig. 5.80 (a) and (b) shows a comparative study of the fatigue strength coefficient and fatigue strength exponent under uniaxial tensile load on surface modified substrate and bending load on modified surface of the substrate prepared by C-TIG and P-TIG arcing processes used at different heat inputs. Fig. 5.80 (a) shows that during uniaxial tensile loading of single-pass surface modified substrate produced by both the C-TIG and P-TIG arcing the fatigue strength coefficient (A) and the fatigue strength exponent (B) become relatively less and more respectively with respect to that observed in case of multi-pass surfacing at any heat input. However, the A and B are in general found to be relatively more in case of the lower heat input of 0.39 kJ/mm than that observed at the higher heat input of 0.60 kJ/mm used in surface modification. It is also noted that at any heat input the use of P-TIG arcing appreciably enhances the A but reduces the B of surface modified substrate with respect to that observed in case of using C-TIG arcing process. The higher fatigue strength coefficient (A) of P-TIG arcing modified component is in agreement to the well-known capacity of P-TIG process for microstructure modification of matrix for improvement of its mechanical properties.

The characteristics of fatigue strength coefficient (A) and the fatigue strength exponent (B) are found (Fig. 5.80 (b)) very much different in case of applying bending load to the modified surface from that observed during uniaxial tensile loading on surface modified substrate as discussed above. This because the A and B were dependent on the type of test and loading direction [Kogoh et. al., 1990, Liu et. al., 2007] and here the modified surface is directly reacting to the tensile load of the bending force unlike to the tensile load experienced by the modified surface along with the substrate under uniaxial tensile force. The fig. 5.80 (b) shows that during using either of the C-TIG or P-TIG arcing process the multi-pass surface modification significantly reduces the A and enhances the B with respect to those observed in case of the single-pass modification at any heat input. But in both the C-TIG and P-TIG arcing process of surface modification the increase of heat input from 0.39 to 0.60 kJ/mm the A decreases significantly in case of single-pass but marginally at multi-pass procedure. Whereas, under the same condition the increase of heat input marginally increases and decreases the B during using the single-pass and multi-pass procedure of modification respectively. Here also it is observed that the use of P-TIG arcing has significant potential to improve the strength coefficient (A) of modified matrix, due to its considerable ability to modify the matrix

microstructure, over that marked in case of surface modified by C-TIG arcing at a given heat input. This is especially recognised at single-pass procedure because of tempering effect of multi-pass that broadly neutralises any unique characteristics of earlier pass. However, the tempering effect of multi-pass in surface modification by C-TIG or P-TIG arcing appreciably enhances the fatigue strength exponent (B) of the modified matrix under bending load as shown in fig 5.80 (b).

The specific observations made from different facets of the present work have already been given in the corresponding chapters. The final generic conclusions drawn from the present work can be summarized as follows.

1. The C-TIG arcing process has been successfully employed for surface modification of AISI 4340 structural steel with a depth of penetration up to 2.5 mm. Surface properties of modified zone is primarily governed by the isotherm and thermal cycle created by the use of TIG arcing process parameters. A precise control of C-TIG arcing parameter can produce desired phase transformation in the matrix.

2. The hardness in FZ and HAZ of single-pass C-TIG arcing process was increased up to 175 ± 20 % and 50 ± 20 % respectively as compared to base metal.

3. The single-pass C-TIG arcing process improves yield strength and UTS of the order of 50 % (600 MPa) and 28 % (900 MPa) respectively, but reduces the ductility and toughness by 65 % (6%) and 67 % (38 J/mm^3) respectively at an appropriate arcing parameter as compared to those of the base metal. Whereas the flexural properties is significantly reduced except in case of the surface modification at arc travel speed of 6 cm/min. Residual stresses and microstructural modification was relatively more prominent for such behavior. Tensile residual stresses are observed in the range of 150 $\pm$ 10 MPa up to a depth of 0.25 mm followed by compressive residual stress in the range of 200 MPa in longitudinal direction.

4. The fatigue characteristics (S-N curve) under tensile loading shows that the endurance limit of σ_{max} can be increased up to 577 MPa depending on the single-pass C-TIG arcing process parameter. It shows improvement of the order of 45 % as compared to base material. Such improvement is primarily associated with the improvement in tensile yield strength by 50 %.

5. Hardness of the modified zone prepared by multi-pass C-TIG arcing process is reduced up to 30 ± 5 % as compared to that observed during use of single-pass TIG arcing process due to the tempering effect. Hardness of modified surface can be raised up to 445 ± 25 HV by using multi-pass C-TIG arcing. When the base metal hardness was 250 HV.

6. The tensile and three point bend properties were significantly improved with the help of surface modification by multi-pass C-TIG arcing process as compared to single-pass C-TIG arcing process. Such improvement was primarily attributed to 1) tempering of microstructure and 2) development of compressive residual stress in the modified zone.

7. Multi-pass surface modification can significantly improve the flexural yield strength and maximum strength of the base metal from 540 and 1160 MPa respectively to 880 and 1511 MPa respectively. Such improvements are primarily attributed to the desired phase transformation in the matrix microstructure due to appropriate variation in the isotherm and thermal cycle at different operating parameters of the TIG arcing process.

8. As the static mechanical properties was increased by multi-pass modification using C-TIG arcing process, subsequently the dynamic (fatigue) properties (endurance limit) are significantly improved to $25 - 37$ % and $13 - 30$ % under tensile and bending load respectively. Such improvement was observed because multi-pass C-TIG arcing process has introduced compressive residual stress in longitudinal and transverse direction in the range of 163 to 289 MPa and 45 to 110 MPa respectively.

9. The changes in characteristics of the modified surface produced by multi-pass C-TIG arcing process are realized as a function of heat input, which is varied by change in arcing current and arc travel speed at a given arc voltage of the TIG arcing process. In this regard the optimum arcing current and arc travel speed are found to be 100 A and 12 cm/min, respectively, at an arc voltage of about 10.5 ± 1.0 V.

10. For industrial application, multi-pass TIG arcing process is applied over the surface which significantly increases the surface characteristics. However, some reduction in properties is found due to tempering of modified zone which will be acceptable because the improvement was observed in mechanical properties in static and dynamic loading.

11. The bead geometry obtained by C-TIG arcing process can be increased up to 4-8 % by employing P-TIG arcing process at a same heat input and arc travel speed. However, it is found that the hardness of FZ and HAZ has been increased by 35 ± 10 HV by employing P-TIG arcing instead of C-TIG arcing at a given heat input and travel speed. This was primarily happened due to increase in cooling rate of FZ and HAZ which promotes harder phase transformation in the matrix.

12. During single-pass modification the use of P-TIG arcing process instead of C-TIG arcing process reduces the ductility and flexural extension. That directly affects the fatigue properties (S-N curve) by reducing it up to 16 - 20 % during tensile loading. Similar behavior was also observed in case of multi-pass P-TIG arcing process.

13. For proper control of parameters to achieve desired properties and thermal characteristics, a thermal model is established and justified by experimental verification as a guide to govern and control the arcing parameters to achieve desired phase transformation and properties in the modified zone.

14. Finally, it may be concluded that both the C-TIG and P-TIG arcing processes are suitable for surface modification of AISI 4340 structural steel for industrial application in terms of achieving significantly high surface hardness and high depth of required modified zone along with high compressive residual stresses. However in this regard the P-TIG arcing process is found superior to the C-TIG arcing process in terms of higher depth of modified zone, lower HAZ width, and higher hardness. If the selection criterion for the surface modification is mechanical properties, then C-TIG arcing process has been found superior to P-TIG arcing process.

LIST OF PUBLICATIONS

In International Journals:

1. **Sudhir Kumar**, P.K.Ghosh and Ravindra Kumar, "Surface modification of AISI 4340 steel by multi-pass TIG arcing process", Journal of Materials Processing Technology 249 (2017), 394–406. doi:10.1016/j.jmatprotec.2017.06.035.

2. **Sudhir Kumar**, P.K.Ghosh "TIG arc processing improves tensile and fatigue properties of surface modified AISI 4340 steel", International Journal of Fatigue, 2018, (accepted). doi:10.1016/j.ijfatigue.2018.06.036

In conferences:

1. **Sudhir Kumar**, P.K.Ghosh and Ravindra Kumar, **"**Surface modification of AISI 4340 structural steel by single and multi-pass TIG arcing process". Procd. Intl. Conf. Advances in Materials & Processing: Challenges and Opportunity (AMPCO 2017), Indian Institute of Technology (IIT) Roorkee, December (2017)

SCOPE FOR FUTURE WORK

In light of the understanding on the work presented in this report, it is realised that following aspects of studies have to be carried out further to improve the reliability and performance of modified surface by TIG arcing process.

1. The effect of TIG arcing process should be tried for other materials like aluminium, magnesium and titanium etc. to establish more extensive utilization of the process.

2. The distortion analysis should be performed in order to understand the efficacy of TIG arcing process to maintain acceptable dimensional tolerance of modified component under the development of significant residual stresses over the surface.

3. Studies on P-TIG arcing should be carried with detail variation of pulse parameters having significant influence on thermal characteristics of the process affecting differently the phase transformation in the matrix of different substrate.

4. The TIG arcing process can be used for introducing nano particle over the substrate surface (composite) to increase the surface properties.

5. The wear analysis may be tried at different loads and sliding speeds to understand the detailed analysis of the wear mechanism.

6. TEM analysis may be performed to understand the phase transformation in detail.

1. Agrawal B.P., **Ghosh P.K.,** [2010], Thermal Modeling of Multipass Narrow Gap Pulse Current GMA Welding by Single Seam per Layer Deposition Technique, Mater. Manuf. Process. 25, 1251–1268.

2. Agrawal B.P., **Ghosh P.K.,** [2014], Influence of thermal characteristics on microstructure of pulse current GMA weld bead of HSLA steel, Int. J. Adv. Manuf. Technol. 77, 1681–1701.

3. **Ali, N.**, Fan, Q.H., Ahmed, W., Gracio, J., 2002. Deposition of polycrystalline diamond films using conventional and time-modulated CVD processes. Thin Solid Films 420–421, 155–160.

4. **Arivarasu, M.**, Devendranath R., K., and Arivazhagan, N., [2014], "Comparative studies of high and low frequency pulsing on the aspect ratio of weld bead in gas tungsten arc welded AISI 304L Plates.", Procedia Eng. 97, pp. 871–880.

5. **Asi, O.**, Can, A.Ç., Pineault, J., Belassel, M., [2007], "The relationship between case depth and bending fatigue strength of gas carburized SAE 8620 steel.", Surf. Coatings Technol., Vol. 201, pp. 5979–5987.

6. **ASTM**, 2013. Determining Residual Stresses by the Hole-Drilling Strain-Gage Method. Stand. Test Method E837-13a i, 1–16

7. **ASTM** – E855-08, 2013. Standard Test Methods for Bend Testing of Metallic Flat Materials for Spring Applications Involving Static Loading. Annu. B. ASTM Stand. 03.01, 1–8.

8. **ASTM** Int., 2017. Standard Practice for Conducting Force Controlled Constant Amplitude Axial Fatigue Tests of Metallic Materials. Astm 1–6.

9. **ASTM** Int., 2016. Standard Test Methods for Tension Testing of Metallic Materials 1. Astm 1–27.

10. **ASTM**, S.T.M., 2014. E 0290 Bend Testing of Material for Ductility. Astm 1–10.

11. **Atamert, S.** and Bhadeshia, H. K. D. H., [1989], "Comparison of the microstructures and abrasive wear properties of stellite hardfacing alloys deposited by arc welding and laser cladding.", Metall Trans. A, Vol. 20 (6), pp. 1037–1054.

12. Bag, S., **De, A.,** 2008. Development of a three-dimensional heat-transfer model for the gas tungsten arc welding process using the finite element method coupled with a genetic algorithm-based identification of uncertain input parameters. Metall. Mater. Trans. A Phys. Metall. Mater. Sci. 39, 2698–2710.

13. **Bakshi, S.R.** and Harimkar S.P., [2015] "Surface Engineering for Extreme Conditions.", JOM, Vol. 67, pp. 1526-1527.

14. **Balasubramanian, V.**, Ravisankar, V. and Reddy, M. G., [2008], "Effect of pulsed current welding on fatigue behaviour of high strength aluminium alloy joints.", Mater. Des., Vol. 29, pp. 492–500.

15. **Baragetti, S.,** La Vecchia, G.M., Terranova, A., 2005. Variables affecting the fatigue resistance of PVD-coated components. Int. J. Fatigue 27, 1541–1550.

16. **Barkoula, N.M.,** Alcock, B., Cabrera, N.O., Peijs, T., [2008], "Fatigue properties of highly oriented polypropylene tapes and all-polypropylene composites.", Polym. Polym. Compos., Vol. 16, pp. 101–113.

17. **Barnes, Stuart,** Nash, Michael J., Kwok, Y. K.. 2003. Surface modification of powder metallurgy components with a direct diode laser. Journal of Engineering Materials and Technology, Volume 125 (Number 4), pp. 372-377

18. **Batahgy A. M.,** Ramadan, R.A. and Moussa, A., [2013], "Laser Surface Hardening of Tool Steels- Experimental and Numerical Analysis." J. S. Engg. Mat. Ad. Tech., Vol. 3 (02), pp. 146–153.

19. **Béjar, M.A.** and Henríquez, R., [2009], "Surface hardening of steel by plasma-electrolysis boronizing.", Mater. Des. 30, pp. 1726–1728.

20. **Bendeich,** P., Alam, N., Brandt, M., Carr, D., Short, K., Blevins, R., Curfs, C., Kirstein, O., Atkinson, G., Holden, T., Rogge, R., 2006. Residual stress measurements in laser clad repaired low pressure turbine blades for the power industry. Mater. Sci. Eng. A 437, 70–74.

21. Bhadeshia, H.K.D.H., Honeycombe, R.W.K., 2005. Steels Microstructure and Properties, third. ed. Butterworth-Heinemann, London.

22. **Bochnowski, W.,** [2010], "The influence of the arc plasma treatment on the structure and microhardness C120U carbon tool steel.", Vol. 10, pp. 331–334.

23. **Boiko V. I.,** Valyaev A.N., Pogrebnyak A. D. and Uspekhi F. N., [1999],"Metal modification by high-power pulsed particle beams.", Vol.169 (11), pp. 1243-1248.

24. **Briant, C.L.,** [1981], "The effect of nickel, chromium, and manganese on phosphorus segregation in low alloy steels." Scripta Metallurgica, Vol. 15(9), pp. 1013-1018.

25. **Bugaev S.P.,** Korovin S.D., Koval N.N., Oks E.M., Proskurovsky D.I. and Sochugov N.S., [2002], "Intense low-energy electron and ion beams and their application. Conference Record of the Twenty-Fifth International Power Modulator Symposium", High-Voltage Workshop., pp. 548-55.

26. **Calik A.**, [2009], "Effect of cooling rate on hardness and microstructure of AISI 1020 , AISI 1040 and AISI 1060 Steels.", Int. J. Phys. Sci., Vol. 4, pp. 514–518.

27. Cao, Y.J., Sun, J.Q., Ma, F., Chen, Y.Y., Cheng, X.Z., Gao, X., Xie, K., 2017. Effect of the microstructure and residual stress on tribological behavior of induction hardened GCr15 steel. Tribol. Int. 115, 108–115.

28. **Cary, H.B.**, [1995], "Arc Welding Automation.", 1st Edn., CRC Press, New York., ISBN: 10: 0824796454, pp: 325.

29. **Chatterjee, A.**, Moitra, A., Bhaduri, A.K., **Chakrabarti, D.,** Mitra, R., [2014], "Effect of heat treatment on ductile-brittle transition behaviour of 9Cr-1Mo steel.", Procedia Eng. Vol. 86, pp. 287–294.

30. **Chen, S.B.**, Lou, Y. J., WU L. and Zhao, D. B., [2000], " Intelligent Methodology for Sensing , Modeling and Control of Pulsed GTAW : Part l Bead on plate welding.", Welding research supplement, pp. 151s–163s.

31. **Chiumenti M.**, Miguel C., Salmi A., Carlos A., Narges D. and Kazumi M., [2010] "Finite element modeling of multi-pass welding and shaped metal deposition processes.", Computer Methods in Applied Mechanics and Engineering, Vol. 199, pp. 2343-2359.

32. **Clare, A.,** Oyelola, O., Folkes, J. and Farayibi, P., [2012], "Laser cladding for railway repair and preventative maintenance.", J. Laser Appl., Vol. 24 (3), pp. 032404-32414.

33. **Collins J.A.**, [1993], "Failure of Materials in Mechanical Design: Analysis, Prediction, Prevention.", 2nd ed. New York: John Wiley & Sons.

34. **Cook, G.E.** and Hussam, E. D., [1985], "The Effect of high-Frequency pulsing of a welding arc.", IEEE trans. Ind. App., Vol 1A-21 (5), pp. 1294–1299.

35. **Cordovilla, F.,** García-Beltrán, Á., Sancho, P., Domínguez, J., Ruiz-de-Lara, L., Ocaña, J.L., 2016. Numerical/experimental analysis of the laser surface hardening with overlapped tracks to design the configuration of the process for Cr-Mo steels. Mater. Des. 102, 225–237.

36. **David A. P.**, Easterling, K.E and Sherif, M., [2009], "Phase Transformations in Metals and Alloys.", CRC Press, London,

37. **Davis C.L.** and King J.E., [1993], "Effect of cooling rate on intercritically reheated microstructure and toughness in high strength low alloy steel.", Mater. Sci. Technol., Vol. 9, pp. 8–15.

38. **Damborenea, D. J.**, [1998], "Surface modification of metals by high power lasers.", Surf. Coatings Technol., Vol. 100-101, pp. 377–382.

39. **De, A.** and DebRoy T., [2011], "A perspective on residual stresses in welding. Sci. Technol." Weld. Join., Vol. 16, pp. 204–208.

40. **De A.,** Walsh C., Maiti S.K. and Bhadeshia H.K.D.H., [2003], "Prediction of cooling rate and microstructure in laser spot welds, Sci. Technol.", Weld. Join., Vol. 8, pp. 391–399.

41. **Dieter, G.E.,** [1988], "Mechanical Metallurgy", *McGraw-Hill book company*, UK.

42. **Dieter, R.,** [1992], "Heat Effects of Welding: Temperature Field, Residual Stress, Distortion", Springer-verlag, Newyork.

43. D.K. Singh, P.K. Ghosh, M. Breazu and **L. Issler,** [1991] "Mechanical properties of TIG welded Al-Zn-Mg alloy", *Indian Weld. J.*, Vol.24(4): pp. 225-230.

44. **Durgutlu, A.**, [2004], "Experimental investigation of the effect of hydrogen in argon as a shielding gas on TIG welding of austenitic stainless steel.", Mater. Des., Vol. 25, pp. 19–23.

45. **Dziedzic, A.** and Bylica A, [2008], "The microstructure of HS 6-5-2 steel in the areas overlapping remelting obtained by the use of GTAW method.", Vol. 8, pp. 47–52.

46. Elmesalamy, A., **Francis, J. A.,** & Li, L. [2014], "A comparison of residual stresses in multi pass narrow gap laser welds and gas-tungsten arc welds in AISI 316L stainless steel", *International Journal of Pressure Vessels and Piping*, Vol.*113*: pp.49-59.

47. **Fan, F.G** and Kovacevic. R., [2004], "A unified model of transport phenomena in gas metal arc welding including electrode, arc plasma and molten pool", *Journal of Physics D: Applied Physics*, Vol. 37, pp 2531–2544.

48. **Fan H.G.**, Shi Y.W. and Na S.J. [1997], "Numerical analysis of the arc in pulsed current gas tungsten arc welding using a boundary-fitted coordinate." Journal of Materials Processing Technology, Vol. 72, pp. 437-445.

49. **Farahani, E.**, Shamanian, M. and Ashrafizadeh, F., [2012], "A Comparative Study on Direct and Pulsed Current Gas Tungsten Arc Welding of Alloy 617.", Int. J. on Manufacturing and Material Science, Vol. 2(1), pp. 1–6.

50. **Francis, J.A**., Bhadeshia, H.K.D.H. and Withers, P.J., [2013], "Welding residual stresses in ferritic power plant steels", *Materials Science and Technology*, Vol. 23(9), pp. 1009-1020.

51. **Farfan S.,** Rubio-Gonzalez C., Cervantes-Hernandez T. and Mesmacque G., [2004] "High Cycle Fatigue, Low Cycle Fatigue and Failure Modes of a Carburized Steel. Intl. J. Fatigue" Vol. 26(6),pp. 673–678.

52. **Franjo C**, Darko L. and Vojteh L., [2010], "Surface Modifications of Maraging Steels used in the Manufacture of moulds and dies.", Materials and Technology, Vol. 44, pp. 85–91.

53. Fu, Y., Hu, J., Shen, X., Wang, Y., Zhao, W., 2017. Surface hardening of 30CrMnSiA steel using continuous electron beam. Nucl. Instruments Methods Phys. Res. Sect. B Beam Interact. with Mater. Atoms 410, 207–214.

54. **Garcés, Y.,** Sánchez, H., Berríos, J., Pertuz, A., Chitty, J., Hintermann, H., Puchi, E.S., 1999. Fatigue behavior of a quenched and tempered AISI 4340 steel coated with an electroless Ni-P deposit. Thin Solid Films 355, 487–493.

55. **Ghosh, P.K.,** [2017], "Pulse Current Gas Metal Arc Welding- *Materials Forming, Machining and Tribology*", Springer Singapore,

56. **Ghosh, P.K.** and Kumar, R., [2015], "Surface Modification of Micro-Alloyed High-Strength Low-Alloy Steel by Controlled TIG Arcing Process.", Metall. Mater. Trans. A, Vol. 46, pp. 831–842.

57. **Ghosh, P.K.** and Dorn, L**.,** [1993], "Thermal behaviour of pulsed MIG Al-Zn-Mg weld – An analytical model analysis", *International Journal on Joining of Materials*, Vol. 5(4), pp 143-150.

58. Ghosh, P.K., Dorn, L. and **Issler, L.,** [1994], "Fatigue crack growth behaviour of pulsed current MIG weld of Al-Zn-Mg alloy", *International Journal on Joining of Materials*, Vol. 6(4): pp. 163-168.

59. **Ghosh, P.K.** and Rai, B.K., [1998], "Correlations of pulse parameters and bead characteristics in pulsed current flux cored GMAW process", *Indian Welding Journal*, Vol. 31(4), pp.30-39.

60. **Ghosh, P.K.** and Sharma, V., [1991], "Weld bead chemistry and its characteristics in pulsed MIG welded Al-Zn-Mg alloy", *Materials Transactions JIM*, Vol. 32(2), pp.145-150.

61. **Ghosh, P.K.**, [1996], "An analysis of weld characteristics as a function of pulse current MIG welding parameters", *International Journal on Joining of Materials*, Vol. 8(4), pp. 157-161.

62. **Ghosh, P.K.,** Dorn, L**.,** and Goecke, S.F. [2001], "Universality of co-relationships among pulse parameters for different MIG welding power sources", *International Journal on Joining of Materials*, Vol. 13(2), pp. 40-47.

63. **Ghosh, P.K.,** Goyal, V. K., Dhiman, H.K., Kumar, M., [2006] "Thermal and metal transfer behaviour in pulsed current GMA weld deposition of Al-Mg alloy", *Sci.*

Technol. Weld. Joining, Vol. 11(2), pp. 232-42.

64. **Ghosh, P.K.**, Dorn, L., Hubner, M. and Goyal, V.K., [2007 (a)], "Arc characteristics and behaviour of metal transfer in pulsed current GMA welding of aluminium alloy", *Journal of Materials Processing Technology*, Vol. 194, pp. 163-175.

65. **Ghosh, P.K.**, Kulkarni, S.G., Kumar, M. and Dhiman, H.K., [2007 (b)], "Pulsed current GMAW for superior weld quality of austenitic stainless steel sheet", *ISIJ International,* Vol. 47(1), pp. 138–45.

66. Ghosh, P.K., Kumar, R., 2015. Surface Modification of Micro-Alloyed High-Strength Low-Alloy Steel by Controlled TIG Arcing Process. Metall. Mater. Trans. A 46, 831–842.

67. **Ghosh, P.K.**, Dorn, L., Kulkarni, S. and Hoffmann, F., [2008], "Arc characteristics and behaviour of metal transfer in pulsed current GMA welding of stainless steel", *Journal of Material Processing Technology*, Vol. 209, pp. 1262-1274.

68. **Goyal, V.K.,** Ghosh, P.K., Saini, J.S., [2008 (b)] "Analytical studies on thermal behaviour and geometry of weld pool in pulsed current gas metal arc welding", *J. Met. Proc. Tech*, Vol. 209, pp. 1318-1336.

69. Grigoruants A. G., [1994], "Basics of Laser Material Processing", CRC Press, Florida, pp. 150-160.

70. **Grum J.**, [2007], "Comparison of different techniques of laser surface hardening.", J. Achiev. Mater., Vol. 24, pp. 17–25.

71. **Grum J.** and Ferlan D., [1997], "Residual internal stresses after induction hardening and grinding.", In: Proceedings of the 17th ASM Heat Treating Society Conference, Indianapolis, Indiana, 1997, pp 629–639.

72. **Grum, J.**, Božič, S. and Zupančič, M., [2001], "Influence of quencing process parameters on residual stresses in steels.", Metalurgija, Vol. 40, pp. 0–13.

73. Guguloth, K., Sivaprasad, S., **Chakrabarti, D.** and Tarafder, S., [2014], "Low-cyclic fatigue behavior of modified 9Cr-1Mo steel at elevated temperature.", Mater. Sci. Eng. A, Vol. 604,pp. 196–206.

74. **Guile, A. E.,** [1984], "Electric arcs: their electrode processes and engineering applications.", IEE Proc. A Phys. Sci. Meas. Instrumentation, Manag. Educ. Rev., Vol. 131(7), pp.450-480.

75. Häßler, M., Rose, S., **Füssel, U.**, Schneider, H.I. and Werner, C., [2014], "TIG narrow gap welding -new approaches to evaluate and improve the shielding gas coverage and the energy input.", Weld. World, Vol. 59, pp. 71–76.

76. Hertel, M., **Füssel, U.** and Schnick, M., [2014], "Numerical simulation of the plasma-MIG process - Interactions of the arcs, droplet detachment and weld pool formation.", Weld. World, Vol. 58, pp. 85–92.

77. Hidekazu M.,, B. Miloslav, V. Adan, R. Sherif, D. Catrin, D. David, N.K., 2008. Residual stress measurements in laser clad repaired low pressure turbine blades for the power industry. Trans. Join. Weld. Res. Inst. 37, 75–80.

78. **Inoue, T.**, Nagaki, S., Kishino, T. and Monkawa, M., [1981], "Description of transformation kinetics, heat conduction and elastic-plastic stress in the course of quenching and tempering of some steels.", Ingenieur-Archiv, Vol. 50, pp. 315–327.

79. **Ivanov Y.F.**, Rotshtein V.P., Proskurovsky D.I., Orlov P.V., Polestchenko K.N., Ozur G.E. and Goncharenko I.M., [2000], "Pulsed electron-beam treatment of WC–TiC–Co hard-alloy cutting tools: wear resistance and microstructural evolution.", Surface and Coatings Technology, Vol. 125:1-3, pp. 251-256.

80. **Ivanov Y.**, Matz W., Rotshtein V., Günzel R. and Shevchenko N., [2002], "Pulsed electron-beam melting of high-speed steel: structural phase transformations and wear resistance.", Surface and Coatings Technology, Vol. 150:2-3, pp. 188-198.

81. **Ji-Liang, D.,** Tsyr-Jang, C., Yen-Hung, T., 1989. Effect of laser surface hardening on fatigue crack growth rate in AISI-4130 steel. Eng. Fract. Mech. 33, 483–491.

82. **Joshi, A**., Yogesha, K.K., Jayaganthan, R., 2017. Influence of cryorolling and followed by annealing on high cycle fatigue behavior of ultrafine grained Al 2014 alloy. Mater. Charact. 127, 253–271

83. **Kah, P.**, Martikainen, J., [2013], "Influence of shielding gases in the welding of metals.", Int. J. Adv. Manuf. Technol., Vol. 64, pp. 1411–1421.

84. **Kanchanomai C.** and Limtrakarn W., [2008], "Effect of Residual Stress on Fatigue Failure of Carbonitrided Low-Carbon Steel." Journal of Materials Engineering and Performance, Vol. 17(6) , pp. 879–887.

85. **Karl-Erik T.**, [1984], "Steel and Its Heat Treatment", Sec. editin, Oxford publication, Sweden.

86. Karmakar, A., Sahu, P., Neogy, S., **Chakrabarti, D.,** Mitra, R., Mukherjee, S., Kundu, S., [2017], "Effect of Cooling Rate and Chemical Composition on Microstructure and Properties of Naturally Cooled Vanadium-Microalloyed Steels.", Metall. Mater. Trans. A, Vol. 48 (4), pp. 1–15.

87. **Khan, T.I.**, Rizvi, S.A. and Matsuura, K., [2000], "The effect on wear behaviour of H13 tool steel surfaces modified using a tungsten arc heat source.", Wear, Vol. 244, pp. 154–164.

88. **Kim, W.H.** and Na, S.-J., [1998], "Heat and fluid flow in pulsed current GTA weld pool.", Int. J. Heat Mass Transf., Vol. 41, pp. 3213–3227.

89. **Kobasko, N.I.**, Totten, G.E.L and Canale, C.F., [2007], "Intensive Quenching: Improved Hardness and Residual Stress.", Heat Treatment of Metals, Vol. 32 (5), pp. 84–89.

90. **Kobasko, N.I.**, [2010], "Stress State of Steel Parts During Intensive Quenching." ASTM International.

91. **Kobasko, N. I.**, [2012], "Steels of optimal chemical composition combined with intensive quenching.", Int. Heat Treat. Surf. Eng., Vol. 6, pp. 153–159.

92. **Kogoh S,** Ogino H, Nakagawa T, Kobayashi M, Asami K. Fatigue strength of spheroidal graphite cast iron at elevated temperatures under axial load. Int J Fatigue, 1990;12:199–205.

93. **Korkut, M.H.**, Yilmaz, O. and Buytoz, S., [2002], "Effect of aging on the microstructure and toughness of the interface zone of a gas tungsten arc (GTA) synthesized Fe-Cr-Si-Mo-C coated low carbon steel.", Surf. Coatings Technol., Vol.157, pp. 5–13.

94. **Kumar P.**, Kolhe K. P. and Morey S. J, [2011], "Process Parameters Optimization of an Aluminium Alloy with Pulsed Gas Tungsten Arc Welding (GTAW) Using Gas Mixtures.", Mater. Sci. Appl., Vol. 2, pp. 251–257.

95. **Kobasko, N. I.** and Morganyuk V. S., [1985], "Numerical Study of Phase Changes, Current and Residual Stresses in Quenching Parts of Complex Configuration," Proceedings of the 4Th International Congress on Heat Treatment of Materials, Berlin, Germany, Vol. 1, pp. 465-486.

96. **Kolbus L. M. S**, Payzant E. A. , Cornwell P. A. , Watkins T. R. , Babu S. S. , Dehoff R. R. , Lorenz M. , Ovchinnikova O. ,and Duty C. [2015], "Comparison of Residual Stresses in Inconel 718 Simple Parts Made by Electron Beam Melting and Direct Laser Metal Sintering", Metallurgical and Materials Transactions A, Vol. 46 (3), pp. 1419–1432.

97. **Kristoffersen H.** and Vomacka P., [2001], "Influence of process parameters for induction hardening on residual stresses." Materials & Design, Vol. 22 (8), pp. 637–644.

98. Kumar, R., Ghosh, P.K., Kumar, S., 2017. Thermal and metallurgical characteristics of surface modification of AISI 8620 steel produced by TIG arcing process. J. Mater. Process. Technol. 240, 420–431.

99. **Kumar, A.** and Sundarrajan, S., [2009], "Optimization of pulsed TIG welding process parameters on mechanical properties of AA 5456 Aluminum alloy weldments.", Mater. Des., Vol. 30, pp. 1288–1297

100. **Lai, J.**, Huang, H., Buising, W., [2016]. ScienceDirect ScienceDirect Effects of microstructure and surface roughness on the fatigue strength of high-strength steels modeling of Huang a high pressure turbine blade of an airplane gas turbine engine. Procedia Struct. Integr. 2, 1213–1220.

101. Lakhkar, R.S., Shin, Y.C., Krane, M.J.M., 2008. Predictive modeling of multi-track laser hardening of AISI 4140 steel. Mater. Sci. Eng. A 480, 209–217.

102. **Lee, W.-S.,** Su, T.-T., [1999]. Mechanical properties and microstructural features of AISI 4340 high-strength alloy steel under quenched and tempered conditions. J. Mater. Process. Technol. 87, 198–206.

103. **Lee M.K.,** Kim G.H., Kim K.H., Kim W.W., [2006], "Effects of the surface temperature and cooling rate on the residual stresses in a flame hardening of 12Cr steel.", Journal of Materials Processing Technology, Vol. 176 (3), pp. 140–145.

104. **Lee, S. C.** and Ho Weio-Youe, [1989] "The effects of surface hardening on fracture toughness of carburized steel.", Metallurgical Transactions A, Vol. 20 (3), pp. 519-525.

105. **Leggatt, R.H.**, [2008], "Residual stresses in welded structures.", Int. J. Press. Vessel. Pip., Vol. 85, pp. 144–151.

106. **Leskovšek, V.,** Podgornik, B. and Nolan, D., [2008], "Modelling of residual stress profiles in plasma nitrided tool steel." Materials Characterization, Vol. 59 (4), pp. 454-461.

107. **Lin R.** and Ericsson T., [1992] "Fatigue endurance limit and residual stress of steels surface hardened by rapid heating.", In: Proceedings of the 3rd ECRS, Frankfurt/Main, Germany, 4–6/11, pp 505–514.

108. **Li, P.J.** and Zhang, Y.M., [2001], "Precision Sensing of Arc Length in GTAW Based on Arc Light Spectrum.", J. Manuf. Sci. Eng., Vol. 123 (1), pp. 62-65.

109. Liu, A.F., 2005. Mechanics and Mechanisms of Fracture, first ed. ed. ASM International, Ohio

110. Liu Y, Yu JJ, Xu Y, Sun XF, Guan HR, Hu ZQ. High cycle fatigue behavior of a single crystal superalloy at elevated temperatures. Mater Sci Eng A, 2007;454–455:357–66.

111. **Liu, Q.**, Yang, C.H., Ding, K., Barter, S.A. and **Ye, L.**, [2007], "The effect of laser power density on the fatigue life of laser-shock-peened 7050 aluminium alloy", Fatigue & Fracture of Engineering Materials & Structures, Vol. 30, pp. 1110-1124.

112. Llaneza, V., Belzunce, F.J., 2015. Study of the effects produced by shot peening on the surface of quenched and tempered steels: Roughness, residual stresses and work hardening. Appl. Surf. Sci. 356, 475–485.

113. Mandal, S., Tewary, N.K., Ghosh, S.K., **Chakrabarti, D.** and Chatterjee, S., [2016], "Thermo-mechanically controlled processed ultrahigh strength steel: Microstructure, texture and mechanical properties.", Mater. Sci. Eng. A, Vol. 663, pp. 126–140

114. **Mangonon, P. L.**, [1976], "Effect of alloying elements on the microstructure and properties of a hot-rolled low-carbon low-alloy bainitic steel.", Metallurgical Transactions A, Vol. 7(9), pp 1389–1400.

115. **Manti, R.** and Dwivedi, D.K.,[2007], "Microstructure of Al-Mg-Si weld joints produced by pulse TIG welding.", Mater. Manuf. Process., Vol. 22, pp. 57–61.

116. Manvatkar, V.D., Gokhale, A.A., Jagan Reddy, G., Venkataramana, A. and **De, A.,** [2011], "Estimation of melt pool dimensions, thermal cycle, and hardness distribution in the laser-engineered net shaping process of austenitic stainless steel.", Metall. Mater. Trans. A Phys. Metall. Mater. Sci., Vol. 42, pp. 4080–4087.

117. **Matlock, D.K.**, Alogab, K. A. and Richards, M.D., Speer, J.G., [2005], "Surface processing to improve the fatigue resistance of advanced bar steels for automotive applications.", Mater. Res., Vol. 8, pp. 453–459.

118. **Mazar Atabaki**, M., Nikodinovski, M., Chenier, P., Ma, J., Liu, W., Kovacevic, R., [2014], "Experimental and numerical investigations of hybrid laser arc welding of aluminum alloys in the thick T-joint configuration.", Opt. Laser Technol., Vol. 59, pp. 68–92.

119. **McDaniels, R.L.,** White, S.A., Liaw, K., Chen, L., McCay, M.H., Liaw, P.K., [2008]. Effects of a laser surface processing induced heat-affected zone on the fatigue behavior of AISI 4340 steel. Mater. Sci. Eng. A 485, 500–507.

120. **Mencík J.**, [2013], "Mechanics of Components with Treated or Coated Surfaces." Springer Science & Business Media, Vol. 42.

121. **Messler, R. W. Jr.,** [1999], "Principles of welding" *John Wiley and sons*, New York.

122. **Meyers M.A.** and Wittman C.L., 1990, "Effect of metallurgical parameters on shear band formation in low-carbon (ý 0.20 Wt Pct) steels.", Metall. Trans. A, Vol. 21, pp. 3153–3164.

123. **Ming D. J.** and Yih-fong, T., [2004], "Optimisation of electron-beam surface hardening of cast iron for high wear resistance using the Taguchi method.", Int. J. Adv. Manuf. Technol., Vol. 24, pp. 190–198.

124. **Mohamadzadeh, H.**, Saghafian, H. and Kheirandish, S., [2009], " Sliding Wear Behavior of a Grey Cast Iron Surface Remelted by TIG.", Mater. Sci. Technol., Vol. 25, pp. 622–628.

125. **Mohanty, O.N.**, [1994], "Residual stresses in heat treatment.", Tata steel, Jamshedpur,http://eprints.nmlindia.org/5773/1/pp1-9.PDF.

126. **Mohseni, E.**, Zalnezhad, E., Sarhan, A.A.D. and Bushroa, A.R., [2014], "A Study on surface modification of al7075-t6 alloy against fretting fatigue phenomenon.", Adv. Mater. Sci. Eng., Vol. 2014, pp. 17.

127. Montross, C.S., Wei, T., **Ye, L**., Clark, G. and Mai, Y.W., [2002], "Laser shock processing and its effects on microstructure and properties of metal alloys: A review.", Int. J. Fatigue Vol. 24, pp. 1021–1036.

128. **Madhusudhan Reddy, G**., Srinivasa Rao, K., 2015. Microstructure and corrosion behaviour of gas tungsten arc welds of maraging steel. Def. Technol. 11, 48–55.

129. **Murphy, A.B.**, Tanaka, M., Yamamoto, K., Tashiro, S., Sato, T. and Lowke, J.J., [2009], "Modelling of thermal plasmas for arc welding: the role of the shielding gas properties and of metal vapour.", J. Phys. D. Appl. Phys., Vol 42, pp. 20.

130. **Murphy, A. B.**, Tanaka, M., Tashiro, S., Sato, T. and Lowke, J.J., [2009], "A computational investigation of the effectiveness of different shielding gas mixtures for arc welding.", J. Phys. D. Appl. Phys., Vol. 42, pp. 115-205.

131. **Murphy, A. B.**, Tanaka, M., Yamamoto, K., Tashiro S, Sato, T. and Lowke, J. J. [2009], "Modelling of thermal plasmas for arc welding: the role of the shielding gas properties and of metal vapour." Journal of Physics D: Applied Physics, Vol. 42(19), pp. 20.

132. Murugan, N. and **Parmar, R.S.,** [1994], "Effect of MIG process parameters on the geometry of the bead in the automatic surfacing of stainless steel", *Journal of Material Processing Technology*, Vol. 41: pp. 381-398.

133. **Nadkarni, S. V.**, [2010], "Modern Arc Welding Technology", Ador Welding Limited, New Delhi.

134. **Nascimento, M.P.,** Souza, R.C., Miguel, I.M., Pigatin, W.L., Voorwald, H.J.C., [2001]. Effects of tungsten carbide thermal spray coating by HP/HVOF and hard chromium electroplating on AISI 4340 high strength steel. Surf. Coatings Technol. 138, 113–124.

135. **Needham, J.C.,** [1965], "Pulse controlled consumable electrode welding arcs", *British welding Journal*, Vol. 12(4), pp. 191-197.

136. **Nemchinsky, V.A.,** [1997], "Electrode evaporation in an arc with pulsing current", *Journal of Physics D: Applied Physics*, Vol. 30, pp. 2895–2899.

137. **Nemkov, V.S.** and Goldstein, R.C., A., [2004], "Design Principles for Induction Heating and Hardening Processing.", Handbook of Metallurgical process design, pp. 591-640.

138. **Nguyen N.T.,** Matsuoka Ohta, K., and Maeda Y., "Analytical Solutions for Transient Temperature of Semi-Infinite Body Subjected to 3-D Moving Heat Sources.", Weld. Res. Suppl. I, pp. 265–274.

139. **Norman, A.F.,** Drazhner, V. and Prangnell, P.B., [1999], "Effect of welding parameters on the solidification microstructure of autogenous TIG welds in an Al–Cu–Mg–Mn alloy.", Mater. Sci. Eng. A, Vol. 259, pp. 53–64.

140. **Orlowicz, A.U.W.,** Trytek, A., [2005], "Use of the GTAW method for surface hardening of cast-iron.", Weld. Int., Vol. 19, pp. 341–348.

141. **Ormanova M.,** Petrov P and Kovacheva D., [2017], " Electron beam surface treatment of tool steels.", Vacuum, Vol. **135**, pp. 7-12.

142. **Pal, K.** and Pal, S.K., [2011], "Effect of pulse parameters on weld quality in pulsed gas metal arc welding: A review.", J. Mater. Eng. Perform., Vol. 20, pp. 918–931.

143. Panfil, D., Kulka, M., Wach, P., Michalski, J., Przestacki, D., 2017. Nanomechanical properties of iron nitrides produced on 42CrMo4 steel by controlled gas nitriding and laser heat treatment. J. Alloys Compd. 706, 63–75

144. **Panjan, P.,** Drnovšek, A., Kovač, J., [2018]. Tribological aspects related to the morphology of PVD hard coatings. Surf. Coatings Technol. 343, 138–147.

145. **Parmar R.S,** [1997], "Welding engineering and technology", Khanna publishers, pp.530-532.

146. Pashby, I. R., **Barnes, S.** and Bryden, B. G., [2003], "Surface hardening of steel using a high power diode laser.", Journal of Materials Processing Technology, Vol. 139, pp. 585-588.

147. Patel, P., Mridha, S., Baker, T.N., 2014. Influence of shielding gases on preheat produced in surface coatings incorporating SiC particulates into microalloy steel using TIG technique. Mater. Sci. Technol. 30, 1506–1514

148. **Picraux, S.T.** and L.E. Pope, [1984], "Tailored surface modification by ion implantation and laser treatment.", Science, Vol. 226, pp. 615-622.

149. **Phillips, I.T.S.**, Costa, K.D., I, R., Chambers and T. V, Hill, R., [1994], "Pulse welding process." United States Patent No. US4273988 A.

150. **Poursaiedi, E.,** Salarvand, A., [2016]. Effect of Coating Surface Finishing on Fatigue Behavior of C450 Steel CAPVD Coated with (Ti,Cr)N. J. Mater. Eng. Perform. 25, 3448–3455.

151. Prakash G. G., Pramod S. L., Chandran Prathap, Zhang Cheng, Agarwal Arvind, Fabijanic Daniel, and **Bakshi Srinivasa Rao.,** [2013], "Microstructure and wear properties of Ni-Cu-Cr-Al multi-component coatings prepared by plasma spraying", **TMS Annual Meeting and Exhibition**, San Antonio, USA

152. **Praveen, P.**, Yarlagadda, P.K.D.V. and Kang, M.J., [2005], "Advancements in pulse gas metal arc welding", *Journal of Materials Processing Technology*, Vol. 164–165, pp. 1113–1119.

153. **Przybylowicz, K.,** [1999], "Advantages and limitations of steel boronizing process.", Inzynieria Materialowa, Vol. 20(5), pp. 251-254.

154. **Qi, B.J.**, Yang, M.X., Cong, B.Q. and Liu, F.J., [2013], "The effect of arc behavior on weld geometry by high-frequency pulse GTAW process with 0Cr18Ni9Ti stainless steel.", Int. J. Adv. Manuf. Technol., Vol. 66, pp. 1545–1553.

155. Qiu, Y., Pang, J.C., Zhang, M.X., Zou, C.L., Li, S.X., Zhang, Z.F., 2018. Influence of temperature on the high-cycle fatigue properties of compacted graphite iron. Int. J. Fatigue 112, 84–93

156. **Quintino, L.** and Alllum, C.J., [1984], "Pulsed GMAW: Interactions between process parameters, Part I", *Welding and Metal Fabrication*, Vol. 16(4), pp. 126-129.

157. **Rajasekaran, S.**, Kulkarni, S.D., Mallya, U.D. and Chaturvedi, R.C., [1998], "Droplet detachment and plate fusion characteristics in pulsed current gas metal arc welding", *Welding Journal*, Vol. 6, pp. 254s-268s.

158. Rajeev G.P., Kamaraj M., and **Srinivasa R. Bakshi.,** [2014] "Comparision of Stellite Coatings on Valve Steel Material Prepared by Plasma Transferred Arc and Cold Metal Transfer Techniques." **2014 TMS Annual Meeting and Exhibition**, San Diego, USA.

159. **Randhawa, H.S.**, Ghosh., P.K., and Gupta, S.R., [2000], "Some basic aspects of geometrical characteristics of pulsed current vertical-up GMA weld", *ISIJ International*, Vol. 40 (1), pp. 71-76.

160. **Randhawa, H.S.**, Ghosh., P.K., and S.R. Gupta, [1998], "Geometric characteristics of pulsed current positional GMA weld", *ISIJ Int.*, Vol. 38(4), pp. 276-284.

161. Ray, A., Arora, K.S., Lester, S., **Shome, M**., [2014], "Laser cladding of continuous caster lateral rolls: Microstructure, wear and corrosion characterisation and on-field performance evaluation.", J. Mater. Process. Technol., Vol. 214, pp. 1566–1575.

162. **Razzak, M.A.**, [2012], "Heat treatment and effects of Cr and Ni in low alloy steel.", Mater. Sci., Vol. 34, pp. 1439–1445.

163. **Reddy G. M.**, Gokhale A. A. and Rao, K.P., [2013], "Optimisation of pulse frequency in pulsed current gas tungsten arc welding of aluminium–lithium alloy sheets.", Materials Science and Technology, Vol. 14(1), pp. 61-66.

164. **Reddy G. M.**, and Mohandas, T., [2001], "Explorative studies on grain refinement of ferritic stainless steel welds", Journal of Materials Science Letters, Vol. 20: pp.721–723.

165. Reich, M., Osten, J., Milkereit, B., Kalich, J., **Füssel, U.** and Kessler, O., [2014], "Short-time heat treatment of press hardened steel for laser assisted clinching." Mater. Sci. Technol., Vol. 30, pp. 1287–1296.

166. **Renk T.J.**, Provencio P.P., Prasad S.V., Shlapakovski A.S., Petrov A.V., Yatsui K., Jiang W and Suematsu H., [2004], "Materials modification using intense ion beams.", Proceedings of the IEEE, Vol. 92(7), pp. 1057-1081.

167. **Richard L. L**, [1973], "Welding and Welding Technology", McGraw Hill, 1st edition, Newyork.

168. **Rosenthal, D.**, [1941], "Mathematical theory of heat distribution during welding and cutting." Welding Res. Suppl., pp. 220s-234s.

169. **Rotshtein, V.P.**, Proskurovsky, D.I., Ozur, G.E., Ivanov, Y.F. and Markov, A.B., [2004], "Surface modification and alloying of metallic materials with low-energy high-current electron beams.", Surface and Coatings Technology , Vol. 180-181, pp. 377-381.

170. **Rowan, O.K.**, Sisson, R.D., [2009], "Effect of Alloy Composition on Carburizing Performance of Steel.", J. Phase Equilibria Diffus., Vol 30, pp. 235–241.

171. **Sadowski, A.J.,** Rotter, J.M., Reinke,T., Ummenhofer,T. [2015],"Statistical analysis of the material properties of selected structural carbon steels", Structural Safety, Vol. 53C: pp.26-35.

172. Samanta, S., Das, S., **Chakrabarti, D.,** Samajdar, I., Singh, S.B. and Haldar, A., [2013], "Development of multiphase microstructure with bainite, martensite, and retained austenite in a Co-containing steel through quenching and partitioning (Q&P) treatment.", Metall. Mater. Trans. A, Phys. Metall. Mater. Sci., Vol. 44, pp. 5653–5664.

173. **Saedi, H.R.** and Unkel, W., [1988], "Arc and Weld Pool Behavior for Pulsed Current GTAW.", Weld. Res. Suppl., pp. 247s-255s.

174. **Saeidi, N.,** Ekrami, A., 2009. Comparison of mechanical properties of martensite/ferrite and bainite/ferrite dual phase 4340 steels. Mater. Sci. Eng. A 523, 125–129.

175. **Sakai T.,** Morita Y., Iwao T. and Yumoto M., [2010], "Heat transfer and heat efficiency of pulsed arc as a function of current frequency.", IEEE International Conference on Plasma Science.

176. Sandip, P. H., **Srinivasa R. Bakshi** and Arvind Agarwal, [2013], "Recent Developments in Surface Engineering of Materials.", **JOM,** Vol. 65, pp. 739-740.

177. **Schmich, E.,** Schillinger, N., Reber, S., [2007]. Silicon CVD deposition for low cost applications in photovoltaics. Surf. Coatings Technol. 201, 9325–9329.

178. Schnick M, **Fuessel U.,** Hertel M, Haessler M, Kohoff A S and Murphy A. B. [2010], "Modelling of gas–metal arc welding taking into account metal vapour" J. Phys. D: Appl. Phys.,Vol. 43, pp 11.

179. Schnick, M., Rose, S., **Füssel, U.,** Mahrle, A., Demuth, C. and Beyer, E., [2012], "Experimental and Numerical Investigations of the Interaction between a Plasma Arc And a Laser.", Weld. World, Vol. 56, pp. 93-100.

180. **Schöpfel A.** and Störzel. K., [1997], "Optimization of process parameters for induction heat treating by means of numerical simulation.", In: Proceedings of the 17th ASM Heat Treating Society Conference including the 1st International Heat Treating Symposium, Indianapolis, pp. 595–600.

181. **Selvakumar, N.,** Barshilia, H.C., 2012. Review of physical vapor deposited (PVD) spectrally selective coatings for mid- and high-temperature solar thermal applications. Sol. Energy Mater. Sol. Cells 98, 1–23.

182. Shariff S. M., **Pal, T. K.,** Padmanabham and G., Joshi, [2010], " Sliding wear behaviour of laser surface modified pearlitic rail steel.", Surface Engg., Vol. 26, pp.199-208.

183. **Shipley, R.J.** and Moore, D.A., [2002], "ASM Handbook-Analysis of Distortion and Deformation." Vol. 11, pp. 1047–1058.

184. **Shirali, A.A.** and Mills, K.C., [1993], "The effect of Welding Parameters on Penetration in GTA Welds.", Weld. J., pp. 347s–353s.

185. Singh, A., **Srinivasa R. B.,** Agarwal A. and Sandip P. Harimkar, [2010], "Microstructure and Tribological Behavior of Spark Plasma Sintered Iron-based Amorphous Coatings", Materials Science and Engineering A, Vol. 527, pp. 5000-5007.

186. **Shome, M.,** [2007], "Effect of heat-input on austenite grain size in the heat-affected zone of HSLA-100 steel.", Mater. Sci. Eng. A, Vol. 445-446, pp.454–460.

187. **Shome, M.** and Mohanty, O.N., [2006], "Continuous cooling transformation diagrams applicable to the heat-affected zone of HSLA-80 and HSLA-100 steels.", Metall. Mater. Trans. A, Vol. 37,pp. 2159–2169.

188. **Shome, M.,** Gupta, O.P. and Mohanty, O.N., [2004], "A modified analytical approach for modelling grain growth in the coarse grain HAZ of HSLA steels.", Scr. Mater., Vol. 50, pp. 1007–1010.

189. **Shome, M.,** Gupta and Mohanty, O.N., [2004], "Effect of simulated thermal cycles on the microstructure of the heat-affected zone in HSLA-80 and HSLA-100 steel plates." Metall. Mater. Trans. A., Vol. 35, pp. 985–996.

190. Sirin, S.Y., Sirin, K., Kaluc, E., [2013]. Influence of initial conditions on the mechanical behavior of ion nitrided AISI 4340 steel. Mater. Sci. Eng. A 564, 232–241.

191. Sirin, S.Y., Sirin, K., Kaluc, E., [2008]. Effect of the ion nitriding surface hardening process on fatigue behavior of AISI 4340 steel. Mater. Charact. 59, 351–358.

192. Sirin, S.Y., Kaluc, E., 2012. Structural surface characterization of ion nitrided AISI 4340 steel. Mater. Des. 36, 741–747

193. Speidel, A., Lutey, A.H.A., Mitchell-Smith, J., Rance, G.A., Liverani, E., Ascari, A., Fortunato, A., **Clare, A.,** [2016], "Surface modification of mild steel using a combination of laser and electrochemical processes.", Surf. Coatings Technol., Vol. 307, pp. 849–860.

194. **Stava, E. K**., [1990], "Method and apparatus for TIG welding.", U.S. Patent No. 4,947,021.

195. **Stephan, E.**, Johannes, Z., Roland, B., Roland, N., Gerhard, P and Bernd, R., [2015], "Advanced Gas Tungsten Arc Weld Surfacing Current Status and Application.", Soldag. Inspeção, Vol. 20(3), pp. 300–314.

196. **Stott, F.H.**, Wood, G.C. and Stringer, J., [1995], "The influence of alloying elements on the development and maintenance of protective scales.", Oxid. Met., Vol. 44, pp. 113–145.

197. **Sun, S.** Da, Liu, Q., Brandt, M., Luzin, V., Cottam, R., Janardhana, M., Clark, G., [2014]. Effect of laser clad repair on the fatigue behaviour of ultra-high strength AISI 4340 steel. Mater. Sci. Eng. A.

198. **Suresh, M.V.**, Vamsi Krishna, B., Venugopal, P. and Prasad R. K., [2004], "Effect of pulse frequency in gas tungsten arc welding of powder metallurgical preforms.", Sci. Technol. Weld. Join., Vol. 9, pp. 362–368.

199. **Tadamalle A.P.**, Ramjee E. and Reddy K. V, [2014],"Estimation of Weld Pool Geometry and Cooling Rate in Laser Welding", All India Manufacturing Technology, Design and Research Conference, pp. 1–7.

200. **Terent, V.F.,** Michugina M.S., Kolmakov A.G., Kvedaras V., Čiuplys V., Čiuplys A. and Vilys J., [2007], "The effect of nitriding on fatigue strength of structural alloys." Mechanika, Vol. 2(64), ISSN 1392 - 1207.

201. **Tewary N.K.**, Syed B., Ghosh S.K., Kundu S., Shariff S.M. and Padmanabham G., [2014], "Microstructural evolution and mechanical behaviour of surface hardened low carbon hot rolled steel.", Mater. Sci. Eng. A., Vol. 606, pp. 58–67.

202. **Thompson,** A.W., Chesnutt, J.C., 1979. Identification of a fracture mode: the tearing topography surface. Metall. Trans. A 10, 1193–1196

203. **Tong, Z.**, Zhentai, Z. and Rui, Z., [2013], "A dynamic welding heat source model in pulsed current gas tungsten arc welding.", J. Mater. Process. Technol., Vol. 213, pp. 2329–2338.

204. **Totten, G. E.**, [2002], "Handbook of Residual Stress and Deformation of Steel.", ASM International, Ohio,USA

205. **Traidia A.** and Roger F. [2011], "Numerical and experimental study of arc and weld pool behaviour for pulsed current GTA welding.", International Journal of Heat and Mass Transfer, Vol. 54, pp. 2163–2179.

206. **Traidia, A.**, Roger, F. and Guyot, E., [2010], "Optimal parameters for pulsed gas tungsten arc welding in partially and fully penetrated weld pools.", Int. J. Therm. Sci., Vol. 49, pp. 1197–1208.

207. **Tsai, C.L.** and Hou, C.A., [2013], "Theoretical Analysis of Weld Pool Behavior in the Pulsed Current GTAW Process.", J. Heat Transfer, Vol. 110, pp. 160–165.

208. **Tseng,** K.H. and Chou, C.P., [2001], "Effect of pulsed gas tungsten arc welding on angular distortion in austenitic stainless steel weldments."Science and Technology of Welding and Joining, Vol. 6(3), pp. 149-153.

209. **Ummenhofer,T.,** Weidner,P., [2013],"Improvement factors for the design of welded joints subjected to high frequency mechanical impact treatment", Steel construction, Vol.6(3): pp.191-199.

210. **Uzlov, I. G.** and Danchenko, N. I. [1971] "Effect of cooling rate during quenching on the properties of carbon steel", Metal Science and Heat Treatment,Vol.13(5), pp 407–409.

211. **Venkatramani**, **N.,** [2002], "Industrial plasma torches and applications.", Curr. Sci., Vol. 83, pp. 254–262.

212. Walker, J.C., Cook, R.B., Murray, J.W., **Clare, A.T**., [2013], "Pulsed electron beam surface melting of CoCrMo alloy for biomedical applications.", Wear, Vol. 301, pp. 250–256.

213. **Wang, L**., Wood, R.J.K. and Sun, J.,[2008], "Unlubricated metal on metal sliding contact and its acoustic emission signatures.", 3rd World Congress on Engineering Asset Management and Intelligent Maintenance Systems Conference, Springer11, pp. 1614-1624.

214. **Wavare S. B.** and. Ramgir M. S, [2015], Magnetic Arc Blow in Arc Welding Affects Weld Bead Parameters**,** J. Mat. Sci. Mech. Engg., Vol. 2, pp. 38-40.

215. Wei, D., Wang, X., Wang, R., Cui, H., [2018]. Surface modification of 5CrMnMo steel with continuous scanning electron beam process. Vacuum 149, 118–123.

216. Wood W.A., [1955], Bull.Inst.Met., vol.3, Sep., pp.5-6.

217. Yang, C.H., Hodgson, P.D., Liu, Q.C. and **Ye, L.,** [2008], "Geometrical effects on residual stresses in 7050-T7451 aluminum alloy rods subject to laser shock peening", Journal of Materials Processing Technology, Vol. 201(1-3), pp. 303-309.

218. **Yang, M.,** Qi, B., Cong, B., Liu, F., Yang, Z., [2013], "Effect of pulse frequency on microstructure and properties of Ti-6Al-4V by ultrahigh-frequency pulse gas tungsten arc welding.", Int. J. Adv. Manuf. Technol., Vol. 68, pp. 19–31.

219. Yang, Y., Yan, M.F., Zhang, S.D., Guo, J.H., Jiang, S.S., Li, D.Y., 2018. Diffusion behavior of carbon and its hardening effect on plasma carburized M50NiL steel: Influences of treatment temperature and duration. Surf. Coatings Technol. 333, 96–103.

220. **Yasumoto, K.**, Nagamichi, T, Yasuhiro, Maehara, Y. and Gunj, K, [1987], "Effects of alloying elements and cooling rate on austenite grain growth in solidification and the subsequent cooling processes of low alloy steels." I.S.I.J, Vol. 73(14), pp. 1738-1745.

221. Yilbas, B.S., 2017. Laser Beam Processing for Surface Modifications, in: Comprehensive Materials Finishing. Elsevier, pp. 137–153

222. Yip, M. W., **Barnes, S.** and Sarhan, A., [2014], "Effects of laser cladding of silicon carbides particles and iron based powder.", Applied Mechanics and Materials, Vol. 548-549, pp. 289-293.

223. Yip, M W, **Barnes, S.,** [2013], "CO2 laser cladding of mild steel using iron based powder and silicon carbide particles.", 4th International Conference on Material and Manufacturing Technology (ICMMT 2013), Seoul, Korea, 11-12 May 2013, Published in Advanced Materials Research: Material and Manufacturing Technology IV, pp. 269-272.

224. Yip, M. W., **Barnes, S.** and Sarhan, A., [2014], "Effects of laser cladding of silicon carbides particles and iron based powder.", 3rd International Conference on Informatics, Environment, Energy and Applications (IEEA 2014), Shanghai, China.

225. **Yousefieh, M.**, Shamanian, M. and Saatchi, A., [2011], "Influence of Heat Input in Pulsed Current GTAW Process on Microstructure and Corrosion Resistance of Duplex Stainless Steel Welds.", J. Iron Steel Res. Int., Vol. 18, pp. 65–69.

226. Zähr, J., **Füssel, U.**, Hertel, M., Lohse, M., Sende, M. and Schnick, M.,[2012], "Numerical and Experimental Studies of the Influence of Process Gases in Tig Welding Numerical and Experimental Studies of the Influence of Process Gases in Tig Welding.", Weld. World, Vol. 56, pp. 85–92.

227. Zhao, T., Jiang, Y., [2008]. Fatigue of 7075-T651 aluminum alloy. Int. J. Fatigue 30, 834–849.